MEASUREMENT OF THE CHARGED CURRENT MUON NEUTRINO DIFFERENTIAL CROSS SECTION ON SCINTILLATOR WITH ZERO PIONS IN THE FINAL STATE WITH THE T2K ON/OFF-AXIS NEAR DETECTORS.

By

Andrew Bruce Cudd

A DISSERTATION

Submitted to
Michigan State University
in partial fulfillment of the requirements
for the degree of

Physics – Doctor of Philosophy

2020

ABSTRACT

MEASUREMENT OF THE CHARGED CURRENT MUON NEUTRINO DIFFERENTIAL CROSS SECTION ON SCINTILLATOR WITH ZERO PIONS IN THE FINAL STATE WITH THE T2K ON/OFF-AXIS NEAR DETECTORS.

By

Andrew Bruce Cudd

The Tokai to Kamioka (T2K) is a long-baseline neutrino oscillation experiment in Japan producing precise measurements of neutrino oscillations and neutrino interactions with nuclear targets. T2K utilizes a muon (anti-)neutrino beam produced at the J-PARC proton accelerator facility which is measured at a suite of near detectors, ND280 and INGRID, and the far detector, Super-Kamiokande. One of the dominant systematic uncertainties for the oscillation analysis is from the uncertainty in neutrino interaction modeling with complex nuclei, which will eventually become the limiting uncertainty for the next generation of neutrino oscillation experiments. Therefore measurements of neutrino cross sections on nuclear targets is essential for understanding how to model these complicated nuclear interactions.

This thesis presents a novel neutrino cross section measurement utilizing both of the T2K near detectors, ND280 and INGRID, in a joint statistical fit. Because the T2K near detectors are exposed to neutrinos from the same beamline, the uncertainties in the neutrino flux prediction will be correlated. This fact combined with the different neutrino energy spectra seen at each detector will allow for some separation of flux and cross section effects, and presents an opportunity to study the neutrino cross section as a function of energy using the same neutrino beam. This analysis is the first cross section measurement on T2K to use samples from multiple detectors in the same beamline. This thesis presents a description of the statistical analysis framework, the event selection, the treatment of systematic uncertainties, and the extracted ν_μ CC-0π double differential cross section in bins of muon kinematics for ND280 and INGRID, including the correlations between the detectors.

ACKNOWLEDGEMENTS

Despite the fact that there is only a single author on this thesis, there are numerous people who helped me write this titanic document which captures the last five years or so of my work and life (which when divided evenly equates to roughly 6.8 days of my life per page at the time of writing). Truly this work and I stand on the shoulders of giants.

I want to thank my parents, Lisa and Steven, and sister, Megan, for supporting me from the beginning and all throughout school. Thank you for the never ending encouragement to follow my interests and ideas, especially when they included building an arcade cabinet that remains in your garage, and for always being there when life was both great and awful. I now will finally join the rest of the family in holding an advanced degree and no longer being a student.

This thesis would not have been possible in the slightest without the guidance of my advisor, Kendall. Thank you for taking the risk of hiring me as your first graduate student and pushing me to succeed, even when I had zero idea what I was doing. I appreciate immensely how you managed to fit me in your schedule nearly whenever I needed to talk about my analysis, or more recently, my job search, and all the excitement you have for science which helped remind me that my work is more than just making pretty plots. You are the best advisor.

A huge thanks to all of my fellow T2K collaborators who have all contributed in some way to my thesis analysis, from helping run the experiment to providing necessary software, data inputs, and discussion. In particular I want to thank (in no particular order), Stephen, Ciro, Margherita, Callum, Benjmain, and Dan for all their knowledge and expertise on cross section analyses and statistical fitting. Luke for being my postdoc/T2K collaborator and helping me out with whatever I needed with my analysis, and for being a model of good code. Lucie for testing my fit software and finding all sorts of bugs, and then patiently waiting for me to wake up and fix them due to the time zone difference. Yue and Mitchell and the rest

of the US/Canada T2K group for making Minouchi a fun place to stay. Mark Hartz and Nakaya-san for helping me apply for fellowships and Mark hosting me when I succeeded that one time. Thank you to rest of T2K for making this an incredible experiment and welcoming experience (and for giving me a reason to travel to Japan).

Thank you to the MSU T2K/DUNE group for making the office a fun place work all these years. Thank you Jacob for the valuable discussions on T2K work, ROOT issues, and sports, and for accompanying me while traveling Japan. Thank you Jake and Dan for participating in our team building exercises (i.e. playing Smash), for providing a non-T2K perspective when I needed it for my analysis, and for trusting me to give you advice on your analyses (even if it was bad).

A good work–life balance was essential for surviving my time in graduate school. The life part would not have been nearly as fun and satisfying without Bryan, Lisa, Sean, Zak, and (math) Brandon being my regular gaming group. The weekends playing board games and rolling dice was a necessary escape from the stress of graduate school life, and a great space to complain about all that stress. I will miss our usual fall traditions of willingly getting lost in a maze of corn and picking apples.

Thank you to the MSU support staff, particularly Brenda and Kim, for making nearly all the administrative work invisible to me. Brenda, thanks for helping me schedule my numerous flights and travel arrangements. Kim, thanks for helping me and Kendall figure out what we were supposed to be doing to get me graduated. Dean and Mike, thanks for taking the time to help me out whenever I needed it in the lab, especially when it included detonating a barrel full of water using LN2. Thank you Carl for getting me kick started at MSU and writing all those reference letters.

Finally, DOE Support provided by U.S. DOE Award DE-SC0015903.

TABLE OF CONTENTS

LIST OF TABLES

LIST OF FIGURES

CHAPTER 1

EXECUTIVE SUMMARY

1.1 Analysis overview

The analysis presented in this thesis is a measurement of the neutrino cross section on plastic scintillator in a simultaneous fit of muon neutrino interactions in the T2K near detectors, ND280 and INGRID. The primary goal of the analysis is to provide the first correlated measurement between the two near detectors, and to provide a new analysis framework for future combined detector measurements on T2K. Chapter 2 and Chapter 3 provide background on neutrino theory, the motivation, and an introduction to the T2K experiment. Chapter 4 describes the data and MC input to the statistical fit, Chapter 5 describes the model assumptions used for the prediction and how they are included in the fit, and Chapter 6 describes the fit and the output used to calculate the cross section. Finally Chapter 7 describes the validation of the analysis and Chapter 8 presents the results. A simple flow chart of the analysis is shown in Fig. 1.1 to emphasize the design of the measurement.

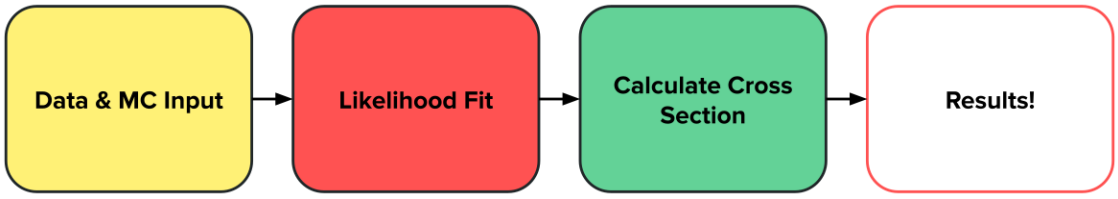

Figure 1.1: Simple flow chart diagram of the major steps of the analysis. Chapter 4 details the data and MC input, Chapter 6 details the likelihood fit and cross section calculation, and Chapter 8 shows the results.

This is the first T2K analysis to perform a joint cross section measurement using detectors at different positions in the neutrino beam. The different positions in the neutrino beam produce different neutrino flux distributions that are highly correlated. The flux correlations can be used to reduce the overall flux uncertainties and produce a correlated cross section

measurement. The resulting cross section will be a unique data set to compare to theoretical and empirical models including the T2K tuned model used for the T2K oscillation analysis.

1.2 Specific contributions

The work presented in this thesis is built upon existing analyses and effort from the T2K collaboration and is properly referenced and cited where applicable. In addition to performing the analysis, I contributed new and original components to make this analysis possible which are briefly summarized here. This goal of this analysis is to perform a joint statistical fit of two existing analyses (one from ND280 and one from INGRID) which are largely used in their original forms but were updated in several ways by myself. The ND280 analysis was processed using the latest MC updates/corrections, newer versions of internal T2K software, and uses newly collected data. The INGRID analysis was updated to match the systematic uncertainty treatment as the ND280 analysis. I also helped develop the multinucleon shape uncertainty and parameterization used in this analysis and used in the T2K oscillation analysis.

The joint measurement requires a unified treatment of the flux model between the two analyses. I ran the T2K beam and flux simulation to create the necessary inputs for this analysis, and I produced the official T2K flux result for the 2017 winter oscillation analysis. Additionally, I fixed several bugs in the flux simulation, improved the scripts used to run the simulation chain, and wrote the new flux simulation documentation.

The majority of my contributions are in developing the next version of the statistical fitting software which makes the joint fit possible. A new version of the fit software was written to accommodate multiple detectors and is designed to be a generic tool for all T2K cross section analyses, and provides improved performance as analyses increase in complexity. The fit software was parallelized using OpenMP, made configurable via input text files, now includes an improved treatment of Monte Carlo statistical error, and provides built-in principle component analysis to list the major updates. New executables were also written

to perform the transformation of analysis specific inputs into a generic format used in the main fit software. The new code is version controlled via Git and is now being used by other T2K cross section analyses. Finally, I have been exploring new ways to validate cross section analyses and present the data and diagnostics in the most helpful way.

CHAPTER 2

NEUTRINO THEORY

2.1 Introduction to neutrinos

Neutrinos are neutral leptonic fermions that are the second most abundant particle in the universe. Despite the sheer number of neutrinos everywhere, they have remained mysterious with several of their fundamental properties still unknown. Neutrinos interact with other particles only via the weak force and gravity, leading to a frustratingly small probability to have an interaction which can be studied.

Neutrinos were originally postulated in 1930 by Wolfgang Pauli as a possible solution to explain the continuous spectrum observed from nuclear beta decay. The prevailing theory at the time was beta decay was a two-body decay – a nucleus producing an electron and smaller daughter nucleus. The kinematics of a two-body decay are such that each decay product is mono-energetic due to energy and momentum conservation and can be calculated exactly. However, a continuous energy spectrum was observed for the electron when measured which contradicted the two-body assumption. A continuous energy spectrum would be possible if the decay contained more than two particles, or, as suggested at the time, that energy and momentum conservation may not be as universal as once thought. Pauli proposed a third invisible particle was also produced in beta decay to keep energy and momentum conservation; however, it was thought to be undetectable.

In 1934 Enrico Fermi published his theory of beta decay in which a neutron would decay into a proton, electron, and Pauli's proposed particle, which Fermi named a neutrino (meaning "little neutral one"). Additionally, experimental evidence had been collected that refuted the idea that energy conservation was invalid for beta decay, further necessitating the need for this third invisible particle, the neutrino.

In 1951 Reines and Cowan started Project Poltergeist to definitively detect the signature

of a neutrino. The proposed signature was an inverse beta decay reaction where a neutrino interacts with a proton to produce a positron and a neutron, and the gamma rays from positron-electron annihilation would be detected. The goal was to show an increase in annihilation gamma rays when the detector was exposed to a neutrino source compared to without a neutrino source, however the main issue was where to find an intense source of neutrinos. Reines and Cowan's initial idea for a neutrino source was to use the explosion of an atomic bomb and place a detector relatively close to the detonation [6] (sketch of the setup shown in Fig. 2.1). The atomic bomb would produce a large flux of neutrinos in a short pulse minimizing the number of background counts during detection. The proposal to use an atomic bomb was approved by the director of Los Alamos National Laboratory and was considered as the best shot for an experiment at the time.

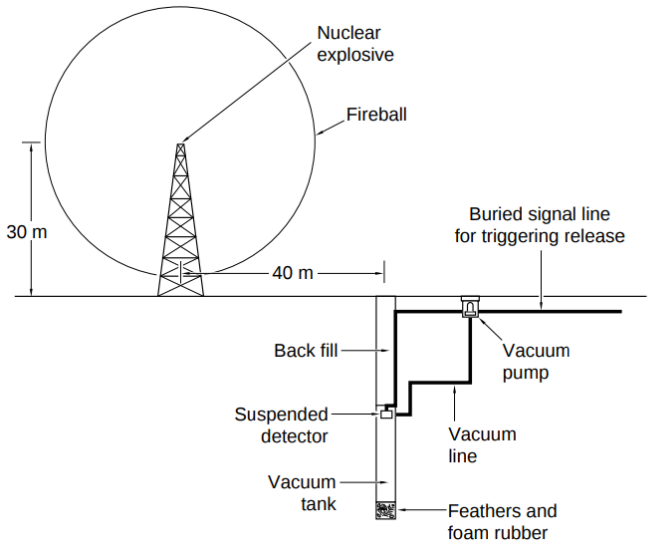

Figure 2.1: Schematic of the proposed experiment to use an atomic bomb as an intense source of neutrinos. Figure from Ref. [6].

Eventually Reines and Cowan were persuaded to instead use the flux of neutrinos from the Savanah River nuclear reactor, and in 1956 had collected conclusive evidence of neutrino detection [18]. The detector observed the inverse beta decay reaction and detected the gamma rays from positron-electron annihilation and neutron capture on cadmium. This two-pulse signature from prompt annihilation and delayed capture gave a robust signal of

neutrino detection compared to background sources.

Less than a decade later, the muon neutrino was discovered by Lederman, Schwartz, and Steinberger *et. al.* using the AGS at Brookhaven National Lab [19]. Not only did this show that neutrinos are paired with a specific lepton, muon neutrinos are separate from electron neutrinos, it was the first demonstration of producing neutrinos using an accelerator. The accelerator was used to create a beam of charged pions that would decay into muons and muon neutrinos. It would then take until the year 2000 for the DONUT collaboration at Fermilab to directly detect the tau neutrino [20], completing the three known generations of leptons. Precision measurements of the Z^0 boson decay width from the LEP collider gave evidence that there exist only three active light neutrinos [21], the three neutrinos known today – the electron, muon, and tau neutrinos.

Parallel to the discovery of each type of neutrino, several experiments were observing anomalies in the flux of neutrinos expected from the sun and the atmosphere when compared to theory. Ray Davis and the Homestake experiment measured the solar neutrino flux and measured a rate of about one third of the expected value from solar models. Both the experiment and the solar models were investigated for deficiencies or errors, but no major errors were found, and the discrepancy remained. Several more experiments such as SAGE [22] and GALLEX [23] continued to observed the deficit of expected solar neutrinos, and it was not until the SNO experiment which was able to solve the puzzle of the missing neutrino flux. In 1969 Gribov and Pontecorvo proposed the electron neutrinos from the sun were oscillating into other flavors of neutrinos due to neutrino mixing [24], an idea Pontecorvo proposed in the late 1950's [25] and Maki, Nakagawa, and Sakata also proposed in 1962 [26]. Measurements from the SNO experiment [27] and the Super-Kamiokande [28] experiment in 2002 and 1998 respectively showed conclusive evidence of neutrino oscillation, with the SNO result showing the lower than expected solar neutrino flux was due to oscillations. The discovery of neutrino oscillations from both SK and SNO would eventually earn the 2015 Nobel Prize in Physics. The measurement of neutrino oscillations also gave conclusive

evidence that neutrinos must have some non-zero mass, otherwise they could not oscillate, instead of being massless as originally included in the Standard Model.

2.2 Neutrino oscillations

2.2.1 Neutrino oscillation theory

The current formalism of neutrino oscillations is the PMNS formalism, originally proposed and developed by Pontecorvo, Maki, Nakagawa, and Sakata [24, 26], and has been highly successful in predicting the effects of neutrino oscillations. The key hypothesis in the PMNS formalism is that neutrinos interact with the weak force in their flavor states, while they propagate through space in their mass state, and the mass and flavor states are superpositions of each other. This section follows a similar procedure to the one presented in Giunti and Kim [29]. Defining the mass eigenstates as $|\nu_k\rangle, k = 1, 2, 3$ and the flavor eigen states as $|\nu_\alpha\rangle, \alpha = e, \mu, \tau$ the superposition of flavor states as mass states can be written as:

$$|\nu_\alpha\rangle = \sum_k U^*_{\alpha k} |\nu_k\rangle \tag{2.1}$$

where $U_{\alpha k}$ is a unitary matrix that describes the mixing between the different eigenstates, commonly called the PMNS matrix (or PMNS mixing matrix). The unitarity condition is to ensure total probability is conserved, or that neutrino oscillation does not cause a net gain or loss of neutrinos. The PMNS matrix is written as a 3×3 matrix with elements corresponding to each of the three flavor and mass eigenstates:

$$U_{\alpha k} = \begin{pmatrix} U_{e1} & U_{e2} & U_{e3} \\ U_{\mu 1} & U_{\mu 2} & U_{\mu 3} \\ U_{\tau 1} & U_{\tau 2} & U_{\tau 3} \end{pmatrix} \tag{2.2}$$

which closely resembles the Cabbibo-Kobayashi-Maskawa (CKM) quark mixing matrix in QCD in form [29]. The superposition of eigenstates allows for a neutrino of created as one flavor to interact as a different flavor after some time or distance of propagation (e.g. an electron neutrino being detected as a muon neutrino after propagation). The neutrino mass

states are eigenstates of the Hamiltonian,

$$\mathcal{H}\left|\nu_k\right\rangle = E_k\left|\nu_k\right\rangle \tag{2.3}$$

$$E_k = \sqrt{\vec{p}^2 + m_k^2}, \tag{2.4}$$

where E_k are the energy eigenvalues in natural units where $\hbar = c = 1$ (which are used throughout the rest of this chapter). The mass eigenstates evolve in time according to the Schrödinger equation which gives

$$\left|\nu_k(t)\right\rangle = e^{-iE_k t}\left|\nu_k\right\rangle. \tag{2.5}$$

The time evolution of the flavor eigenstates can be written using the mass eigenstates and the mixing matrix. Assume a neutrino created with a definite flavor α at time $t = 0$, using Eqs. 2.5 and 2.1 the time evolution of a flavor state is given by

$$\left|\nu_\alpha(t)\right\rangle = \sum_k U_{\alpha k}^* e^{-iE_k t}\left|\nu_k\right\rangle. \tag{2.6}$$

Equation 2.1 can be inverted to express mass states as a superposition of flavor states and applied to Eq. 2.6 to give

$$\left|\nu_\alpha(t)\right\rangle = \sum_\beta \sum_k U_{\alpha k}^* e^{-iE_k t} U_{\beta k}\left|\nu_\beta\right\rangle. \tag{2.7}$$

Thus a neutrino that starts out ($t = 0$) as pure flavor state α becomes a superposition of different flavor states as it propagates through space ($t > 0$). The strength of the mixing is determined by the values of the PMNS mixing matrix, and if the matrix were diagonal no mixing (i.e. oscillation) would take place. The probability of a neutrino to transition (or oscillate) from flavor $\alpha \to \beta$ is given by the following

$$P(\nu_\alpha \to \nu_\beta)(t) = \left|\left\langle \nu_\beta | \nu_\alpha \right\rangle\right|^2 = \sum_{k,j} U_{\alpha k}^* U_{\beta k} U_{\alpha j} U_{\beta j}^* e^{-i(E_k - E_j)t}. \tag{2.8}$$

Assuming the neutrinos are ultrarelativistic ($|\vec{p}| >> m_k$), the dispersion relation can be approximated by expanding the small mass term as

$$E_k \simeq E + \frac{m_k^2}{2E} \tag{2.9}$$

where $E = |\vec{p}|$ is the neutrino energy, neglecting the mass contribution. The difference in energy between flavor states then can be written as

$$E_k - E_j \simeq \frac{\Delta m_{kj}^2}{2E}, \tag{2.10}$$

where Δm_{kj}^2 is the squared mass difference

$$\Delta m_{kj}^2 \equiv m_k^2 - m_j^2. \tag{2.11}$$

Since the neutrinos are ultrarelativistic they travel essentially at the speed of light, allowing for one more approximation of $t = L$, which when put together with the previous approximations gives the familiar neutrino transition probability as a function of neutrino energy and travel distance:

$$P(\nu_\alpha \to \nu_\beta)(L, E) = \sum_{k,j} U_{\alpha k}^* U_{\beta k} U_{\alpha j} U_{\beta j}^* \exp\left(-i \frac{\Delta m_{kj}^2 L}{2E}\right). \tag{2.12}$$

The derivation for anti-neutrinos follows the same pattern and only differs from the neutrino oscillation probability by the complex conjugates of the mixing matrix elements. A different way to write the oscillation probability is to separate the real and imaginary parts of the mixing matrix elements ($U_{\alpha i}$) as follows

$$P(\nu_\alpha \to \nu_\beta)(L, E) = \delta_{\alpha\beta} - 4 \sum_{k>j} \mathfrak{Re}[U_{\alpha k}^* U_{\beta k} U_{\alpha j} U_{\beta j}^*] \sin^2\left(\frac{\Delta m_{kj}^2 L}{4E}\right) \tag{2.13}$$

$$\pm 2 \sum_{k>j} \mathfrak{Im}[U_{\alpha k}^* U_{\beta k} U_{\alpha j} U_{\beta j}^*] \sin\left(\frac{\Delta m_{kj}^2 L}{2E}\right), \tag{2.14}$$

where the positive imaginary term is for neutrinos and the negative imaginary term is for anti-neutrinos. The PMNS matrix is commonly written as a product of three matrices with

a set of mixing angles $\theta_{12}, \theta_{13}, \theta_{23}$ and a complex phase δ:

$$U = \begin{pmatrix} 1 & 0 & 0 \\ 0 & c_{23} & s_{23} \\ 0 & -s_{23} & c_{23} \end{pmatrix} \begin{pmatrix} c_{13} & 0 & s_{13}e^{-i\delta} \\ 0 & 1 & 0 \\ -s_{13}e^{i\delta} & 0 & c_{13} \end{pmatrix} \begin{pmatrix} c_{12} & s_{12} & 0 \\ -s_{12} & c_{12} & 0 \\ 0 & 0 & 1 \end{pmatrix} \tag{2.15}$$

where $c_{ij} = \cos\theta_{ij}, s_{ij} = \sin\theta_{ij}$. The unitarity of the mixing matrix and invariance under phase transformations of the Lagrangian results in requiring only three angles and a phase to completely parameterize the mixing matrix. The (1,2) parameters are commonly referred to as the "solar" parameters, the (1,3) as "reactor" parameters, and the (2,3) as "atmospheric" parameters. The δ is commonly referred to as the Dirac CP violating phase, δ_{CP}. The mixing matrix parameters along with the mass differences between the three active neutrino states form the parameters which govern neutrino oscillations, which are the target measurements for past, current, and future neutrino oscillation experiments.

The above derivation is for neutrino oscillations in a vacuum. When neutrinos propagate through matter, they are subject to an additional effective potential due to coherent interactions with the medium [29]. This extra potential when included in the Hamiltonian alters the neutrino oscillation probability and is known as the Mikheyev–Smirnov–Wolfenstein (MSW) effect (or often simply called matter effects). The matter potential changes sign between neutrinos and anti-neutrinos causing the oscillations in matter to be different between neutrinos and anti-neutrinos. By measuring a resonance in the oscillation spectrum induced by matter effects for either neutrinos or anti-neutrinos, the sign of Δm^2_{32} and thus neutrino mass ordering can be determined. The derivation of the matter effect terms in the neutrino oscillation probability can be found in Chapters 9 and 13 in Ref. [29].

2.2.2 Status of neutrino oscillations

The study and measurement of neutrino oscillations has rapidly progressed since definitive evidence was presented nearly twenty years ago. Most of the parameters that govern neutrino

oscillations have been measured to $\sim 5\%$ precision, summarized in Table 2.1, with the main exception being the charge-parity violating phase δ_{CP}.

Parameter	Best-fit	3σ range
$\Delta m^2_{21}[10^{-5}\ \text{eV}^2]$	7.37	6.93 - 7.96
$\lvert\Delta m^2_{32}\rvert[10^{-3}\ \text{eV}^2], \Delta m^2_{32} > 0$	2.56	2.45 - 2.69
$\lvert\Delta m^2_{32}\rvert[10^{-3}\ \text{eV}^2], \Delta m^2_{32} < 0$	2.54	2.42 - 2.66
$\sin^2\theta_{12}$	0.297	0.250 - 0.354
$\sin^2\theta_{23}, \Delta m^2_{32} > 0$	0.425	0.381 - 0.615
$\sin^2\theta_{23}, \Delta m^2_{32} < 0$	0.589	0.384 - 0.636
$\sin^2\theta_{13}, \Delta m^2_{32} > 0$	0.0215	0.0190 - 0.0240
$\sin^2\theta_{13}, \Delta m^2_{32} < 0$	0.0216	0.0190 - 0.0242
$\delta/\pi, \Delta m^2_{32} > 0$	1.38	2σ: 1.0 - 1.9
$\delta/\pi, \Delta m^2_{32} < 0$	1.31	2σ: 0.92 - 1.88

Table 2.1: Neutrino oscillation parameter values from the PDG [1], which are calculated using a global fit of neutrino data.

Current generation long-baseline (e.g. T2K, NOvA) and atmospheric experiments (e.g. IceCube, SK) focus on precisely measuring $\sin^2\theta_{23}$, Δm^2_{32}, searching for evidence of CP violation through measuring δ_{CP}, and determining the neutrino mass ordering. A comparison of the $\sin^2\theta_{23}, \Delta m^2_{32}$ contours using recent results from a variety of experiments is shown in Fig. 2.2. Out of the three mixing angles, $\sin^2\theta_{23}$ is the least well known, and is a focus of long-baseline experiments. An interesting question is if $\sin^2\theta_{23}$ is maximal (equal to 0.5), which could imply some new underlying symmetry, or if it is non-maximal, which octant it falls in (whether it is greater or less than 0.5).

Long-baseline oscillation experiments measure the neutrino event rate at their far detector and compare it to the expected event rate under the neutrino oscillation hypothesis to extract

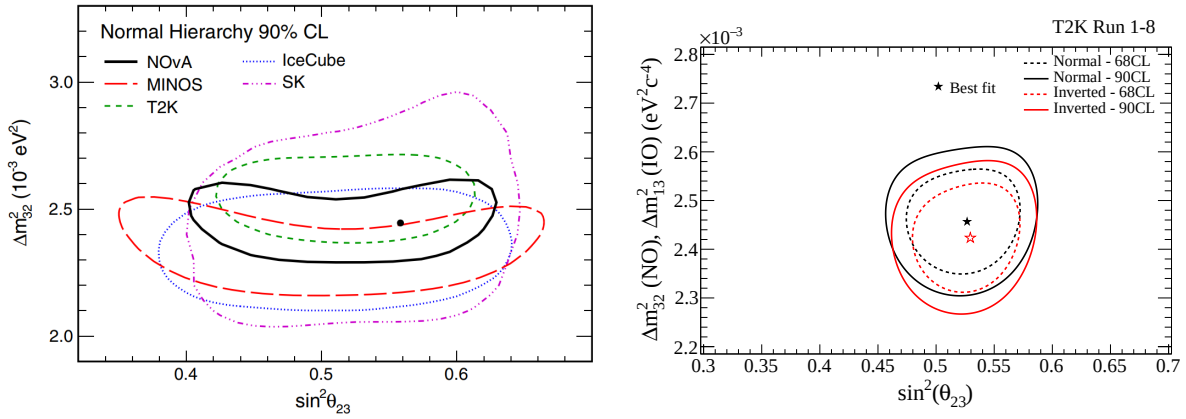

Figure 2.2: Left: Comparison of measured 90% confidence level contours for Δm^2_{32} vs $\sin^2\theta_{23}$ for T2K (2017) [7], NOvA (2018), SK (2018) [8], IceCube (2018) [9], and MINOS (2014) [10]; Fig. from Ref. [11]. Right: Updated 2018 T2K contours including additional data and analysis improvements; Fig. from Ref. [12].

the oscillation parameters. The event rate can be parameterized in the following way,

$$N(\vec{x}) = \int \Phi(E_\nu) \times \sigma(E_\nu;\vec{x}) \times R(E_\nu;\vec{x}) \times P(\nu_i \to \nu_j; E_\nu)\, \mathrm{d}E_\nu \tag{2.16}$$

where $\vec{x}$ are the measured observables, Φ is the neutrino flux, σ is the neutrino cross section, R is the detector response (which includes the efficiency), and $P(\nu_i \to \nu_j)$ is the oscillation probability between neutrinos of flavor i and j (which can be the same). Crucially each term in the rate is a function of the neutrino energy, which is not known a priori. Shown in Fig. 2.3 is the neutrino energy spectra (or neutrino flux) for several different experiments and detectors. Instead the neutrino energy for each interaction must be estimated or reconstructed using the interaction model and from some other observables in the detector, such as the outgoing muon kinematics.

The reconstruction of the neutrino energy is limited by both the resolution of the detector, and the accuracy of the interaction model. Shown in Fig. 2.4 is the neutrino event distribution at SK for the T2K experiment (from Ref. [12]), where a clear dip in muon (anti-)neutrino events can be seen. Roughly speaking, the depth and position of this dip gives the values for $\sin^2\theta_{23}$ and Δm^2_{32} respectively. If the neutrino energy spectrum was systematically lower, for example, it would directly bias the measured value for Δm^2_{32}.

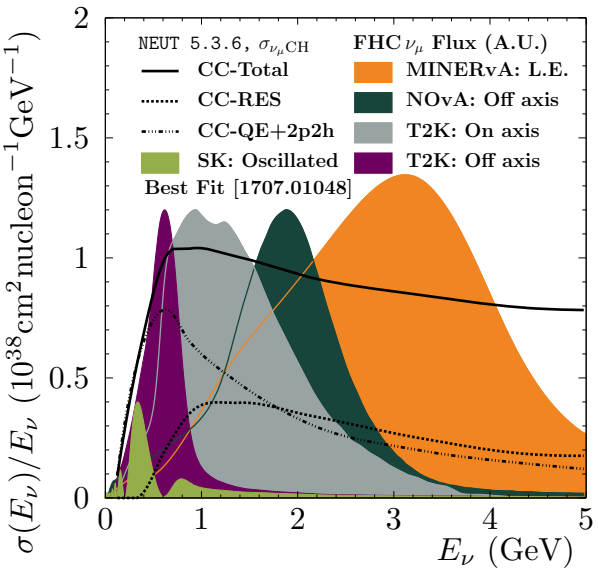

Figure 2.3: The neutrino energy spectrum for the T2K experiment (both on-/off- axis near detectors and far detector after oscillation), plus the neutrino energy spectrum for NOvA and the MINERvA low energy mode. Overlaid are the neutrino cross section predictions for different combinations of interaction channels. Note that the different energy spectra cover a wide energy range where the cross section predictions change rapidly.

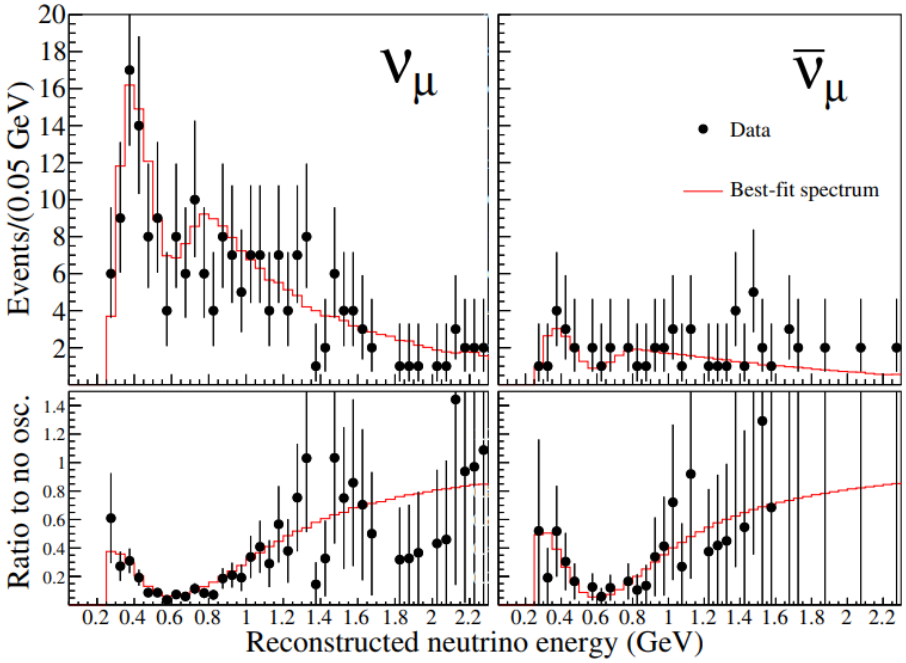

Figure 2.4: Reconstructed energy distributions at SK for the ν_μ (left) and $\overline{\nu}_\mu$ (right) -enriched samples with the total predicted event rate shown in red. Ratios to the predictions under the no oscillation hypothesis are shown in the bottom figures. Figure from Ref. [12].

For T2K and NOvA the current limiting factor to the precision of neutrino oscillation measurements is the collected statistics, however one of the largest systematic uncertainty sources is related to the modelling of neutrino interactions (shown in Fig. 2.5). The next generation long-baseline experiments will collect vast amounts of events, which will require the reduction of the overall impact of the systematic uncertainties to level of a few percent.

	ν_e CCQE-like	ν_μ	ν_e CC1π^+
Source of uncertainty	$\delta N/N$	$\delta N/N$	$\delta N/N$
Flux (w/ ND280 constraint)	3.7%	3.6%	3.6%
Cross section (w/ ND280 constraint)	5.1%	4.0%	4.9%
Flux+cross section			
(w/o ND280 constraint)	11.3%	10.8%	16.4%
(w/ ND280 constraint)	4.2%	2.9%	5.0%
FSI + SI + PN at SK	2.5%	1.5%	10.5%
SK detector	2.4%	3.9%	9.3%
All			
(w/o ND280 constraint)	12.7%	12.0%	21.9%
(w/ ND280 constraint)	5.5%	5.1%	14.8%

Source of uncertainty	ν_e signal (%)	Total beam background (%)
Cross sections and FSI	7.7	8.6
Normalization	3.5	3.4
Calibration	3.2	4.3
Detector response	0.67	2.8
Neutrino flux	0.63	0.43
ν_e extrapolation	0.36	1.2
Total systematic uncertainty	9.2	11
Statistical uncertainty	15	22
Total uncertainty	18	25

Figure 2.5: Effect of the 1σ variations of the systematic uncertainties on the predicted event rate for T2K (left) and NOvA (right). T2K table from Ref. [7] and NOvA table from Ref. [11].

2.3 Neutrino interactions

2.3.1 Interactions on free nucleons

The dominant interaction mode for the analysis presented in this thesis is charged-current quasi-elastic (CCQE) scattering. The interaction consists of W-boson exchange between an incoming neutrino and a nucleon producing a charged lepton and iso-spin flipped nucleon,

$$\nu_\ell + n \to \ell^- + p \tag{2.17}$$

$$\overline{\nu}_\ell + p \to \ell^+ + n \tag{2.18}$$

where $\ell = e, \mu, \tau$. The nucleon is a composite object, comprised of three valence quarks, which prevents the analytic calculation of the cross section for this process. Instead the cross section is parametrized using a series of parameters known as form factors, which can be measured through processes such as beta decay and electron scattering [29, 30]. These form factors characterize the internal charge distribution and structure of a nucleon. Using these form factors, the differential cross section as a function the four-momentum transfer squared (Q^2) in the laboratory frame is given by:

$$\frac{\mathrm{d}\sigma}{\mathrm{d}Q^2} = \frac{m_N^2 G_F^2 |V_{ud}|^2}{8\pi E_\nu^2} \left[A(Q^2) \pm B(Q^2)\frac{s-u}{m_N^2} + C(Q^2)\frac{(s-u)^2}{m_N^4} \right] \tag{2.19}$$

where G_F is the Fermi constant, V_{ud} is an element of the CKM matrix, m_N is the nucleon mass, E_ν is the neutrino energy, the Mandelstam variables s and u, and the $\pm$ is for neutrinos and anti-neutrinos respectively in the Llewellyn Smith formalism [31]. The functions A, B, C of Q^2 are given by:

$$A = \frac{m_\ell^2 + Q^2}{m_N^2}\left\{\left(1+\frac{Q^2}{4m_N^2}\right)F_A^2 - \left(1+\frac{Q^2}{4m_N^2}\right)\left(F_1^2 + \frac{Q^2}{4m_N^2}F_2^2\right) + \frac{Q^2}{m_N^2}F_1F_2 \right.$$
$$\left. - \frac{m_\ell^2}{4m_N^2}\left[(F_1+F_2)^2 + (F_A+2F_P)^2 - \frac{1}{4}\left(1+\frac{Q^2}{4m_N^2}\right)F_P^2\right]\right\} \quad (2.20)$$

$$B = \frac{Q^2}{m_N^2}F_A(F_1+F_2) \quad (2.21)$$

$$C = \frac{1}{4}\left(F_A^2 + F_1^2 + \frac{Q^2}{4m_N^2}F_2^2\right) \quad (2.22)$$

where F_1, F_2, F_A, F_P are the charged current nucleon form factors as a function of Q^2. For electron and muon neutrino interactions the term in A proportional to $m_\ell^2/4m_N^2$ is commonly neglected since the nucleon mass is much larger than the electron or muon mass. The F_1, F_2 form factors are vector form factors in the electroweak current, which are determined through electron scattering. The electromagnetic form factors are assumed to have a dipole functional form when fitting to data, with extensions to the form factors to describe discrepancies seen at high Q^2 [32]. The F_A, F_P terms are the axial vector and pseudoscalar form factors which are present only for neutrino interactions. The pseudoscalar form factor can be written in terms in the axial vector form factor, and analogous to the electromagnetic form factors, the axial vector form factor is commonly assumed to have a dipole functional form which is given by

$$F_A(Q^2) = \frac{g_A}{\left(1+Q^2/M_A^2\right)^2} \quad (2.23)$$

$$F_P(Q^2) = \frac{2m_N^2}{m_\pi^2+Q^2}F_A(Q^2) \quad (2.24)$$

where m_π is the pion mass, and g_A and M_A are free parameters. The g_A parameter can be precisely determined through beta decay measurements, while M_A must be measured through neutrino scattering. The dipole functional form is an assumption which has worked more or less well in the past, however this may no longer be the case as more precise measurements are performed. Different functional forms for the axial vector form factor have been explored, such as the Z-expansion model presented in Ref. [33].

Neutral current quasi-elastic scattering involves the exchange of a Z^0 boson with a nucleon,

$$\nu_\ell + N \rightarrow \nu_\ell + N \tag{2.25}$$

$$\overline{\nu}_\ell + N \rightarrow \overline{\nu}_\ell + N \tag{2.26}$$

where $\ell = e, \mu, \tau$, and N is either a proton or neutron. The formalism to describe the neutral current interaction is very similar to the charged current interaction, with slightly different form factors for the nucleons.

2.3.2 Nuclear medium effects

Neutrino interactions on nucleons within a nucleus incur a myriad of additional effects due to being in a bound state and the presence of other nucleons. These extra effects must be considered for precise modeling of neutrino interactions. Additionally, the nuclear medium allows for further scattering and interactions of the outgoing particles and are further discussed in Section 2.3.6. This section presents a short overview of the key nuclear-medium effects that are included in the interaction modeling for this analysis.

Initial state

The Llewellyn Smith formula detailed in Eq. 2.19 describes neutrinos scattering with free nucleons which have a simple initial state, the free particle. For bound nucleons in a nucleus, an initial state model must be used to provide the initial wave function for the interacting nucleon. The initial state conditions are comprised of Fermi motion of the nucleons, the binding energy of the nucleons, and both short- and long-range interactions between nucleons.

Fermi motion

Fermi motion refers to the motion of the nucleons relative to the nucleus as a whole – the nucleons are not all moving the in the same direction with the same momentum. This initial momentum causes each nucleon to have a different and unknown Lorentz boost in the lab frame for each neutrino interaction [34]. Models which attempt to predict the momentum

distribution of the nucleons are referred to as spectral functions. The most common ones used in neutrino interaction simulations are variations of the Fermi gas model, and the spectral function from Benhar et. al. A good summary of these models can be found in Ref. [35].

Fermi gas models treat the nucleons inside the nucleus as a gas of non-interacting fermions contained inside some nuclear potential well. The nucleons fill momentum states from the lowest momentum state up to some maximum momentum, known as the Fermi momentum (p_F). The Relativistic Fermi Gas (RFG) model [36] assumes the nuclear potential is constant for all nucleons. The assumption of the constant potential gives rise to a sharp cutoff of the momentum distribution at the Fermi momentum (sometimes referred to as the Fermi cliff feature). The more sophisticated Local Fermi Gas (LFG) model [13, 37] instead treats the nuclear potential as a function of the radius of the nucleus, using the local nuclear density $\rho(r)$ where r is the radial position of a given nucleon (commonly referred to as the local density approximation). This smooths out the momentum distribution of the nucleons, removing the sharp cutoff seen in the RFG model. However, like in the RFG model, the LFG model still treats the nucleons as non-interacting.

The spectral function (SF) from Benhar et. al. [38] instead allows for two and three body nucleon–nucleon interactions. The Benhar SF starts with a shell model of the nucleons and considers modifications to the orbitals from the interactions of two and three nucleons and the short range correlations of pairs of nucleons [34, 38]. This results in a smooth initial momentum distribution of nucleons. More sophisticated models for the initial state nucleons exist, such as relativistic mean field models and the relativistic plane wave impulse approximation, but are still in the early stages of being implemented in neutrino simulations [39, 40, 41].

Binding energy

In addition to the Fermi motion, the bound nucleons have an associated binding energy which is required to eject the nucleon from the nucleus. The definition of the binding energy for a given nucleon is dependent on the model being used [42]. The Benhar spectral

function uses the shell model to calculate the binding energy of each nucleon as a probability distribution of Fermi momentum and missing energy. A different method is to have a constant binding energy for each nucleon based on the mass difference between the initial and daughter nucleus and has been used in conjunction with Fermi gas models.

W boson self energy

As mentioned above, it is known that the bound nucleons within a nucleus are correlated within the nuclear potential. One way to describe the long-range correlations between nucleons is the random phase approximation (RPA) [43]. The random phase approximation includes the effect of the nuclear medium providing a screening of the electroweak propagator, which manifests as a Q^2 dependent correction on the neutrino cross section.

Multinucleon Processes

Multinucleon processes refer to interactions which involve multiple correlated nucleons at the interaction vertex (a type of short-range correlation). The neutrino interaction model from Nieves et. al. [13] includes a description of multinucleon processes, which is summarized here as an example. The Nieves et. al. model for multinucleon processes, specifically two-particle two-hole (2p2h) interactions, considers the seven interaction vertices shown in Fig. 2.6 where the virtual pion is connected to a second correlated nucleon (the model also accounts for diagrams where the π is replaced by a ρ propagator).

The vertices are commonly classified into two categories based on the stimulation of a Δ baryon resonance (such as in the top two diagrams in Fig. 2.6); and they can be calculated independently to separate the impact of each on the total 2p2h cross section. The separation of Δ resonance production is due to the regions of kinematic phase space the interactions occupy, due to the higher energy required to excite the Δ resonance. The total strength of the multinucleon process as predicted by the Nieves et. al. model is shown in the right of Fig. 2.6, which clearly shows two different populations. Δ resonance events largely contribute to the population at higher energy and momentum transfer.

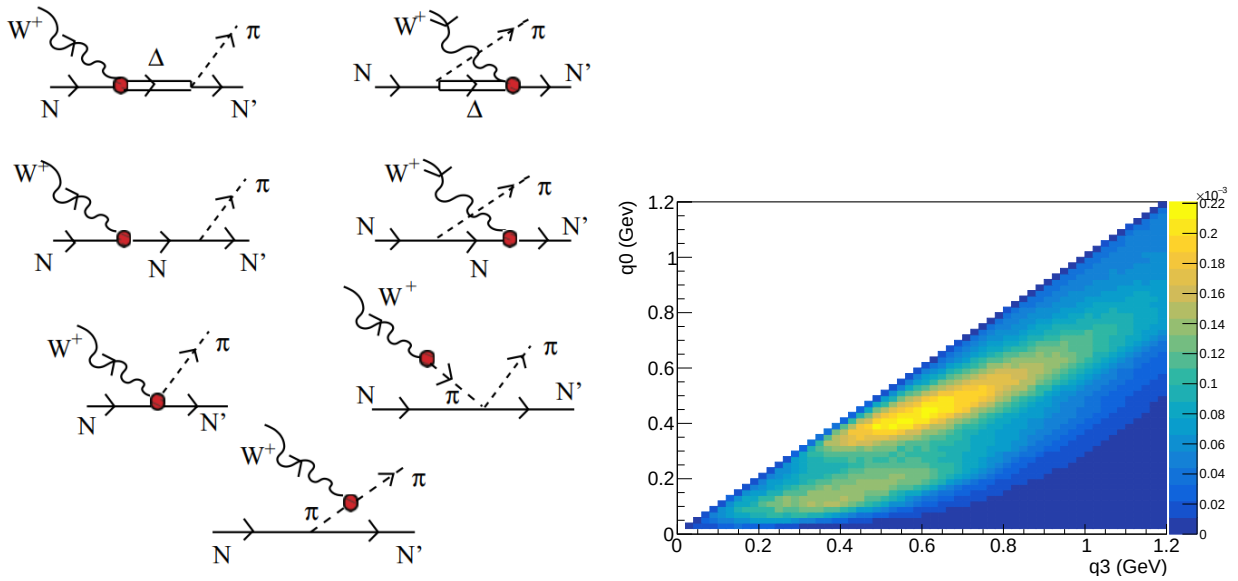

Figure 2.6: Left: The $WN \to N\pi$ vertices considered by the Nieves model for multinucleon processes. Only one nucleon line is shown, the second nucleon is implied to be coupled to the virtual pion. Fig. from Ref. [13]. Right: The distribution of the strength of the multinucleon processes as predicted by the Nieves et. al. model in energy (q_0) and momentum (q_3) transfer space.

2.3.3 Coherent scattering

Coherent scattering occurs when a neutrino scatters coherently with the nucleus, that is the neutrino interacts with the entire nucleus instead of scattering off of a particular nucleon. This is only possible at very low values of Q^2 and can be completely elastic (known as coherent elastic scattering) or produce a pion in the interaction (known as coherent pion production). Coherent pion production is characterized by the following modes, including both charged current and neutral current interactions:

$$\nu_\ell + A \to \nu_\ell + A + \pi^0 \tag{2.27}$$

$$\nu_\ell + A \to \ell^- + A + \pi^+ \tag{2.28}$$

where A is the target nucleus. Coherent pion production is commonly modeled in neutrino interaction simulations using the Rein-Sehgal model [44], but other models such as the Berger-Sehgal model [45] and microscopic models are available [46].

2.3.4 Resonant pion production

Resonant pion production occurs when the incident neutrino has enough energy to excite a nucleon resonance, which can subsequently decay producing one or more pions. The threshold for resonant pion production is the energy needed to excite a Delta baryon and is the dominant interaction channel for the single to few GeV energy region. Many nucleon resonant states (N^* or Δ) contribute to the cross section for resonant pion production, with a strong contribution from the $\Delta(1232)$ resonant state. The single pion production charged-current channels are:

$$\nu_\ell + n \rightarrow \ell^- + n + \pi^+ \tag{2.29}$$

$$\nu_\ell + n \rightarrow \ell^- + p + \pi^0 \tag{2.30}$$

$$\nu_\ell + p \rightarrow \ell^- + p + \pi^+ \tag{2.31}$$

where the intermediate baryon resonance decays back to a proton or neutron and a pion while still in the nuclear medium. The intermediate baryon resonance can also decay into other mesons other than pions, most notably kaons, which is known more generally as resonant meson production.

2.3.5 Shallow and deep inelastic scattering

Eventually the neutrino has enough energy to resolve and scatter off of individual quarks inside the nucleons, a process known as deep inelastic scattering (DIS). There is no precise cut-off between resonant and deep inelastic scattering processes, however a good rule of thumb is the region of $W > 2.0$ GeV and $Q^2 > 1.0$ GeV^2 is primarily only deep inelastic scattering [47]. In deep inelastic scattering a neutrino interacts with a quark inside the target nucleon (N) producing a lepton and a hadronic jet (X):

$$\nu_\ell + N \rightarrow \ell^- + X \tag{2.32}$$

If the nucleon is bound within a nucleus, the interaction is affected by several nuclear medium effects such as initial Fermi motion, nucleon–nucleon correlations, nuclear shadowing, etc. Deep inelastic processes are described using a set of structure functions, which are in turn expressed using parton distribution functions (PDFs). A parton distribution function describes the momentum distribution of the quarks and gluons inside the nucleon.

Shallow inelastic scattering (also referred to as multi-pion production) refers to the transition region between single resonant production and deep inelastic scattering. This region is very challenging to model as it marks the transition from the pion-nucleon description to the quark-gluon description of neutrino interactions [47], and is poorly understood both theoretically and experimentally. Compared to quasi-elastic scattering and resonant pion production, DIS processes are comparatively well modeled at high energy (5 to 10 GeV and higher) [47].

2.3.6 Final state interactions

Particles created in a neutrino interaction must escape the nucleus, propagating through the nuclear medium. The outgoing particles can interact with other nucleons before exiting the nucleus, undergoing scattering, being absorbed, or stimulating additional production of hadrons, which are referred to final state interactions (FSI)[1].

When detecting a neutrino interaction, only the particles which escape the nucleus are seen as the neutrino, being a neutral, weakly interacting particle, is not visible to the detector. Therefore, all the information about the neutrino interaction must be inferred from the produced particles. For example, in the absence of any other interactions, a pion produced in a neutrino interaction would indicate non-quasi-elastic scattering (e.g. single resonant production). Interactions that alter the kinematics or state of these particles before detection will obscure the information about the initial neutrino interaction. To continue the example,

[1]For clarification, in this analysis final state interactions only refer to interactions within the nucleus before the outgoing particles have escaped (if at all).

if the pion produced was subsequently absorbed in the nucleus, the interaction would then appear to be a quasi-elastic scatter rather than pion production. The ejected proton from quasi-elastic scattering could stimulate pion production while exiting the nucleus, again changing what interaction appeared to have taken place at the vertex. Inferring the original vertex interaction would require a model to predict the final state interactions inside the nucleus.

For this reason, modern neutrino interaction experiments define the signal as a function of the final state particles in an event, which are the particles that the detector can measure after any final state interactions have occurred. The combination of final state particles in an event is called the topology of an event. For example, an event which produces a single muon and zero pions is referred to as a CC-0π event, which stands for charged-current zero pion event. Similarly, an event with a single muon and a single charged positive pion would be referred to as a CC-1π^+ event, a charged-current single positively charged pion event. Defining the signal or desired event type by the final state particles is less interaction model dependent as there is no attempt to correct for the unknown processes which occurred inside the nucleus.

2.3.7 Neutrino event generators

The simulation of a neutrino interaction is commonly performed with a Monte Carlo (MC) simulation program known as a neutrino interaction (or event) generator. These neutrino event generators use a variety of theoretical and empirical models to simulate the interaction of a neutrino on some nuclear target (e.g. a free nucleon or a carbon nucleus). The output of an event generator contains the kinematics of each incident neutrino, the kinematics of all outgoing particles, and information about the event such as the simulated reaction (e.g. quasi-elastic or resonant production). Given an input flux of neutrinos (e.g. monoenergetic or based on an experiment), the cross section for a given neutrino process or event topology can be predicted, along with kinematic distributions of the outgoing particles.

A neutrino event generator is the initial step in a chain to produce the expected distributions for experiment, and often used to perform validation checks of analyses and evaluate systematic uncertainties. It is important to understand the limitations of the current iteration of the event generators. The models of neutrino interactions are often only inclusive models, only predicting the lepton kinematics. However, a prediction of the outgoing hadron kinematics is often necessary, but the full calculation of the desired semi-inclusive process either does not exist or may be too expensive to simulate enough events. Modern neutrino generators address this problem by factorizing the simulation of a neutrino event into separate, but manageable pieces. For a simplified example, the neutrino reaction on an initial state nucleon is simulated and lepton kinematics are produced, then the hadron production is simulated separately, and finally the outgoing particles are propagated through the nucleus.

Currently, there are four main neutrino event generators used in experiment for simulation: NEUT [48], GENIE [49], NuWro [50], and GiBUU [51]. Each is primarily developed by a separate group of researchers and uses their own implementations of the included theoretical/empirical models. This can, and often will, give different results for the same predicted interaction process between the different generators.

2.3.8 Current status and motivation

The modern picture of neutrino interaction theory and measurement would best be described as complicated – neither theory nor measurement can paint a consistent picture of neutrino interactions. In fact, an entire workshop series named TENSIONS [52] is dedicated to discussing how measurements not only disagree with theory, but are in tension between different experiments.

The disagreement on the value for the axial mass M_A in the dipole functional form for the axial form factor illustrates the situation nicely. Early measurements of the neutrino CCQE cross section using hydrogen and deuterium bubble chambers resulted in an extracted value of $M_A \sim 1.0$ GeV, which matched the theory well within the experimental uncertainties [53].

However more recent and modern neutrino experiments use complex targets, such as carbon or oxygen nuclei, for which nuclear effects are much more important. The K2K experiment extracted a value of $M_A = 1.21 \pm 0.12$ GeV from interactions on a water (oxygen) target [54], the MiniBooNE experiment extracted a value of $M_A = 1.35 \pm 0.17$ GeV from a CCQE measurement on a scintillator (carbon) target [55], and finally the NOMAD experiment extracted a value of $M_A = 1.05 \pm 0.05$ GeV from a CCQE measurement on a carbon target [56].

Suddenly the measurements no longer agree on the value for the axial mass, but one thing they all have in common is the use of a complex target (compared to hydrogen/deuterium). One prevailing idea is that the lack of multinucleon effects in the prediction (or further nuclear medium effects) can explain the inflated values for M_A seen by MiniBooNE as multinucleon effects should enhance the cross section and allow for a decreased M_A value. Both the Martini et. al. group and the Nieves et. al. group have shown good agreement between their models which include multinucleon effects and the MiniBooNE data while using a value of $M_A \sim 1.0$ GeV [13, 57]. This is one example of tension between experimental data and theory, and there are plenty of other sources of tension.

The precise value of M_A and the nature of multinucleon processes (both normalization and shape) are a couple of the most pressing questions for T2K as they heavily affect quasi-elastic scattering, which is the primary source of signal events for the T2K oscillation analysis. T2K relies on the neutrino interaction model for the mapping from measured muon kinematics to reconstructed energy and any bias will affect the extracted oscillation parameters. Multinucleon processes have the potential to bias the enery reconstruction (as shown in Fig. 2.7) where multinucleon events are systematically biased to lower reconstructed energy. As T2K continues to take more data (including the proposed phase two of running) the uncertainties in the modeling of neutrino interactions will become increasingly important [58], and eventually become the limiting uncertainty for the next generation of neutrino oscillation experiments, such as HyperK [59]. Neutrino scattering and cross section measurements are

critical for improving the understanding of neutrino interactions with matter, which is the main motivation for the analysis presented in this thesis.

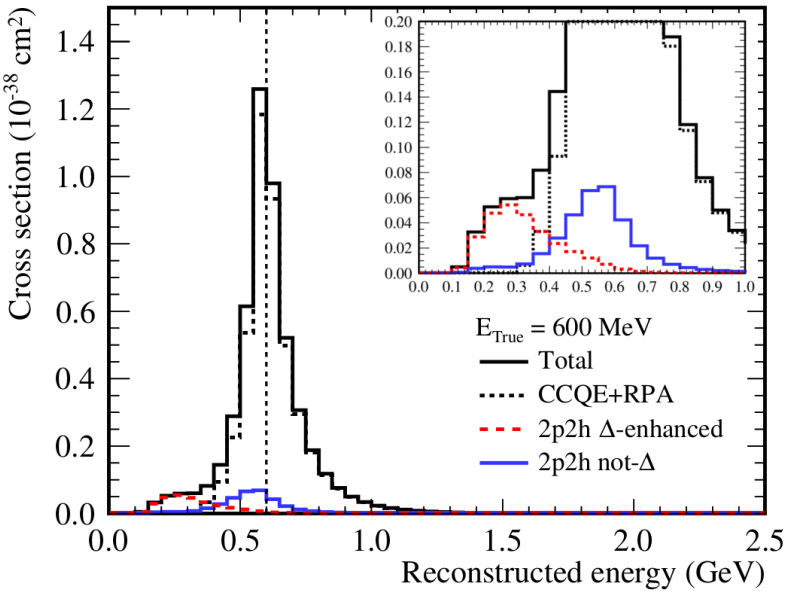

Figure 2.7: Neutrino energy reconstruction calculated for a monoenergetic source of 600 MeV neutrinos, showing the contribution for with and without multinucleon processes. If the reconstruction was perfect, the reconstructed energy would be a delta function at 600 MeV. Instead the reconstructed energy is spread out, and shows a bias toward lower energy from the multinucleon processes. Fig. from Ref. [7].

CHAPTER 3

T2K LONG BASELINE NEUTRINO EXPERIMENT

The Tōkai to Kamioka (T2K) experiment is a long-baseline neutrino oscillation experiment designed to provide measurements of neutrino oscillation parameters. T2K consists of a relatively pure (anti-)muon neutrino beam produced at the J-PARC facility which travels $\sim$ 295 km across Japan to the Super-Kamiokande (SK) detector through a series of detectors positioned 280 meters from the target (shown in Fig. 3.1). T2K studies four channels of neutrino oscillations to measure neutrino oscillation parameters: muon neutrino disappearance ($\nu_\mu \to \nu_\mu$), muon anti-neutrino disappearance ($\bar{\nu}_\mu \to \bar{\nu}_\mu$), electron neutrino appearance ($\nu_\mu \to \nu_e$), and electron anti-neutrino appearance ($\bar{\nu}_\mu \to \bar{\nu}_e$).

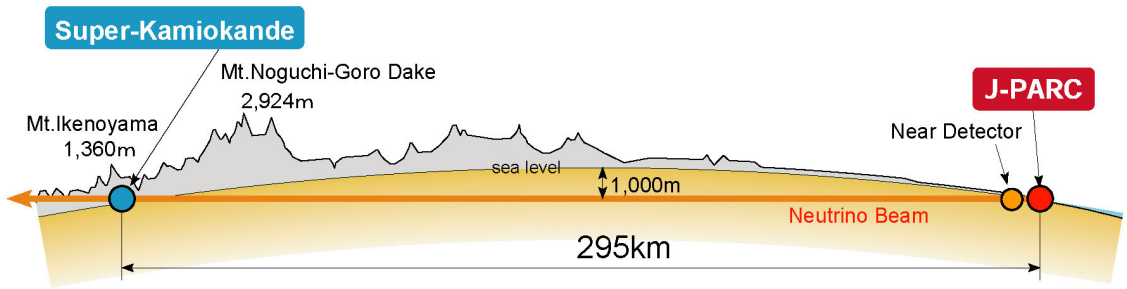

Figure 3.1: Schematic of the T2K experiment showing the location of J-PARC, the near and far detectors, and the 295 km baseline.

The ν_μ disappearance channel is used to make precision measurements of θ_{23} and Δm^2_{32}, while the ν_e appearance channel is used to make measurements of all the oscillation parameters which are accessible by T2K. By comparing the rates between the neutrino and anti-neutrino channels a measurement of the charge-parity violating phase, δ_{CP}, can be performed [7, 12]. The distance to the far detector, SK, is referred to as the baseline. It was chosen since the peak of the neutrino energy spectrum (0.6 GeV) sits at the first oscillation maximum which coincides where the ν_μ survival probability is at a minimum. The ν_e ap-

pearance channel was used to give the first indication of a non-zero value of θ_{13} [60] and the first ν_e appearance measurement in an ν_μ beam [61].

In addition to the neutrino oscillation measurements, T2K has a rich neutrino cross section program producing a variety of high-quality measurements in part due to the well constrained flux from external measurements and a capable well-understood detector. Cross section measurements are important for both understanding the neutrino interaction model used in the oscillation analysis and collaborating with theory groups to improve neutrino modeling. The T2K near detector complex provides a high event rate environment and detector configurations to produce measurements on multiple targets, multiple final states, and multiple flavors of neutrinos. Neutrino cross sections on both carbon and water have been published [62, 63]. Anti-neutrino cross sections on carbon and the ratio with the corresponding neutrino cross section have been performed [64]. New methods of investigating the neutrino cross section have been performed with the single-transverse variables analysis [65] with current analyses looking at using the vertex activity to perform measurements. T2K has produced cross sections both with the on- and off-axis detectors [66], and is investigating methods to use all the detectors in a simultaneous analysis, one of which will be presented in this thesis.

3.1 Beam setup

The T2K neutrino beam is produced at the Japan proton accelerator research complex (J-PARC) in Tōkai-mura, Japan. The initial proton beam is created by accelerating H^- ions in a linear accelerator (LINAC) to 400 MeV/c before passing them to the Rapid Cycling Synchrotron (RCS). The ions pass through a charge stripping foil converting them into H^+ ions (i.e. protons) as they enter the RCS and accelerated to 3 GeV/c. Finally, the protons are passed to the Main Ring (MR) synchrotron and accelerated to a final momentum of 31 GeV/c before being fast extracted into the neutrino beamline. The first section of the neutrino beamline, the primary beamline, bends the proton beam to the direction of SK and

provides final focusing and beam measurements before the protons impinge on a graphite target. A series of beam monitors measure properties of the proton beamline, such as the beam profile and position, to monitor the condition of the proton beam and provide input parameters to the neutrino flux simulation.

The proton collisions with the graphite target produce primarily mesons which are then focused (or deflected) by three magnetic horns. The target is a 91.4 cm long graphite rod 2.6 cm in diameter corresponding to 1.9 interaction lengths for the incident protons which ensures most protons will interact within the target. The three magnetic horns are driven at $\pm$250 kA to produce a large magnetic field (1.7 T) which focus or deflect charged particles depending on the polarity of the current. The positive current mode is known as Forward Horn Current (FHC) mode and produces a primarily neutrino beam from the decay of positively charged particles while the negative current mode is known as Reverse Horn Current (RHC) and produces a primarily anti-neutrino beam from the decay of negatively charged particles. The horns deflect particles with the incorrect sign for the given configuration reducing the background contamination, but this is not perfect and some wrong-sign background remains. Additionally, muons present in the beamline will decay; and, along with other kaon decay modes, produce electron neutrinos adding to the background contaminants. After exiting the magnetic horns, the secondary particles travel through a helium filled decay volume about 96 meters in length and decay to neutrinos. The main neutrino production channels for FHC (neutrino mode) are listed in Tab. 3.1, and the corresponding anti-neutrino production channels are the charge conjugates of the neutrino production channels. Secondary beamline particles which do not decay into neutrinos are stopped by the beam dump at the end of the decay volume except for high momentum muons. Muons with momentum above 5 GeV/c will penetrate through the beam dump and pass through a muon monitor (known as MUMON) which provides measurements of the beam position and intensity from the incoming muon flux. Using MUMON, the neutrino beam direction is determined to be the direction from the target to the center of the muon beam profile.

Decay mode	**Branching fraction (%)**
$\pi^+ \to \mu^+ + \nu_\mu$	99.9877
$\pi^+ \to e^+ + \nu_e$	1.23×10^{-4}
$\mathrm{K}^+ \to \mu^+ + \nu_\mu$	63.55
$\mathrm{K}^+ \to \pi^0 + \mu^+ + \nu_\mu$	3.353
$\mathrm{K}^+ \to \pi^0 + e^+ + \nu_e$	5.07
$\mathrm{K}^0_L \to \pi^- + \mu^+ + \nu_\mu$	27.04
$\mathrm{K}^0_L \to \pi^- + e^+ + \nu_e$	40.55
$\mu^+ \to e^+ + \bar{\nu}_\mu + \nu_e$	100

Table 3.1: Neutrino production decay modes for neutrino beam (FHC) mode.

The T2K neutrino beamline was built using a technique known as an off-axis neutrino beam where the far detector, Super-Kamiokande, is not at the center of the neutrino beam. This was chosen for two main benefits: 1) it produces a narrow neutrino energy spectra at some known energy; and 2), it reduces the rate of wrong-sign ν_e contamination for appearance searches. Most neutrinos in the beam come from pion decay which is a two-body kinematic process. This approach utilizes the fact that the outgoing neutrino energy becomes increasingly independent of parent pion energy as the outgoing neutrino angle (with respect to the parent pion) increases (as shown in Fig. 3.2). The neutrino energy (E_ν) can be approximated using the parent pion energy (E_π) and the neutrino-pion angle ($\theta_{\pi\nu}$) as

$$E_\nu = \frac{m_\pi^2 - m_\mu^2}{2(E_\pi - p_\pi \mathrm{cos}\theta_{\pi\nu})}, \tag{3.1}$$

where m_π, m_μ are the pion and muon mass, and p_π is the pion momentum. The T2K experiment uses an off-axis angle of 2.5 degrees (43.6 mrad) from the beam center chosen to maximize the neutrino flux at the oscillation maximum at SK which occurs at $E_\nu \sim 0.6$ GeV (as shown in Fig. 3.3).

T2K has been collecting data since 2010 and has collected about one third of the planned amount of data. The amount of data collected is given in terms of the number of Protons On Target, or POT. POT is calculated by measuring the current of the proton beam which is used to determine the number of protons in the beam which then collide with the target. The number of protons on target is a good metric for quantifying the data collected since it

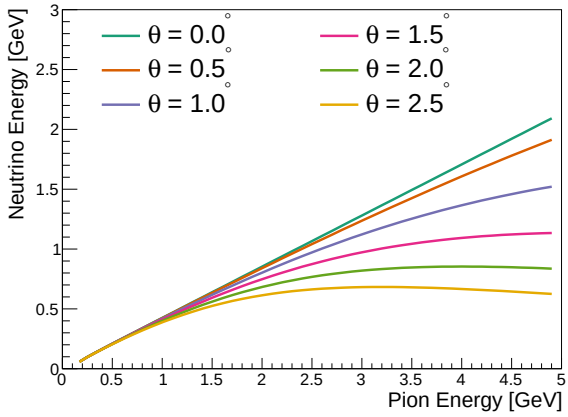

Figure 3.2: Neutrino energy as a function of parent pion energy for various off-axis angles. As the off-axis angle increases, the neutrino energy becomes increasingly independent of the pion energy. T2K uses a 2.5 degrees off-axis beam corresponding to a neutrino energy peak of 0.6 GeV.

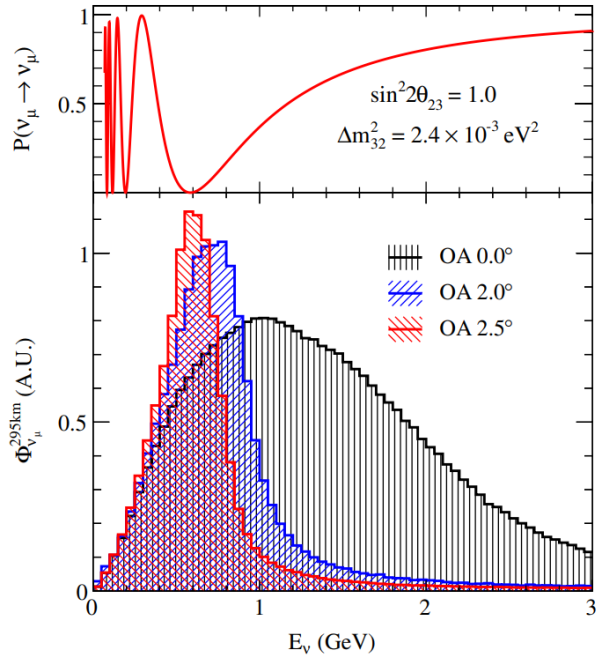

Figure 3.3: The neutrino flux shown at different off-axis angles (arbitrarily normalized) compared to the neutrino oscillation probability. T2K uses a 2.5 degree off-axis beam corresponding to the oscillation maximum at 0.6 GeV. Figure from Ref. [14]

is directly proportional to the amount of beam delivered and its power which can be easily compared to other experiments. The total POT collected over time and the corresponding T2K run periods are displayed in Fig 3.4.

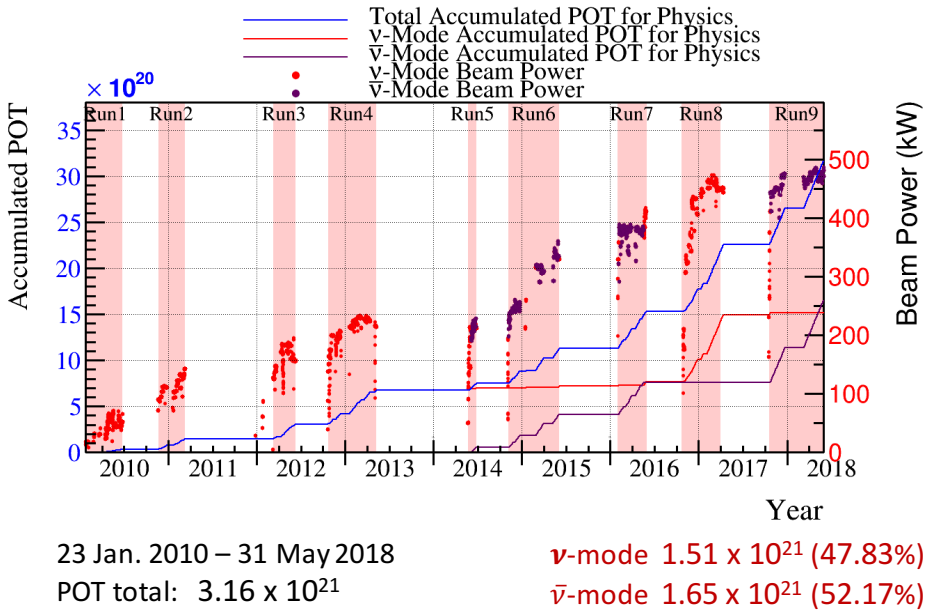

Figure 3.4: Accumulated protons on target for both neutrino and anti-neutrino beam modes and beam power for each T2K data run (the shaded red regions). This analysis uses data from Run 2,3,4 and 8.

3.2 Flux prediction

The prediction of the neutrino flux at the T2K detectors is based on a simulation that begins with the primary proton beam colliding with the graphite target and ending with the decay of the secondary mesons into neutrinos [14]. FLUKA 2011 [67, 68] is used to simulate the initial interactions of the protons inside the target and baffle which produce the majority of the secondary particles. FLUKA is used at this stage because it achieves the best agreement to external hadron production data. The kinematic information of each secondary particle is saved and passed on to JNUBEAM – the next stage of the simulation chain. JNUBEAM is a Geant3 based Monte Carlo simulation which propagates all the

secondary particles from FLUKA through the secondary beamline (magnetic horns, decay volume, etc.), including any further interactions with the material in the secondary beamline which are simulated using GCALOR. The neutrinos produced in the secondary beamline are forced to point to SK or a random point in a near detector plane to save simulation time, and the kinematic information and probability to travel in a given direction for each neutrino are saved in the final output. The final flux and energy spectrum are predicted from the saved events weighted by previously mentioned probabilities. The latest T2K neutrino prediction for forward horn current, separated by neutrino flavor, is shown in Fig. 3.5.

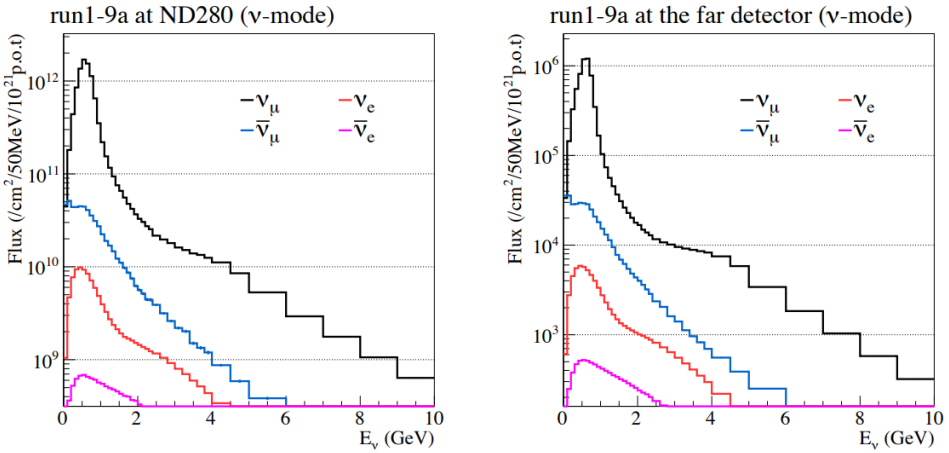

Figure 3.5: The predicted flux at ND280 and SK for forward horn current running separated by neutrino flavor averaged over T2K runs 1-9 [15].

The neutrino flux simulation uses several in-situ measurements from both the primary and secondary beamline as inputs to tune the simulation and verify the output. The primary beamline uses a collection of beam monitors to measure the proton beam profile, beam center, and intensity as it collides with the graphite target as inputs to the FLUKA simulation. Measurements of the average current provided to the three magnetic horns are provided to JNUBEAM to provide accurate magnetic field strengths. Measurements of the muon flux from MUMON and direct measurements of the neutrino flux by the on-axis detector (INGRID) are both used to verify the output of the simulation and track the stability of the neutrino beam.

External data on hadron production and scattering is used to tune and improve the interaction model used by FLUKA and JNUBEAM. The flux simulation primarily relies on external data from the NA61/SHINE experiment for hadron production and the HARP experiment for pion re-scattering [69] along with several other data sets for the kinematic phase space not covered by NA61/SHINE. The NA61/SHINE experiment at the CERN SPS is a dedicated hadron production experiment which uses a 31 GeV/c proton beam and both a thin carbon target (2 cm thickness) and a replica of the T2K target. NA61/SHINE makes measurements of both the total and differential production/multiplicity of hadrons from the target, primarily protons, pions, and kaons, which are the most relevant particles for the T2K flux simulation [70, 71, 72]. The hadron production data are used to tune the multiplicity of exiting hadrons as well as how often hadrons interact within the target and other material in the beamline. The thin-target data has been fully analyzed and included in the T2K flux simulation used in this thesis, while the first round of replica-target data will be included in upcoming T2K analyses.

3.3 The Interactive Neutrino GRID detector

The Interactive Neutrino GRID (INGRID) detector is positioned on-axis at 280 meters downstream of the graphite target [16]. The primary function of INGRID is to provide precise measurements of the neutrino beam center, profile, and rate, and make measurements of various neutrino cross-sections. INGRID consists of sixteen identical modules with 14 arranged in a cross pattern and 2 diagonal off-axis modules extending 10 meters both vertically and horizontally (shown in Fig. 3.6) to span the expected neutrino beam profile.

The center modules of the horizontal and vertical planes overlap with each other and are placed directly on-axis with the primary proton beam. A standard INGRID module is constructed from alternating layers of scintillating bars and iron plates with scintillating veto panels surrounding the module as shown in Fig. 3.6. The iron plates provide a large target mass for neutrino interactions, the inner scintillating bars provide particle tracking,

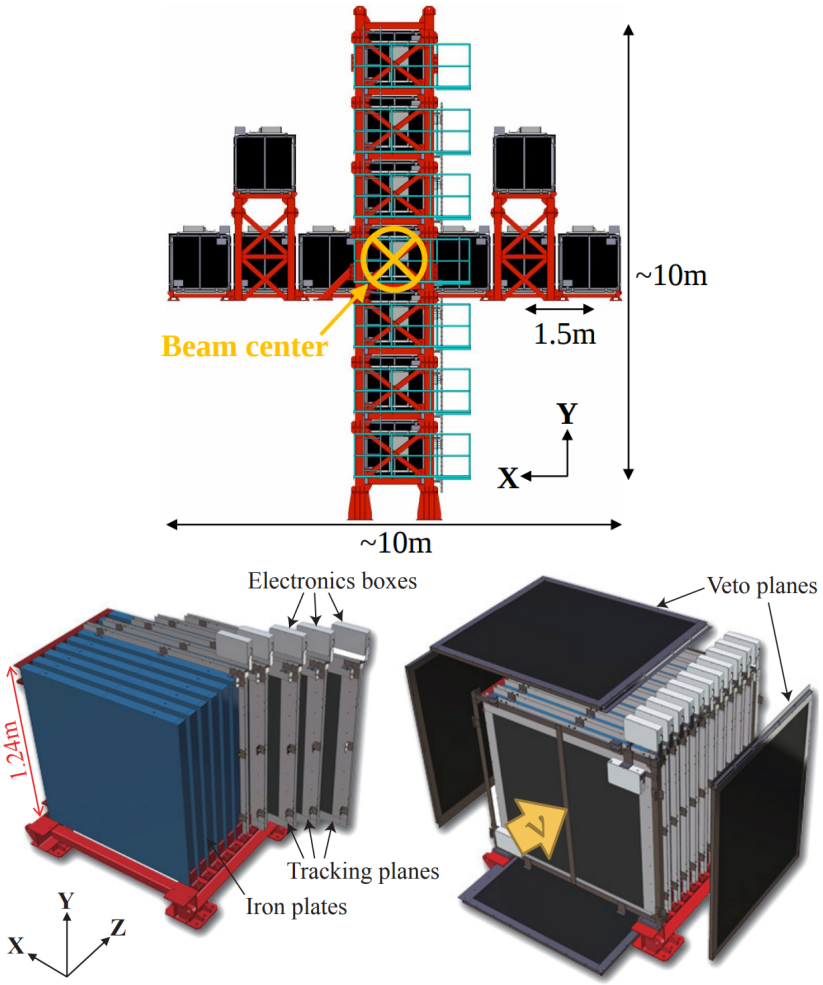

Figure 3.6: The INGRID detector configuration showing the horizontal and vertical planes (top) and a depiction of an INGRID standard module (bottom). The INGRID standard module is shown highlighting the iron plates and inner scintillator panels on the left and the outer veto panels on the right. Figure from Ref. [16].

and outer panels veto particles entering from outside the module. The veto planes primarily eliminate cosmic muons (INGRID sits near the surface) and muons from neutrino interactions in the surrounding concrete and rock of the detector hall. The scintillation light is read out by wavelength shifting fibers in the center of each bar connected to a multi-pixel photon counter to convert the light to an electrical signal. Two special INGRID modules exist to provide cross-section measurements at the on-axis position: the Proton Module and the Water Module. Both modules collect data placed in between the center modules of the vertical and horizontal plane. The Proton Module is designed to measure neutrino cross-

sections on scintillator, and contains 34 scintillator bars (some with differing dimensions from the standard module) and the same outer veto planes as shown in Fig. 3.7 to create a finer grained and fully active tracking module.

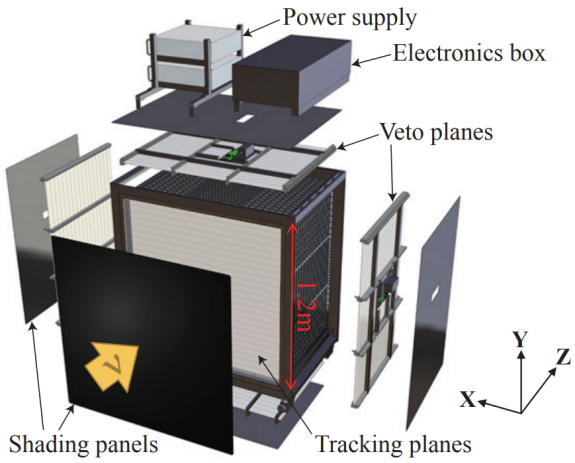

Figure 3.7: View of the Proton Module. Similar to the standard modules but containing finer grained scintillator bars and no iron plates. Figure from Ref. [16].

The Water Module is designed to provide a water target to measure neutrino cross sections containing a lattice of scintillator bars and wavelength shifting fibers for tracking. INGRID measures the position of the neutrino beam center by comparing the interaction rates of each standard module to a precision better than 10 cm, corresponding to 0.4 mrad precision at 280 meters downstream from the graphite target.

Both the horizontal and vertical beam position measured by INGRID matches quite well with the measurement from MUMON and is stable across all the T2K run periods as shown in Fig. 3.8. The neutrino interaction rate is measured by INGRID daily to a precision of 4% [14] as shown in Fig. 3.8. The drop in event rate during negative horn current mode (RHC mode) is due to the lower interaction cross section for anti-neutrinos.

3.4 The Near Detector at 280 meters

The Near Detector at 280 Meters (ND280) is placed at 280 meters downstream of the graphite target and unlike INGRID, it is centered at 2.5 degrees off-axis [16]. ND280 is com-

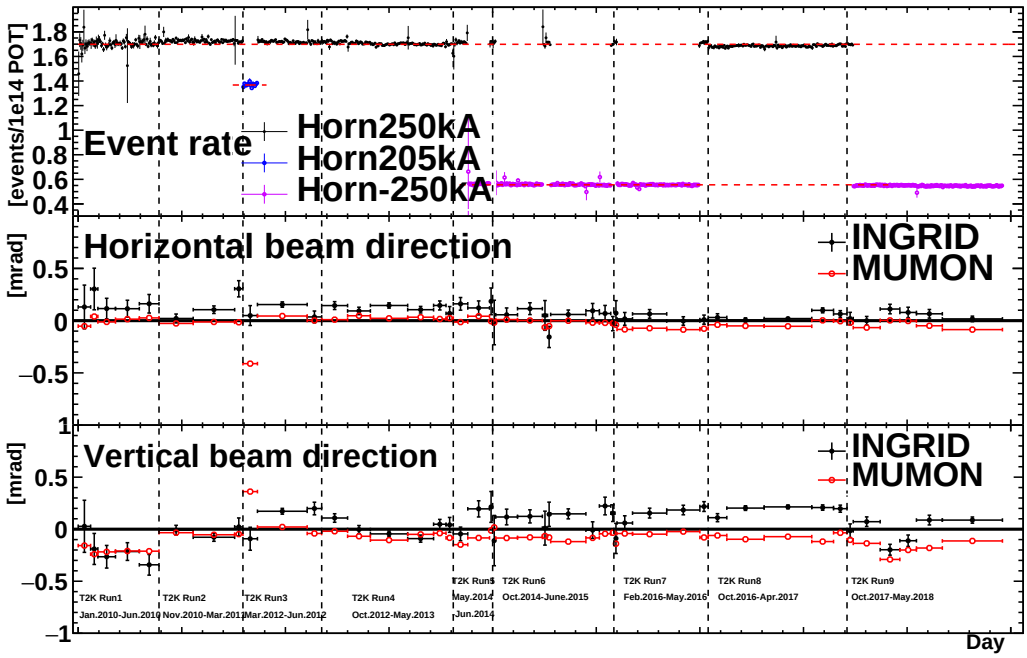

Figure 3.8: Neutrino beam direction in both the vertical and horizontal position measured by INGRID and MUMON for each T2K run period. In general INGRID and MUMON match quite well and the neutrino beam position is fairly stable. The event rate measured by INGRID is also plotted and very stable across the T2K run periods.

prised of five separate sub-detectors and its primary function is to measure neutrino–nuclei interactions by tracking the particles involved in the interactions. The five sub-detectors include the following: the Time Projection Chambers (TPCs), the Fine-Grained Detectors (FGDs), the Pi-Zero Detector (PØD), the Electromagnetic Calorimeters (ECAL), and the Side-Muon Range Detectors (SMRDs). A summary of the primary functions of each sub-detector used in the analysis is presented in Tab. 3.2. The sub-detectors are placed inside the UA1 magnet except for the SMRDs, which are interleaved with the magnet yoke, in the configuration shown in Fig. 3.9. The UA1 magnet produces a 0.2 T magnetic field to enable sign selection and precise momentum measurements of charged particles. The PØD is designed to identify π^0 events, to track charged particles, and to measure neutrino interactions on carbon, water, and lead as targets. The PØD is not used in the analysis presented in this thesis – more details can be found in Ref. [73].

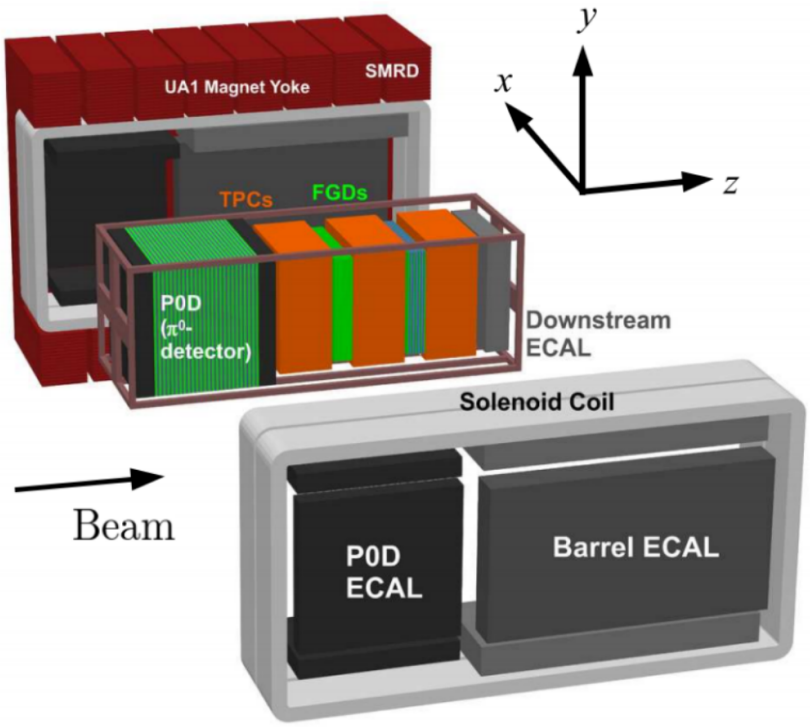

Figure 3.9: Exploded view of the ND280 detector showing the inner tracking region, with each sub-detector visible. The SMRDs are interleaved with the magnet yoke. Taken from [16].

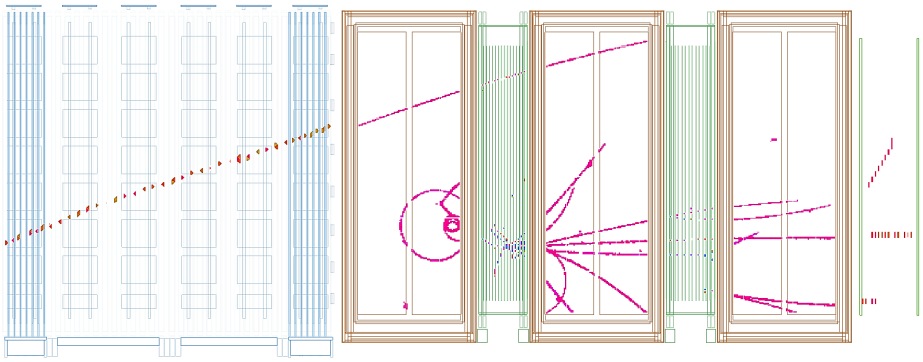

Figure 3.10: ND280 event display showing the PØD, FGDs, and TPCs. A neutrino interaction occurred in FGD1 producing many tracks with an unrelated muon traversing the PØD and TPCs. The downstream ECAL is shown, while the barrel ECAL and SMRDs are not shown.

Sub-detector	Primary Functions
Fine-Grained Detector (FGD)	Charged particle tracking, target material
Time Projection Chamber (TPC)	Charged particle tracking, particle ID, momentum measurement
Electromagnetic Calorimeter (ECal)	Charged particle tracking, photon and π^0 ID
Side Muon Range Detector (SMRD)	Veto planes for cosmic muons, high angle tracking

Table 3.2: List of ND280 sub detectors and their primary function.

3.4.1 Fine-Grained Detectors

Two Fine-Grained Detectors (FGDs) provide the main target in ND280, consisting of fully active scintillator bars in the first FGD with a combination of scintillator bars and water target in the second FGD. This provides a high mass of carbon (from plastic scintillator) and water as a target material for analyses with each FGD supplying 1.1 tons of target material and tracking of particles from the initial interaction vertex. Charged particles traversing the FGDs create scintillation light; and by combining which X and Y bars were hit, the particle can be tracked in three dimensions. If the particle stops in the FGD, the length of the track from the interaction vertex is used to determine its momentum knowing the energy loss per unit distance in the scintillator. The amount of light collected in each bar is proportional to deposited energy which is used in certain analysis techniques such as quantifying vertex activity. Each scintillator bar has a wavelength shifting fiber threaded through the center which is attached to a multi-pixel photon counter at one end to readout the light signal. The other end of the scintillator bar is mirrored with aluminum and the whole bar has a reflective coating of TiO_2 to increase the amount of light captured.

The first FGD contains 5760 scintillator bars arranged into 30 layers of 192 bars where each layer is oriented in alternating X and Y directions which are perpendicular to the incoming neutrino beam (shown in Fig. 3.11). An XY module consists of one layer of 192 scintillator bars in the horizontal direction and 192 scintillator bars in the vertical direction,

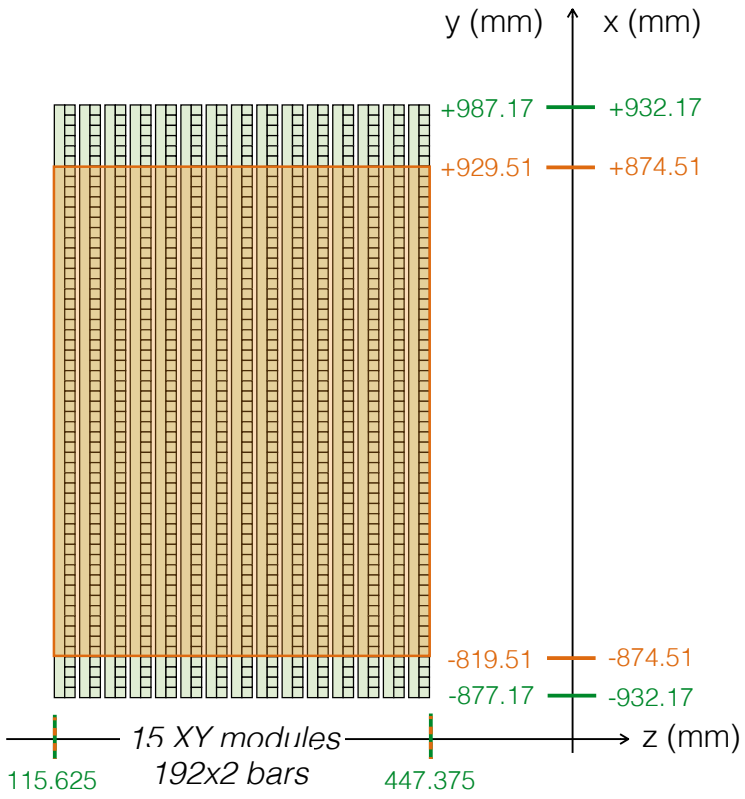

Figure 3.11: View of the FGD1 scintillator bars showing the orientation of the layers. Each pair of horizontal and vertical layers of scintillator bars is defined as a single XY module. The dimensions give the overall size of the FGD and its fiducial volume.

which are perpendicular to each other. This separates the 5760 scintillator bars into 15 XY modules along the z-direction of the FGD. The X and Y layers are glued together with thin sheets of G10 on the outside to provide structural stability. The second FGD uses 7 of the same XY modules as the first FGD alternating with six 2.5 cm water layers (giving a total of 2688 active scintillator bars). The water layers are constructed using thin-walled hollow corrugated polycarbonate filled with pure water sealed at both ends. By comparing the interaction rates of the first and second FGD, or by identifying neutrino interactions that likely occurred in the water layers, the cross-section on oxygen (water) can be determined. The FGDs are each contained in a light-tight dark box that contains the scintillator bars, fibers, and MPPCs while the rest of the electronics are mounted outside of the dark box. Both FGDs were built with the same geometry and readout for interoperability.

3.4.2 Time Projection Chambers

ND280 has three gaseous argon Time Projection Chambers (TPCs) which provide high resolution tracking and identification of charged particles. The TPCs measure the curvature of tracks left by charged particles in the magnetic field along with their energy loss allowing for momentum measurements and particle identification. Each TPC is constructed of an inner box holding an argon-based drift gas and an outer box with a CO_2 insulating gas volume (the outer gap). The walls of the inner box are made from panels with copper-clad G10 skins that have been machined to have a 11.5 mm strip pattern that when combined with the central cathode plane forms an uniform electric drift field within the TPC. A schematic of the layout of a single TPC is shown in Fig. 3.12.

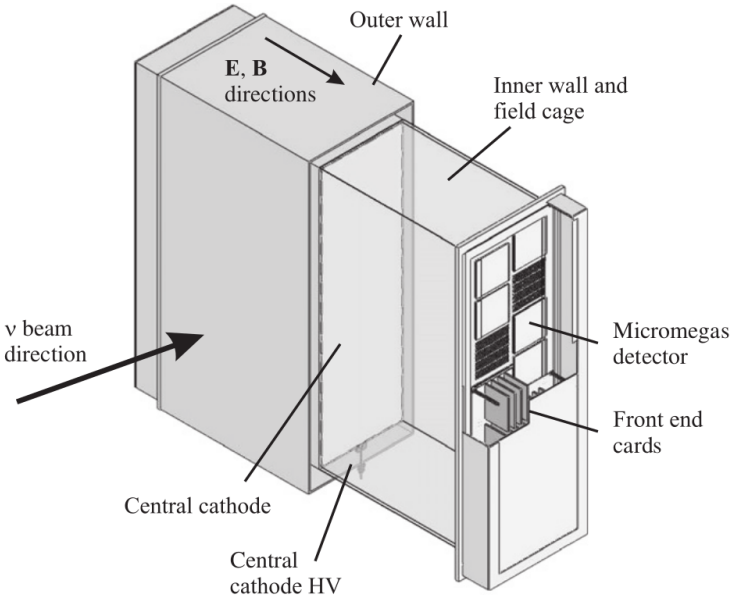

Figure 3.12: Cut-away schematic view of a TPC module showing the main aspects of the TPC design.

Charged particles traversing the TPC gas volume will ionize the drift gas producing electrons along the path that drift away from the central cathode toward the readout planes. The drift electrons are multiplied and sampled with bulk micromegas detectors on the readout planes. The six readout planes (two per TPC) contain 12 micromegas panels measuring 342 mm $\times$ 359 mm (vertical $\times$ horizontal) for a total of 72 micromegas panels. Each micromegas

panel contains 1728 pads arranged in 48 rows of 36 pads where each pad covers an aarea of 7mm $\times$ 9.8 mm. The time of arrival combined with the pattern of the signals in the readout plane combine to give complete 3D reconstruction of the particle tracks within the TPCs. The signals from the micromegas are collected by a set of six front end cards containing custom integrated circuits per micromegas panel.

The drift gas in the TPCs is primarily an argon mixture, chosen for its low diffusion, high speed, and good compatibility with the micromegas. Each TPC contains 3000 liters of the drift gas, which is a mixture of Ar:CF_4:iC_4H_{10} in a 95:3:2 ratio (where iC_4H_{10} is isobutane), and the outer gap volumes contain 3300 liters of CO_2 as a buffer gas. The major contaminants in the drift gas are O_2, CO_2 and H_2O, which can change the drift velocity of the electrons and gain of the micromegas. Both the drift gas and buffer gas are pumped continuously through their respective volumes to refresh the gas and prevent a build up of contaminants. The outer gap volume is flushed five times every 1.5 days whereas each TPC volume is flushed five times every day with approximately 90+% of the gas being purified and recycled in the system.

The TPC measures the momentum of charged particles by measuring the curvature of the track left by the particle. Combined with the spatial resolution of the TPC, the TPC achieves the design goal of a $\delta p_\perp / p_\perp < 0.1$ momentum resolution. In addition to measuring momentum by the radius of curvature, the direction of curvature (curving up or down) can be used to determine the sign of the charged particle allowing for the separation of positive and negatively charged particles. Neutrino and anti-neutrino interactions can be separated by identifying the charge of the outgoing lepton, for example in muon neutrino charged current interactions,

$$\nu_\mu + X \rightarrow \mu^- + X' \tag{3.2}$$

$$\bar{\nu}_\mu + X \rightarrow \mu^+ + X' \tag{3.3}$$

where X, X' is the target before and after the interaction. Particle identification is performed by measuring the energy loss ($\mathrm{d}E/\mathrm{d}x$) of a particle versus its momentum and comparing it

to known values for a given particle type from calibration studies. The energy resolution for a minimum ionizing particle is $7.8 \pm 0.2\%$ and allows for excellent separation between muons and electrons below a momentum of 1.0 GeV/c, see Fig. 3.13.

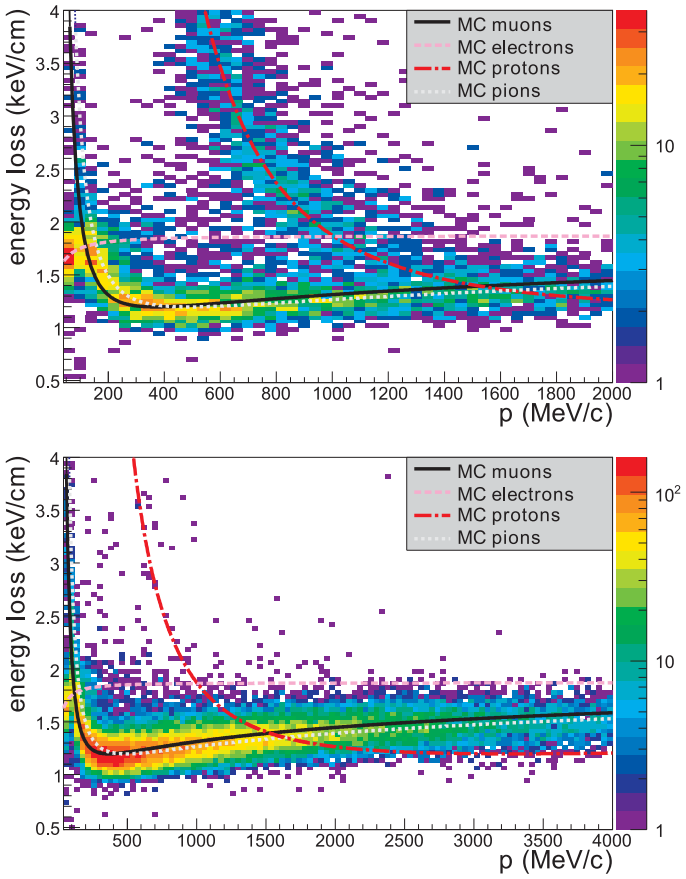

Figure 3.13: Measured energy loss versus momentum for positively (top) and negatively (bottom) charged particles traversing the TPC. Plotted are the expected energy loss curves for electron, muons, protons, and pions. Figures from Ref. [17]

3.4.3 Electromagnetic Calorimeters

The ND280 inner detectors (PØD, FGD, TPC) are surrounded by a sampling Electromagnetic Calorimeter (ECAL). The ECAL is designed to aid in full event reconstruction by detecting photons and measuring their energy and direction in addition to measuring any charged particles that exit the tracking detectors. A key function of photon detection is the identification of pi-zero particles produced in neutrino interactions inside the tracker.

The ECAL is constructed from layers of plastic scintillator bars as active detection material and lead sheets as radiators providing near hermetic coverage of the inner detector volume. It is comprised of 13 individual modules that are arranged into three configurations: 6 barrel-ECAL modules surrounding the inner tracking detector on all sides, 6 PØD-ECAL modules surrounding the PØD, and 1 downstream ECAL module to cover forward going particles. The scintillating panels use a wavelength shifting fiber and multi-pixel photon counter for light detection and readout. Each scintillator bar has a coating of TiO_2 and one end of the bar mirrored with aluminum to provide internal reflection to increase light collection. The downstream ECAL module consists of 34 layers with 1.75 mm thick lead sheets corresponding to 10.6 radiation lengths (X_0). Due to space constraints from the UA1 magnet, the barrel-ECAL modules have 31 layers of the same lead sheets for a total of 9.7 radiation lengths (X_0). The scintillator bars are again constructed in alternating XY layers oriented perpendicular to each other.

3.4.4 UA1 Magnet and Side Muon Range Detectors

The ND280 detector uses the recycled UA1 magnet which provides a 0.2 T dipole magnetic field to measure the momentum and sign of charged particles produced in neutrino interactions. The magnet is built from water-cooled aluminum coils, which provide the magnetic field, and a magnetic flux return yoke. During the installation of the magnet, a detailed magnetic field survey was carried out to map out the magnetic field within the detector volume. The magnetic field strength was determined using an array of Hall probes and carries an uncertainty of 2 mT of each field component at the nominal strength of 0.2 T. This precise measurement of the magnetic field, particularly the transverse component, reduces the uncertainty in the momentum determination of particles.

The side muon range detector provides two main functions: it provides a veto trigger from cosmic muons or muons from interactions in the magnet or the surrounding walls that enter ND280, and it measures high-angle muons (with respect to the beam direction) that escape

from the tracker. The SMRD is comprised of 440 scintillator modules which are inserted in the air gap between the steel plates of the magnet flux return yokes. The magnet consists of 16 individual C-shaped flux return yoke elements, each of which contain 16 steel plates providing 15 air gaps between them. Each module of the SMRD contains several rectangular scintillating panels utilizing a wavelength shifting fiber and multi-pixel photon counter for light readout. In total there are 4016 channels across the SMRD.

CHAPTER 4

EVENT SELECTION

4.1 Signal definition

The signal definition consists of neutrino interaction events on plastic scintillator (C_8H_8) that produce one negatively charged muon, zero pions, and any number of protons as the final state particles where the initial vertex occurred in the fiducial volume of the detector, collectively called the CC-0π topology (example sketches shown in Fig. 4.1). Signal events are described using the measured muon kinematics, $p_\mu, \cos\theta_\mu$ where the angle θ_μ is the polar angle between the incident neutrino z-axis[1] and the outgoing muon direction. It is worth noting that the neutrino z-axis and the detector z-axis are the same at INGRID whereas at ND280 they are slightly out of alignment (which is corrected for in this analysis). Since the signal is defined in terms of the final state particles, interactions where a pion was produced in the initial interaction and subsequently absorbed in the nucleus are included in the signal definition.

The signal is defined to remove as much dependence on the interaction modeling as possible by specifying the definition in terms of the final state particles that are observed in the detector. While harder to predict using neutrino theory, it is less model dependent to define the signal based on what particles the detector was able to measure instead of relying on the nuclear model and Monte Carlo generator to correct back to the initial interaction (cf. Section 2.3.6). The collection of final state particles which define an event is denoted as the topology in the context of this thesis. The CC-0π topology was chosen as the signal definition because it is the most common event type for the T2K energy spectrum, and it is the primary signal event topology for the T2K oscillation analysis. A summary of the signal definition for each detector is presented below.

[1]The z-axis is defined to be the direction of the neutrino propagation.

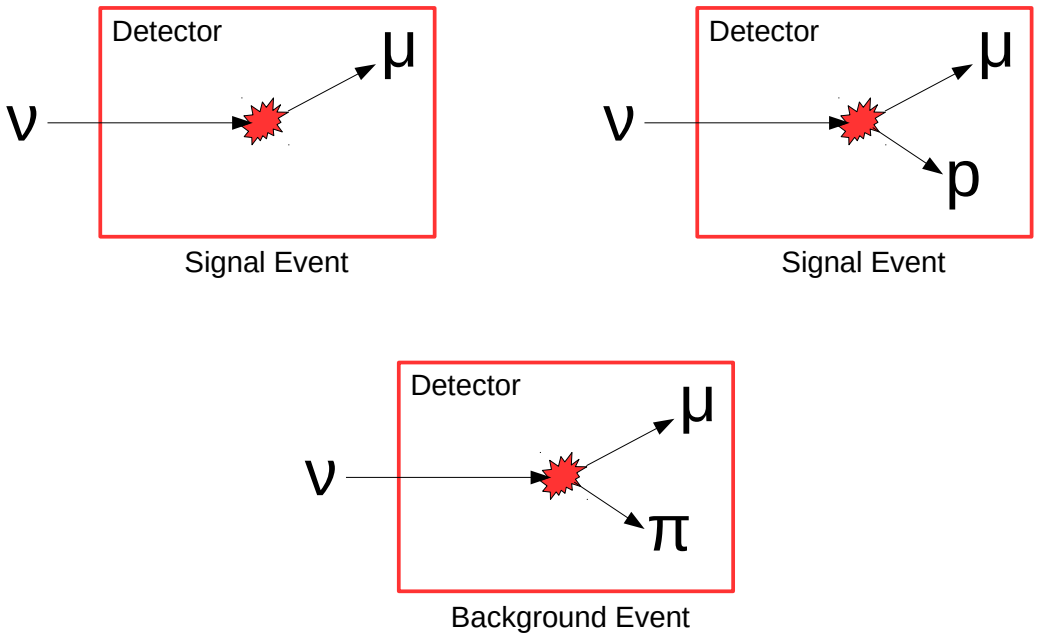

Figure 4.1: Example signal and background event sketches for a generic detector. A neutrino interacts in the detector and several particles are produced. Signal events have zero pions, while background events have one or more pions in the final state.

4.1.1 ND280 signal definition

- **Topology:** one negatively charged muon, zero pions, and any number of protons as the final state particles.
- **Observables:** Muon momentum and angle: $p_\mu, \cos\theta_\mu$
- **Flux:** T2K ν_μ flux, version 13av2.0 (thin-target tuning) [15].
- **Target:** plastic scintillator (C_8H_8) in the FGD1 fiducial volume
- **Phase space:** No restrictions.

4.1.2 INGRID signal definition

- **Topology:** one negatively charged muon, zero pions, and any number of protons as the final state particles.

- **Observables:** Muon momentum and angle: $p_\mu, \cos\theta_\mu$
- **Flux:** T2K ν_μ flux, version 13av2.0 (thin-target tuning) [15].
- **Target:** plastic scintillator (C_8H_8) in the Proton Module fiducial volume
- **Phase space:** Events with $p_\mu > 0.35$ GeV/c and $\cos\theta_\mu > 0.50$.

Note that INGRID is not a magnetized detector and does not have the capability to sign-select muons. Both positive and negative muons from $\bar{\nu}_\mu$ and ν_μ events will be selected by the detector as signal candidates, however only ν_μ events are treated as signal events in the analysis. The kinematic phase space restriction of the muon for the INGRID signal definition is placed based on the efficiency for the Proton Module to detect the outgoing muon (see Section 4.6 for the discussion of efficiency). Given the geometry and capability of the Proton Module, it is not well suited to measuring low momentum or backward going muons. This is the same restriction used in the original INGRID-only analysis detailed in T2K-TN-204 [5].

4.2 Monte Carlo and data samples

This analysis uses T2K data collected at INGRID using the Proton Module taken during Run 2, Run 3, and Run 4 corresponding to 5.9×10^{20} protons-on-target (POT), and ND280 data taken during Run 2, Run 3, Run 4, and Run 8 corresponding to 11.53×10^{20} POT. The difference in delivered POT is due to both the uptime of each detector and the additional run for ND280 (the Proton Module was moved before Run 8). Tables 4.1 and 4.2 report the data statistics collected and the Monte Carlo (MC) statistics used for ND280 and INGRID respectively. The MC samples are weighted to match the POT of the data samples using the data/MC ratio for each run individually. Each run represents a different data taking period including the effect of different proton beam conditions, horn current, etc. and is further subdivided based on whether the PØD water target was in (water) or out (air). This analysis only uses data taking runs in neutrino beam (FHC) mode.

T2K Run	Data POT	MC POT	Data/MC Ratio
Run 2a (air)	0.359 $\times 10^{20}$	9.239 $\times 10^{20}$	0.0389
Run 2w (water)	0.433 $\times 10^{20}$	12.034 $\times 10^{20}$	0.0360
Run 3b (air)	0.217 $\times 10^{20}$	4.478 $\times 10^{20}$	0.0485
Run 3c (air)	1.364 $\times 10^{20}$	26.323 $\times 10^{20}$	0.0518
Run 4a (air)	1.783 $\times 10^{20}$	34.996 $\times 10^{20}$	0.0509
Run 4w (water)	1.643 $\times 10^{20}$	22.622 $\times 10^{20}$	0.0726
Run 8a (air)	1.581 $\times 10^{20}$	36.305 $\times 10^{20}$	0.0435
Run 8w (water)	4.149 $\times 10^{20}$	26.412 $\times 10^{20}$	0.1571
Total	11.529 $\times 10^{20}$	172.409 $\times 10^{20}$	0.0669

Table 4.1: Data-taking periods and the POT used in this analysis for data and MC for ND280.

T2K Run	Data POT	MC POT	Data/MC Ratio
Run 2-4	5.9 $\times 10^{20}$	2.77 $\times 10^{23}$	0.0021
Total	5.9 $\times 10^{20}$	2.77 $\times 10^{23}$	0.0021

Table 4.2: Data-taking periods and the POT used in this analysis for data and MC for INGRID.

The ND280 MC is produced in several steps starting with the NEUT neutrino event generator [48] to simulate neutrino interactions within the ND280 geometry. The output from the NEUT simulation is passed to a GEANT4 [74] simulation of the ND280 detector, which propagates the final state particles through the detector accounting for energy loss, the external magnetic field, secondary interactions, etc. The final step is to process the GEANT4 simulation through the ND280 data acquisition and electronic simulation producing files and objects which simulate real data. Monte Carlo samples are generated for each data taking run separately to account for the detector conditions, such as the configuration of the PØD. The default nuclear model for this analysis is the Benhar et. al. spectral function (SF) with $M_A^{QE} = 1.21$ GeV/c^2 and contributions from the Nieves et. al. multinucleon (2p2h) model [13] produced with NEUT 5.3.2.

The INGRID MC is produced in a similar fashion starting with the NEUT neutrino

event generator for the initial neutrino interactions, then proceeding with a GEANT4 based simulation for the detector. INGRID has a separate NEUT, GEANT4, and electronic simulation from ND280, and produces slightly different files and objects for the simulated data. The INGRID MC software stack is further documented in T2K-TN-204 [5]. The INGRID MC uses NEUT 5.3.3 to produce the neutrino interactions using the same default nuclear model described above, however the differences between NEUT versions 5.3.2 and 5.3.3 have minimal to no impact on this analysis.

The data and MC samples for ND280 have some corrections applied to reduce known data/MC differences. These corrections are based on known hardware failures and discrepancies, or from studies using precise control samples. The corrections are listed in Table 4.3 and are applied during event selection for ND280. The data and MC samples for INGRID undergo a similar procedure with a different set of corrections, which are listed in Table 4.3.

ND280 Corrections
Data Quality
dE/dx Data correction
dE/dx MC correction
Momentum resolution
Momentum by range
Time of Flight (TOF)
TPC expected dE/dx
TPC particle identification (PID)
FGD particle identification (PID)
Ignore Dead Channels

INGRID Corrections
Data Quality
Ignore Dead Channels
Pile-up Correction
Veto Efficiency

Table 4.3: Summary of the ND280 data/MC corrections (left) and INGRID data/MC corrections (right).

4.3 Signal event selection

The signal for this analysis is the CC-0π topology, where a muon candidate, any number of proton candidates, and zero pion candidates are detected in the final state on a CH target (subject to fiducial volume cuts) in either FGD1 (ND280) or the Proton Module (INGRID). This analysis uses previously well developed and tested CC-0π selections for INGRID [5]

and ND280 [3], which have been used in the near detector constraint for the T2K oscillation analysis and previous cross section analyses. A brief description of the selection for each detector is presented here; this section details the signal samples while Section 4.4 details the sideband samples.

4.3.1 ND280 event selection

The ND280 event selection is the nearly same as the most recent CC-0π analyses, detailed in T2K-TN-337 [3] and T2K-TN-338 [75], which are themselves built upon the selection cuts presented in T2K-TN-216 [76] and Refs. [34, 77]. FGD1 is used both as a CH target and a tracker along with the three TPC's and FGD2 providing tracking and particle identification. Events with one negatively charged muon, any number of protons, and no other reconstructed tracks where the vertex was found to be in the FGD1 fiducial volume are selected as signal events. The signal events are then categorized into signal samples by which sub-detectors were used in the reconstruction, and by the presence of a reconstructable proton. This separation of the samples allows for more accurate treatment of detector systematics based on the capabilities of each detector. These samples are defined as the following (and shown as event displays in Fig. 4.2):

- **Sample 0** (μTPC) : a single muon candidate was detected as an FGD-TPC track and no other track candidates present.
- **Sample 1** (μTPC+pTPC) : a single muon candidate and proton candidate were detected as FGD-TPC tracks.
- **Sample 2** (μTPC+pFGD) : a single muon candidate detected as an FGD-TPC track and a single proton candidate as an FGD track.
- **Sample 9** (μTPC+Np) : a single muon candidate detected as an FGD-TPC track and multiple proton candidates present.

- **Sample 3** (μFGD+pTPC) : a single muon candidate detected as an FGD track and a single proton candidate as an FGD-TPC track.

- **Sample 4** (μFGD) : a single muon candidate was detected as an FGD track and no other track candidates present.

Additional samples are defined and used as sidebands to constrain background events, and are described in Section 4.4.1, and for this analysis the μTPC+pFGD and the μTPC+Np samples (samples 2 and 9) are combined when performing the fit due to the low statistics of the μTPC+Np sample. Other sample definitions are possible (e.g. μFGD+pFGD), however these samples either have too few expected events or have very poor reconstruction. This results in five separate signal samples as input for the fit.

The cut flow for each signal sample is shown in Fig. 4.3. An event must pass all cuts for a given sample definition to be placed in that sample, and events which fail a cut may still meet the criteria to be placed in a different sample (signal or sideband). The samples are mutually exclusive, an event can belong to only a single sample (signal or sideband) or may not pass enough cuts to be used in the analysis at all.

- **Event Quality**: Events are required to pass a quality cut ensuring the detector and beam were in good working condition. Beam runs and beam spills which are not considered to be of good quality to be analyzed are rejected. This cut only applies to data events as MC events are assumed to pass the quality cut.

- **Fiducial Volume Cut**: All selected events are required to have their vertex placed in the FGD1 fiducial volume, which is part of the vertex cuts below. The fiducial volume of FGD is defined to be: $|x| < 874.51$ mm, $-819.51 < y < 929.51$ mm, and $136.875 < z < 446.995$ mm in the ND280 coordinate system (see Fig. 3.11). The cuts along x and y exclude the outer five scintillator bars from the fiducial volume in each direction. The cut along z removes events occurring in the first XY module of FGD1, keeping the remaining fourteen XY modules.

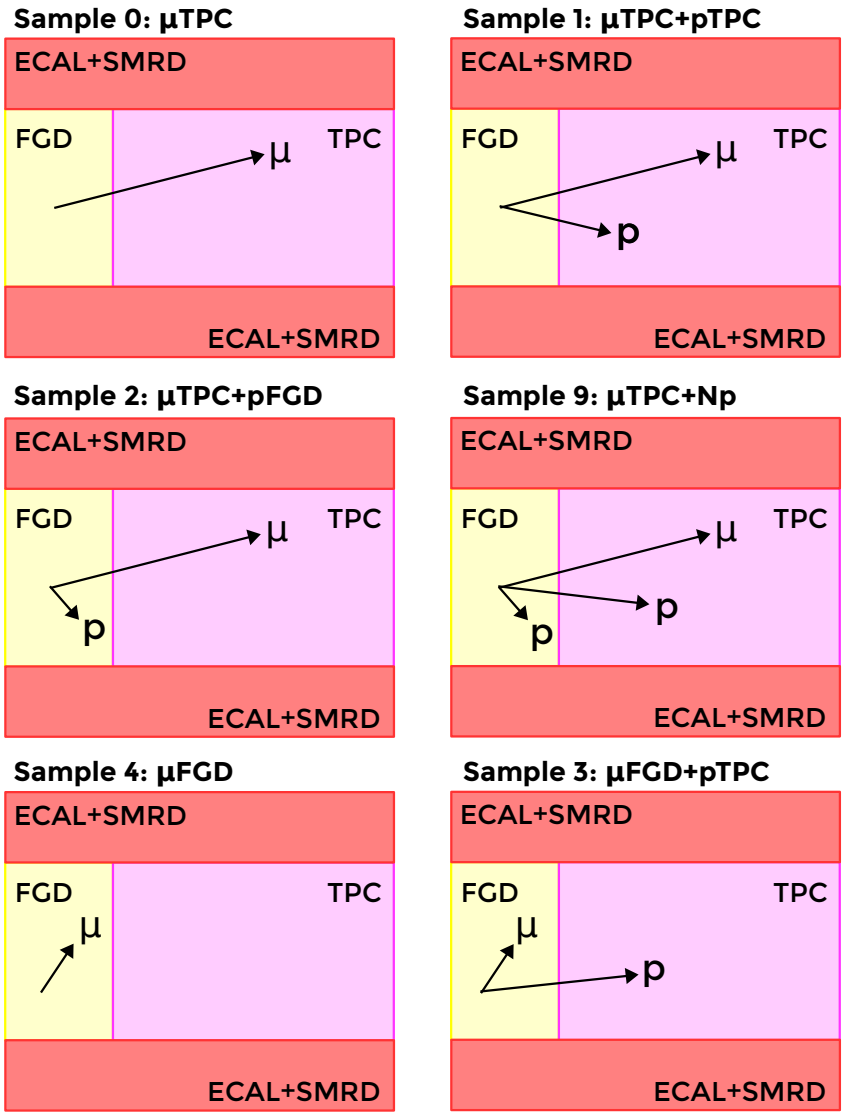

Figure 4.2: Event display cartoon for the ND280 signal samples.

- **HMN Vertex**: The highest momentum negative (HMN) charged vertex position is set by the highest momentum negative charged track which reaches and is identified by the TPC. Requiring the track to be reconstructed in the TPC increases the accuracy of the vertex placement, and the highest momentum negative track is used since this track is most likely the muon from the event.

- **Common vertex**: This cut requires the HMN (or muon candidate) and HMP track (or proton candidate) to share a common vertex. This is defined as the negative track vertex being within 200 mm in both the x and y directions, and within 60 mm in the z direction of the positive track vertex.

- **TPC Muon PID**: The HMN track is considered to be the muon candidate and is checked against the particle identification (PID) algorithm to determine if the particle was most like a muon, pion, electron, or proton. The TPC PID algorithm is based on the measured $\mathrm{d}E/\mathrm{d}x$ of the particle and how it compares to the expected distribution for a given particle type. The pulls δ_i for a given particle type i are calculated by

$$\delta_i = \frac{C^{\mathrm{obs}} - C_i^{\mathrm{exp}}}{\sigma_i^{\mathrm{exp}}} \tag{4.1}$$

where the expected energy loss C^{exp} is estimated by

$$C^{\mathrm{exp}} = \frac{53.87\mathrm{ADC}}{\beta^{2.283}} \left(5.551 - \beta^{2.283} - \log\left[0.001913 + (\beta\gamma)^{-1.249}\right]\right) \tag{4.2}$$

and C^{obs} is the observed energy loss, σ^{exp} is the energy resolution of the TPC, and ADC is the analog to digital counts (ADC) from the detector which is proportional to the energy deposited by the particle [78, 79]. The $\beta = v/c$ and $\gamma = (1-\beta^2)^{-1/2}$ factors are the relativistic kinematics of the track. The likelihood for particle type i is defined as

$$\mathcal{L}_i = \frac{e^{-\delta_i^2}}{\sum_n e^{-\delta_n^2}} \tag{4.3}$$

where the sum is over the particle types: muon, electron, pion, proton. Once the likelihoods are calculated, the values can be used to identify a particle. Electrons are

rejected by requiring the particle to be muon or pion-like

$$\frac{\mathcal{L}_\mu - \mathcal{L}_\pi}{1 - \mathcal{L}_p} > 0.8 \tag{4.4}$$

which is only applied for tracks with momentum less than 500 MeV/c. To identify as a muon, proton, or pion the cuts are

$$\mathcal{L}_\mu > 0.05, \mathcal{L}_p > 0.5, \mathcal{L}_\pi > 0.3 \tag{4.5}$$

The cut values were chosen from MC studies and test-beam data and can be tuned for a given analysis [78, 79].

- **FGD Muon PID**: The FGD PID algorithm is constructed in a similar fashion to the TPC PID algorithm as it defines a set of pulls δ_i for each particle type to calculate a likelihood. The difference is in the function used to calculate the pull, where the expected energy deposited is proportional to the measured track length. The pulls for a given particle type i are calculated by

$$\delta_i = \frac{E^{\text{obs}} - E_i^{\text{exp}}(x)}{\sigma_i^{\text{exp}}(x)} \tag{4.6}$$

where E is the observed or expected energy deposited, x is the measured track length, and σ is the expected energy resolution for a particle type. Based on detector studies and MC, the function used to calculate the expected energy as a function of track length is given by

$$E_i = A_i x^{B_i} + C_i x \tag{4.7}$$

where A_i, B_i, C_i are constants for each particle type extracted from fits to data [80]. The likelihood for a particle type i is based on the Gaussian distributions of the pulls and is defined as

$$\mathcal{L}_i = \frac{G_i(\delta_i)}{\sum_n G_n(\delta_n)} \tag{4.8}$$

where the sum is over the particle types: muon, electron, pion, proton.

- **One negative track**: This cut is failed if there are extra negative tracks (identified by the TPC) which share a common vertex with the HMN track. This cut identifies events with a single muon and no other particles.

- **Only muon/proton tracks**: This cut is failed if there is a track present which was identified to be neither muon-like nor proton-like by the PID algorithm which shares a common vertex with the HMN or HMP track. This cut identifies events with a single muon and any number of protons.

- **No Michel electron**: This cut requires no identifiable Michel electrons (the electron from muon decay) are found in the FGD. This cut is applied after the muon candidate has been identified, thus a Michel electron could have been produced by a low energy pion decaying into a muon, which itself subsequently decays into an electron. A Michel electron is identified by seeing a charge deposition consistent with an electron in the FGD occurring about one muon lifetime (2.2 μs) after the event start time.

- **Zero/One/Multiple protons**: This cut separates events into different samples based on how many proton tracks were identified by the PID algorithm sharing a common vertex with the HMN track.

- **FGD/TPC proton**: This cut separates events with a single proton track into different samples based on if the proton stopped in the FGD or was identified as a TPC proton track.

- **HMP vertex**: Similar to the HMN vertex cut, the highest momentum positive (HMP) charged vertex position is set by the highest momentum positive charged track which reaches and is identified by the TPC. Requiring the track to be reconstructed in the TPC increases the accuracy of the vertex placement. Tracks are required to have at least 18 segments in the TPC to be reconstructed as a track.

- **Leading proton track**: This cut requires the track used to set the HMP vertex is identified as proton-like by the TPC PID algorithm.

- **Long FGD track**: This cut requires the FGD muon candidate to be long enough (greater than 500 mm) to have a reliable measure of its kinematics.

- **Stopping muon**: This cut requires the FGD muon candidate to be within the active region of ND280. The muon must be fully contained as the PID algorithm and momentum measurements are based on the range traversed in the FGD and the ECAL/SMRD.

- **HA muon**: This cut searches for a high angle (HA) track which is identified as a muon candidate (by the FGD PID algorithm) where the vertex is in the FGD fiducial volume. A high angle track is one where it does not enter the TPC, which generally requires a high angle relative to the forward direction.

- **ECAL PID 1 & 2**: If the HA muon candidate reaches the ECAL, the $\mathrm{d}E/\mathrm{d}x$ and length of the track in the ECAL are used to further verify the particle identity. This cut looks for $\mathrm{d}E/\mathrm{d}x$ consistent with a muon (ECAL PID 1), and for the ratio length to estimated energy of the track to be consistent with a muon hypothesis (ECAL PID 2).

<table>
<tr><th>muTPC</th><th>muTPC+pTPC</th><th>muTPC+pFGD</th><th>muTPC+Np</th><th>muFGD+pTPC</th><th>muFGD</th></tr>
<tr><td colspan="6">Event Quality</td></tr>
<tr><td colspan="4">HMN Vertex</td><td>HMP Vertex</td><td>HA Muon</td></tr>
<tr><td colspan="4">Muon PID</td><td colspan="2">Only Muon/Proton Tracks</td></tr>
<tr><td colspan="4">One Negative Track with Common Vertex</td><td>Leading Proton Track</td><td>Stopping Muon</td></tr>
<tr><td colspan="4">Only Muon/Proton Tracks</td><td>Long FGD Track</td><td>Ecal PID 1</td></tr>
<tr><td colspan="4">No Michel Electron</td><td>FGD Muon PID</td><td>Ecal PID 2</td></tr>
<tr><td rowspan="2">No Protons</td><td colspan="2">One Proton</td><td rowspan="2">Multiple Protons</td><td>Common Vertex</td><td>No Michel e</td></tr>
<tr><td>TPC Proton</td><td>FGD Stopping Proton</td><td>Stopping Muon</td><td rowspan="3">No Protons</td></tr>
<tr><td colspan="3" rowspan="2"></td><td>No Michel e</td></tr>
<tr><td>One Proton</td></tr>
</table>

Figure 4.3: Chart showing the selection cuts used to define each ND280 signal sample.

The muon candidate kinematic distributions for each ND280 signal sample are displayed in Fig. 4.4 and Fig. 4.5 split by the true topology, showing the proportion of true signal

and background events. In addition, Fig. 4.6 and Fig. 4.7 show the kinematic distributions split by true reaction, and distributions as a function of momentum transfer can be found in Appendix F. For both sets of plots, the 'out FV' refers to events which actually occurred outside the fiducial volume, but were still selected, and the 'BKG' (or 'other') category is a catch-all for every other type of event not belonging to a listed category. The samples where the muon candidate was reconstructed in the TPC have similar momentum and angle distributions with samples where a proton candidate were found to have more muons at higher angles. The samples where the muon candidate was reconstructed in the FGD have very few forward going muons and lower momentum muons. The sharp drop of events at a cosine of arond zero is due to a low reconstruction efficiency for muons which are traveling (nearly) straight upwards as they travel parallel to the scintillator bars and do not cross enough bars to be reconstructed. The samples have a high purity of true CC-0π events, with the main background split fairly evenly between CC-1π and CC-Other events. The final CC-0π signal is extracted by adding the contributions of each signal sample together, but the separation is valuable when running the fit because each sample is affected by different systematics and backgrounds. The purity for each sample and the total is also listed in Tab. 4.4.

Sample	CC-0π	CC-1π	CC-Other	Background	Out of FV	Events
Sample 0: μTPC	86.66	4.83	3.98	1.17	3.36	15526.90
Sample 1: μTPC+pTPC	73.58	9.87	11.43	3.03	2.09	3480.27
Sample 2: μTPC+pFGD	82.75	8.48	5.36	1.31	2.09	2332.07
Sample 9: μTPC+Np	57.88	16.03	17.57	3.36	5.17	317.41
Sample 3: μFGD+pTPC	84.25	4.19	2.78	2.13	6.66	1533.94
Sample 4: μFGD	63.19	1.95	1.33	3.27	30.25	2220.59
Combined Total	81.93	5.72	5.00	1.71	5.64	25411.18

Table 4.4: Purity of each ND280 signal sample and the purity of the combined total.

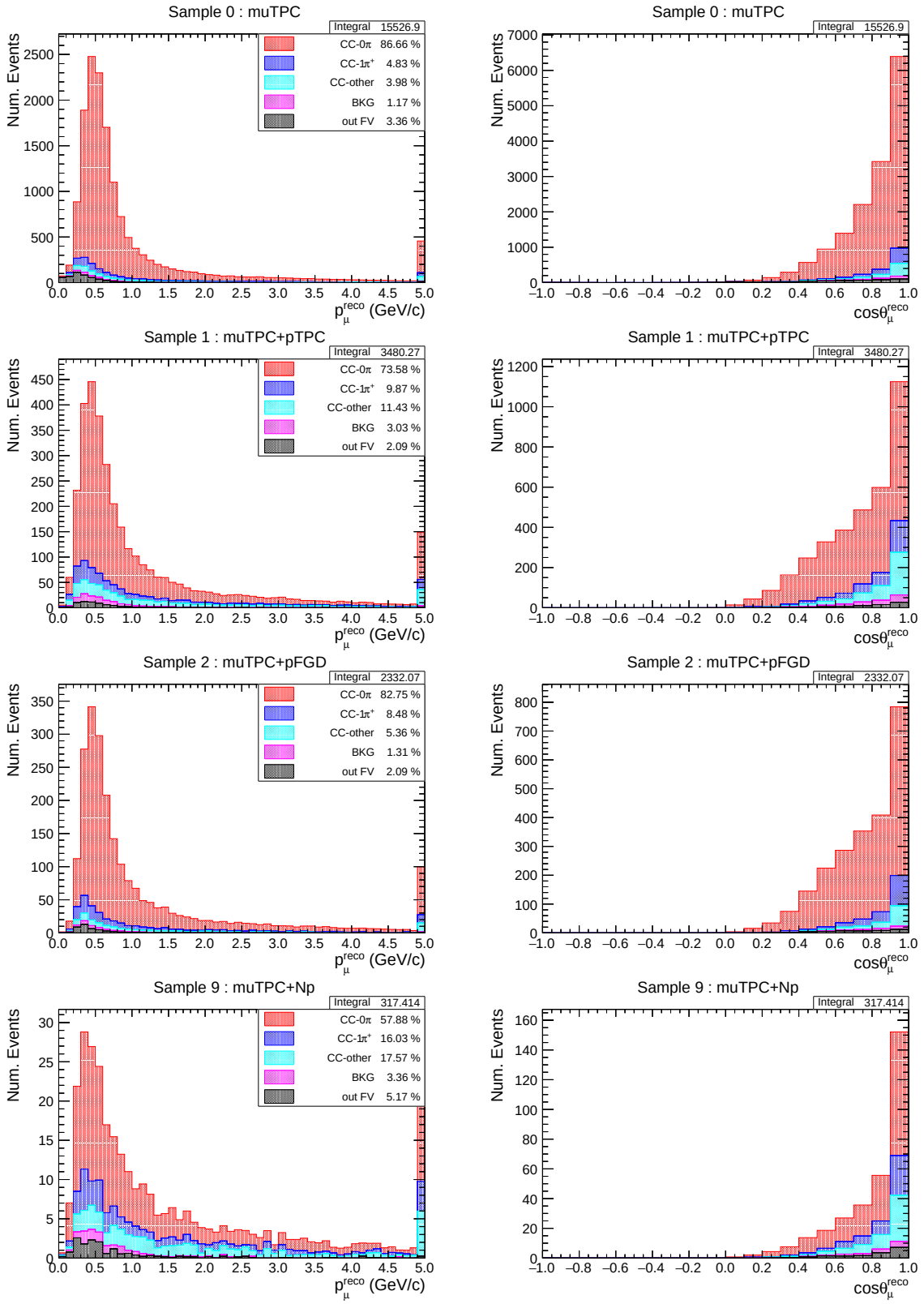

Figure 4.4: Event distribution for reconstructed muon momentum and angle for the ND280 signal samples with a muon track in the TPC stacked by true topology. The purity of each topology is listed in the legend. The last bin for muon momentum contains all events with momentum greater than 5 GeV/c.

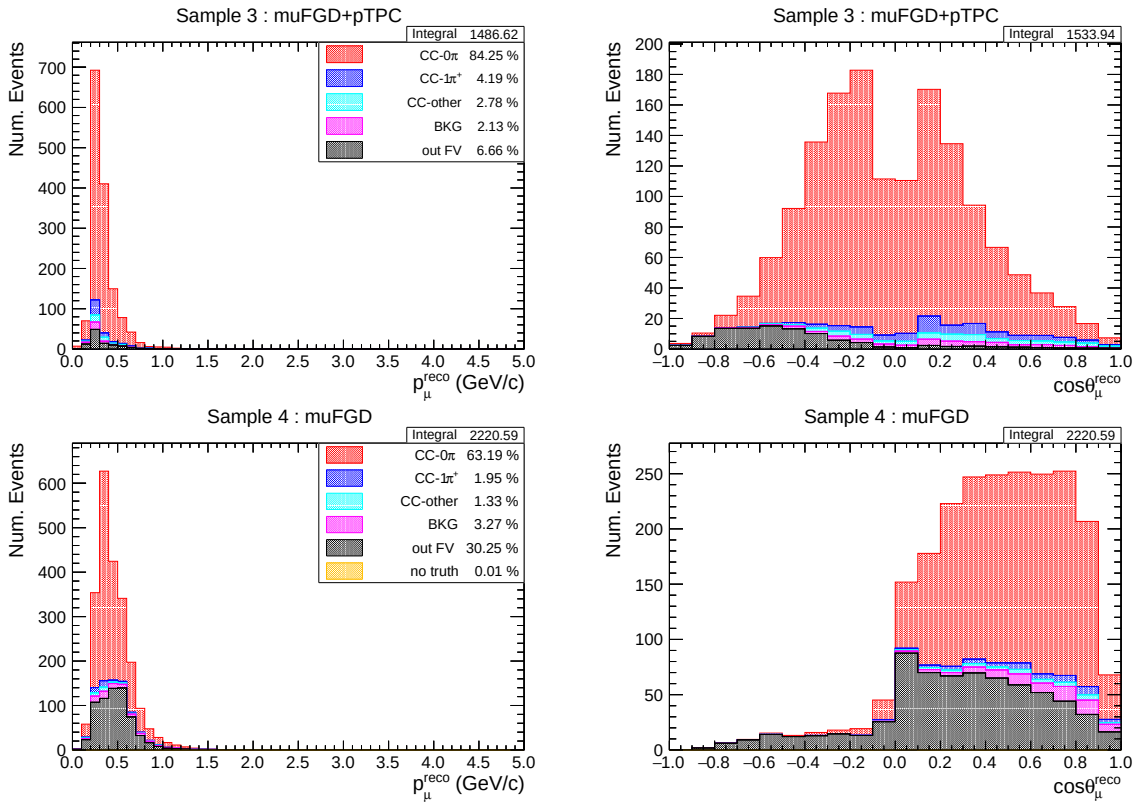

Figure 4.5: Event distribution for reconstructed muon momentum and angle for the ND280 signal samples with a muon track in the FGD stacked by true topology. The purity of each topology is listed in the legend. The last bin for muon momentum contains all events with momentum greater than 5 GeV/c.

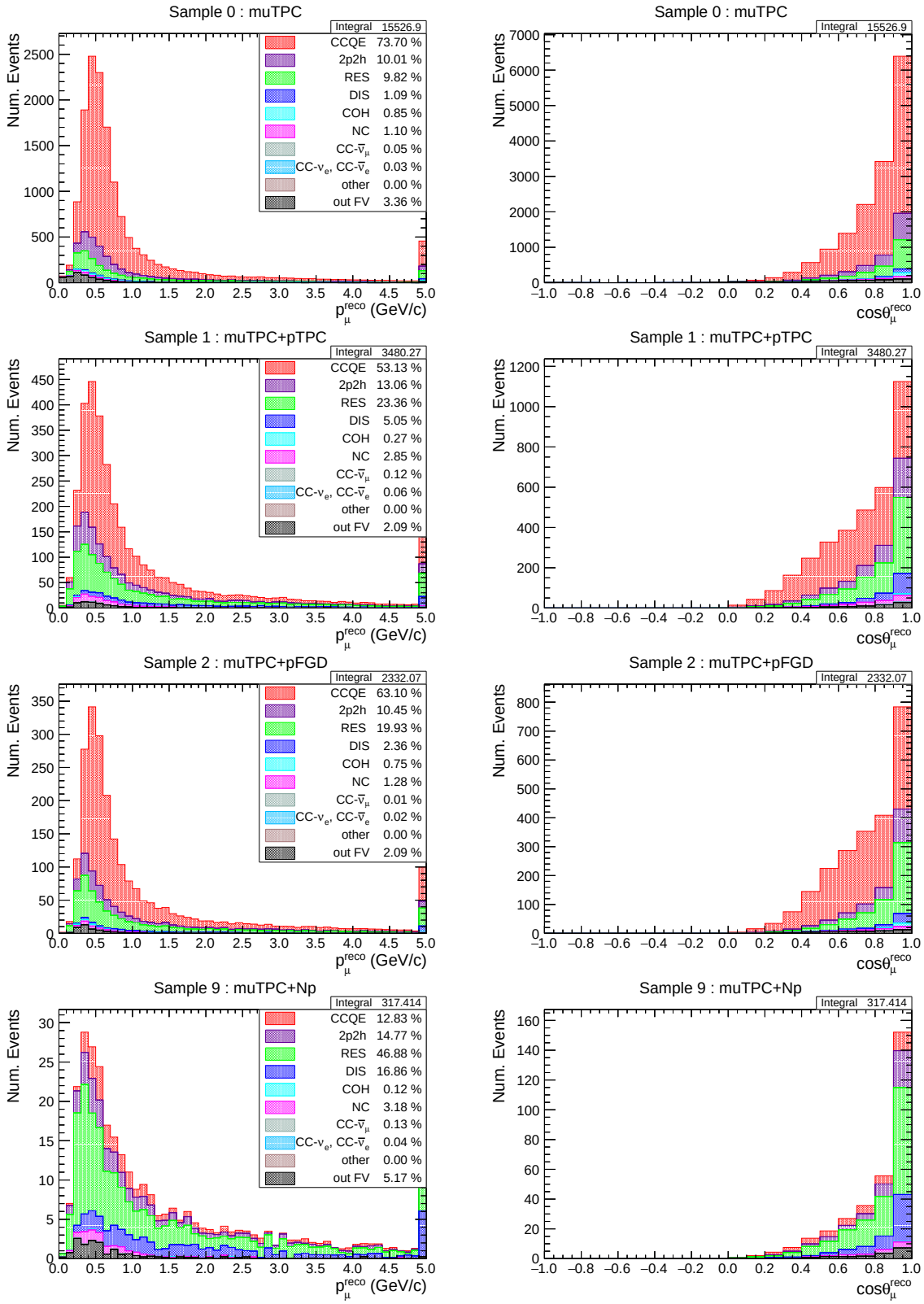

Figure 4.6: Event distribution for reconstructed muon momentum and angle for the ND280 signal samples with a muon track in the TPC stacked by true reaction. The purity of each reaction is listed in the legend. The last bin for muon momentum contains all events with momentum greater than 5 GeV/c.

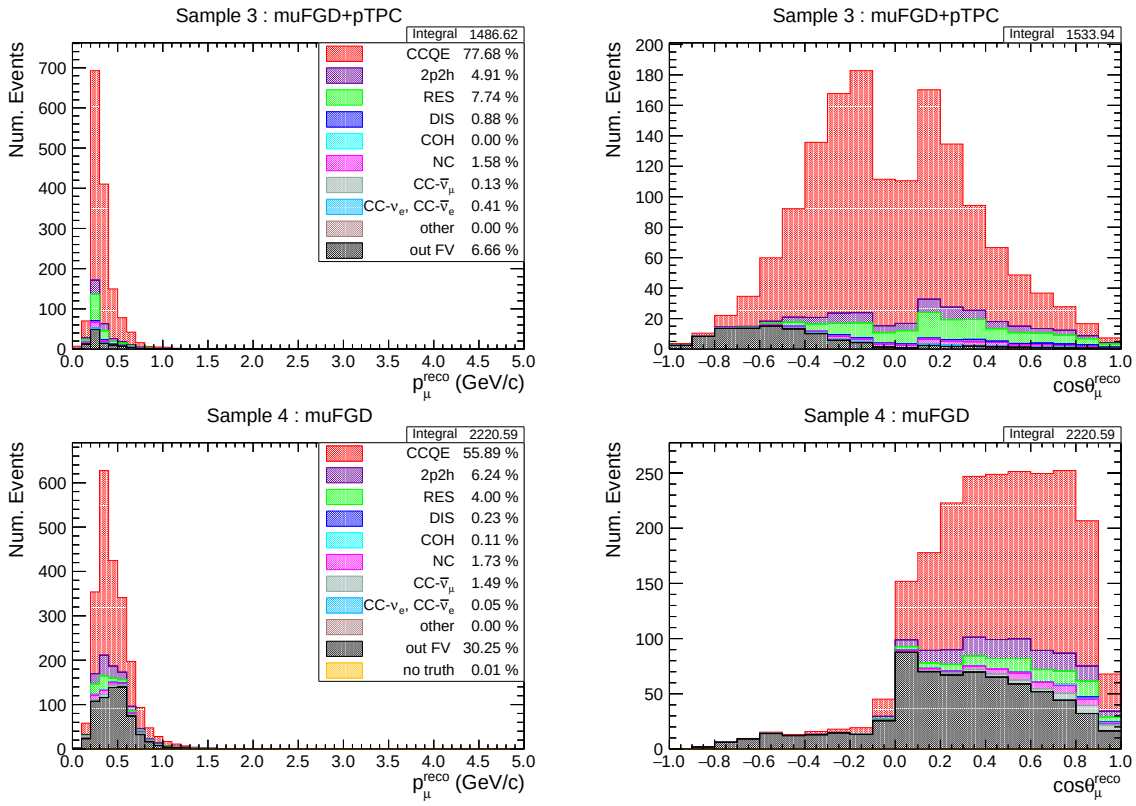

Figure 4.7: Event distribution for reconstructed muon momentum and angle for the ND280 signal samples with a muon track in the FGD stacked by true reaction. The purity of each reaction is listed in the legend. The last bin for muon momentum contains all events with momentum greater than 5 GeV/c.

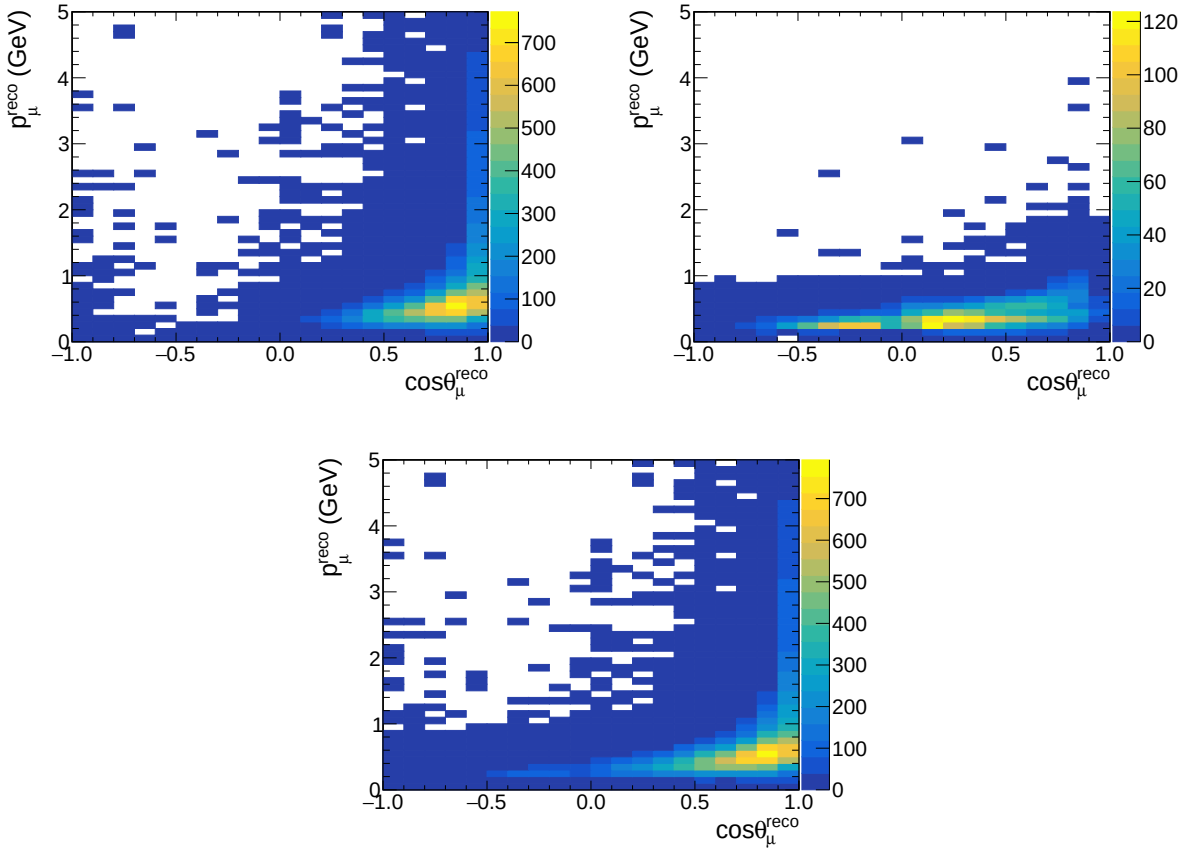

Figure 4.8: Two dimensional event distribution for reconstructed muon momentum vs angle for the ND280 signal samples with a muon track in the TPC (left) or a muon track in the FGD (right). The combination is shown in the bottom plot.

4.3.2 INGRID event selection

The INGRID CC-0π selection is the same one described in T2K-TN-204 [5] and is briefly described here. The selection uses the scintillator in the Proton Module (PM) as a CH target and both the PM and the adjacent downstream standard INGRID module for tracking. The signal selection is separated into samples based on where the muon candidate stopped in the detectors, or where it exited the detectors, listed as follows and illustrated in Figure 4.9:

- **PM early stopping** : the track stopped and is fully contained in the PM scintillator.
- **PM escaping** : the track escapes the PM but does not deposit any energy in the INGRID module.
- **INGRID early stopping** : the track escapes the PM and deposits energy in the INGRID module, but is not reconstructed as an INGRID track.
- **INGRID stopping** : the track escapes the PM and is reconstructed as an INGRID track which stops in the module.
- **INGRID side-escaping** : the track escapes the PM and is reconstructed as an INGRID track which has hits in an INGRID side channel.
- **INGRID through-going** : the track escapes the PM and is reconstructed as an INGRID track which has hits in the last layer.

The samples where the muon candidate could have exited INGRID can only be used to place a lower limit on the muon momentum of approximately 1 GeV/c. All samples are used, but all events that are not fully contained will fall in the last momentum bin from 1 to 30 GeV/c. The remaining events that are fully contained provide a measurement of the muon momentum (determined by range). All events have reliable angle reconstruction and measurements.

The CC-0π sample selects events which satisfy the following criteria. Note that INGRID is not a magnetized detector and does not have any capability to sign-select muons. Both

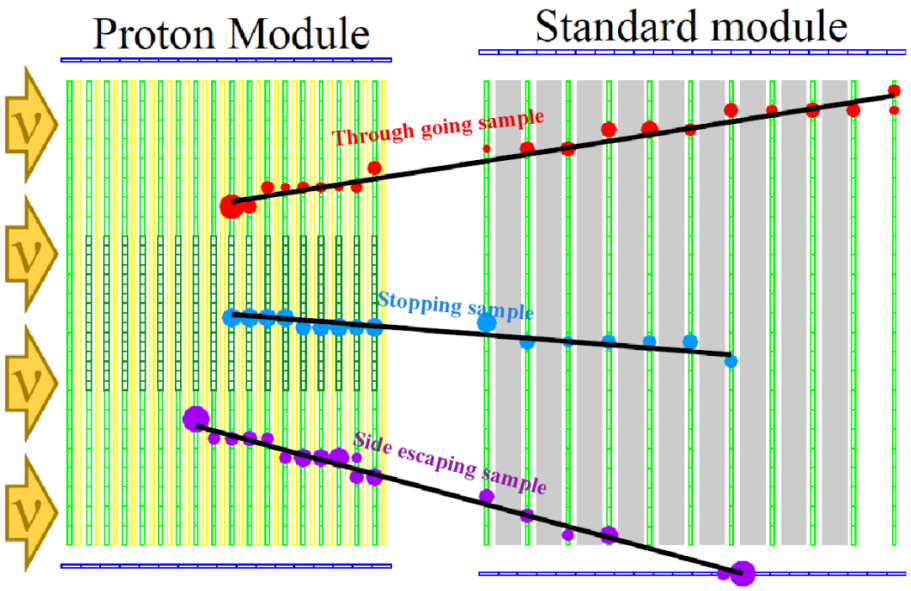

Figure 4.9: Event display for the Proton Module showing the different INGRID samples. Green is tracking scintillator, blue is veto scintillator, and gray are iron plates. Figure from Ref. [5]

positive and negative muons from $\bar{\nu}_\mu$ and ν_μ events are selected as candidate signal events and the $\bar{\nu}_\mu$ events are background constrained with data when performing the analysis (and are generally a negligible contamination).

- **Event quality**: Events are required to pass a quality cut ensuring the detector and beam were in good working condition. This cut is only applied to data events as MC events are assumed to pass the quality cut.

- **Beam timing**: Events are required to be ± 100 ns of the expected beam bunch arrival time to reduce the cosmic background. The timing of the event is defined as the timing of the largest charge deposition hit in the event.

- **Track multiplicity**: Events are required to have only one or two reconstructed tracks. A CC-0π event in general will have a muon and a single proton knockout, thus large majority of CC-0π events are one or two track events. However this will reject true CC-0π events which eject multiple reconstructed protons. This is a small impact on the analysis given how often two proton tracks are able to be successfully reconstructed.

- **Muon PID**: The PID algorithm used for the PM/INGRID tracks is based on a multivariate boosted decision tree (BDT), which uses a Bayesian confidence level as a preliminary PID plus the energy deposition distribution near the end of the track (the last five hits). The Bayesian confidence level uses Bayes' theorem to identify a particle based on its $\mathrm{d}E/\mathrm{d}x$ measurement, for example the muon confidence level is

$$\mu_{CL} = P(\mu|\frac{\mathrm{d}E}{\mathrm{d}x}) = \frac{P(\mathrm{d}E/\mathrm{d}x|\mu)\cdot P(\mu)}{P(\mathrm{d}E/\mathrm{d}x)} \tag{4.9}$$

  where the $\mathrm{d}E/\mathrm{d}x$ information is from each hit in the track. Since track hits can overlap due to the granularity of the scintillator, only hits which are exclusive to a given track are used in the confidence level. Assuming the energy loss per hit is independent, the probability for a track to be muon-like (μ) or not muon-like (η) can be written as

$$\mu_{CL} = \frac{(\prod_i^{nhits} P([\frac{\mathrm{d}E}{\mathrm{d}x}]_i|\mu)\cdot P(\mu)}{(\prod_i^{nhits} P([\frac{\mathrm{d}E}{\mathrm{d}x}]_i|\mu)\cdot P(\mu) + (\prod_i^{nhits} P([\frac{\mathrm{d}E}{\mathrm{d}x}]_i|\eta)\cdot P(\eta)} \tag{4.10}$$

  All tracks reconstructed in a given event which share a vertex have their $\mathrm{d}E/\mathrm{d}x$ distribution measured and then normalized to generate probabilities for a track to be muon-like and not muon-like, using the confidence level constructed as above.

  This information combined with the charge deposition distribution near the end of the track are given as inputs to the BDT. The charge distribution near the end of the track is used because the $\mathrm{d}E/\mathrm{d}x$ for a given particle depends on its momentum. Protons are much more likely to deposit most of their energy at the end of the track, whereas the energy deposition for muons and pions will be more even along the track. The boosted decision tree was trained using AdaBoost [81] through the TMVA package [82], and two confidence levels were built: one to identify muon tracks (μ_{CL}), and one to separate protons from pions (p_{CL}) that were rejected by the muon confidence level. For further details see Ref. [5].

- **Single muon track**: One and only one muon candidate track (positive or negative). If the candidate is an INGRID stopping track, it is muon-like if $\mu_{CL} > 0.1$, and if it is an INGRID early stopping track the muon cut is $\mu_{CL} > -0.05$.

- **Zero pion tracks**: If there is a second track, it must be proton-like, $p_{CL} > 0.17$.

- **Time clustering cut**: Requires more than 3 hits in an 100 ns time window. In this case all hits within ±50 ns of the average timing of these events are selected as a hit cluster to remove most of the hits created by random noise.

- **Active planes cut**: Requires at least three active tracking scintillator planes, and the track has to have a reconstructed distance of at least 15cm to pass this cut. This further reduces the random noise and external background created by photons or neutrons.

- **Upstream veto**: Events having their most upstream hit in the veto planes, defined as the first four layers of the PM, are rejected. Additionally the PM has a set of edge veto planes where an event showing a hit in the edge veto at a distance less than 80 mm to the extrapolated track upstream position are rejected.

- **Fiducial volume cut**: The fiducial volume is defined as a transverse central $(\pm 50) \times (\pm 50)$ cm^2 region of the PM (totaling 100 cm in each direction). Events in which the most upstream hit is not contained in the fiducial volume are rejected.

The muon candidate kinematic distributions for the INGRID sample are displayed in Fig. 4.10 split by true topology, showing the proportion of true signal and background events. The CC-0π topology in Fig. 4.10 has been subdivided into categories by how many protons were in the event, all of which combine together to form the total CC-0π signal. The other background category is a combination of contributions from $\bar{\nu}_\mu$, ν_e, out of fiducial volume, and other detector background events. The INGRID sample has a decent purity of true CC-0π events considering the limitations compared to ND280, which is shown in Tab. 4.5. In addition, Fig. 4.11 shows the same kinematic distributions split by true reaction.

INGRID	CC-0π	CC-1π	CC-Other	Background	Events
Stopping	62.81	15.44	4.86	16.89	1634.37
Stop+Escaping	67.16	15.92	5.04	11.88	9921.24

Table 4.5: Purity of the INGRID signal sample for both stopping only and stopping plus through-going tracks.

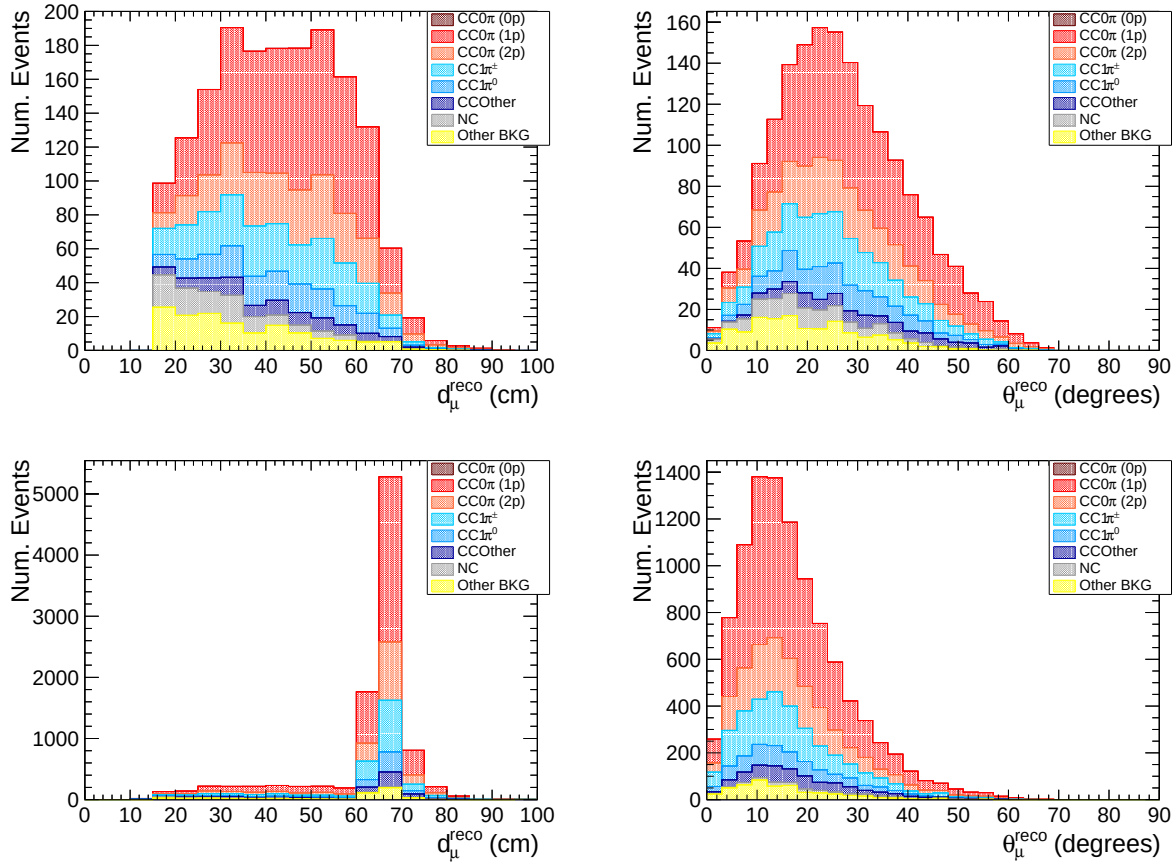

Figure 4.10: Event distribution for reconstructed muon equivalent distance in iron and angle for the INGRID (early) stopping signal samples (top) and all INGRID signal samples (bottom) stacked by true topology.

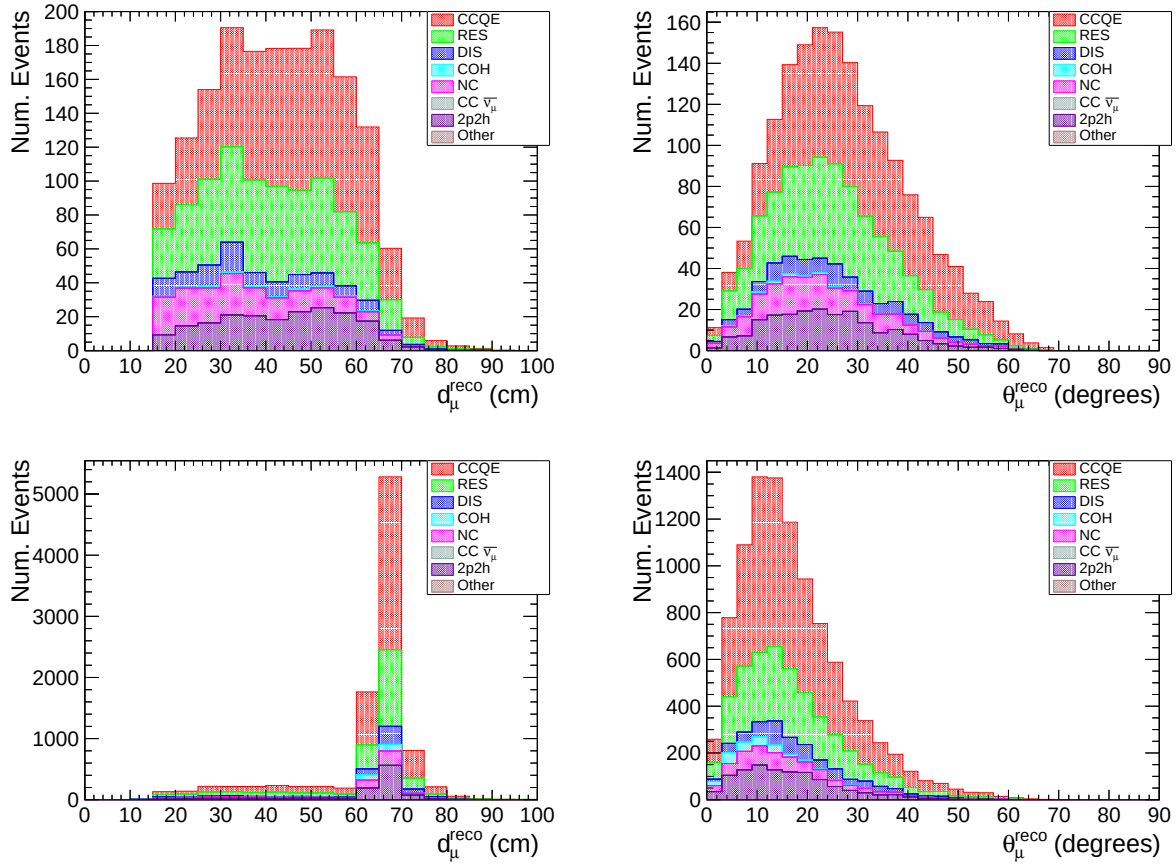

Figure 4.11: Event distribution for reconstructed muon equivalent distance in iron and angle for the INGRID (early) stopping signal sample (top) and all INGRID signal samples (bottom) stacked by true reaction.

4.4 Sideband selection

The primary backgrounds for this analysis are events where one or multiple pions were misidentified or not reconstructed (either through detector error or FSI), causing the event to appear like a CC-0π event. To improve the performance of the analysis, several sideband (or control) samples have been developed to select events with one or multiple pions. This gives the fit the ability to constrain the rate of charged-current single or multiple pion production rates.

4.4.1 ND280 sideband selection

The ND280 CC-0π analysis has three main sideband samples to constrain the backgrounds by selecting events with one or more charged pions in the final state or the presence of a Michel electron. The sideband samples are constructed in a similar method to the signal samples, but several cuts have been flipped or changed to select background events instead of signal events. The three sideband samples are (shown as event displays in Fig. 4.12):

- **Sample 5** (CC-1π^+) : a single muon with an FGD-TPC track and a single positively charged pion candidate were detected with no other track candidates present (only two tracks present).
- **Sample 6** (CC-Other) : a single muon with an FGD-TPC track and multiple tracks detected in the TPC where the highest momentum positive track is identified as a pion candidate.
- **Sample 7** (CC-Michel) : a single muon with an FGD-TPC track, at least one Michel electron detected, and no pion tracks.

The cut flow for each sideband sample is shown in Fig. 4.13. An event must pass all cuts for a given sample definition to be placed in that sample, and events which fail a cut may still meet the criteria to be placed in a different sample. The sideband samples use many

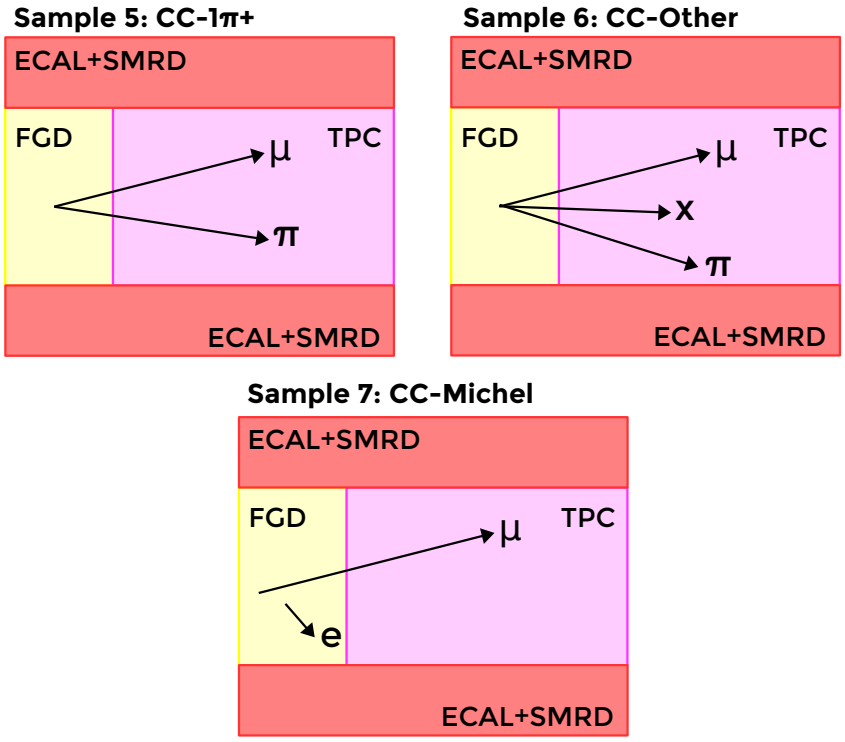

Figure 4.12: Event display cartoon for the ND280 sideband samples.

of the same cuts which are described in Sec. 4.3.1, and sideband specific cuts are described here.

- **HMP Pion Track**: This cut requires the highest momentum positive (HMP) track to be π^+-like according to the TPC PID algorithm described earlier. Resonant pion production from a neutrino event should produce a positive or neutral charged pion in the absence of any FSI effects.

- **TPC Tracks**: This cut is based on the number of tracks that reach the TPC which share a common vertex the FGD fiducial volume.

- **Michel Electron**: This cut requires the presence of a single Michel electron identified in the FGD.

<table>
<tr><th>CC1pi+</th><th>CC1pi+e</th><th>CCOther</th></tr>
<tr><td colspan="3">Event Quality</td></tr>
<tr><td colspan="3">HMN Vertex</td></tr>
<tr><td colspan="3">Muon PID</td></tr>
<tr><td colspan="2">One Negative Track</td><td>HMP Pion Track</td></tr>
<tr><td>HMP Pion Track</td><td>Only Muon/Proton</td><td rowspan="2">Multiple TPC Tracks</td></tr>
<tr><td>Two TPC Tracks</td><td>Michel Electron</td></tr>
</table>

Figure 4.13: Chart showing the selection cuts used to define each ND280 sideband sample.

Sample	CC-0π	CC-1π	CC-Other	Background	Out of FV	Events
Sample 5: CC-1π	7.02	69.29	14.95	6.99	1.75	1715.49
Sample 6: CC-Other	0.72	10.70	71.71	10.86	6.00	2825.08
Sample 7: CC-Michel	10.30	60.87	10.50	1.91	16.42	1424.66

Table 4.6: Purity of each ND280 sideband sample.

The muon candidate kinematic distributions are displayed in Fig. 4.14 split by the true topology, showing the proportion of true signal and background events. In addition, Fig. 4.15 shows the same kinematic distributions split by true reaction, and distributions as a function of momentum transfer can be found in Appendix F. For both sets of plots, the 'out FV' refers to events which actually occurred outside the fiducial volume, but were still selected, and the 'BKG' (or 'other') category is a catch-all for every other type of event not belonging to a listed category. The three sideband samples have good purity, and importantly have few to no signal events. The purity for each sideband sample is also listed in Tab. 4.6. Figure 4.17 shows the distribution of the desired background events (CC-1π^+ and CC-Other) in both the signal and sideband samples as a function of true Q^2. The distribution of CC-1π^+ events matches very well between both the signal and sideband samples, and the distribution of CC-Other events shows some overlap between the signal and sideband samples at low muon momentum. The same plots as a function of muon momentum and pion momentum can be found in T2K-TN-380 [83].

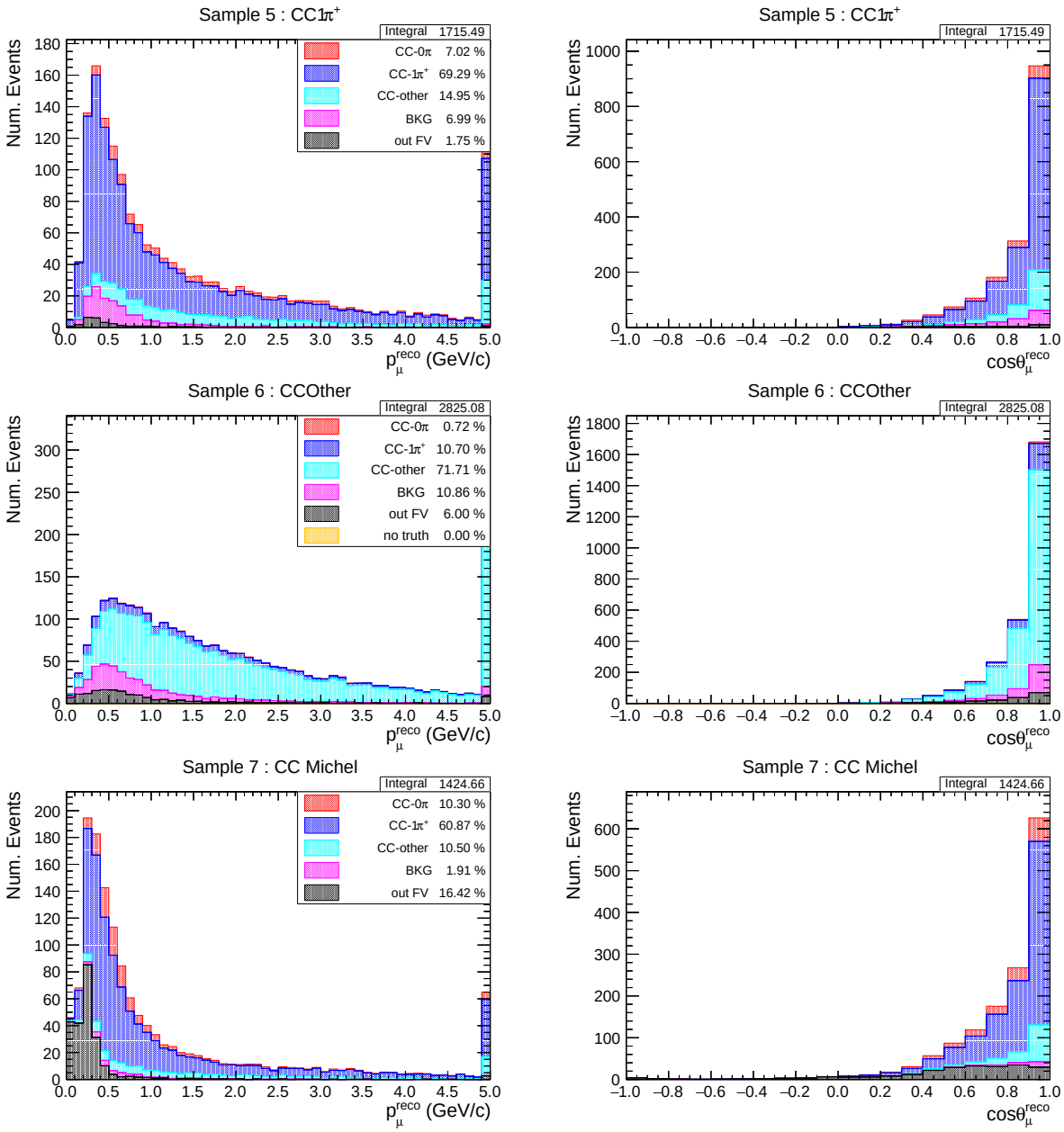

Figure 4.14: Event distribution for reconstructed muon momentum and angle for the ND280 sideband samples stacked by true topology. The purity of each topology is listed in the legend. The last bin for muon momentum contains all events with momentum greater than 5 GeV/c.

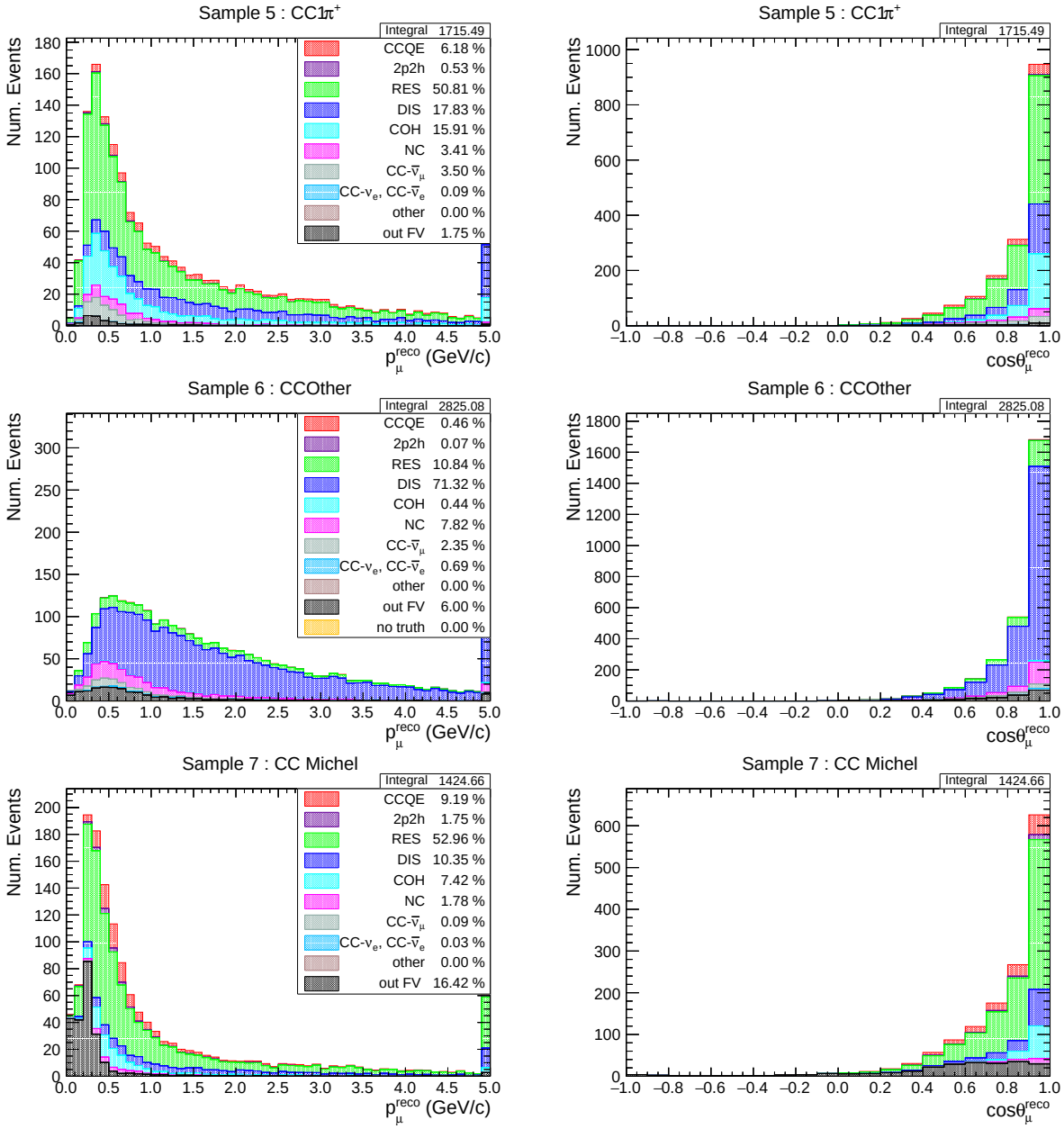

Figure 4.15: Event distribution for reconstructed muon momentum and angle for the ND280 sideband samples stacked by true reaction. The purity of each reaction is listed in the legend. The last bin for muon momentum contains all events with momentum greater than 5 GeV/c.

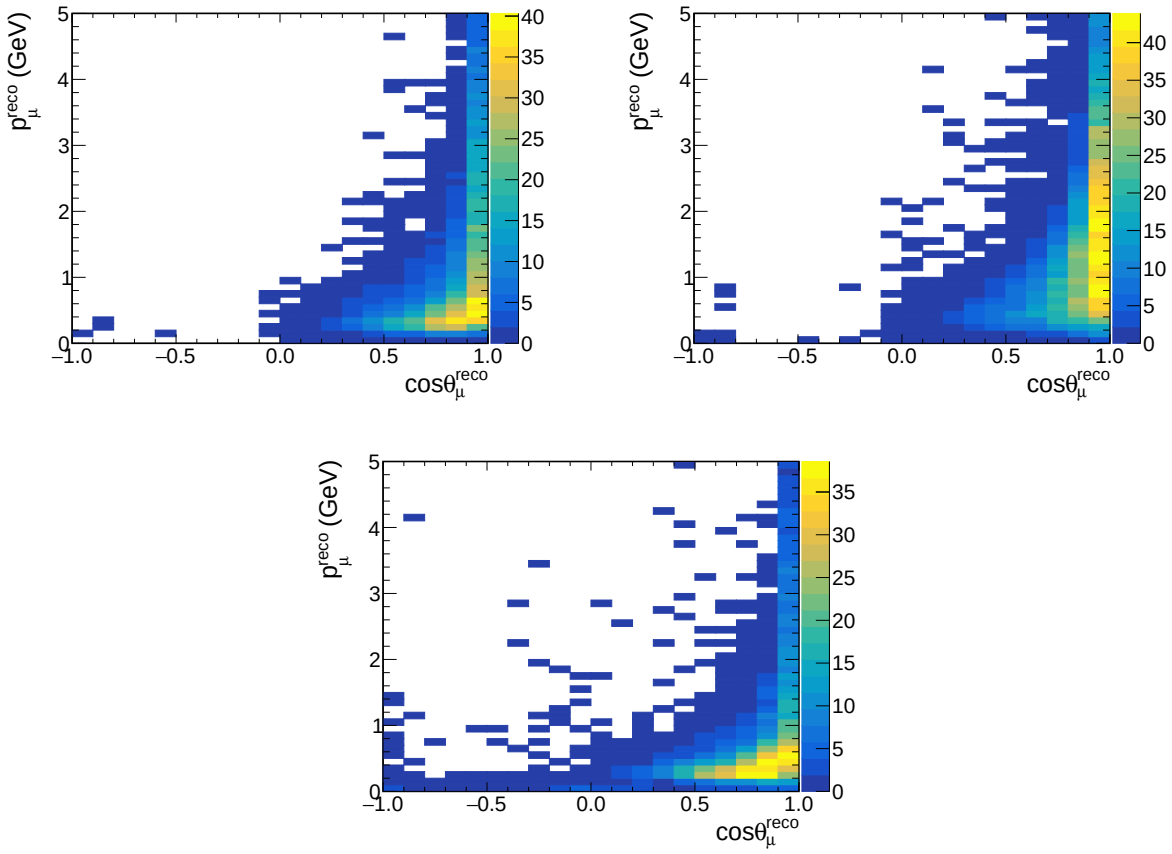

Figure 4.16: Two dimensional event distribution for reconstructed muon momentum vs angle for the ND280 sideband samples. CC-1π in the top left, CC-Other in the top right, CC-Michel at the bottom.

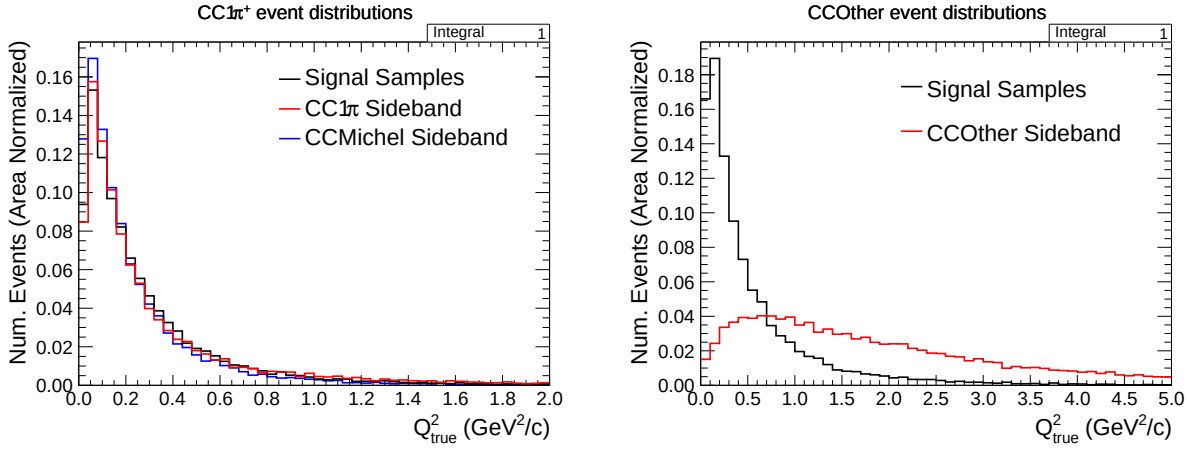

Figure 4.17: Area normalized event distributions as a function of Q^2 for the background events compared between the signal samples and the corresponding sidebands. The CC-1π^+ distribution is on the left, and matches quite well. The CC-Other distribution is on the right and is quite different between the signal and sideband.

4.4.2 INGRID sideband selection

The INGRID CC-0π as developed in T2K-TN-204 has a single CC-1$\pi^{\pm}$ sideband [5]. Unfortunately there is no INGRID CC-Other or CC-Michel sideband to include similar to the ND280 selection. The INGRID CC-1$\pi^{\pm}$ sample selects events which satisfy the following criteria.

- **Event quality**: Events are required to pass a quality cut ensuring the detector and beam were in good working condition. This cut is only applied to data events as MC events are assumed to pass the quality cut.

- **Beam timing**: Events are required to be $\pm$100 ns of the expected beam bunch arrival time to reduce the cosmic background. The timing of the event is defined as the timing of the largest charge deposition hit in the event.

- **Track Multiplicity**: Exactly two or three reconstructed tracks. The CC-1$\pi^{\pm}$ sample requires a muon and pion candidate, so two tracks minimum are required.

- **Muon track**: A single muon candidate track with $\mu_{CL} > 0.1$ (same as the CC-0π selection).

- **Pion track**: A single pion candidate track with $p_{CL} < -0.06$. This cut value has been tuned to increase efficiency of selecting pion candidates.

- **Optional proton track**: If a third track is reconstructed, it should be proton-like with $p_{CL} > -0.06$.

- **Time clustering cut**: Requires more than 3 hits in an 100 ns time window. In this case all hits within $\pm$50 ns of the average timing of these events are selected as a hit cluster to remove most fhte hits created by random noise.

- **Active planes cut**: Requires at least three active tracking scintillator planes. This further reduces the random noise and external background created by photons or neutrons.

- **Upstream veto**: Events having their most upstream hit in the veto planes, defined as the first four layers of the PM, are rejected. Additionally the PM has a set of edge veto planes where an event showing a hit in the edge veto at a distance less than 80 mm to the extrapolated track upstream position are rejected.

- **Fiducial volume cut**: The fiducial volume is defined as a transverse central $(\pm 50) \times (\pm 50)$ cm^2 region of the PM (totaling 100 cm in each direction). Events in which the most upstream hit is not contained in the fiducial volume are rejected.

Unlike ND280, INGRID has no magnetic field to determine the charge of a particle/track, so the CC-1π sideband will select both π^+, π^- as pion candidates. The events in the sample are categorized based on where (if) the muon stopped in the detectors like the CC-0π selection.

The muon candidate kinematic distributions for the INGRID sideband sample are displayed in Fig. 4.18 split by true topology, showing the proportion of true signal and background events. The CC-0π topology in Fig. 4.18 has been subdivided into categories by how many protons were in the event, all of which combine together to form the total CC-0π category. The other background category is a combination of contributions from $\bar{\nu}_\mu$, ν_e, out of fiducial volume, and other detector background events. In addition Fig. 4.19 shows the kinematic distributions split by true reaction. While the purity of CC-1π events is not great, the sideband samples contain relatively few true signal events allowing the sideband sample to be quite useful providing a data driven constraint on the total background event rate.

INGRID	CC-0π	CC-1π	CC-Other	Background	Events
Stopping	10.27	56.50	20.50	12.73	560.18
Stop+Escaping	11.21	52.60	26.93	9.26	2454.82

Table 4.7: Purity of the INGRID sideband sample for both stopping only and stopping plus through-going tracks.

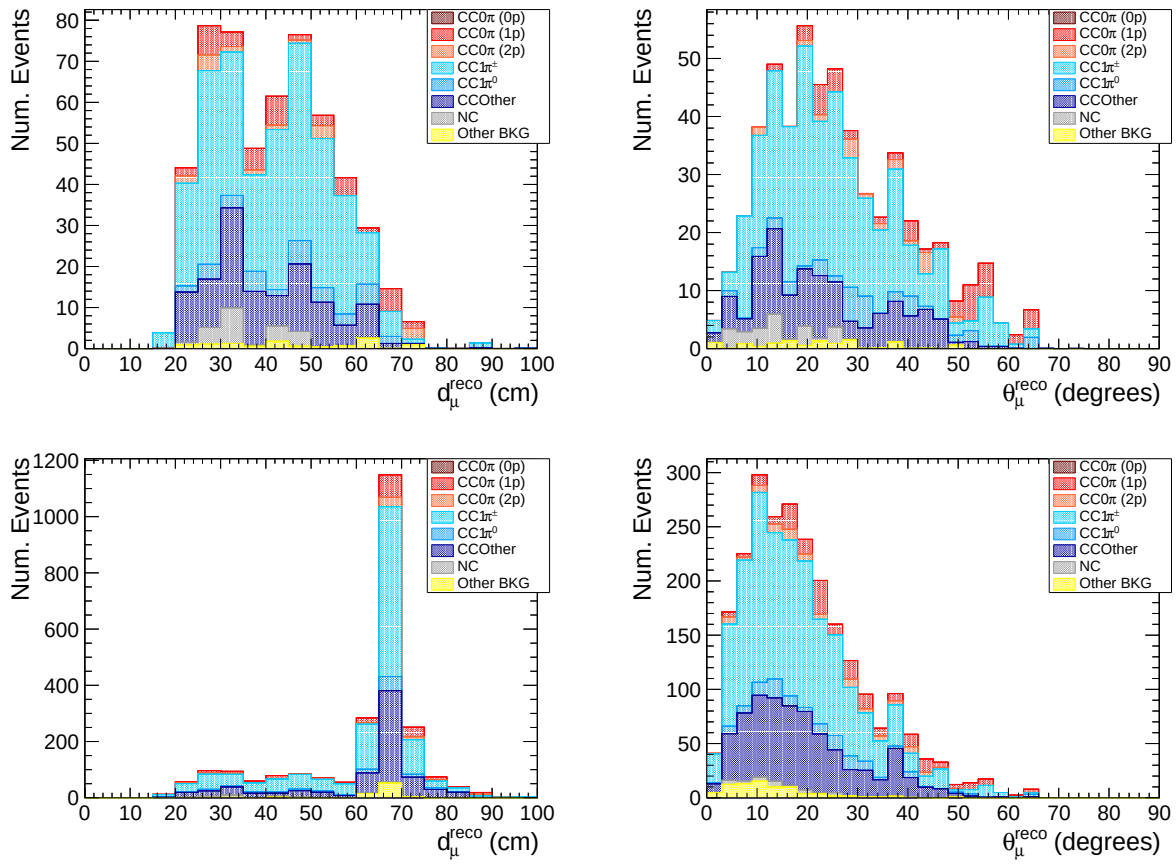

Figure 4.18: Event distribution for reconstructed muon equivalent distance in iron and angle for the INGRID (early) stopping sideband samples and all INGRID sideband samples stacked by true topology. The roughness of the distribution is due to the combination of low statistics and the binning choice to match the signal region.

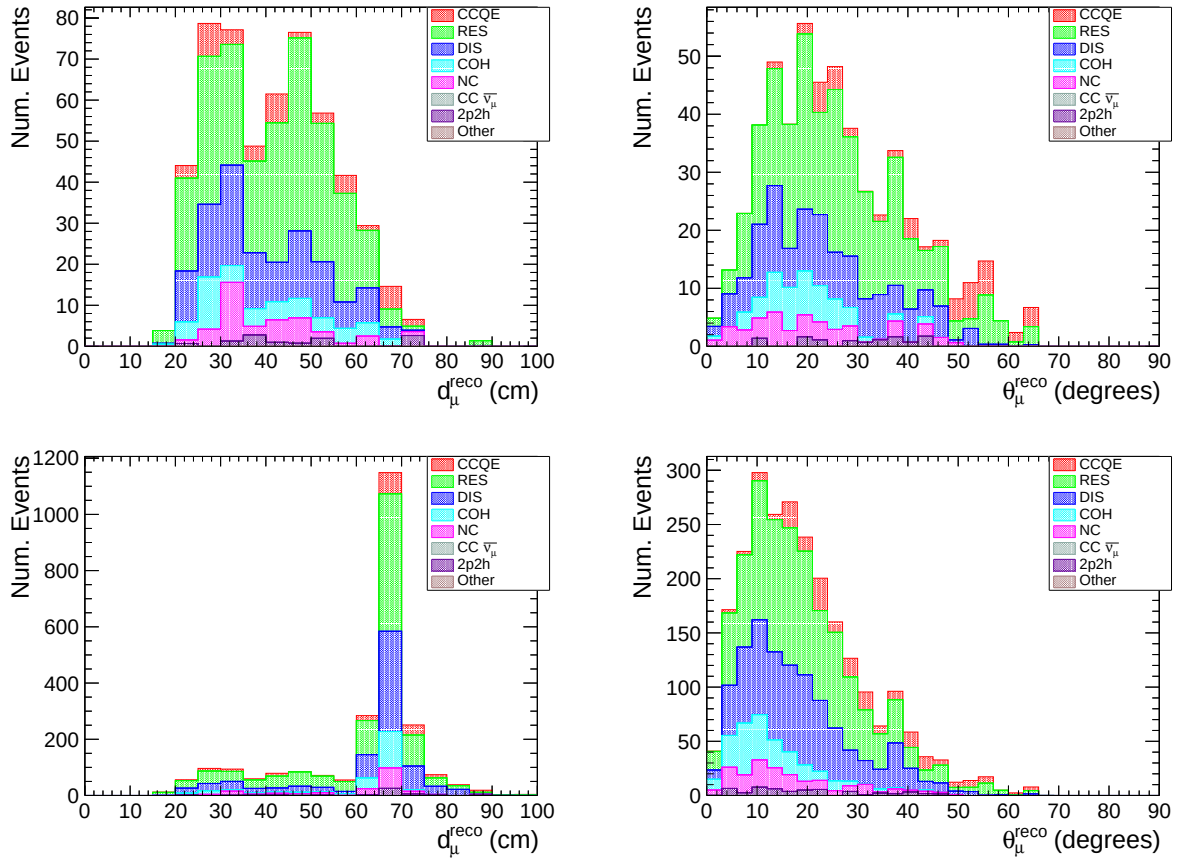

Figure 4.19: Event distribution for reconstructed muon equivalent distance in iron and angle for the INGRID (early) stopping sideband samples and all INGRID sideband samples stacked by true reaction. The roughness of the distribution is due to the combination of low statistics and the binning choice to match the signal region.

4.5 Analysis binning

The choice of analysis binning must be considered carefully to provide a precise and useful cross-section measurement. If the bins are too wide, then information about the shape of the distribution will be lost, while if the bins are too thin, then some bins could have few to zero events causing minimization issues and large statistical errors for those bins. The following criteria were considered when choosing the analysis binning:

- **Statistics**: Each bin should have a sufficient number of events to prevent minimization issues.
- **Detector resolution**: The analysis should have bins of a similar size or larger than the measured detector resolution. Measured variables in the detector cannot provide more precision than the detector is capable of in a model independent way.
- **Efficiency**: The efficiency across bins ideally should be relatively high and consistent. Bins with low efficiency will rely more on the MC to perform the efficiency correction.

In this analysis the binning for each detector has been optimized separately and is described for each detector below. The analysis binning refers to the binning used for the signal parameters in the statistical fit (described in Chapter 6 and the final cross section result. The sample binning used in other parts of the fit (e.g. detector systematics) may be different than the binning presented here.

4.5.1 ND280

The analysis binning for ND280 uses muon kinematic variables $p_\mu, \cos\theta_\mu$ for both the extracted cross section and measured data bins. The choice of binning, as shown in Tab. 4.8, is the same as T2K-TN-337 [3]. The μFGD and μFGD+pTPC samples use a reduced data binning which can be found in Appendix E to avoid empty bins which is driven by the event kinematics.

Bin index	$\cos\theta_\mu$	p_μ [GeV/c]
0	-1, 0.2	0, 30
1	0.2, 0.6	0, 0.3
2	0.2, 0.6	0.3, 0.4
3	0.2, 0.6	0.4, 0.5
4	0.2, 0.6	0.5, 0.6
5	0.2, 0.6	0.6, 30
6	0.6, 0.7	0, 0.3
7	0.6, 0.7	0.3, 0.4
8	0.6, 0.7	0.4, 0.5
9	0.6, 0.7	0.5, 0.6
10	0.6, 0.7	0.6, 0.8
11	0.6, 0.7	0.8, 30
12	0.7, 0.8	0, 0.3
13	0.7, 0.8	0.3, 0.4
14	0.7, 0.8	0.4, 0.5
15	0.7, 0.8	0.5, 0.6
16	0.7, 0.8	0.6, 0.8
17	0.7, 0.8	0.8, 30
18	0.8, 0.85	0, 0.3
19	0.8, 0.85	0.3, 0.4
20	0.8, 0.85	0.4, 0.5
21	0.8, 0.85	0.5, 0.6
22	0.8, 0.85	0.6, 0.8
23	0.8, 0.85	0.8, 1.0
24	0.8, 0.85	1.0, 30
25	0.85, 0.9	0, 0.3
26	0.85, 0.9	0.3, 0.4
27	0.85, 0.9	0.4, 0.5
28	0.85, 0.9	0.5, 0.6
29	0.85, 0.9	0.6, 0.8
30	0.85, 0.9	0.8, 1.0
31	0.85, 0.9	1.0, 1.5
32	0.85, 0.9	1.5, 30
33	0.9, 0.94	0, 0.4
34	0.9, 0.94	0.4, 0.5
35	0.9, 0.94	0.5, 0.6
36	0.9, 0.94	0.6, 0.8
37	0.9, 0.94	0.8, 1.25
38	0.9, 0.94	1.25, 2.0
39	0.9, 0.94	2.0, 30
40	0.94, 0.98	0, 0.4
41	0.94, 0.98	0.4, 0.5
42	0.94, 0.98	0.5, 0.6
43	0.94, 0.98	0.6, 0.8
44	0.94, 0.98	0.8, 1.0
45	0.94, 0.98	1.0, 1.25
46	0.94, 0.98	1.25, 1.5
47	0.94, 0.98	1.5, 2.0
48	0.94, 0.98	2.0, 3.0
49	0.94, 0.98	3.0, 30
50	0.98, 1.0	0, 0.5
51	0.98, 1.0	0.5, 0.7
52	0.98, 1.0	0.7, 0.9
53	0.98, 1.0	0.9, 1.25
54	0.98, 1.0	1.25, 2.0
55	0.98, 1.0	2.0, 3.0
56	0.98, 1.0	3.0, 5.0
57	0.98, 1.0	5.0, 30

Table 4.8: ND280 binning used for the extracted cross section and data distribution in muon kinematics $p_\mu, \cos\theta_\mu$

4.5.2 INGRID

The analysis binning for INGRID uses muon kinematic variables $p_\mu, \cos\theta_\mu$ for the extracted cross section measurement, and muon kinematic variables d_μ, θ_μ for the measured data variables where d_μ is the reconstructed equivalent distance in iron for the muon. The choice of binning, as shown in Tab. 4.9, is mostly the same as T2K-TN-204 [5]. The reconstructed binning has angular bin widths of 10 degrees from 0 to 60 degrees, and distance bin widths of 5 cm from 0 to 80 cm (except for the first distance bin, which is from 0 to 10).

Bin index	$\cos\theta_\mu$	p_μ [GeV/c]
0	0.5, 0.82	0.35, 0.5
1	0.5, 0.82	0.5, 0.7
2	0.5, 0.82	0.7, 1.0
3	0.5, 0.82	1.0, 30.0
4	0.82, 0.94	0.35, 0.5
5	0.82, 0.94	0.5, 0.7
6	0.82, 0.94	0.7, 1.0
7	0.82, 0.94	1.0, 30.0
8	0.94, 1.00	0.35, 0.5
9	0.94, 1.00	0.5, 0.7
10	0.94, 1.00	0.7, 1.0
11	0.94, 1.00	1.0, 30.0

Bin index	θ_μ	d_μ [cm]
0	0, 10	0, 10
1	0, 10	10, 15
2	0, 10	25, 20
⋮	⋮	⋮
13	0, 10	70, 75
14	0, 10	75, 80
15	10, 20	0, 10
16	10, 20	10, 15
17	10, 20	15, 20
⋮	⋮	⋮
88	50, 60	70, 75
89	50, 60	75, 80

Table 4.9: INGRID binning used for the extracted cross section (left) and data distribution (right) in muon kinematics. Note that the data is measured using muon distance in iron and the cross section is measured in muon momentum.

The muon momentum is determined by the range traveled in the both the Proton Module and the standard INGRID module located directly behind the Proton Module following the same procedure from T2K-TN-204 [5]. The data is binned in distance traveled instead of momentum since the distance is the directly measured quantity. The detector smearing (or transfer) matrix handles the mapping between measured distance to momentum (shown in Fig. 4.20) when calculating the cross section. Muons in the Proton Module and INGRID travel through both plastic scintillator and iron plates before stopping, and both materials must be accounted for to accurately calculate the momentum. Thus, an equivalent distance

in iron is calculated from the distance traveled in the plastic and iron as follows:

$$d_\mu = d_\mu^{Fe} + \frac{\rho^{CH}}{\rho^{Fe}} d_\mu^{CH} \tag{4.11}$$

where d_μ^X is the actual distance traveled in iron (Fe) or plastic (CH) and ρ^X is the corresponding material density. This analysis uses $\rho^{CH} = 1.03\,\mathrm{g/cm^3}$ and $\rho^{Fe} = 7.87\,\mathrm{g/cm^3}$ from T2K-TN-204 [5].

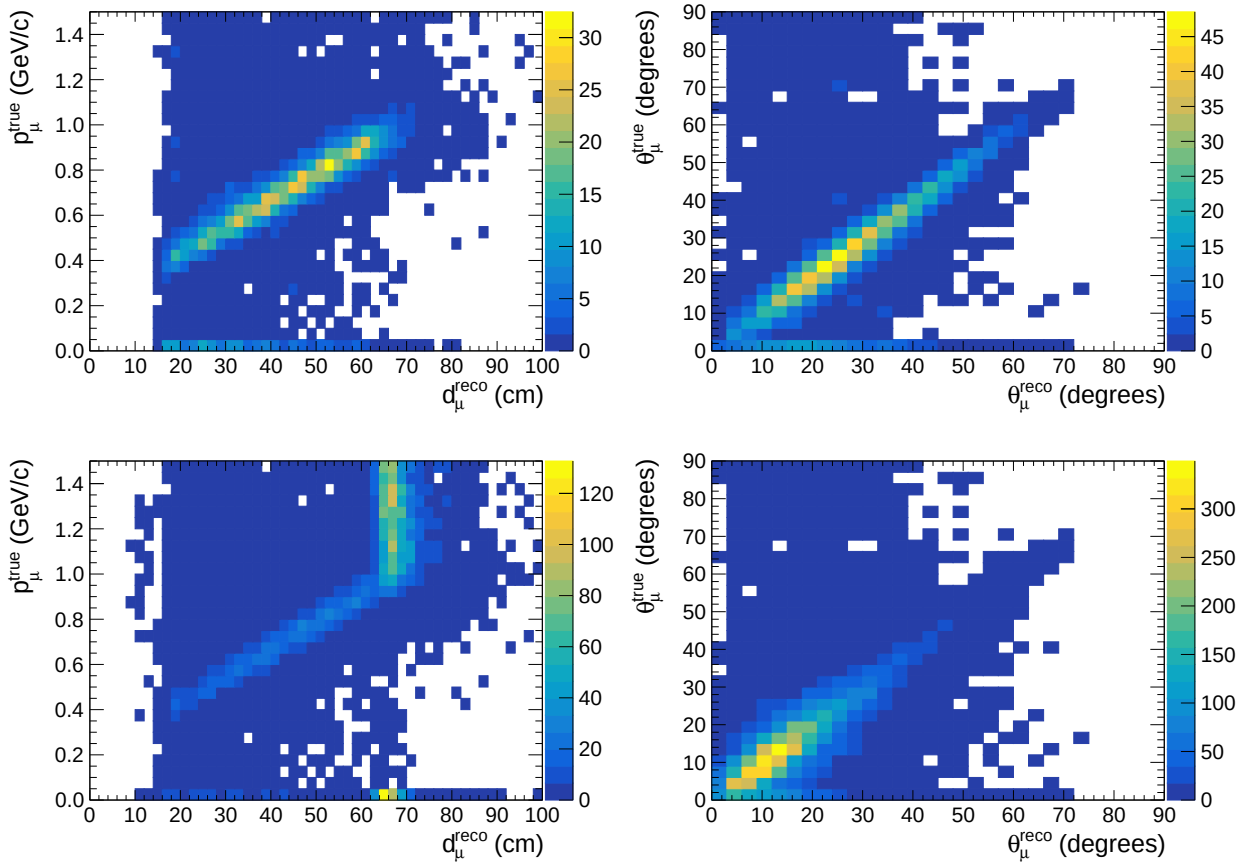

Figure 4.20: Smearing matrix between true and reconstructed variables for the INGRID CC-0π selection using the INGRID (early) stopping samples (top) and all INGRID signal samples (bottom).

Once muons reach an energy of about 1.0 GeV/c or greater they traverse the entire detector and escape. Depending on the angle through the detector, this corresponds to a maximum of approximately 65 to 75 cm equivalent distance in iron, which can be easily seen in the bottom-right plot of Figure 4.20. The population of events at a true momentum and

angle of zero are due to reconstruction failures where the selected muon was not a true muon (e.g. a pion), which has a default value for true momentum and angle equal to zero.

4.6 Efficiency and purity

The efficiency and purity of the analysis are calculated separately for each detector selection and are defined as:

$$\text{Efficiency} = \frac{\text{Number of selected signal events}}{\text{Total number of signal events}} \tag{4.12}$$

$$\text{Purity} = \frac{\text{Number of selected signal events}}{\text{Number of selected events}} \tag{4.13}$$

The efficiency is simply the ratio of selected signal events to the total number of signal events, while the purity is the ratio to selected signal events to all selected events. Since the efficiency correction requires knowing the total number of signal events, it is estimated directly from the MC simulation. This adds additional model dependence to the measurement which is quantified as an uncertainty on the efficiency (see Section 5.5).

4.6.1 ND280

The signal efficiency for each sample and the total for the ND280 selection is shown in Fig. 4.21 in one dimensional projections of muon momentum and angle. The two dimensional total signal efficiency and purity are shown in Fig. 4.22. The efficiency is higher for forward going muons as these events are usually reconstructed in the TPCs, which have excellent reconstruction capabilities. Backward going events are hard to reconstruct as accurate time of flight information is needed to separate events which originated in the FGD fiducial volume versus events that were outside and stopped in the FGD. The efficiency in momentum is fairly flat, with the samples where the muon is reconstructed in the FGD dropping off past 1 GeV where they have enough energy to escape. The relatively low efficiency for the samples with protons is related to being able to differentiate and reconstruct protons versus pions.

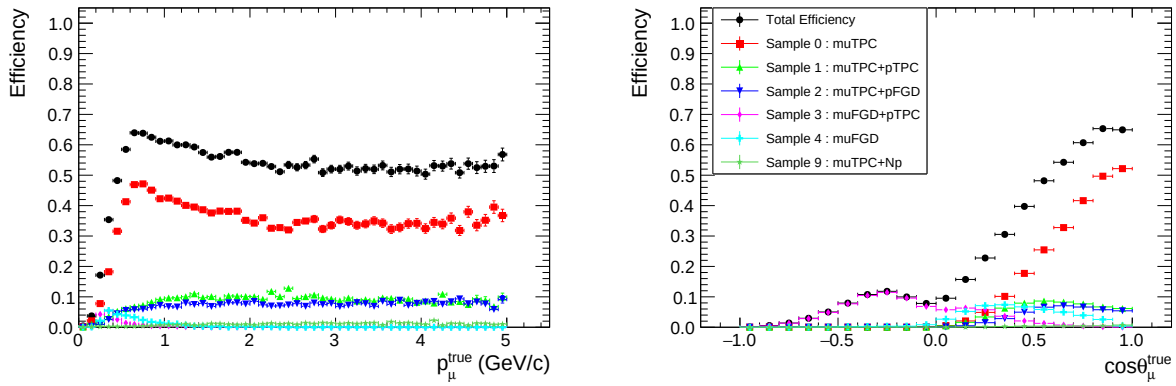

Figure 4.21: ND280 signal efficiency for each sample as a function of true muon momentum (left) and true muon angle (right).

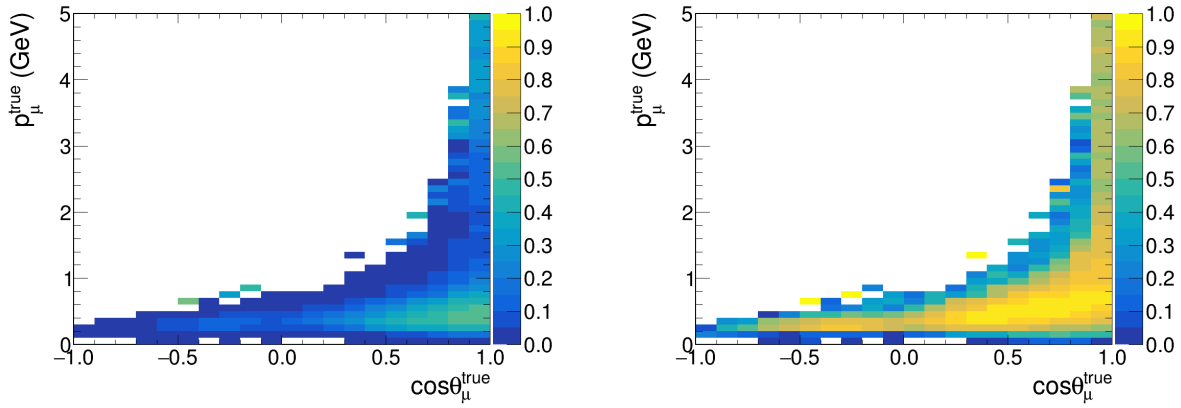

Figure 4.22: ND280 total signal efficiency (left) and purity (right) as a function of both true muon momentum and angle.

4.6.2 INGRID

The signal efficiency for the INGRID stopping sample and the signal efficiency for all INGRID samples combined are both shown in Fig. 4.23. INGRID has essentially zero efficiency past about 60 to 70 degrees as the muons are traveling nearly parallel to the scintillator bars and do not cross enough bars to be reconstructable. Additionally, the minimum muon momentum to cross enough scintillator bars is about 300 to 400 MeV, and once muons reach about 900 to 1000 MeV they do not stop in the detectors which shows up as a drop in efficiency for the stopped sample.

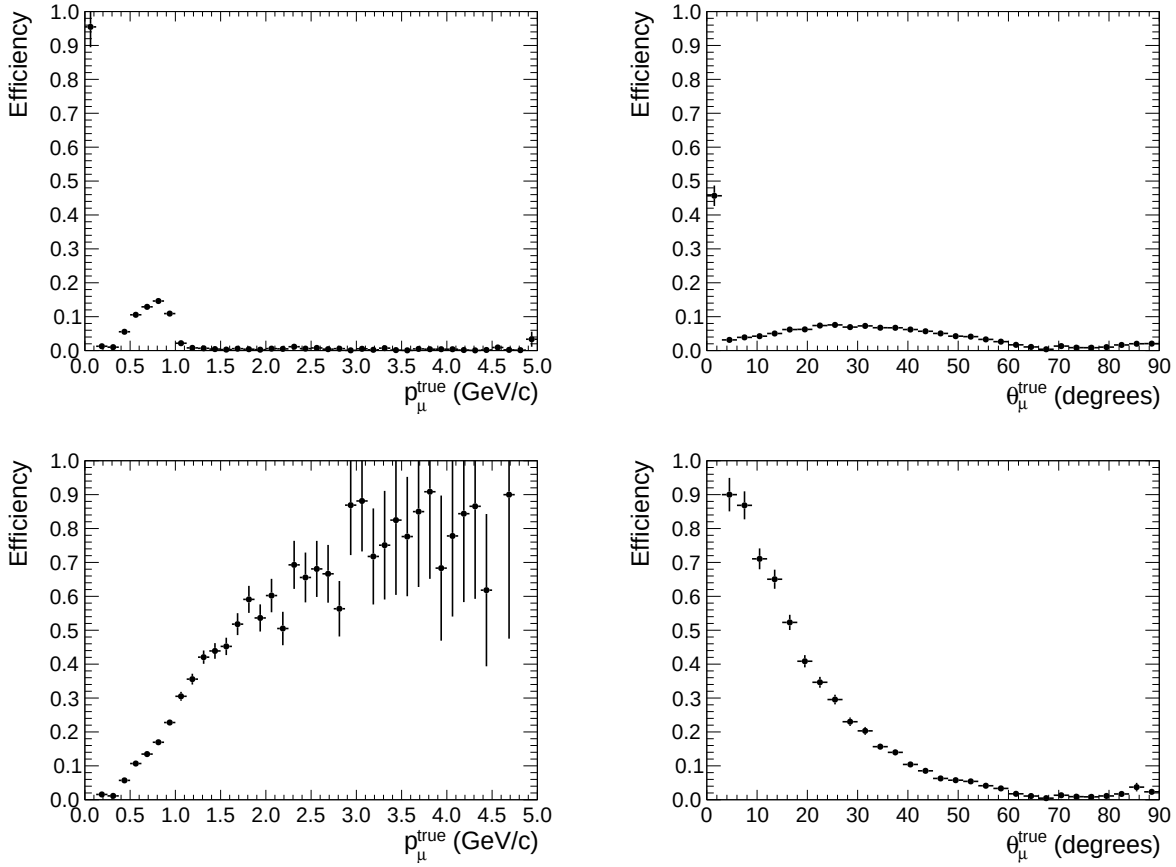

Figure 4.23: INGRID signal efficiency for the stopping sample (top) and all samples combined (bottom) as a function of true muon momentum (left) and true muon angle (right). Note the efficiency axis scale is different between the top and bottom plots.

CHAPTER 5

SYSTEMATIC UNCERTAINTIES

This chapter describes the systematic (or nuisance) parameters which are included in the fit to represent plausible variations of the detector, flux, and neutrino interaction models used in the Monte Carlo simulation. The systematic parameters are varied alongside the signal parameters, but are constrained by an accompanying covariance matrix. When moved from their nominal values, the systematic parameters add a penalty term to the likelihood proportional to the covariance matrix as defined in Eq. 6.5 and reprinted here:

$$-2\ln\mathcal{L}_{\text{syst}} = \chi^2_{\text{syst}} = \sum_p \left(\vec{p} - \vec{p}_{\text{prior}}\right)\left(V_{\text{cov}}^{\text{syst}}\right)^{-1}\left(\vec{p} - \vec{p}_{\text{prior}}\right) \tag{5.1}$$

where $\vec{p}$ is the vector of systematic parameters, $\vec{p}_{\text{prior}}$ is the prior or nominal value of the systematic parameters, and V_{cov} is the covariance matrix which describes the confidence and error for each parameter as well as the correlations between each parameter. This method approximates and treats the systematic uncertainty as Gaussian distributed in the fit, and the full details are described in Chapter 6.

There are also several sources of systematic uncertainty which are not included as fit parameters, but are incorporated when propagating the errors as described in Sec 6.3, such as the uncertainty in the number of targets, and are described in this chapter.

5.1 Flux systematic uncertainties

The uncertainties for the flux simulation include uncertainties from the initial proton beam, uncertainties from the beamline setup (e.g. horn current, horn alignment), and uncertainties in the interaction models used to simulate the hadron interactions. The uncertainties on the flux prediction are evaluated by varying the inputs to the simulation and calculating the effect on the predicted flux. There are two main methods to evaluating the uncertainties. The first method is used when an error source includes a number of correlated underlying

parameters that can be continuously varied. The parameters are varied randomly according to their covariance matrix and many different flux predictions are produced (typically several hundred sets). The uncertainty on the flux is calculated by constructing a covariance matrix binned in neutrino energy from the N flux predictions. The second method is used when there is only a single parameter to vary or for effects that are either on or off. The parameter is changed by $\pm 1\sigma$ (or turned on or off) and the flux simulation is run to produce a varied flux prediction. The uncertainty on the flux is similarly calculated as a covariance matrix binned in neutrino energy using the $\pm 1\sigma$ variations. Finally the total flux uncertainty is given by adding the covariance matrix for all error sources together, treating each error source as independent. The flux uncertainty matrix is calculated as a covariance matrix between bins in neutrino energy, neutrino flavor, neutrino detector, and neutrino beam mode.

This analysis uses a flux covariance with 20 neutrino energy bins for the forward horn current (FHC) ν_μ flavor prediction for each detector (see Fig. 5.1). Only the ν_μ flavor is included in the fit and covariance matrix due to the low contamination from the background flavors ($\bar{\nu}_\mu$, ν_e, $\bar{\nu}_e$) and to prevent an unrealistic constraint on the flux model. The relatively few background events could provide a very tight constraint on the flux from the background flavors which would affect the ν_μ flux due to the strong correlations in the flux model. The ND280 and INGRID flux predictions were varied simultaneously to produce a covariance matrix which includes correlations between the flux at each detector. This gives a flux covariance matrix with 40 total bins: the first 20 for ND280 and the second 20 for INGRID. Both detectors use the same flux binning (shown in Tab. 5.1), but have separate flux parameters, allowing the flux to vary at each detector (according to the covariance matrix), giving 40 total flux nuisance parameters in the fit. The flux systematic parameters (f_n) are scale factors on the number of events in a given neutrino energy bin for each detector, and have a nominal value of one (see Eq. 6.9).

The flux integral used to normalize the cross section (see Sec. 6.1 and Sec. 6.4) has some systematic uncertainty which is described by the flux covariance matrix. The uncertainty on

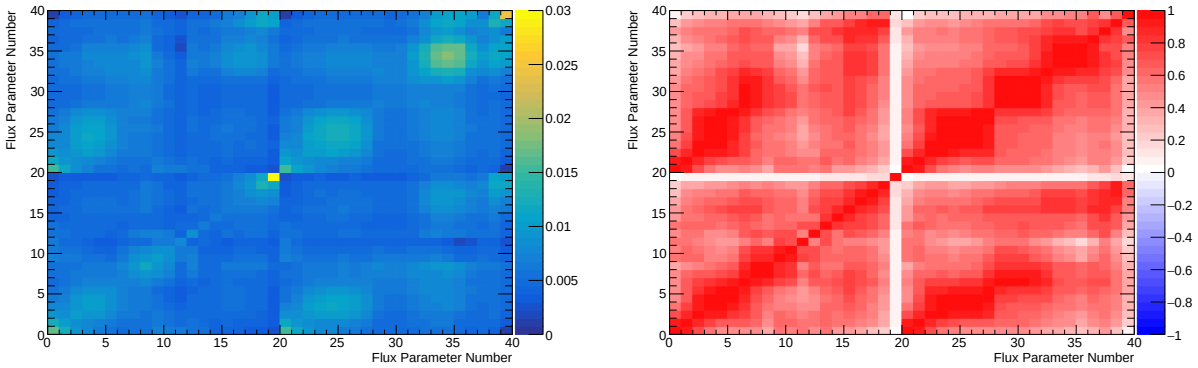

Figure 5.1: Flux covariance (left) and correlation (right) matrices. The bin number corresponds to the parameter number in Tab. 5.1, and ND280 is the first 20 bins and INGRID the second 20 bins.

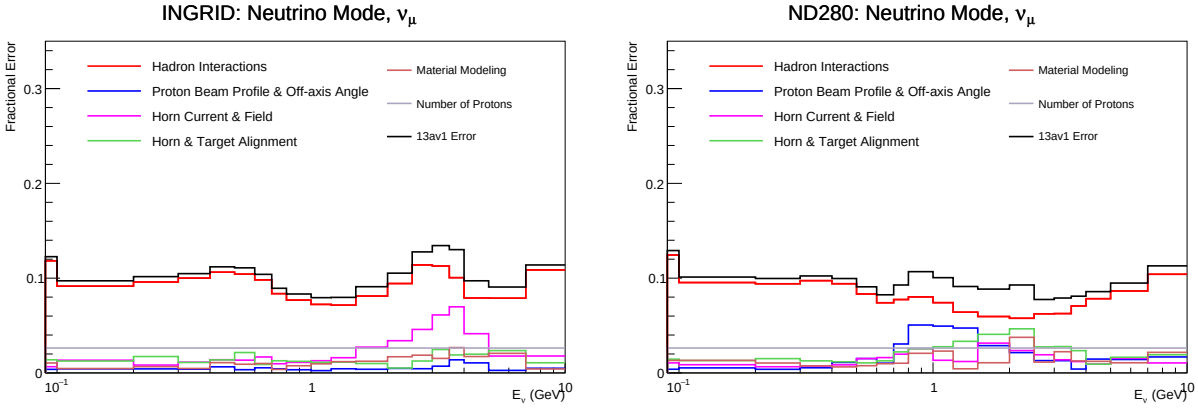

Figure 5.2: The relative flux uncertainty for INGRID (right) and ND280 (left) as a function of neutrino energy bins, separated by the uncertainty source. The flux uncertainty for both detectors is dominated by the uncertainty in the hadron interaction model. The 10 to 30 GeV bin is not shown.

the flux integral is calculated by producing many toy throws of the flux parameters according to the covariance matrix, and calculating the integral for that throw as follows

$$\Phi_{\nu_\mu} = \sum_{n}^{E_{\nu_\mu}} \phi_n f_n \tag{5.2}$$

where Φ_{ν_μ} is the total integrated flux, ϕ_n is the flux for bin n, and f_n is the fitted or thrown flux parameter for bin n. The distribution of these toy throws gives the uncertainty on the flux integral.

ND280	INGRID	Energy bin [GeV]
f_0	f_{20}	0.0 - 0.1
f_1	f_{21}	0.1 - 0.2
f_2	f_{22}	0.2 - 0.3
f_3	f_{23}	0.3 - 0.4
f_4	f_{24}	0.4 - 0.5
f_5	f_{25}	0.5 - 0.6
f_6	f_{26}	0.6 - 0.7
f_7	f_{27}	0.7 - 0.8
f_8	f_{28}	0.8 - 1.0
f_9	f_{29}	1.0 - 1.2
f_{10}	f_{30}	1.2 - 1.5
f_{11}	f_{31}	1.5 - 2.0
f_{12}	f_{32}	2.0 - 2.5
f_{13}	f_{33}	2.5 - 3.0
f_{14}	f_{34}	3.0 - 3.5
f_{15}	f_{35}	3.5 - 4.0
f_{16}	f_{36}	4.0 - 5.0
f_{17}	f_{37}	5.0 - 7.0
f_{18}	f_{38}	7.0 - 10.0
f_{19}	f_{39}	10.0 - 30.0

Table 5.1: The neutrino energy binning used for the flux systematic parameters. Both the ND280 and INGRID flux parameters use the same energy binning, and are treated as separate parameters in the fit.

The fit will return a set of post-fit flux parameters and errors (in the form of a covariance matrix) that can be used to update the nominal flux prediction and in the cross section extraction. The post-fit flux parameters in general will have reduced errors compared to the nominal model and care must be taken such that the fit does not over constrain the flux parameters. An over constraint is most commonly caused when the fit does not have sufficient freedom to vary the background and sideband samples using non-flux parameters, and incorrectly uses the flux parameters to correct most of the difference between data and MC. The base set of neutrino interaction model systematics is adapted from the oscillation analysis, and additional neutrino interaction model systematic parameters have been added to the analysis to prevent the flux parameters from being over constrained (see Section 5.3).

5.1.1 ND280 integrated flux

The nominal flux prediction for the FHC ν_μ mode at ND280 is shown in Figure 5.3 in the binning used for the analysis (highest energy bin not shown, and the full range is from 0 to 30 GeV). The estimated fractional error on the integrated flux using the post-fit errors is 0.067, and the distribution of integrated flux throws is shown in Figure 5.3. The fractional error is the width of a Gaussian fitted to the distribution of integrated flux throws.

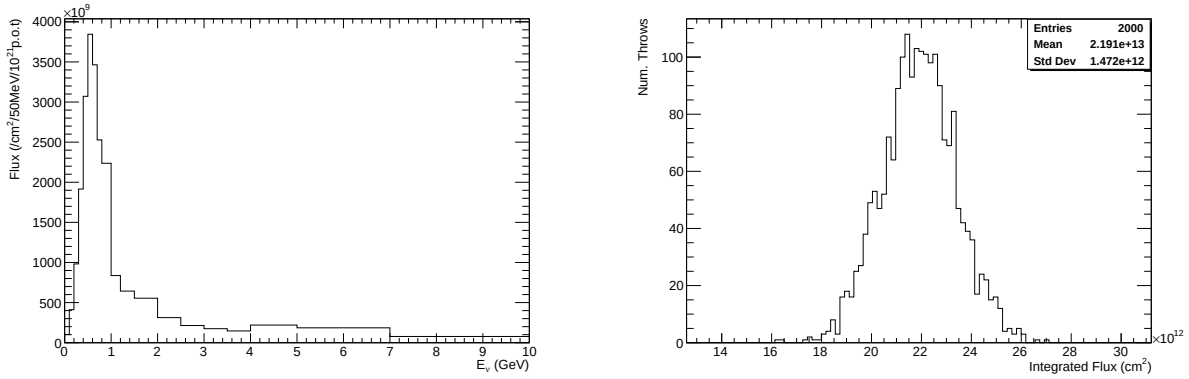

Figure 5.3: ND280 nominal flux prediction (left) using the neutrino energy binning for the flux uncertainties (note that the 10 to 30 GeV bin is not shown). The distribution of integrated flux throws (right) which give the integrated flux error for the cross section extraction.

5.1.2 INGRID integrated flux

The nominal flux prediction for the FHC ν_μ mode at INGRID is shown in Figure 5.4 in the binning used for the analysis (highest energy bin not shown, and the full range is from 0 to 30 GeV). The estimated fractional error on the integrated flux using the post-fit errors is 0.065, and the distribution of integrated flux throws is shown in Figure 5.4. The fractional error is the width of a Gaussian fitted to the distribution of integrated flux throws.

5.2 Detector systematic uncertainties

The detector systematic uncertainties represent the uncertainty on the performance of the detector (such as the particle identification). This analysis uses two different detectors

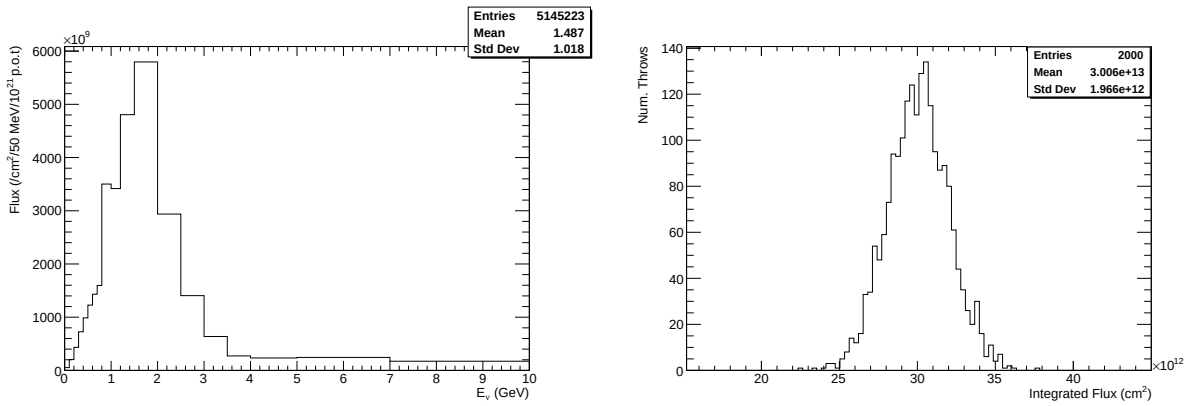

Figure 5.4: INGRID nominal flux prediction (left) using the neutrino energy binning for the flux uncertainties (note that the 10 to 30 GeV bin is not shown). The distribution of integrated flux throws (right) which give the integrated flux error for the cross section extraction.

which require separate treatment of the detector systematics and are treated as completely uncorrelated. The detectors share some similarities in the underlying simulation and parts of the construction, for example the scintillator bars are of a similar construction, and the systematic uncertainties could be correlated in those aspects. However the detector calibrations could be different and this would be a small effect relative to more dominant uncertainties, such as the statistics or flux uncertainties, and has not been considered for this analysis. The detector covariance matrix is the relative uncertainty on the number of reconstructed events in a bin corresponding to reconstructed kinematic variables. Finally, a detector nuisance parameter (d_j) for each detector sample bin is included in the fit, which is allowed to alter the number of events in a reconstructed bin subject to constraints from the covariance matrix (as shown in Sec. 6.2).

5.2.1 ND280 detector systematics

The detector systematics for ND280 have been studied in detail for both cross section analysis and oscillation analysis, and detailed in Refs. [7, 84] and in T2K-TN-212 [85] and T2K-TN-216 [76]. A brief description of the detector systematic uncertainties which have been accounted for is presented here, primarily following the information in Ref. [76], and listed in

Table 5.2. Ideally, the detector systematics should be parameterized in the underlying physics variables in the MC (such as Birks' constant for the scintillator), however this is not possible in all cases. Thus, in practice, some derived parameters (such as the track reconstruction efficiency or the mean energy deposition) that can be computed for both data and MC are used to propagate the detector uncertainties. The ND280 detector systematic uncertainties can be categorized into three different types based on how the are propagated: efficiency-like systematics which simply alter event weights, normalization-like systematics which alter all event weights, and observable variation-like systematics which alter the reconstructed variables of an event and can change the number of selected events. In all cases all the detector systematic parameters are assumed to be Gaussian distributed with the exception of the magnetic field distortions, which are assumed to have a uniform distribution.

Efficiency-like systematics: Efficiency-like systematics are computed through studies comparing data and MC predictions in well-known control samples. For example, a control samples containing muons which originate in the sand/rock surrounding the detector and leave a single track which traverses the entire tracker. The track reconstruction efficiency or matching can be nicely assessed by the redundancy between detectors using the control sample of muons that cross the all of the tracker. However it is possible that the efficiency computed using the control sample does not correspond exactly to the samples used in an analysis, so a model to extrapolate the effect seen in the control sample to the analysis sample is necessary. This analysis assumes the ratio between the efficiencies in data and MC is the same in both the analysis and control samples [76]. The predicted efficiency in an analysis sample can be computed as follows

$$\epsilon_{\text{data}} = \frac{\epsilon^{\text{CS}}_{\text{data}}}{\epsilon^{\text{CS}}_{\text{MC}}} \epsilon_{\text{MC}} \tag{5.3}$$

where ϵ_{data} and ϵ_{MC} are the efficiencies for data and MC respectively for the analysis sample, and CS refers to the control sample. A variation of the predicted data efficiency (ϵ'_{data}) is

given by

$$\epsilon'_{\text{data}} = \left(\frac{\epsilon^{\text{CS}}_{\text{data}}}{\epsilon^{\text{CS}}_{\text{MC}}} + \xi \cdot \sigma^{\text{CS}} \right) \epsilon_{\text{MC}} \tag{5.4}$$

where σ^{CS} is the statistical uncertainty of the efficiency ratio using the control sample (one standard deviation), and ξ is a Gaussian random number centered at zero with a width of one. This will generate a new predicted data efficiency which has been varied according to the statistical uncertainty of the control sample. Event weights are applied based on if the event was successfully reconstructed in the simulation. For events that were successfully reconstructed the following weight is applied to the event

$$w_{\text{eff}} = \frac{\epsilon'_{\text{data}}}{\epsilon_{\text{MC}}} \tag{5.5}$$

and if the event was not reconstructed, then the following weight is applied to the event

$$w_{\text{ineff}} = \frac{1 - \epsilon'_{\text{data}}}{1 - \epsilon_{\text{MC}}} \tag{5.6}$$

Normalization-like systematics: Normalization-like systematics are simpler cases of efficiency-like systematics where the event weight is applied to all events as an overall normalization. A variation of a normalization-like systematic can be generated as follows

$$w = w_0(1 + \xi \cdot \sigma_w) \tag{5.7}$$

where w is the varied event weight, w_0 is the nominal event weight, σ_w is the systematic uncertainty for the normalization (one standard deviation), and ξ is a Gaussian random number centered at zero with a width of one. The new varied event weight is applied to all events in the simulation.

Observable variation-like systematics: Observable variation-like systematics change observable variables (such as the momentum scale or resolution) of a given event rather than the event weight, and are applied to variables which have a different mean or resolution between data and MC. This gives the potential to change the reconstructed topology for an event or cause events to migrate in and out of a given sample/selection as their new

reconstructed variables may pass/fail one of the selection cuts. For example, if there is a cut on momentum, then an event may start to pass or fail a cut if its momentum is sufficiently changed. Thus for each variation of a systematic, the event selection is run again with the new event reconstructed variables. In general the reconstructed values are varied in the following way

$$x' = x + \Delta x + \xi \cdot \sigma_{\Delta x} \tag{5.8}$$

where x and x' are the original and new value of the reconstructed variable respectively, Δx is the correction that should be applied to the MC to match data, $\sigma_{\Delta x}$ is the statistical uncertainty on the correction, and ξ is a Gaussian random number centered at zero with a width of one.

The detector systematic uncertainty is evaluated by generating many variations or throws of each systematic parameter and examining the total effect of all parameters on the reconstructed event distribution separately for each sample. Each throw of the systematic parameters will in general change the number of events in each reconstructed bin of the analysis variables $(p_\mu, \cos\theta_\mu)$, and the event selection is run for each toy throw to allow for event migration. The event distribution in each bin is used to generate a covariance matrix for the effect of all systematic parameters given by

$$V_{ij} = \frac{1}{N} \sum_t (x_{it} - \bar{x}_i)(x_{jt} - \bar{x}_j) \tag{5.9}$$

where V_{ij} is the ij^{th} element of the covariance matrix, N is the number of toy throws, x_{it} is the i^{th} reconstructed kinematic bin for throw t, and $\bar{x}_i$ is the nominal value in reconstructed kinematic bin i. The procedure can also be used to evaluate the effect of each systematic parameter individually. The covariance matrix contains separate bins for each sample since the samples are separated by the particle topology and which sub-detectors were used in the event. For example, systematic variations in the TPC magnetic field will not have much effect on events in the μFGD sample because the TPC was not used in the event.

Ideally the binning for each sample in the detector covariance would use the same binning for the extracted cross section. However this presents two main problems: a large number of detector parameters, and samples having bins with a few to zero events. These cause issues with stability of inverting the detector matrix, and can cause issues with convergence of the fit. Thus some of the samples have a reduced binning to reduce the impact of these issues, but all samples are still separate. The binning for each sample may be found in Appendix E. The μTPC+pFGD and the μTPC+Np samples were combined when running the fit due to the low statistics of the μTPC+Np sample and thus are combined in the detector covariance. Further more, principal component analysis is used to remove a number of detector parameters when running the fit (see Appendix D). The detector fractional covariance and correlation matrices for ND280 are shown in Figure 5.5.

Systematic Name	Systematic Type
TPC PID	Variation
TPC B-field distortions	Variation
TPC momentum scale	Variation
TPC momentum resolution	Variation
TPC cluster efficiency	Efficiency
TPC track efficiency	Efficiency
TPC/FGD charge confusion	Efficiency
FGD PID	Variation
FGD track efficiency	Efficiency
FGD hybrid track efficiency	Efficiency
Michel electron efficiency	Efficiency
TPC-FGD matching efficiency	Efficiency
Vertex migration	Variation
Momentum by range resolution	Variation
Neutrino parent decay position	Variation
Event pile up	Normalization
OOFV background	Normalization
Pion secondary interactions	Normalization
Proton secondary interactions	Normalization

Table 5.2: List of ND280 detector systematic parameters and their propagation type (loosely grouped by detector or general). Each parameter is varied in the simulation to produce the detector covariance amtrix used in the fit.

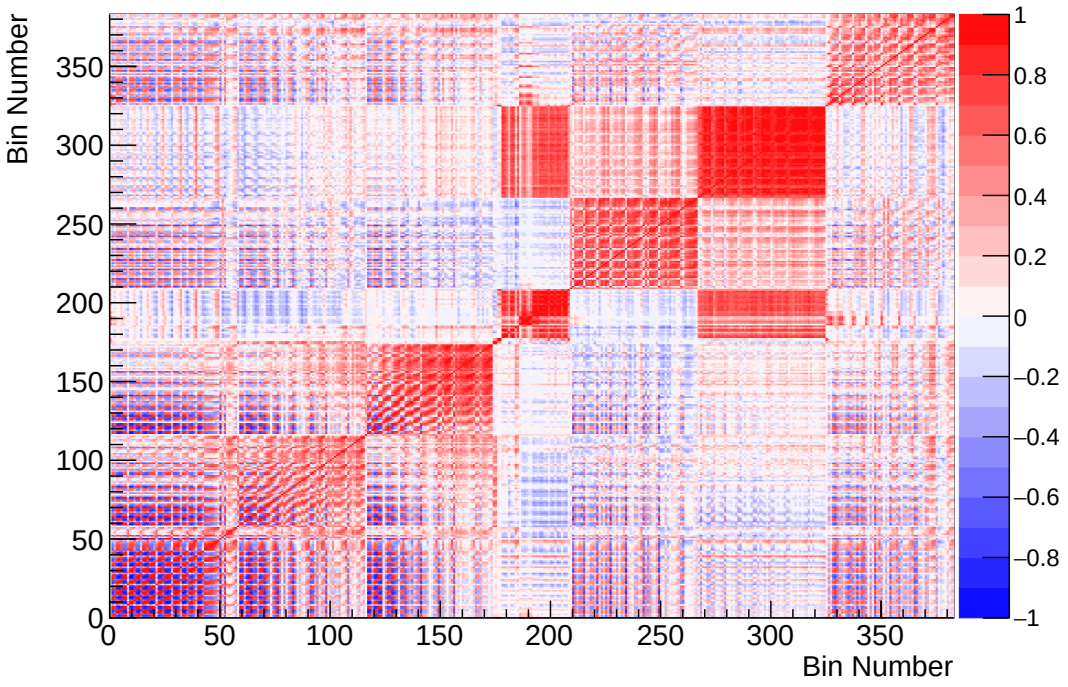

Figure 5.5: ND280 detector correlation matrix binned in muon kinematics for each sample. The detector matrix is generally strongly correlated as the detector systematics tend to affect the same regions of kinematic phase space and samples.

5.2.2 INGRID detector systematics

The detector systematics for the Proton Module (PM) and standard INGRID module have been evaluated and presented in previous T2K analysis, T2K-TN-204 [5] and T2K-TN-352 [86], and this analysis uses the same detector covariance matrix. The detector systematic variations considered for this analysis are listed in Table 5.3 (loosely grouped by type), and a brief summary of how the detector systematic uncertainties are calculated is presented here. The effect of changing a parameter on the cross section is estimated using the detector simulation. Each detector systematic parameter is varied and produces a different weighted MC sample, including a varied efficiency. This new MC sample is used in the analysis to measure a cross section using the standard analysis procedure (as detailed in T2K-TN-204

and T2K-TN-352) and the systematic error is calculated as

$$\delta_X = \frac{\sigma'_X - \sigma_X}{\sigma_X} \tag{5.10}$$

where σ'_X and σ_X is the extracted cross section from the varied MC and the nominal MC respectively for systematic X, evaluated in each true muon momentum and angle bin. The error from each systematic variation is added in quadrature to form the final covariance matrix. The detector fractional covariance and correlation matrices for INGRID are shown in Figure 5.6. The INGRID detector covariance used in this analysis was produced by numerically propagating the original detector covariance matrix in true kinematic bins to reconstructed kinematic bins by throwing many toys. The INGRID signal and sideband samples share the same covariance matrix for the detector systematics as an approximation due to the simplicity of the INGRID analysis and detector uncertainty treatment.

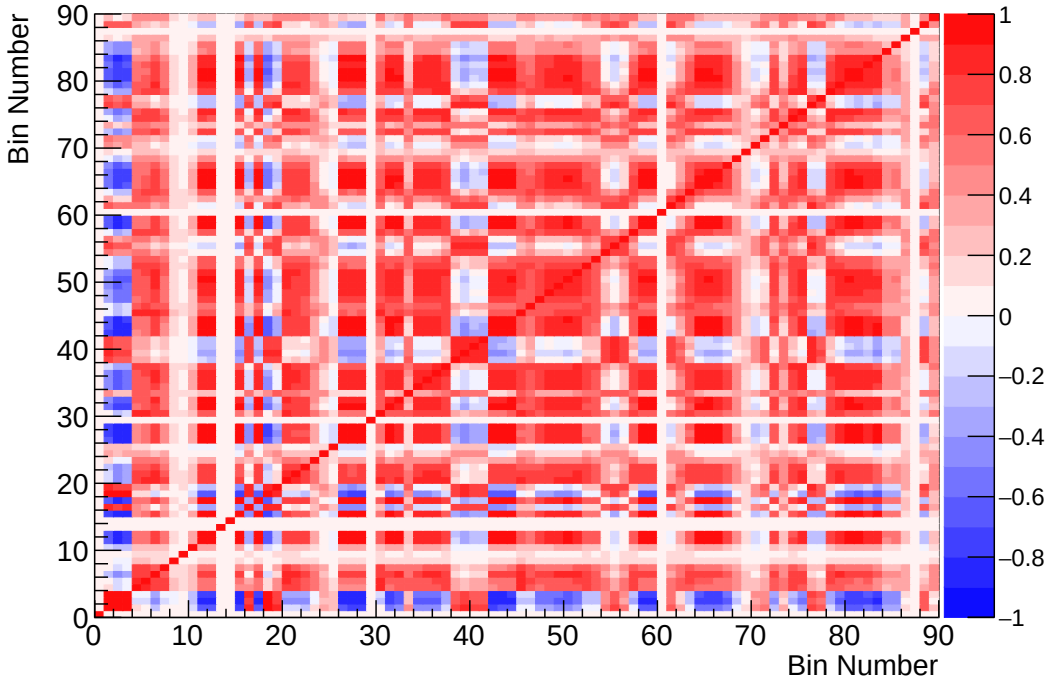

Figure 5.6: INGRID detector correlation matrix binned in muon kinematics for each sample. The detector matrix is generally strongly correlated as the detector systematics tend to affect the same regions of kinematic phase space.

Num.	Systematic Name
1	Dark noise
2	Hit efficiency
3	Scintillator light yield
4	Scintillator quenching
5	External backgrounds
6	2D track reconstruction
7	PM-INGRID track matching angle
8	PM-INGRID track matching position
9	3D track matching
10	Vertex longitudinal cut
11	Vertex transverse cut
12	Edge veto cut
13	Fiducial volume cut
14	Event pile up
15	Pion secondary interactions
16	Proton secondary interactions

Table 5.3: List of INGRID detector systematic parameters, loosely grouped by effect. Each parameter is varied in the simulation to produce the detector covariance matrix used in the fit.

5.3 Neutrino interaction systematic uncertainties

The nominal MC prediction for the signal and background is produced using a neutrino interaction model which is known to be incomplete. This analysis uses a set of systematic parameters designed to parametrize the uncertainty in the neutrino interaction models used to calculate the MC prediction, and is based on the treatment used in the T2K oscillation analysis. These parameters correspond to scaling factors on the corresponding physics parameter in the model, and have a covariance matrix describing the uncertainty and correlation between the parameters. The covariance matrix and uncertainty for each parameter has been motivated from work performed by the T2K Neutrino Interactions Working Group (NIWG) group and presented in T2K-TN-315 [2]. The systematic parameters are briefly described here (listed in Table 5.4), and the input covariance matrix is shown in Fig. 5.7.

CCQE modeling: The nominal model for CCQE interactions used for this analysis is the Benhar et. al. spectral function model [38] with additional contributions from the Nieves et. al. multinucleon model [13] as implemented in NEUT [48], which has three systematic parameters. The value of the axial mass, M_A^{QE}, as discussed in Sec. 2.3.1 can be varied which will affect the shape and normalization of the signal event distribution. The 2p2h events have both an overall normalization parameter, which uniformly increases or decreases the number of 2p2h ν_μ events, and a shape parameter. The 2p2h ν_μ shape parameter changes the proportion of 2p2h events which are Δ-like versus non-Δ-like (see Sec. 2.3.2) keeping the normalization constant. The 2p2h shape parameter applies a multiplicative event weight based on the neutrino energy, energy transfer, and momentum transfer (E_ν, q_0, q_3) on an event-by-event basis.

Resonant single pion modeling: The model used for resonant single pion production is the Rein-Sehgal model [87, 88], including lepton mass effects and modified form factors focusing on the $\Delta(1232)$ contribution. There are three parameters for the NEUT implementation of the Rein-Sehgal model which can be varied, M_A^{RES} the axial mass for the resonant interaction, C_0^A one of the axial form factors in the Graczyk-Sobczyk parameterization at

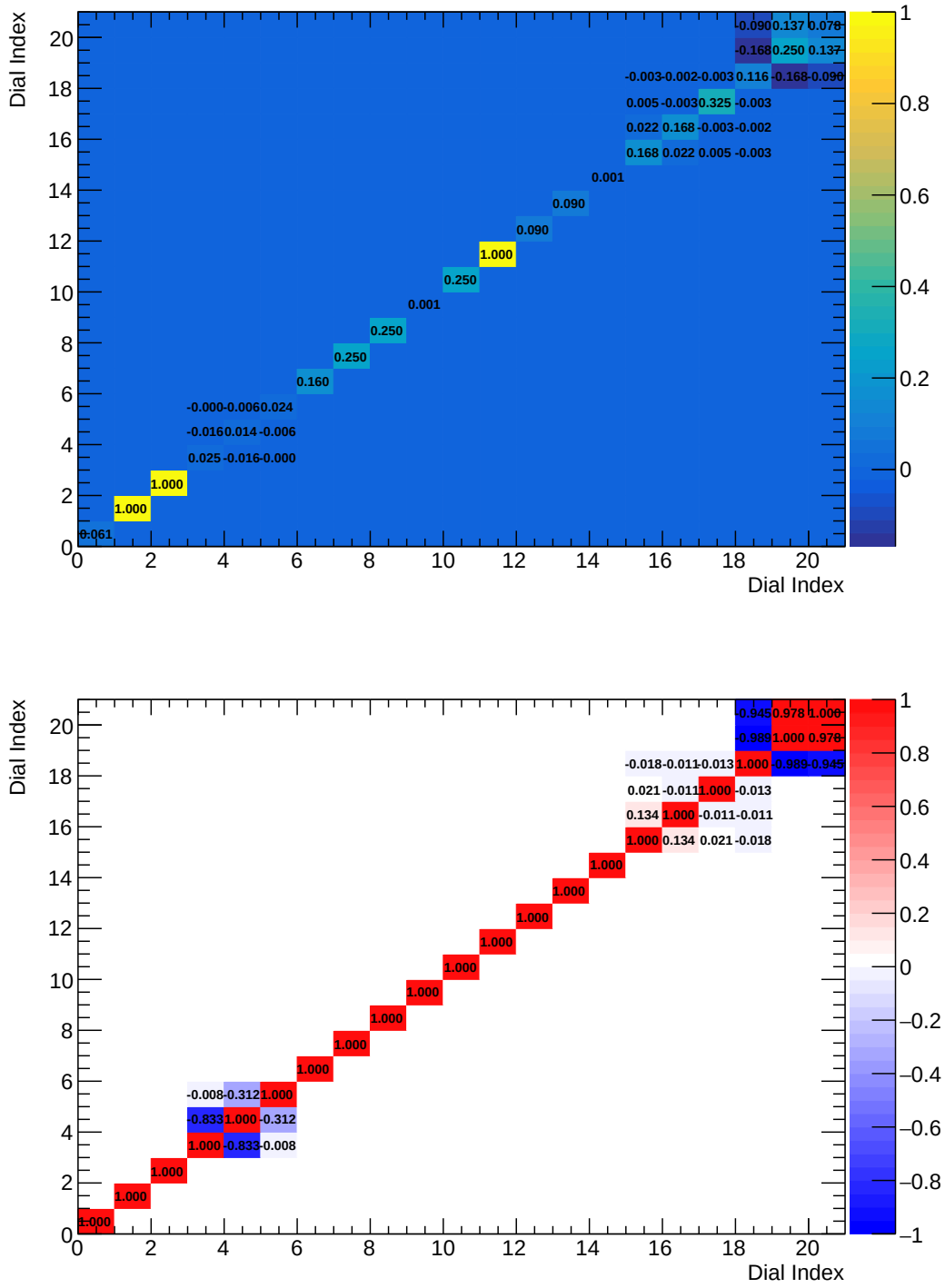

Figure 5.7: Cross section systematic parameter covariance matrix (top) and correlation matrix (bottom). The covariance values have been normalized to be the relative variance, and he parameters are arranged following their indices listed in Tab. 5.4.

Index	Parameter	Type	Prior	Error
0	M_A^{QE}	Signal shape	1.21	0.3
1	2p2h ν norm.	Signal normalization	1.0	1.0
2	2p2h ν shape	Signal shape	1.0	1.0
3	M_A^{Res}	Background shape	0.95	0.15
4	C_A^5	Background shape	1.01	0.12
5	$I_{1/2}$ Bkg Resonant	Background normalization	1.3	0.2
6	DIS Multiple pion	Background shape	1.0	0.4
7	CC-1π $E_\nu < 2.5$ GeV	Background normalization	1.0	0.5
8	CC-1π $E_\nu > 2.5$ GeV	Background normalization	1.0	0.5
9	CC DIS	Background normalization	1.0	0.5
10	CC Multi-π	Background normalization	1.0	0.5
11	CC Coherent on C	Background normalization	1.0	1.0
12	NC Coherent	Background normalization	1.0	0.3
13	NC Other	Background normalization	1.0	0.3
14	CC ν_e	Background normalization	1.0	0.03
15	FSI Inelastic, LE	Background shape	1.0	0.41
16	FSI π absorption	Background shape	1.1	0.41
17	FSI Charge exchange, LE	Background shape	1.0	0.57
18	FSI Inelastic, HE	Background shape	1.8	0.34
19	FSI π production	Background shape	1.0	0.50
20	FSI Charge exchange, HE	Background shape	1.8	0.28

Table 5.4: Neutrino interaction modeling parameters used in this analysis along with their index, type, prior, and error. Values taken from Ref. [2, 3].

$Q^2 = 0$, and the scale of the $I_{1/2}$ non-resonant background contribution. The prior values and errors were set by tuning the NEUT prediction to select ANL and BNL bubble chamber experimental data (for the detailed procedure see T2K-TN-315 [2]). Additionally this analysis includes two overall normalization parameters for CC-1π production to prevent over constraints on the flux parameters.

Coherent pion modeling: The model used for coherent single pion production is the Rein-Sehgal model [44] for coherent interactions. Two systematic parameters are used to vary the overall normalization of both charged current and neutral current coherent events on carbon. The Rein-Sehgal model is well known to overestimate the cross section when compared to recent measurements [2]. This is a simpler treatment for coherent pion events

compared to the T2K oscillation analysis.

DIS and multi-pi modeling: Deep inelastic scattering ($W > 2.0$ GeV/c^2) is modeled in NEUT using the PYTHIA 5.7 generator [89]. NEUT uses the structure functions from the GRV98 parton distributions [90] with Bodek-Yang corrections [91]. For the transition region ($W < 2.0$ GeV/c^2), multiple models are superimposed producing both signal resonant production and multiple pion production [2]. There are four systematic parameters which can vary DIS and multi-pi events. Three are overall normalization parameters, one for charged current DIS events, one for charged current multi-pi events, and one for all neutral current events that are not single pion or coherent production. The last parameter is can change the shape of the DIS distribution, and is applied as an event-by-event weight based on the neutrino energy.

Pion final state interaction modeling: NEUT uses an intra-nuclear cascade model to model the final state interactions (FSI) of pions as they traverse the nucleus. Following its creation from a neutrino interaction, the starting position of the pion is chosen based on a nuclear density profile (a Woods-Saxon potential) which is nucleus dependent, and the initial pion kinematics are provided by the interaction model. The pion is then "classically" propagated through the nucleus in finite steps, where the probability to have an interaction at that step is calculated. The pion is stepped through the nucleus until it is either absorbed or has escaped the nucleus. The product of the interaction probabilities for all steps is defined as the escape probability [2].

For pions with low momentum ($p_\pi < 500$ MeV/c), tables computed from the Oset et. al. model [92] are used to determine the interaction probabilities. For pions with high momentum ($p_\pi > 500$ MeV/c) the interaction probabilities are calculated from pions scattering off of free proton and deuteron data compiled by the PDG [1]. The two models are blended together between 400 and 500 MeV/c to avoid discontinuities.

The NEUT FSI model is parameterized by six scale factors, listed in Tab. 5.4. Each parameter scales the corresponding probability for pion interaction at each step in the nu-

cleus for absorption, pion production, inelastic scattering, and charge exchange processes (where LE and HE refer to low energy and high energy respectively). New event weights are calculated by varying the FSI parameters and re-running the NEUT cascade algorithm producing a new escape probability, where the new event weight is the ratio between the new escape probability and the nominal escape probability. The nominal values and error for the FSI parameters are tuned by fitting to external pion scattering data.

Parametrization: The effect on an event from changing a systematic parameter is encoded in a set of response functions, or splines, for each parameter. Rerunning the simulation to change the underlying physics parameters is computationally prohibitive in most cases so the spline treatment is used as an approximation for speed. Based on the event true reaction (e.g. CCQE), true topology (e.g CC-0π), and true kinematic variables as input, the corresponding spline returns an event weight for an arbitrary value of the systematic parameter. The spline response is normalized such that the value of the spline at the nominal value of a parameter is defined to be one. Splines are generated by calculating the new event weights when varying a systematic parameter at specific values (such as the $0\sigma, \pm1\sigma, \pm2\sigma, \pm3\sigma$ values) and binning the event weights as follows

$$r_{i,j,k}(x') = \frac{\sum_n w_n(x')}{T_{i,j,k}(x)} \tag{5.11}$$

where x, x' are the nominal and altered cross section values, w_n is the weight for event n as calculated above, and $T_{i,j,k}$ is the sum of the weights for the nominal MC for bin i, j, k. For an arbitrary value of a dial, the response can be calculated by interpolating the generated spline points. Each systematic parameter has its own set of splines, and the splines are generated separately for each detector.

5.4 Number of targets systematic uncertainty

The cross section is normalized by the number of target nucleons in each detector, which has some systematic uncertainty primarily due to contaminants in the materials. This has been estimated for each detector and propagated to the cross section by varying the number

of targets for each toy throw of the cross section as described in Section 6.3. The number of targets for each throw is varied according to a Gaussian centered at the nominal number of targets with a width equal to the error presented below.

5.4.1 ND280 target uncertainty

The uncertainty on the number of nucleons in FGD1 has been calculated before and a summary of the result from T2K-TN-337 [3] is presented here. The uncertainty in the number of nucleons is calculated using the covariance matrix of the areal densities of each element (shown in Figure 5.8, correlations obtained from T2K-TN-91 [4]). The covariance matrix is used to generate 10,000 toy throws of the areal densities, which then are used to calculate the number of nucleons for that throw (using Eq. 6.19). The ratio between the RMS and the mean of the resulting distribution gives the fractional error on the number of targets. This procedure gives a 0.67% error on the number of targets in FGD1.

5.4.2 INGRID target uncertainty

The uncertainty in the number of nucleons in the Proton Module has been calculated before and the result from T2K-TN-352 [86] is quoted here. The scintillator mass in the Proton Module has been measured to be 291.5 ± 1.1 kg, which results in a 0.38% error on the number of targets.

5.5 Efficiency uncertainty

The efficiency is calculated using the MC simulation for each detector which adds additional model dependence to the analysis. To account for this model dependence, an uncertainty on the efficiency correction in included in the analysis. The MC simulation is varied according to the fit parameters and the efficiency is calculated for many variations. The distribution of efficiency curves is representative of the uncertainty in the efficiency correction

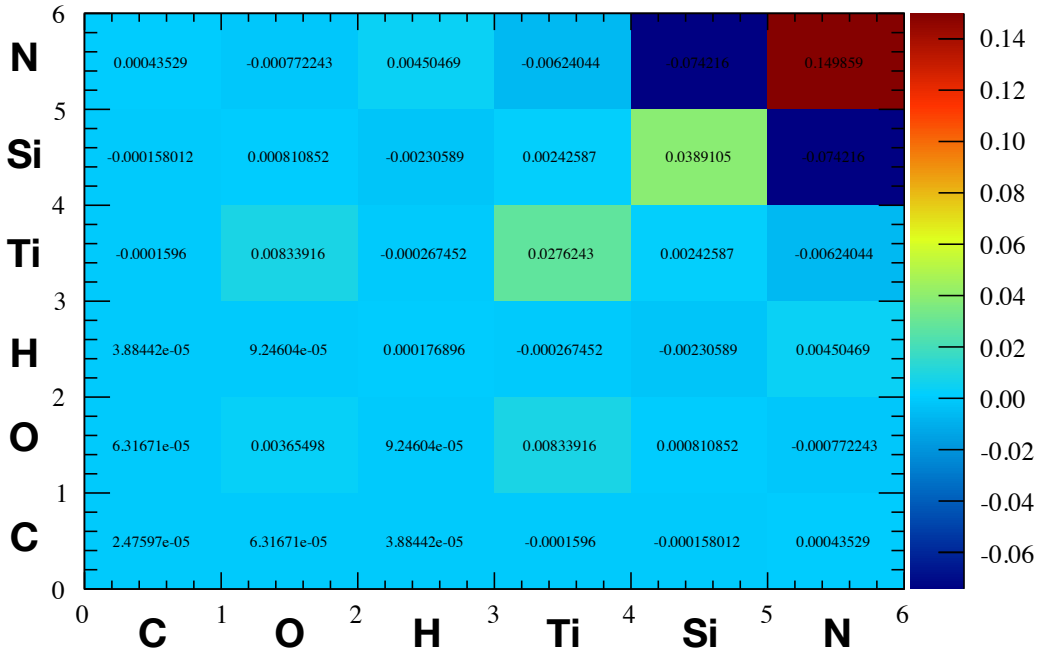

Figure 5.8: Covariance matrix of the areal densities for FGD1 used to determine the uncertainty in the number of targets for ND280. Figure from Ref. [3]

and included in the uncertainty of the cross section result. The overall uncertainty on the efficiency is estimated using an Asimov fit[1].

[1] An Asimov fit is defined as a fit where the "data" is the same as the input simulation – the fit starts at the true best fit point.

CHAPTER 6

STATISTICAL FIT

6.1 Cross section definition

The measurement of the double-differential ν_μ CC-0π cross sections on scintillator (C_8H_8) for INGRID and ND280 are extracted in a simultaneous fit of both INGRID and ND280 data as a function of the muon momentum (p_μ) and cosine of the muon angle ($\cos\theta_\mu$)[1]. The flux-integrated cross section is extracted rather than a flux-unfolded cross section to avoid model dependence from assumptions on the shape of the neutrino energy spectrum. The flux-integrated cross section is defined as:

$$\frac{d\sigma}{dx_i} = \frac{\hat{N}_i^{\text{CC-0}\pi}}{\epsilon_i^{MC}\Phi N^{FV}_{\text{nucleons}}} \times \frac{1}{\Delta x_i} \tag{6.1}$$

where x_i is the variable used for the cross section extraction, $\hat{N}_i^{\text{CC-0}\pi}$ is the number of selected CC-0π signal events in a given bin i as determined from the fit (described in the following sections), ϵ_i^{MC} is the efficiency in each bin, Φ is the integrated flux[2], N^{FV}_{nucleons} is the number of nucleons in the fiducial volume, and Δx_i is the bin width (in this analysis $\Delta x_i = \Delta p_\mu \Delta\cos\theta_\mu$). As indicated in Eq. 6.1, we divide the event rate by the total integrated flux and do not correct for the flux in each separate bin of muon kinematics. The results are experiment-dependent since no bin-by-bin correction for the flux is applied, but it is completely model-independent as no assumption needs to be made on the particular neutrino energy distribution in each muon kinematic bin. The comparison of a model with the final result can be made by convolving the model with the proper flux.

[1]The angle is with respect to the incoming neutrino direction

[2]Integrated over a range of 0 to 30 GeV.

6.2 Fit method

This analysis uses a binned maximum likelihood method to perform a fit to the number of selected events in FGD1 (ND280) and the Proton Module (INGRID) fiducial volumes as a function of outgoing muon kinematics $(p_\mu, \cos\theta_\mu)$. The maximum likelihood method varies a set of signal and nuisance parameters to find the values which best describe the data producing a set of post-fit values, errors, and correlations for each fit parameter. The inputs for the fit are the signal and background samples for each detector as described in Sections 4.3 and 4.4. For this analysis, a new version of the fitting code was written to handle the additional complexities of fitting multiple detectors with different inputs and systematic uncertainties. More details on the software itself can be found in Appendix A.

The output of the fit is the set of parameter values $\vec{\theta}$ which maximize the following likelihood given the data $\vec{y}$:

$$\mathcal{L}(\vec{y};\vec{\theta}) = \mathcal{L}_{\text{stat}}(\vec{y};\vec{\theta}) \times \mathcal{L}_{\text{syst}}(\vec{y};\vec{\theta}). \tag{6.2}$$

Often it is more convenient to work with twice the negative log-likelihood because it approximates a χ^2 distribution in the limit of large statistics (Wilks' Theorem [93]). Since the log-likelihood is a monotonically increasing function, the parameter values which maximize the likelihood will also maximize the log-likelihood [93]. The log-likekihood function to be maximized or χ^2 function to be minimized is given by:

$$\chi^2 = \chi^2_{\text{stat}} + \chi^2_{\text{syst}} = -2\ln\mathcal{L}_{\text{stat}} - 2\ln\mathcal{L}_{\text{syst}} \tag{6.3}$$

where the dependence on the parameters $\vec{\theta}$ and the data $\vec{y}$ is implied. The statistical term, $\mathcal{L}_{\text{stat}}$, is the Poisson likelihood (using Stirling's approximation[3]) which has been modified to include the statistical uncertainty of finite Monte Carlo samples using the Barlow-Beeston method [94] (see Appendix B for the derivation):

$$-2\ln\mathcal{L}_{\text{stat}} = \chi^2_{\text{stat}} = \sum_j^{\text{bins}} 2\left(\beta_j N_j^{\text{exp}} - N_j^{\text{obs}} + N_j^{\text{obs}}\ln\frac{N_j^{\text{obs}}}{\beta_j N_j^{\text{exp}}} + \frac{(\beta_j-1)^2}{2\sigma_j^2}\right) \tag{6.4}$$

[3]Stirling's approximation is $\ln n! = n\ln n - n + \mathcal{O}(\ln n)$

where N_j^{exp} is the number of expected events estimated from the Monte Carlo (also commonly denoted N^{MC}), N_j^{obs} is the number of observed events from data in a given bin j, β_j is the Barlow-Beeston scaling parameter, and σ_j^2 is the relative variance of the Monte Carlo prediction for bin j. This implementation of the Barlow-Beeston method assumes the Monte Carlo prediction is Gaussian distributed in each bin. The systematic term, $\mathcal{L}_{\text{syst}}$, is a penalty term for the systematic uncertainties (e.g. flux uncertainties) being pulled away from their prior (or nominal) values:

$$-2\ln\mathcal{L}_{\text{syst}} = \chi^2_{\text{syst}} = \sum_p \left(\vec{p} - \vec{p}_{\text{prior}}\right)\left(V_{\text{cov}}^{\text{syst}}\right)^{-1}\left(\vec{p} - \vec{p}_{\text{prior}}\right) \tag{6.5}$$

where $\vec{p}$ is the vector of systematic parameters, $\vec{p}_{\text{prior}}$ is the prior or nominal value of the systematic parameters, and V_{cov} is the covariance matrix which describes the error and correlations for each systematic parameter. The systematic penalty term allows for the use of prior knowledge in the fit from both theory and external experimental data. By using the form in Eq. 6.5 and a covariance matrix to describe the uncertainty, the systematic parameters are approximated by and treated as Gaussian distributions in the fit. Finally, the likelihood fit is unregularized to avoid any additional bias from the regularization term at the expense of higher variance in the solution. A discussion on using regularization in the likelihood fit can be found in Appendix C.

The fit performs a specific type of likelihood fit called a template likelihood fit to handle the unfolding or mapping from reconstructed variables (with detector effects) to true variables (without detector effects). The unfolding is performed to remove the detector effects from the data and allow for comparisons between experiments and for easy comparisons to theory[4]. There are different methods and types of unfolding techniques, such as iterative matrix inversion (an example being D'Agostini unfolding [95]), which all have their respective positives and negatives. For further discussions on unfolding see Refs. [93, 96, 97, 98, 99].

[4]An alternative for comparisons to theory is to convolve the theory model with the detector simulation for a given experiment, producing a theory prediction which is in the reconstructed space.

The unfolding technique employed by the template likelihood method is implemented by assigning a free parameter known as a template weight (denoted as c_i's) to each bin of the true distribution which acts as a normalization constant for that bin. The template weight can increase or decrease the number of selected signal events from the MC in a given bin of true variables (not altering the weight of background events). Each iteration the fit routine changes the template weights and observes how the effect is propagated to the reconstructed distribution by comparing the result to the data distribution. The fit finds the combination of values for the template weights and the nuisance parameters which minimizes the χ^2 described above in Eq. 6.3.

The post-fit parameter values are used to calculate the number of signal events in the true distribution which best fits the data, and subsequently used in the extraction of the cross section. This is similar to iterative unfolding by matrix inversion where the template parameters act as the matrix elements. An advantage of this method in contrast to other types of unfolding or a fit for model parameters is that, with fine enough bins, the result is not inherently biased (or the bias is small) to the shape of the input simulation as the template weights are completely free to move the signal model since they have no prior constraint [34]. The input simulation is still used to model the background processes, which can be validated by assessing the goodness of fit in sideband regions.

The template weights are written as c_i where i runs over the number of true bins, giving the number of expected signal events in a bin:

$$N_i^{\text{exp signal}} = c_i N_i^{\text{MC signal}} \tag{6.6}$$

The effect of changing the number of events in a true bin on the number of events in a reconstructed bin needs to be known to compare to the data distribution. The true bins and reconstructed bins are related by a smearing matrix t_{ij}, which is determined from the simulation. The smearing matrix contains the templates used to relate true and reconstructed bins, which can be thought of as the columns or rows of the matrix. The number of events

in a reconstructed bin j from true bins i can be then written as:

$$N_j^{\text{exp signal}} = \sum_i^{true} c_i N_i^{\text{MC signal}} t_{ij} \tag{6.7}$$

where t_{ij} is the detector smearing matrix from true bin i to reconstructed bin j. The total number of selected events in a reconstructed bin j including background events can be written as:

$$N_j^{\text{exp}} = \sum_i^{true} \left(c_i N_i^{\text{MC signal}} + \sum_k^{bkg} N_{ik}^{\text{MC bkg}} \right) t_{ij} \tag{6.8}$$

where k runs over each background type, typically categorized by topology (e.g. CC-1π). In addition to the template weights, the fit includes nuisance (or systematic) parameters for cross section model, detector, and neutrino flux variations. These are included as additional event weights as follows:

$$N_j^{\text{exp}} = \sum_i^{true} \left[c_i \left(N_i^{\text{MC signal}} \prod_a^{model} w(a, \vec{x}) \right) + \sum_k^{bkg} N_{ik}^{\text{MC bkg}} \prod_a^{model} w(a, \vec{x}) \right] t_{ij} d_j \sum_n^{E_\nu} v_{in} f_n \tag{6.9}$$

The parameters varied in the fit are the template weights (c_i) and the systematic parameters: cross section (a), detector (d_j), and flux (f_n).

- The index i runs over true muon kinematic analysis bins. The index j runs over reconstructed muon kinematic analysis bins.
- The t_{ij} term is the detector smearing matrix from true bin i to reconstructed bin j.
- The product $\prod_a^{model}$ runs over the systematic parameters related to the theoretical modeling of the signal and background. The $w(a, \vec{x})$ terms are weights to account for the effect of changing the value of some theoretical model parameter, a, (e.g. M_A^{RES}) for a given event based on kinematics, true reaction, and true topology encoded in $\vec{x}$ (see Section 5.3). Each model parameter has an associated nominal value and uncertainty, which are obtained from fits to external data.

- The d_j terms are systematic parameters describing the detector uncertainty which act as weights to increase or decrease the total number of events in a reconstructed bin. The nominal values are defined to be 1 (the nominal detector MC) and have a covariance matrix which is calculated using the detector simulation (see Section 5.2).

- The f_n terms are systematic parameters describing the flux uncertainty for a true bin i as a function of true neutrino energy bin n. The v_{in} terms are the weights which describe the flux weights from neutrino energy bins n corresponding to true bin i. The flux parameters act as weights increasing or decreasing the number of events in true neutrino energy bins, which may belong to a number of true analysis bins. The nominal values of f_n are defined to be 1 (the nominal flux MC) and have a covariance matrix which is supplied by the T2K Beam MC group (see Section 5.1).

The covariance matrix for each set of systematic parameters is used in Eq. 6.5 to calculate the contribution from moving the systematic parameters from their nominal values. Equation 6.9 gives the total number of events in reconstructed bin j for the current value of all the fit parameters.

The Minuit2 minimizer [100] is used with the MIGRAD and HESSE algorithms to perform the multidimensional minimization of the χ^2 function. MIGRAD uses a variable metric method based on the Davidon-Fletcher-Powell algorithm [101, 102] to explore the parameter space and find the minimum of the χ^2 function, according to some specified tolerance. HESSE uses the method of finite differences to calculate the matrix of second derivatives (the Hessian matrix) around the best-fit point found by MIGRAD, which is then inverted to give the covariance matrix for the fit parameters. The HESSE method assumes the likelihood surface around the best-fit point can be described by a multi-variate Gaussian. The final output of the fit is a vector of the best-fit parameters and a covariance matrix describing their post-fit error and correlations. The number of selected signal events in a true bin can

be calculated using:

$$N_i^{\text{exp signal}} = \sum_j^{reco} \left(c_i N_i^{\text{MC signal}} \prod_a^{model} w(a, \vec{x}) \right) (t_{ij})^{-1} d_j \sum_n^{E_\nu} v_{in} f_n \tag{6.10}$$

where the post-fit values are used for the fit parameters. The post-fit number of selected signal events is used in Eq. 6.1 with a bin-by-bin efficiency correction (see Section 4.6), flux normalization (see Section 6.4), number of targets normalization (see Section 6.5), and bin-width correction to calculate the flux-integrated differential cross section.

Particular care has been taken to improve the performance and to allow the fit to converge in almost all cases. Specifically it is important to avoid or limit the number of degeneracies between parameters, and overall minimize the total number of fitted parameters, even at the expense of larger systematic errors. Dimensionality reduction is performed on the detector parameters through principal component analysis, keeping 99% of the total detector information. All other parameters are retained due to their limited number compared to the number of detector parameters. The techniques used to perform principal component analysis and dimensionality reduction are described in Appendix D.

6.3 Error propagation

The output of the fit is the best-fit value for the parameters and a covariance matrix describing the errors on the parameters (calculated using the HESSE method). The final step is calculating the cross section using the best-fit parameters, and propagating the post-fit errors to the cross-section. However the dependence of the cross section on the fit parameters is in general some high dimensional unknown function, so an analytical expression for the error propagation is also unknown. Instead the errors from the fit are propagated numerically to the cross section through the Monte Carlo procedure described below.

The fit is run and allowed to converge, producing a set of post-fit parameters and their associated covariance matrix. The post-fit covariance matrix is Choleksy decomposed into its lower triangular form (and its transpose) which represents the parameter errors and

has the same multivariate distribution and correlations as the original covariance matrix [103]. A random deviation of the fit parameters is generated by multiplying the Cholesky decomposition and a vector of random numbers distributed about a Gaussian of mean zero and width one. This random deviation is added to the post-fit parameters to create a random variation of the fit parameters that is distributed according to the covariance matrix [103], as shown below:

$$\Sigma = LL^* \tag{6.11}$$

$$\vec{\theta}_t = \vec{\theta}_f + (L \times \vec{r}_t) \tag{6.12}$$

where Σ is the post-fit covariance matrix, LL^* is the Cholesky decomposition, $\vec{\theta}_t$ is the new varied parameter vector, $\vec{\theta}_f$ is the best-fit parameters, and $\vec{r}_t$ is a vector of random numbers distributed about a Gaussian of mean zero and width one. The varied parameter vector, $\vec{\theta}_t$, represents a plausible variation of the parameters according to the calculated covariance matrix, and the procedure is commonly referred as generating a toy throw of the parameters.

This process is repeated for many variations of the fit parameters (of order 1000 or more) to sample the likelihood space encoded in the post-fit covariance matrix. The cross section is calculated for each variation of the fit parameters and represents the distribution of plausible cross section values according the statistical and systematic uncertainties. The distribution is used to calculate the cross section covariance matrix as follows:

$$V_{ij} = \frac{1}{N} \sum_t (x_{it} - \bar{x}_i)(x_{jt} - \bar{x}_j) \tag{6.13}$$

where V_{ij} is the ij^{th} element of the cross section covariance matrix, N is the number of throws, x_{it} is the i^{th} cross section bin for throw t, and $\bar{x}_i$ is the i^{th} cross section bin calculated using the best-fit parameters. The number of targets, flux integral, and efficiency normalization are also varied with each throw to calculate the cross section. Thus the final cross section covariance includes the uncertainty from the fit parameters and the number of targets, flux integral, and efficiency normalizations.

The procedure used to generate random correlated vectors of the parameters can in some situations generate an unphysical value for a parameter. For example, if a parameter which is only meaningful when positive has a large enough error, then the Gaussian throws will eventually produce a negative value for the parameter with enough random throws. This analysis handles this issue by limiting the range of some parameters to their valid regions, clipping the variations to be within their respective limits. This has the effect of truncating the tails of the Gaussian distribution for these parameters. If the truncated area is sufficiently small, then the distribution can still be approximated as Gaussian and the truncation is a negligible effect on the result.

This method makes two separate assumptions that the errors are Gaussian distributed. The first is a result of the HESSE method, which assumes the likelihood surface around the best-fit point can be described by a multi-variate Gaussian. The second is a result of parameterizing the error on the cross section as a covariance matrix from the toy throws. Both assumptions of Gaussian errors are required to propagate and present errors as described, and to avoid either or both would require a more advanced fit method or more complicated data release. If these are valid assumptions, then the covariance matrix calculated by HESSE describes an N (number of analysis bins) dimensional contour with constant log-likelihood around the best-fit point which represents the probable spread of the fit parameters. The propagated covariance matrix then describes a contour with constant log-likelihood around the best-fit cross-section in each analysis bin. Such a contour is an approximation of a Bayesian credible interval, specified to have the best-fit point at the center and limited to be symmetric [34].

6.4 Integrated flux

This analysis measures the flux-integrated cross section and needs the integrated flux for each detector. The neutrino flux prediction is performed by the Beam MC group as described in Section 3.2. This analysis uses the 13av2 version of the simulation and flux

tuning which uses NA61 thin-target data for the hadron tuning, and only uses the forward horn current (FHC) prediction. INGRID and ND280 are exposed to the same neutrino beam, but are placed at different angles relative to the beam center which gives a different integrated flux and flux shape for each detector. When running in FHC mode, the neutrino beam is primarily composed of ν_μ with small contributions from $\bar{\nu}_\mu$, ν_e, $\bar{\nu}_e$ which gives a low background rate from the non-signal flavors. At INGRID the beam is 95.3% ν_μ, 3.9% $\bar{\nu}_\mu$, and 0.8% $\nu_e/\bar{\nu}_e$, while at ND280 the beam is 92.9% ν_μ, 5.9% $\bar{\nu}_\mu$, and 1.2% $\nu_e/\bar{\nu}_e$. The low background rate is particularly important for the INGRID selection as INGRID lacks the ability to separate ν_μ and $\bar{\nu}_\mu$ interactions and has to rely on background subtraction to remove $\bar{\nu}_\mu$ events.

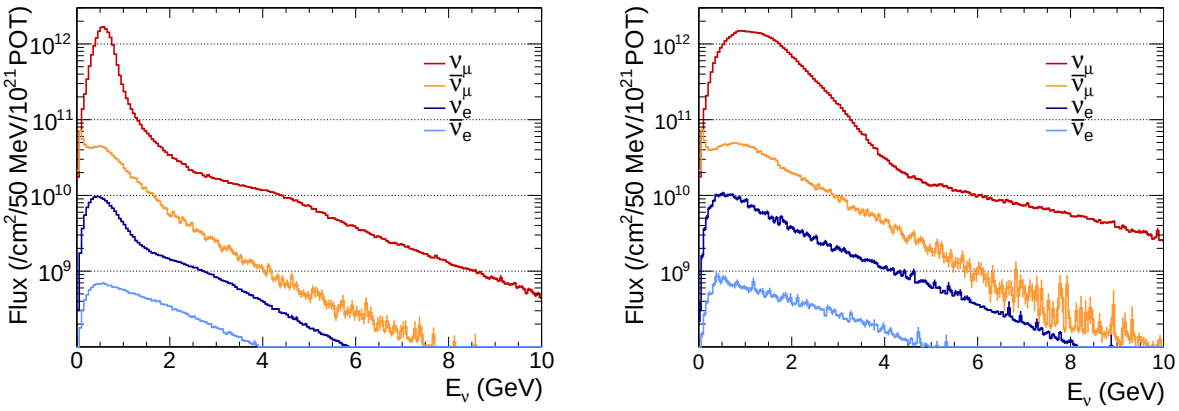

Figure 6.1: Nominal flux prediction at ND280 (left) and INGRID (right) by neutrino flavor. The flux prediction is corrected for the beam conditions for each run individually.

The neutrino flux predictions are calculated for 10^{21} POT and need to be rescaled for each data run individually. The final flux prediction is the POT average of the individual runs calculated by:

$$\Phi_{\nu_\mu} = \frac{1}{10^{21}} \sum_{r}^{\text{run}} P_r \left(\sum_{n}^{E_\nu} \phi_{nr} \right) \tag{6.14}$$

where P is the collected POT for run r and ϕ_{nr} is the neutrino flux for a given energy bin n and run r.

The flux at ND280 is shown in Fig. 6.1, and the integrated ν_μ flux for Run2-4 and Run8 is:

$$\Phi_{\nu_\mu}^{\mathrm{ND}} = 2.19 \times 10^{13}\,\mathrm{cm}^{-2} \tag{6.15}$$

The flux at INGRID is shown in Fig. 6.1, and the integrated ν_μ flux for Run2-4 is:

$$\Phi_{\nu_\mu}^{\mathrm{ING}} = 3.01 \times 10^{13}\,\mathrm{cm}^{-2} \tag{6.16}$$

The Proton Module for the INGRID selection was moved to a different location during Run8, so only the integrated flux for Run2-4 is needed for INGRID.

6.5 Number of targets

The number of targets inside the fiducial volume for each detector must be known to calculate the differential cross section per nucleon (as shown in Eq. 6.1). The total number of nucleons can be calculated in the following way:

$$N_t = N_A B \sum_i M_i \frac{A_i}{\mu_i} \tag{6.17}$$

where N_A is Avogadro's constant, B is the number of detector modules, M_i is the total mass of each element i, A_i is the number of nucleons averaged over natural abundances for each element, and μ_i is the atomic weight of each element. This assumes that each detector module is identical. The total mass of each element in the detector can be written as:

$$M_i = \rho_i V_{FV} = \rho_i^{\mathrm{areal}} \Delta X \Delta Y \tag{6.18}$$

where V_{FV} is the fiducial volume, $\Delta X, \Delta Y$ are the X and Y dimensions of the fiducial volume, and $\rho_i^{\mathrm{areal}} = \rho \Delta Z$ is the areal density[5] for each element i. This allows us to rewrite the previous equation using the areal density as:

$$N_t = N_A B (\Delta X \Delta Y) \sum_i \rho_i^{\mathrm{areal}} \frac{A_i}{\mu_i} \tag{6.19}$$

[5]The areal density is the surface or area desity of an object with units of $\mathrm{kg/m^2}$ (or $\mathrm{g/cm^2}$).

The target volume for ND280 is FGD1, and it is composed of 14 XY supermodules with an xy-plane fiducial volume of $\Delta X = \Delta Y = 174.902\,\text{cm}$ (the first XY supermodule is not part of the fiducial volume). Using the areal densities, the average number of nucleons, and the atomic weight of each element given in Table 6.1 the total number of nucleons in FGD1 is:

$$N_t^{\text{FGD}} = 5.53 \times 10^{29}\,\text{nucleons} \tag{6.20}$$

Element	A	N_i	Nat. abundance (%)	A_i	μ_i (g/mol)	ρ_i^{areal} (g/cm^2)
C	12	6	98.9	12.011	12.01078	1.849
	13	7	1.1			
O	16	8	99.762	16.004	15.99943	0.0794
	17	9	0.038			
	18	10	0.2			
H	1	0	99.985	1.002	1.007947	0.1579
	2	1	0.015			
Ti	46	24	8	48.024	47.8671	0.0355
	47	25	7.5			
	48	26	73.8			
	49	27	5.5			
	50	28	5.4			
Si	28	14	92.22	28.106	28.0855	0.0218
	29	15	4.68			
	30	16	3.09			
N	14	7	99.634	14.004	14.00672	0.0031
	15	8	0.366			

Table 6.1: Information used to compute the total number of nucleons for each chemical element of the FGD1 fiducial volume [4].

The target volume for INGRID is the Proton Module, and it is composed of a single module for the purpose of the math in this section with a fiducial volume of $\Delta X = \Delta Y = 100\,\text{cm}$. Using the areal densities, the average number of nucleons, and the atomic weight of each element given in Table 6.2 the total number of nucleons in the Proton Module is:

$$N_t^{\text{PM}} = 1.76 \times 10^{29}\,\text{nucleons} \tag{6.21}$$

where the areal density for element for the Proton Module was calculated using the total mass of the Proton Module fiducial volume (292.1 kg) and the fraction of each element by

mass found in Ref. [5] (which contains an alternate method for calculating the number of nucleons).

Element	A	N_i	Nat. abundance (%)	A_i	μ_i (g/mol)	ρ_i^{areal} (g/cm^2)
C	12	6	98.9	12.011	12.01078	26.57
	13	7	1.1			
O	16	8	99.762	16.004	15.99943	0.1723
	17	9	0.038			
	18	10	0.2			
H	1	0	99.985	1.002	1.007947	2.223
	2	1	0.015			
Ti	46	24	8	48.024	47.8671	0.222
	47	25	7.5			
	48	26	73.8			
	49	27	5.5			
	50	28	5.4			
N	14	7	99.634	14.004	14.00672	0.02
	15	8	0.366			

Table 6.2: Information used to compute the total number of nucleons for each chemical element of the Proton Module fiducial volume [5]. Silicon is considered to have a negligible contribution.

CHAPTER 7

FIT VALIDATION

This chapter describes the procedure to validate the performance of the analysis and fit framework. The analysis is tested by running a series of fits to a variety of "data" inputs (colloquially referred to as fake/mock/pseudo data) produced by altering the nominal MC simulation that are designed to test a particular aspect of the analysis. The tests are important to quantify the robustness of the fit to biases in the priors, ability to accurately fit underlying physics, and identify possible failure modes of the fit. The studies performed are listed in Table 7.1, and in general each fit is performed with the default MIGRAD strategy, an effective tolerance of 2×10^{-4}, and with 4000 toy throws for the error propagation. For reading the parameter plots in this chapter, the parameters have all been normalized such that their prior is at one, and any deviation from one is the fractional change. Correspondingly the error bars are the fractional or relative error bars and are symmetric about the parameter value (by construction).

The metrics used to evaluate the performance of a given test are the following: pre/post-fit cross section distributions, pre/post-fit reconstructed event distributions, pre/post-fit fit parameters, and the χ^2 calculated between the post-fit and the nominal and pseudo data distributions. Since the pseudo data is modified Monte Carlo, the cross section for the pseudo data is known and is referred to as the "truth" cross section. The fit should ideally find and report the truth cross section as the best-fit cross section assuming it has enough freedom in the parameterization (which would result in a χ^2 of zero). There are two different χ^2 metrics used to judge the performance of the fit which are defined as follows:

- for cross section distributions:

$$\chi^2 = \sum_{i=1}^{N} (\sigma_i^{\text{fit}} - \sigma_i^{\text{true}}) V_{\text{fit}}^{-1} (\sigma_i^{\text{fit}} - \sigma_i^{\text{true}}) \tag{7.1}$$

where σ_i is the cross section for bin i for the post-fit and truth cross section, N is the total number of bins, and V_{fit} is the post-fit covariance matrix. This is used to quantify the compatibility between the post-fit result and a chosen true distribution (e.g. NEUT truth or GENIE).

- reconstructed event distribution:

$$\chi^2 = \sum_{i=1}^{N} 2\left(N_i^{\text{fit}} - N_i^{\text{obs}} + N_i^{\text{obs}} \ln \frac{N_i^{\text{obs}}}{N_i^{\text{fit}}}\right) \tag{7.2}$$

where N^{fit} is the expected number of events in reconstructed bin i from the fit result and N^{obs} is the observed number of events in reconstructed bin i from the data. This is used to quantify the compatibility between the post-fit result and the data directly in the measured quantities. This is simply the statistical χ^2 between the expected number of events from the post-fit result and the observed data. It does not include any contribution from the systematic χ^2 and is intended as a simple sanity check on the performance of the fit.

7.1 Asimov fits

An Asimov fit[1] is the most basic test of the fit machinery since the fit starts at the true best-fit point. The movement of any parameter will raise the χ^2, and the fit should explore the parameters space and determine the best-fit point is the nominal values. This is both useful as a sanity check that the fit functions correctly and will estimate the size of the uncertainty on the cross section and fit parameters. The correct behavior for the Asimov fits is for the post-fit values to match the nominal values for all parameters.

7.1.1 Nominal priors

The Asimov fit was performed with all parameters starting at their nominal value and with the fit starting at the true best-fit point. The post-fit values for all parameters correctly

[1] An Asimov fit is defined as a fit where the "data" is the same as the input simulation.

Fit Name	**Description**
Asimov fit	Basic Asimov fit to test the machinery.
Random template priors	Asimov fit with random template priors.
ND280 only Asimov	Asimov fit using only ND280 samples.
INGRID only Asimov	Asimov fit using only INGRID samples.
Statistical fluctuations	Fit to statistical fluctuations.
Systematic fluctuations	Fit to systematic parameter variations.
Degrees of freedom	200 fits with stat+syst fluctuations.
Neutrino energy weights	Fit to variations based on E_ν weights.
Altered signal weights	Fit to increased INGRID or decreased ND280 signal weights.
Low Q^2 pion suppression	Fit to suppressed RES event weights based on Q^2.
Low Q^2 CC-0π weights	Fit to modified CC-0π event weights based on Q^2.
Alternate RPA model	Fit to an alternate RPA model using the BeRPA parameterization.
Horn current variation	Fit to varied E_ν weights based on an 3σ increase of horn current.
Horn alignment variation	Fit to varied E_ν weights based on an 3σ shift of horn 2 and 3 alignment.

Table 7.1: List of studies used to validate the analysis.

match their nominal values as shown in Fig. 7.1 and indicate that the fit is functioning correctly. The Asimov fit gives an estimate of the expected size of the errors and sensitivity for each parameter for the real data fit. The template (signal) parameters are proportional to the statistical error and are approximately equal to the statistical error from the number of events in each bin. The template parameters corresponding to the backward or high angle bins have larger errors compared to the forward going bins due to the relative population of events.

The post-fit error each systematic parameter is expected in general to be smaller or equal to the prior uncertainty for the Asimov fit. If the post-fit error is about equal to the prior error, then that parameter does not have much of an impact on the fit. The flux parameter errors were roughly uniformly reduced by one or two percentage points compared to their prior errors. This small and uniform reduction is expected from the highly correlated flux uncertainties and from measures taken to limit the constraint on the flux parameters. Most

of the cross section parameters saw a reduction in error compared to their priors with a few remaining approximately equal to their prior. This is expected as the prior errors for the cross section parameters are conservative estimates to prevent an overconstraint. Finally the detector parameters also saw a fairly uniform reduction compared to their prior error.

The reconstructed event distributions for each sample are shown in Figs. 7.2, 7.3, 7.4. The pre-fit, post-fit, and input pseudo data reconstructed event distributions all match perfectly as expected (resulting in in a zero χ^2) since they are identical to begin with. Finally the extracted cross section is shown in Fig. 7.5, and the post-fit cross section perfectly matching the input pseudo data (resulting in a zero χ^2). This is the correct behavior for an Asimov fit and shows that the fit is working for this simple case.

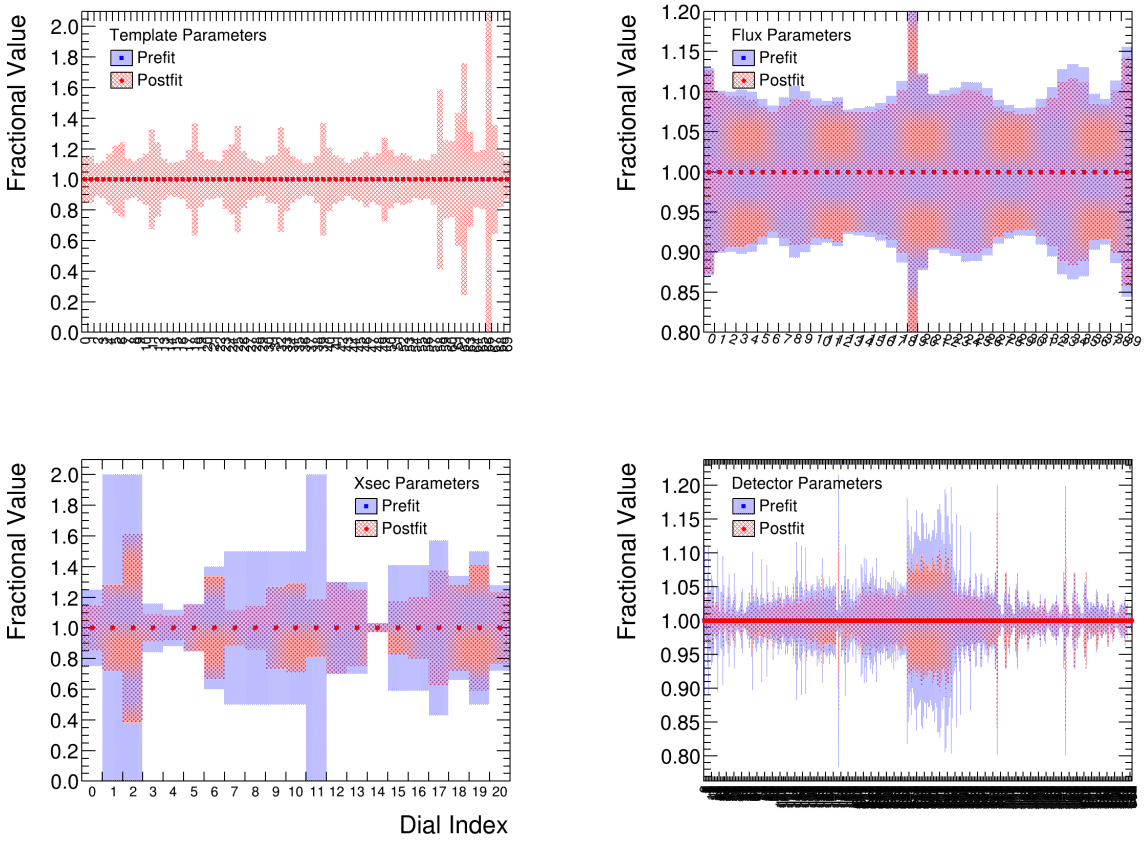

Figure 7.1: Pre/post-fit parameter plots for the Asimov fit with nominal priors.

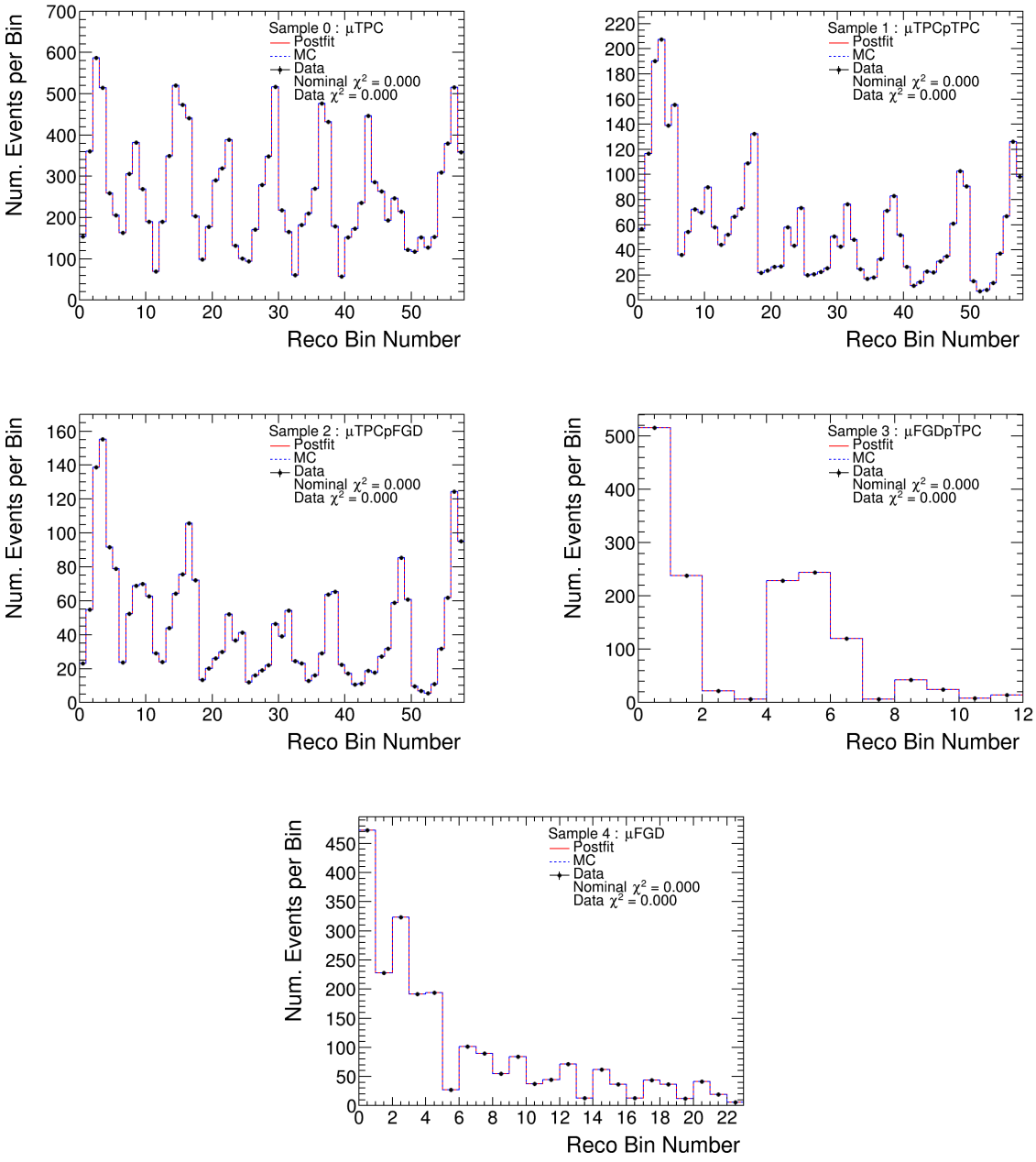

Figure 7.2: Pre/post-fit reconstructed event plots for the Asimov fit with nominal priors, ND280 signal samples only.

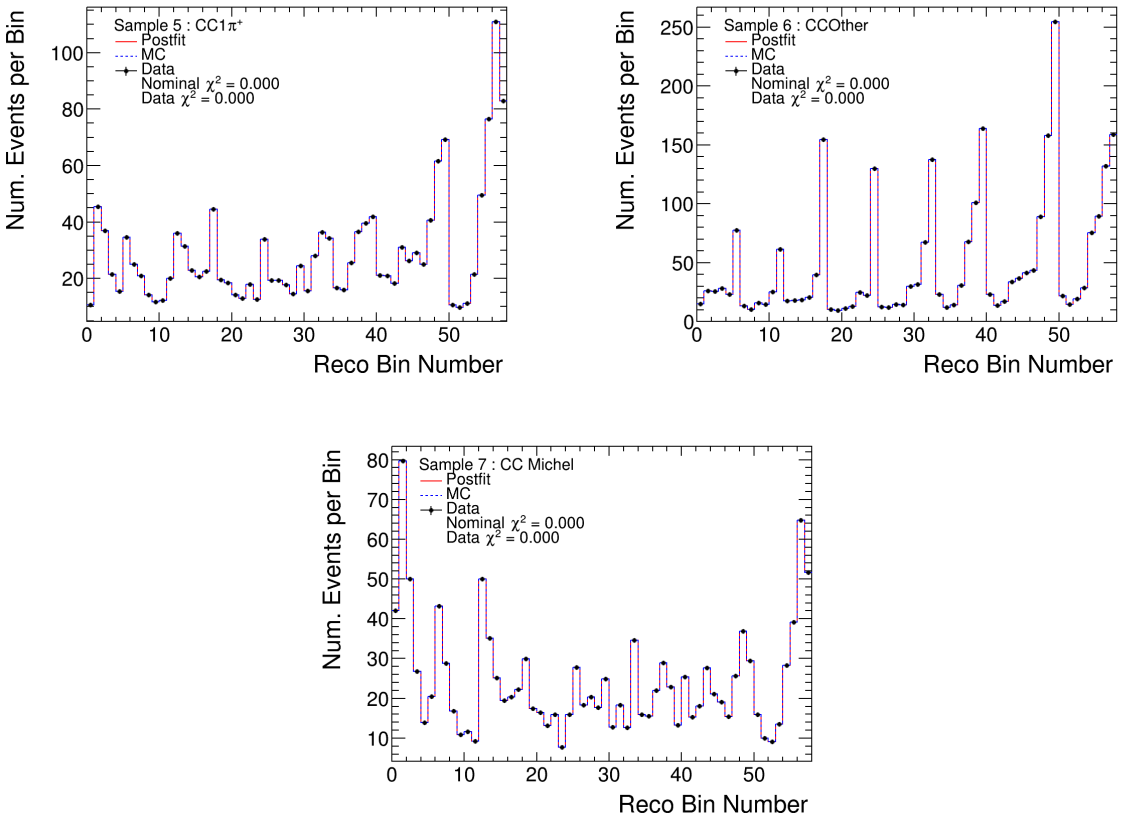

Figure 7.3: Pre/post-fit reconstructed event plots for the Asimov fit with nominal priors, ND280 sideband samples only.

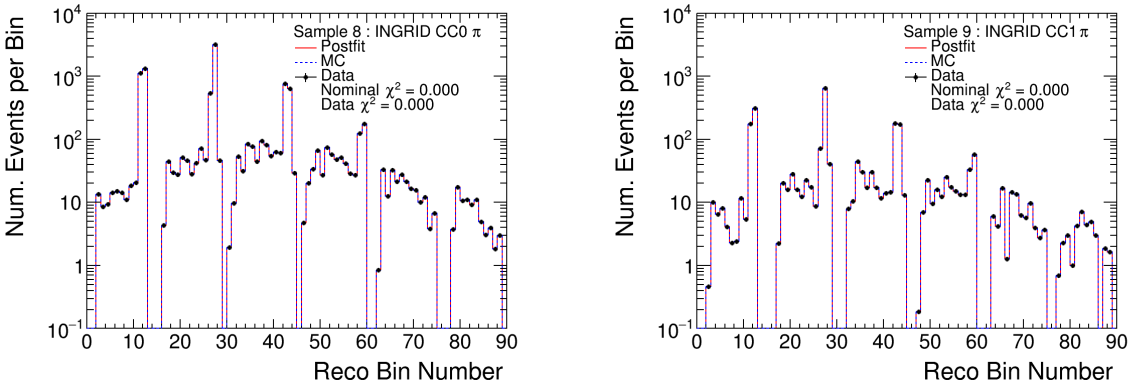

Figure 7.4: Pre/post-fit reconstructed event plots for the Asimov fit with nominal priors, INGRID samples only.

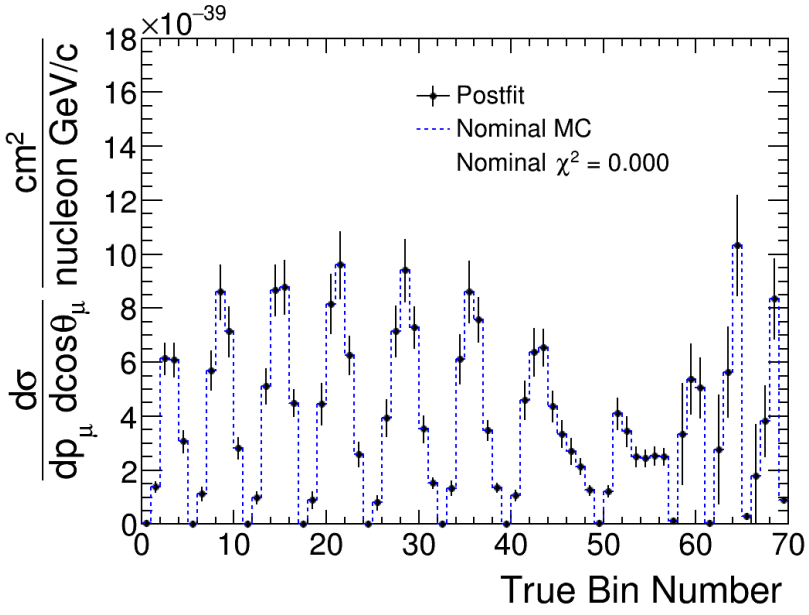

Figure 7.5: Pre/post-fit cross-section plot showing all analysis bins (in true kinematics) for the Asimov fit with nominal priors.

7.1.2 Random template priors

This Asimov fit is a slight variation on the first, and was performed with the template (signal) parameters set to random prior values while keeping all systematic parameters at their nominal values. The template parameter priors were set to a random number drawn from a Gaussian distribution with a mean of one and width of ten percent. The pseudo data input is still the same as the input simulation, but the fit does not start exactly at the best-fit point. This is to test that the fit can accurately find the correct best-fit point from a random point in parameter space.

The post-fit values for all parameters correctly remain at or return to their nominal values as shown in Fig. 7.6. The post-fit parameter errors show similar behavior to the nominal Asimov fit with most parameters seeing a smaller error compared to their prior error. The reconstructed event distributions for each sample are shown in Figs. 7.7, 7.8, 7.9. The pre-fit, post-fit, and input pseudo data reconstructed event distributions all match perfectly as expected (resulting in in a zero χ^2). Finally the extracted cross section is shown in Fig. 7.10, with the post-fit cross section perfectly matching the input pseudo data (resulting in a zero χ^2). This is the correct behavior and shows the fit can correctly find the best-fit point where the best-fit point is a known value.

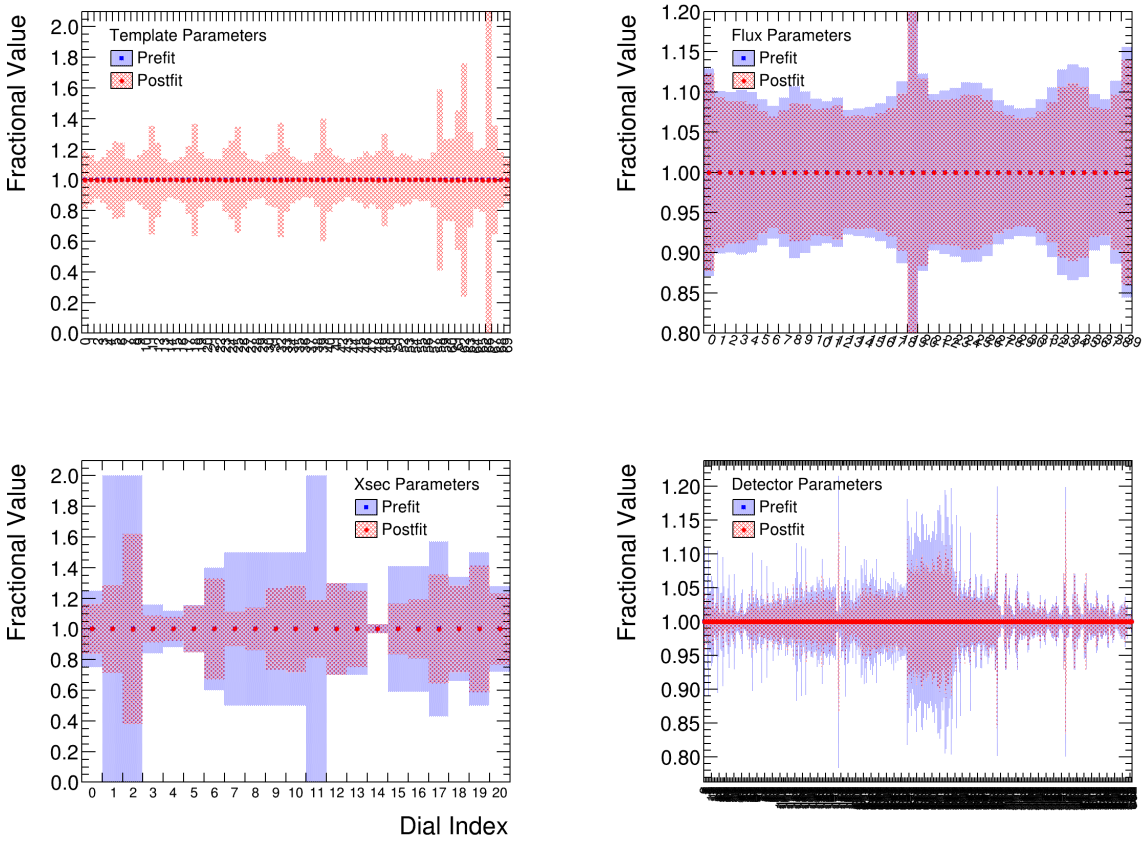

Figure 7.6: Pre/post-fit parameter plots for the Asimov fit with random template priors.

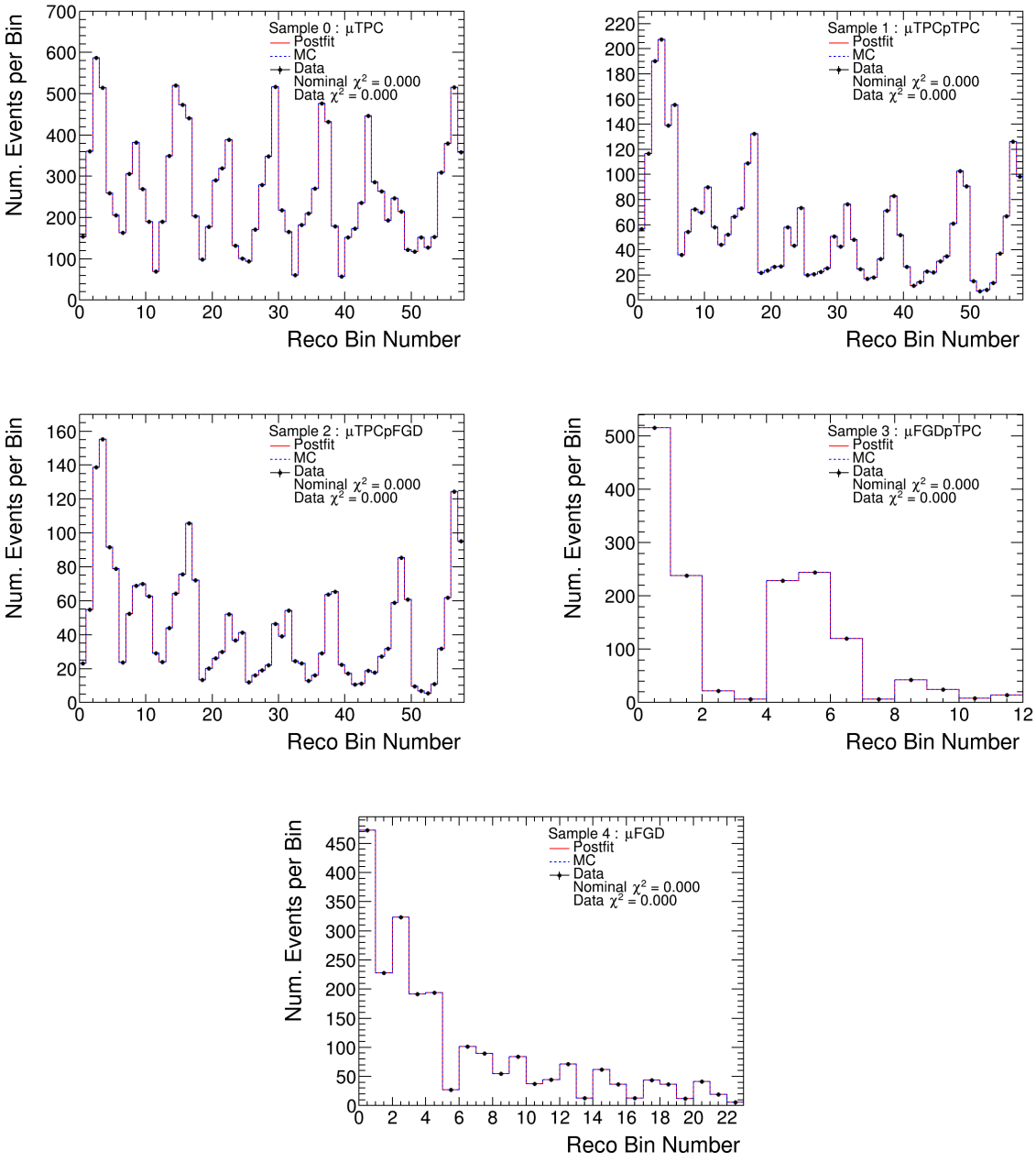

Figure 7.7: Pre/post-fit reconstructed event plots for the Asimov fit with random template priors, ND280 signal samples only.

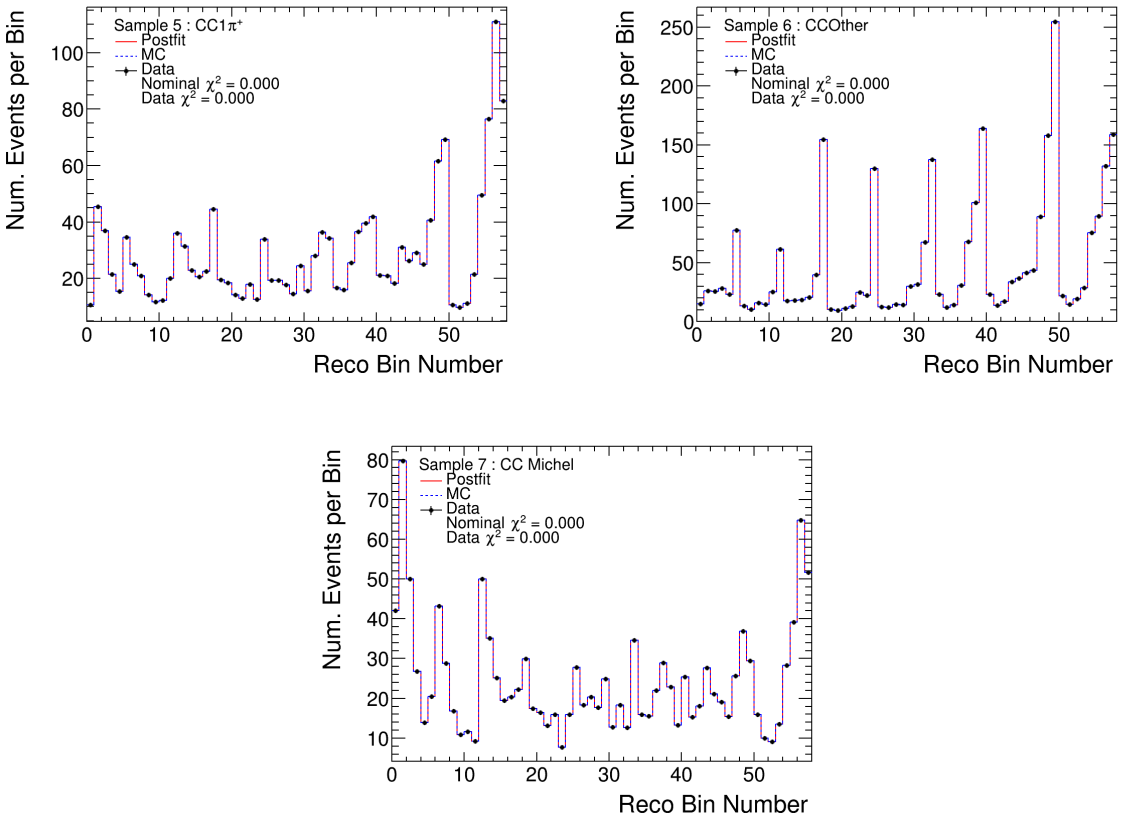

Figure 7.8: Pre/post-fit reconstructed event plots for the Asimov fit with random template priors, ND280 sideband samples only.

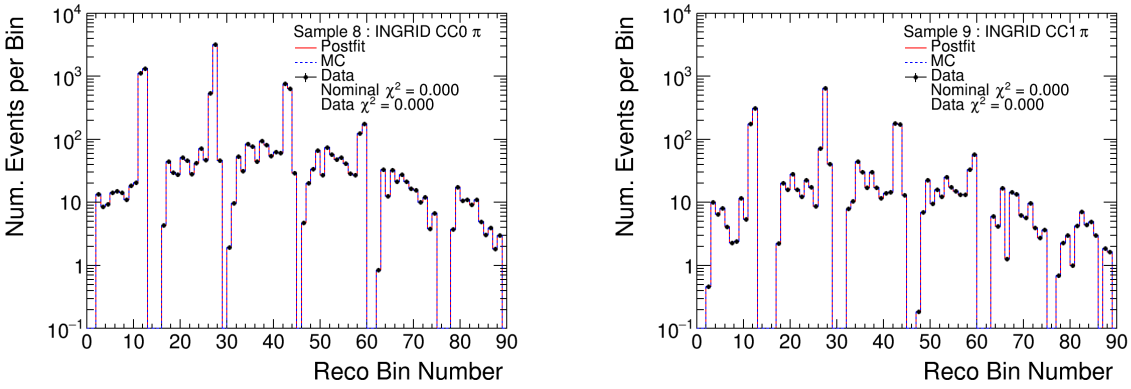

Figure 7.9: Pre/post-fit reconstructed event plots for the Asimov fit with random template priors, INGRID samples only.

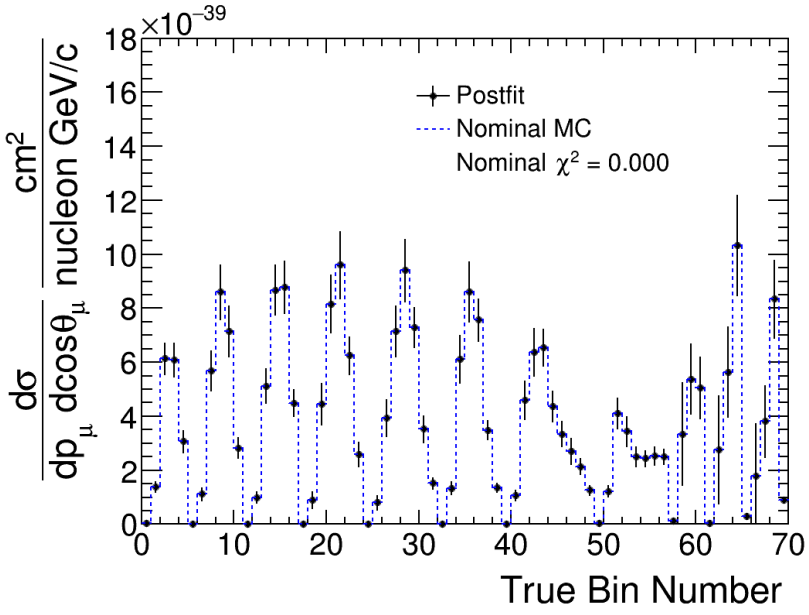

Figure 7.10: Pre/post-fit cross-section plot showing all analysis bins (in true kinematics) for the Asimov fit with random template priors.

7.1.3 ND280 only Asimov fit

This Asimov fit uses only the ND280 samples with all the parameters at their prior values, and does not include any of the INGRID specific parameters or samples.. This is to test how the analysis responds to only using one detector and how the results are different from the combination, isolating potential features which are driven by the data from ND280 or INGRID.

The results of the ND280 only Asimov fit are very similar to the full combined Asimov fit, which is encouraging. The template parameters are nearly identical, and is expected as the ND280 template parameters can only affect ND280 events by construction. The flux parameters still show a slight reduction in error, however it is not as pronounced compared to the combined Asimov fit, particularly in the some of higher energy bins. This is a nice example of how the data and correlations with the INGRID flux can reduce the flux errors in the combined analysis. The cross section parameters show similar large reductions for the normalization parameters, with most parameters having slightly higher error compared to the combined fit. However most of the pion FSI parameters (parameters 15 through 20), end up with a larger error compared to the combined fit.

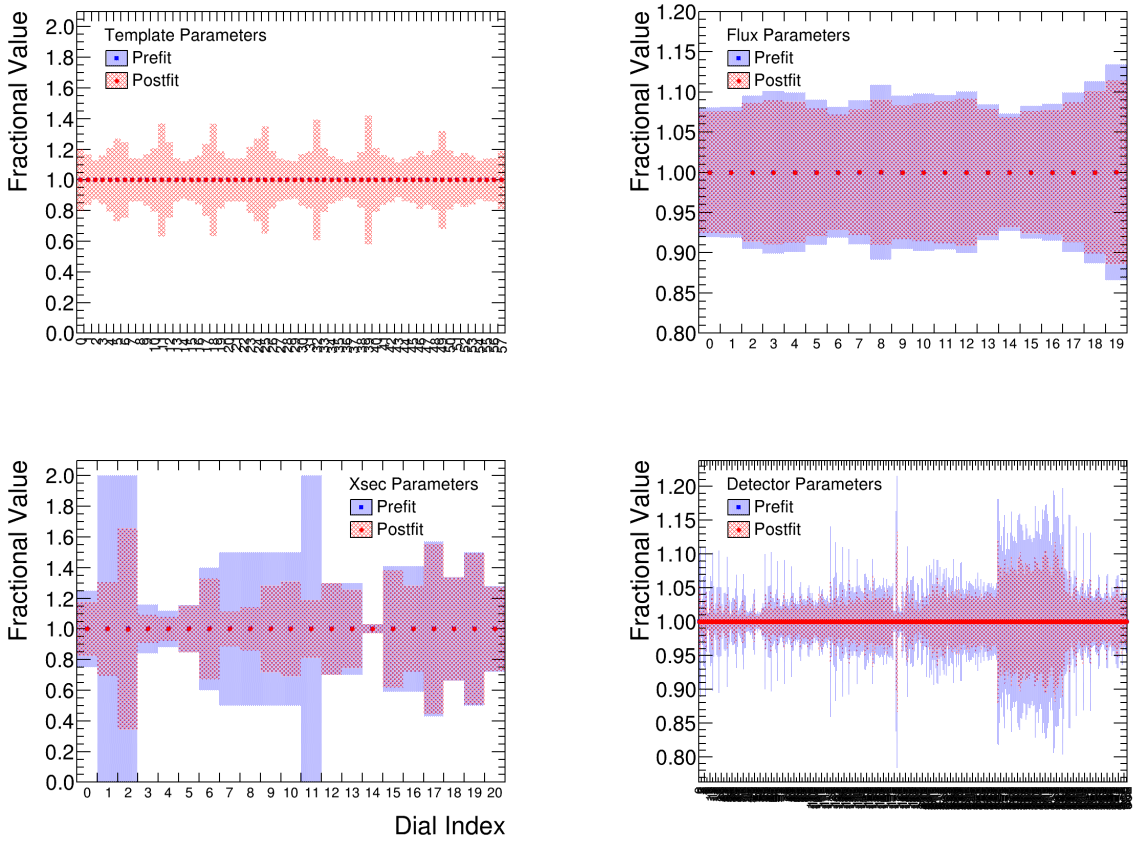

Figure 7.11: Pre/post-fit parameter plots for the Asimov fit using only the ND280 samples.

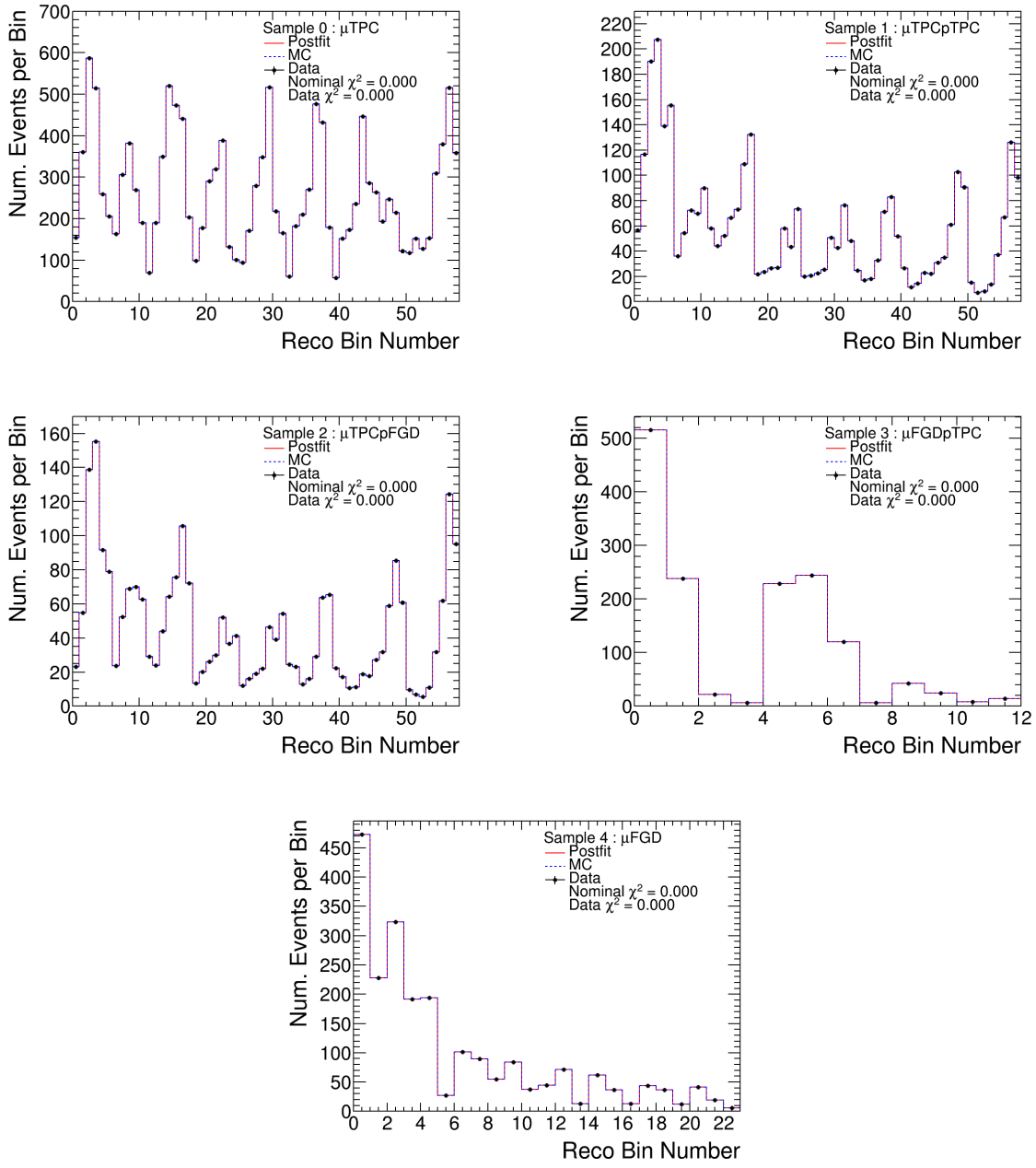

Figure 7.12: Pre/post-fit reconstructed event plots for the Asimov fit using only the ND280 samples, signal samples only.

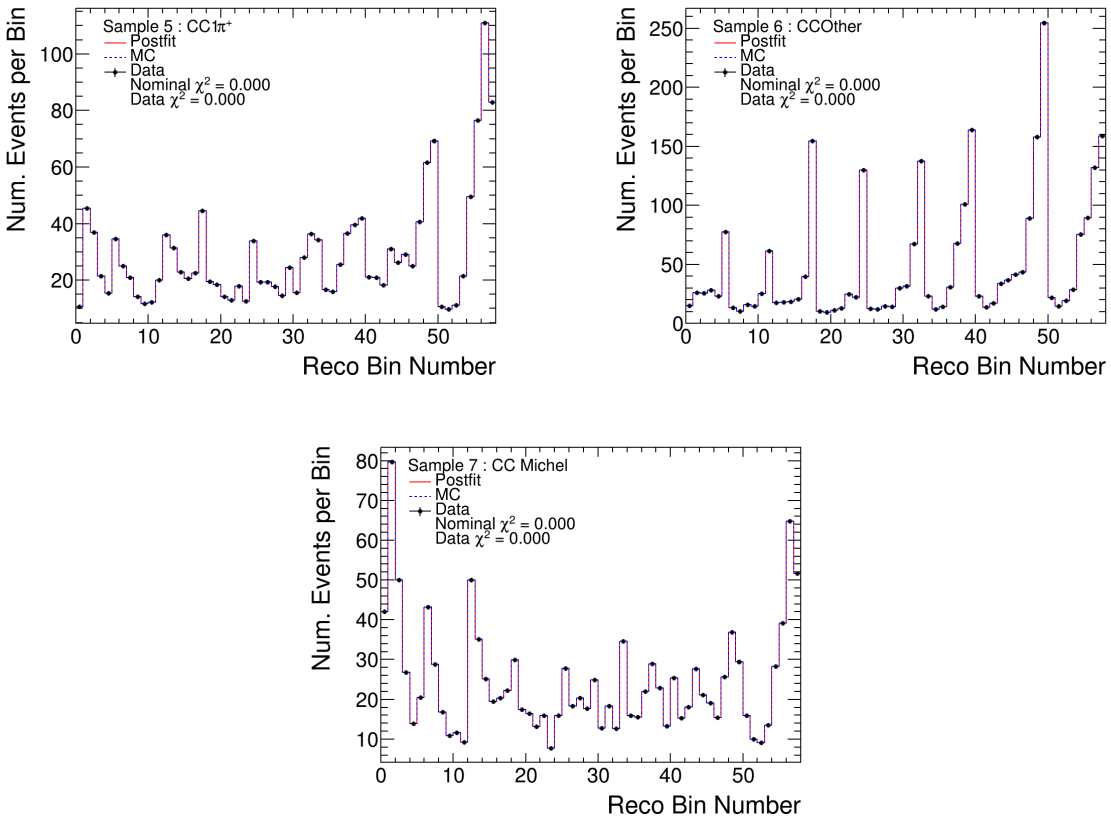

Figure 7.13: Pre/post-fit reconstructed event plots for the Asimov fit using only the ND280 samples, sideband samples only.

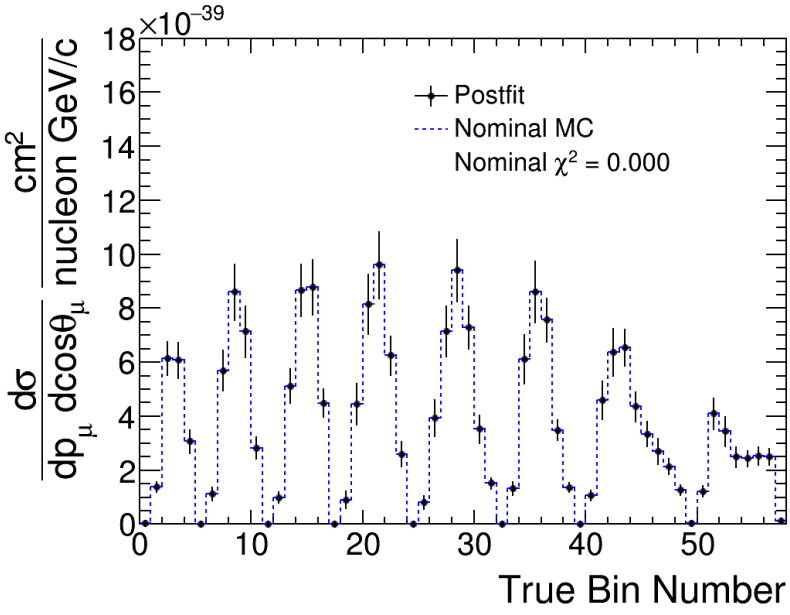

Figure 7.14: Pre/post-fit cross-section plot showing all analysis bins (in true kinematics) for the Asimov fit using only the ND280 samples.

7.1.4 INGRID only Asimov fit

This Asimov fit uses only the INGRID samples with all the parameters at their prior values, and does not include any of the ND280 specific parameters or samples.

The results of the INGRID only Asimov fit are also very similar to the full combined Asimov fit, again which is encouraging. Similar to the ND280 only fit, the INGRID template parameters are nearly the same as the combined fit. The flux parameters show little constraint at the low energy part of the spectrum with the only reduction coming at the higher energy. This is largely expected as the INGRID flux peaks at 1 GeV and has a higher proportion of high energy neutrinos. The cross section parameters still show a similar trend as the combined fit and most parameters see a reduction in error, however the reduction in error is much smaller compared to the ND280 only fit or the combined fit. This suggests most of the constraint on the cross section parameters is due to the ND280 samples. This is expected as ND280 has much higher statistics to provide a stronger constraint. Additionally there are three dedicated sideband samples for ND280 to constrain the background processes compared to the one sideband sample for INGRID. However the most pion FSI parameters for INGRID do show a noticeable reduction, similar to that of the combined fit, indicating that most of the constraint in the combined fit is provided by the INGRID sample.

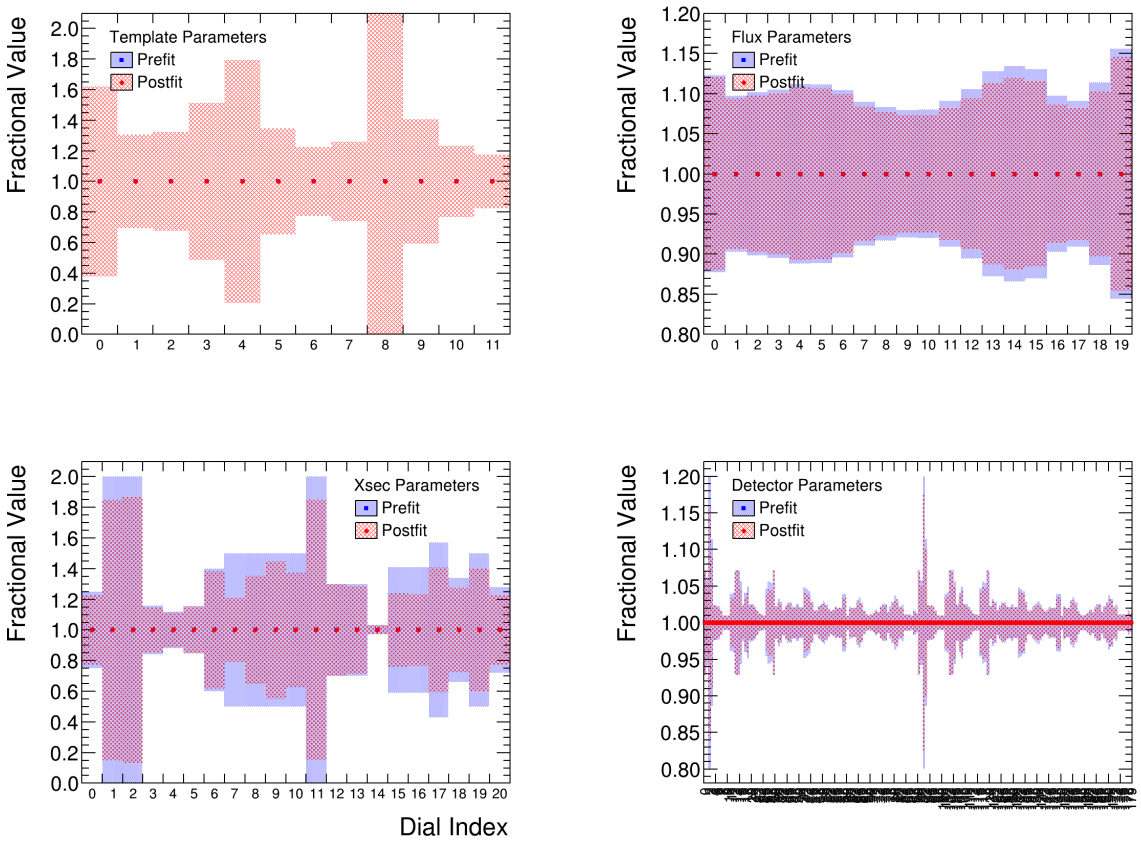

Figure 7.15: Pre/post-fit parameter plots for the Asimov fit using only the INGRID samples.

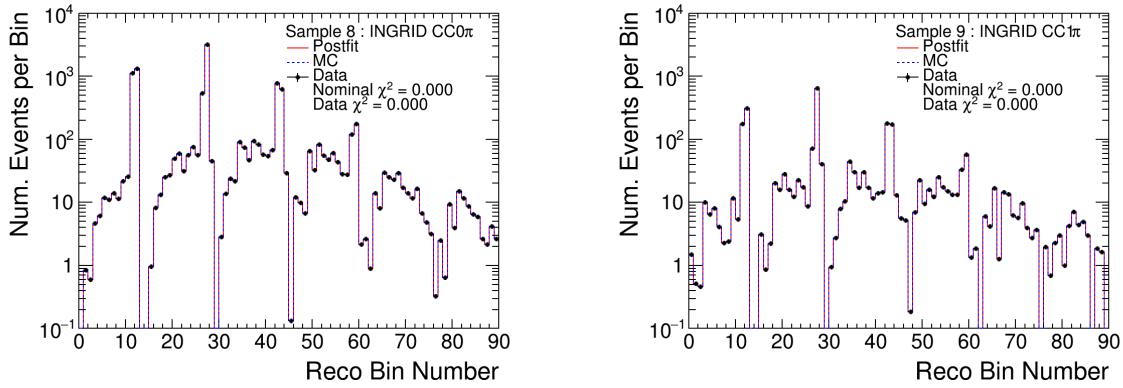

Figure 7.16: Pre/post-fit reconstructed event plots for the Asimov fit with random template priors priors, INGRID samples only.

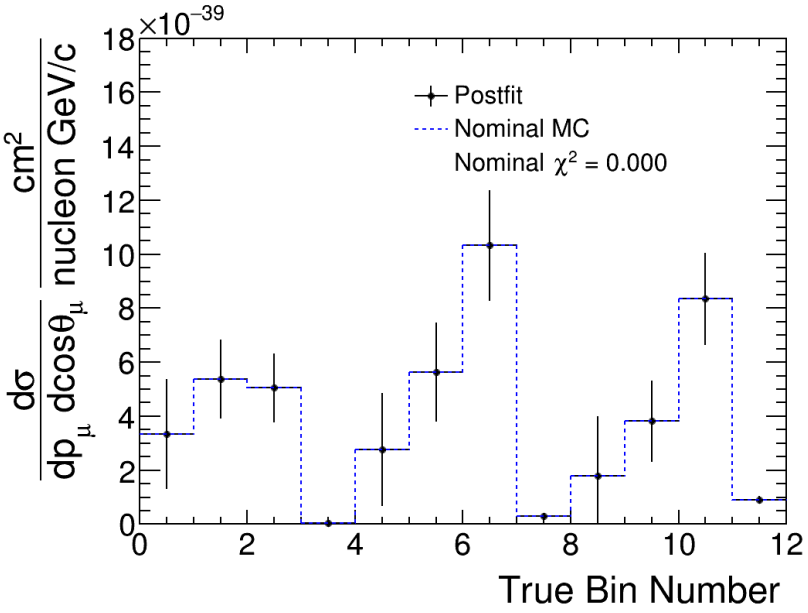

Figure 7.17: Pre/post-fit cross-section plot showing all analysis bins (in true kinematics) for the Asimov fit using only the INGRID samples.

7.2 Statistical fluctuations

This study uses pseudo data that is a statistical fluctuation of the nominal MC simulation. The pseudo data was built by generating a Poissonian fluctuation for each bin of the reconstructed event distribution for each sample, using the nominal MC prediction as the average for the Poisson distribution. The fit was then run with all parameters at their nominal prior, but now fitting to a pseudo data set that is not identical to the input MC. Unlike the previous Asimov fits, the true best-fit value for all the parameters is unknown and the fit should end with a non-zero χ^2.

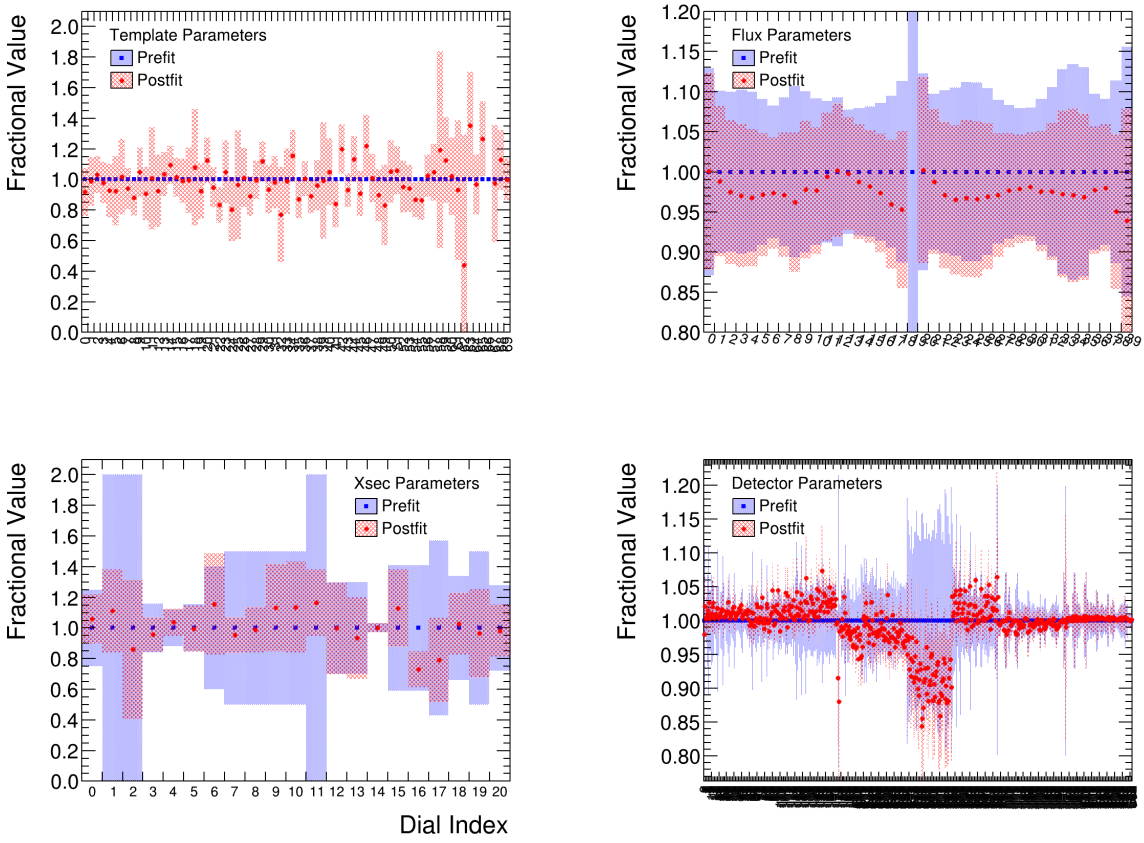

Figure 7.18: Pre/post-fit parameter plots for the fit to statistical fluctuations.

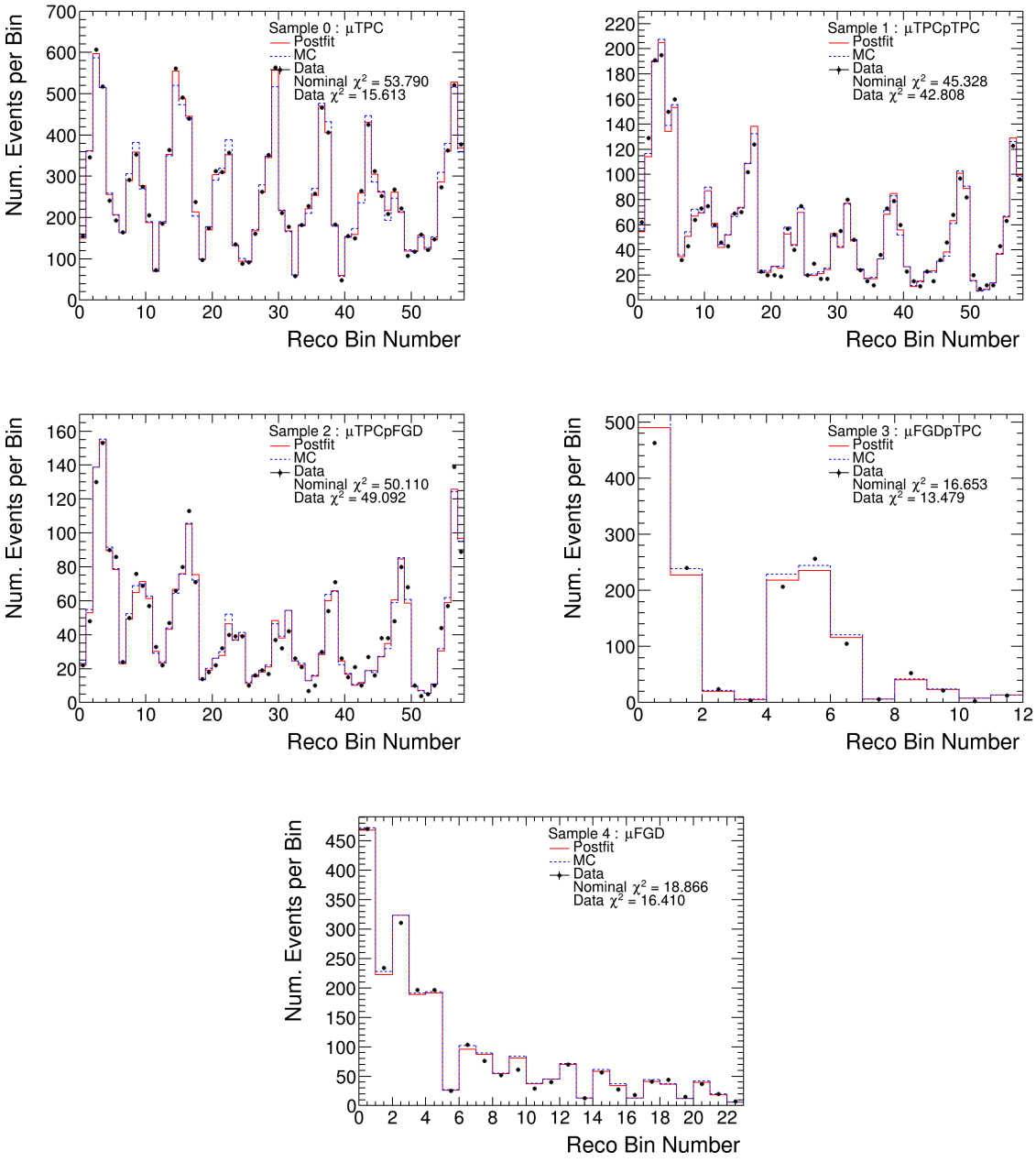

Figure 7.19: Pre/post-fit reconstructed event plots for the fit to statistical fluctuations, ND280 signal samples only.

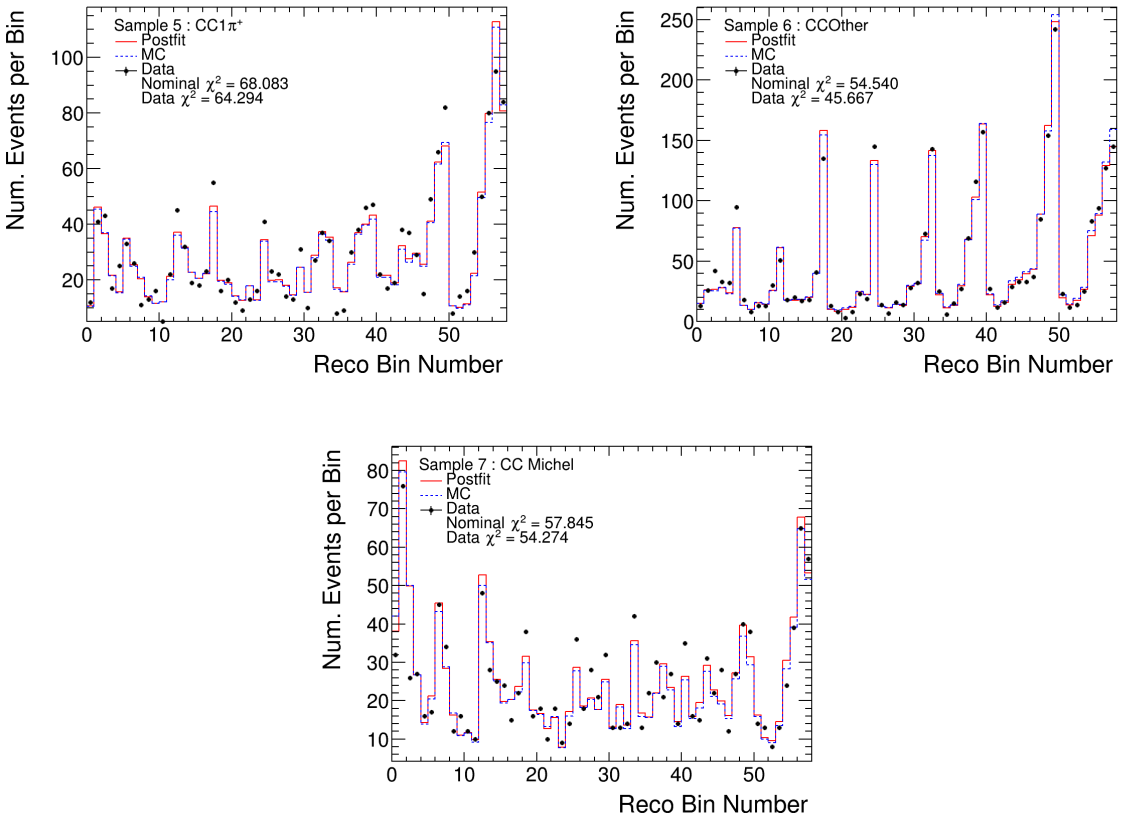

Figure 7.20: Pre/post-fit reconstructed event plots for the fit to statistical fluctuations, ND280 sideband samples only.

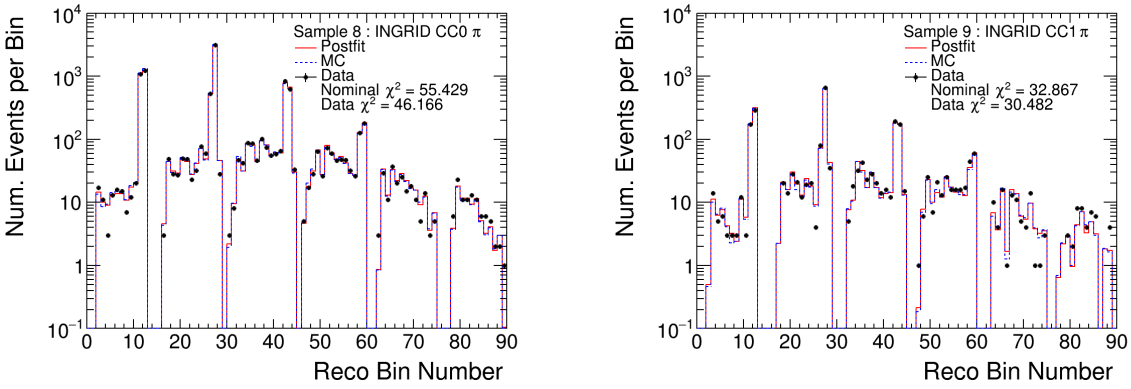

Figure 7.21: Pre/post-fit reconstructed event plots for the fit to statistical fluctuations, INGRID samples only.

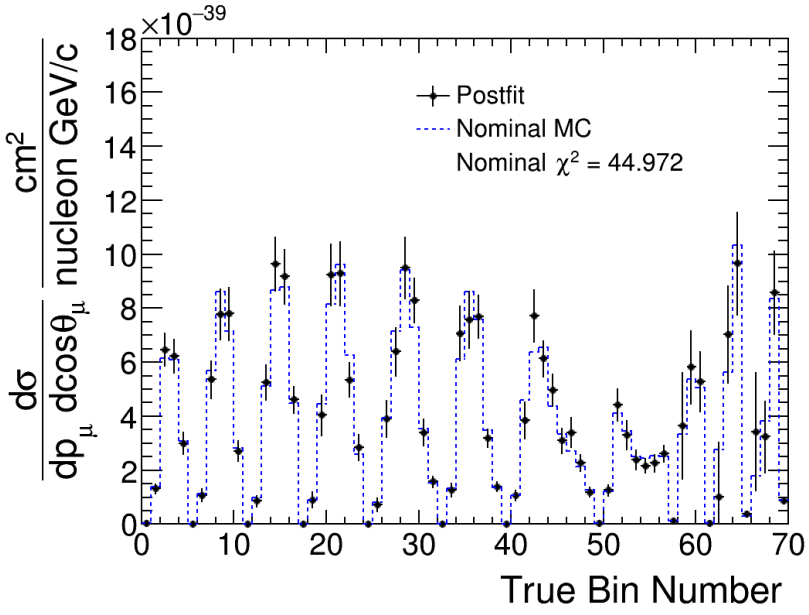

Figure 7.22: Pre/post-fit cross-section plot showing all analysis bins (in true kinematics) for the fit to statistical fluctuations.

7.3 Systematic parameter variations

This study uses pseudo data that is both a statistical fluctuation and systematic variation of the nominal MC simulation according to the changing the systematic parameters. The pseudo data was built by generating a correlated random vector of all the systematic parameters, and weighting the nominal MC simulation using the event weights that correspond to the values of the thrown systematic parameters and then finally applying statistical fluctuations on the result. The fit was run with all parameters at their nominal prior, but now fitting to a pseudo data set that is not identical to the input MC.

Overall the fit performs decently with most of the systematic parameters having post-fit values close to the true varied value, or at least being moved in that direction. The fit parameters are shown in Fig. 7.23 with the pre-fit, post-fit, and true values for each parameter. The true values for the parameters are the values used to generate the pseudo data. Given that moving the systematic parameters away from their nominal value incurs a penalty to the χ^2, it is expected that a subset of parameters will not end up at their true values as the fit will move the template parameters to cover some of the difference. In general the flux parameters show an overall decrease in value to match the true value, following the shape of the thrown parameters. Finally, the statistical fluctuations can result in the parameters having post-fit values away from the true values as the fit is minimizing over the combination of statistical and systematic variations.

Most of the cross section parameters moved in the correct direction, with several having a post-fit value near the true value. However there are some notable exceptions where the parameters moved in the opposite direction of the true value. The DIS shape parameter (index 6) was fit in the opposite direction, but this at least is partially expected given the flux parameters were all decreased as the DIS parameter tends to be highly anti-correlated with the flux parameters. All the systematic parameters are marginalized over when calculating the cross section so the fitted values not matching the true values is not a problem as long as the analysis is unbiased.

The reconstructed event distributions all show large reductions in the χ^2 moving from the nominal MC to the post-fit distributions. The ND280 CC-Michel sample shows the least improvement, however in general the CC-Michel sample has the worst improvement out of the sideband samples. The final cross section is shown in Fig. 7.27 with the post-fit extracted cross section and the true cross section value using the nominal MC and the pseudo data. The χ^2 shows an improvement, with the extracted cross section preferring the values used pseudo data compared to the nominal MC. Of particular note is the negative measurement in bin 66 of the distribution, corresponding to one of the INGRID low momentum (350 to 500 MeV) bins. The 1σ error bars comfortably cover zero, and cover the true value if extended to the 2σ error bars. This behavior is caused by a downward statistical fluctuation in the INGRID samples.

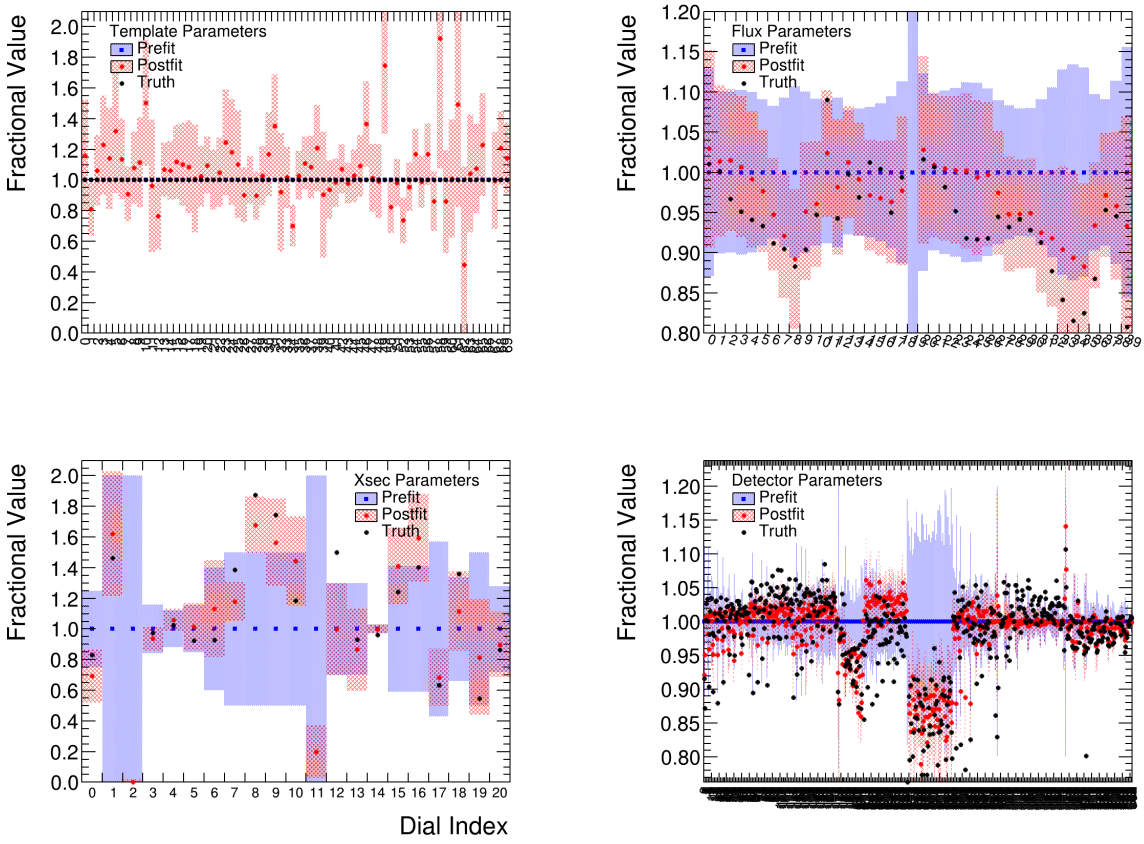

Figure 7.23: Pre/post-fit parameter plots for the fit to systematic parameter variations.

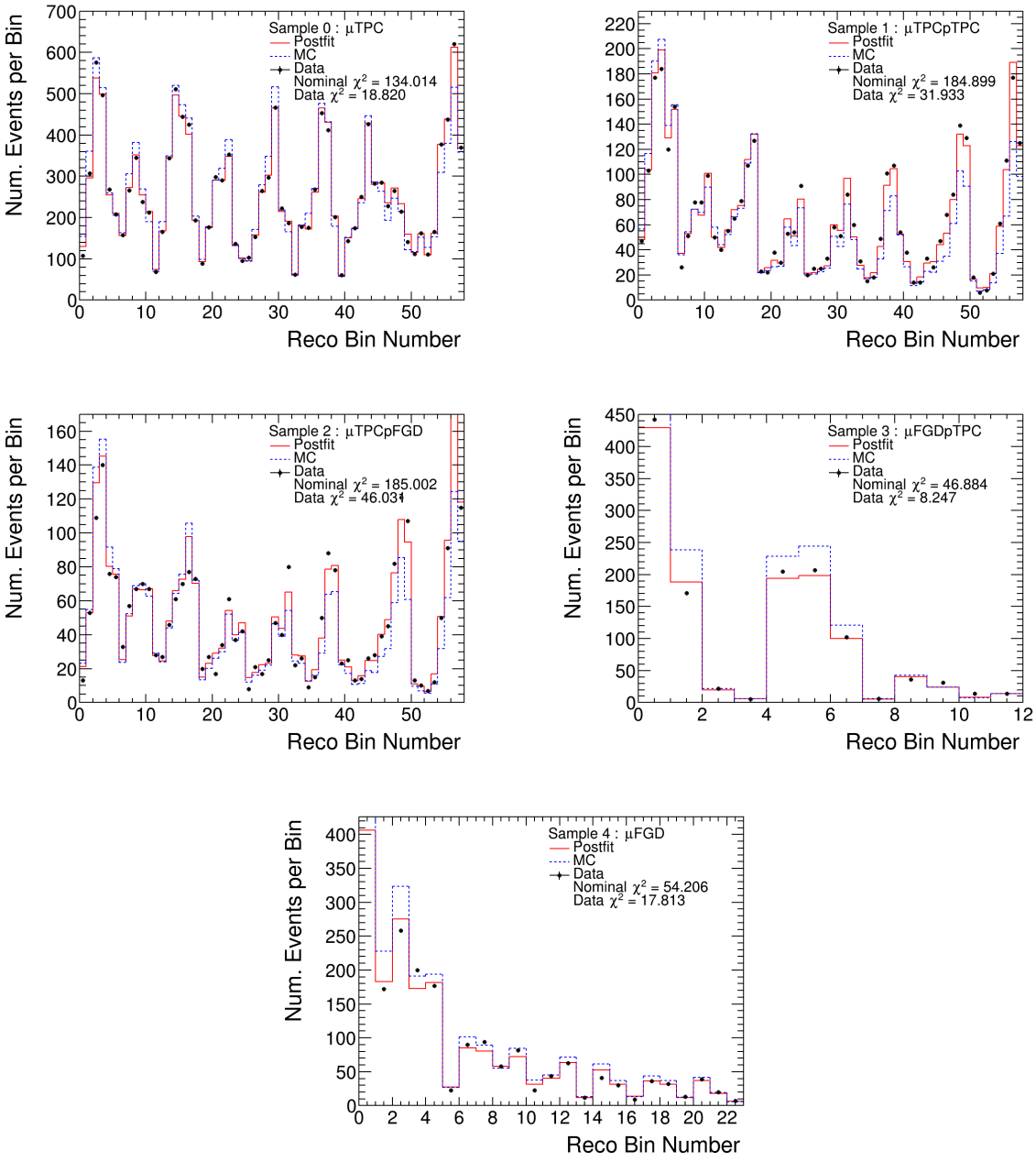

Figure 7.24: Pre/post-fit reconstructed event plots for the fit to systematic parameter variations, ND280 signal samples only.

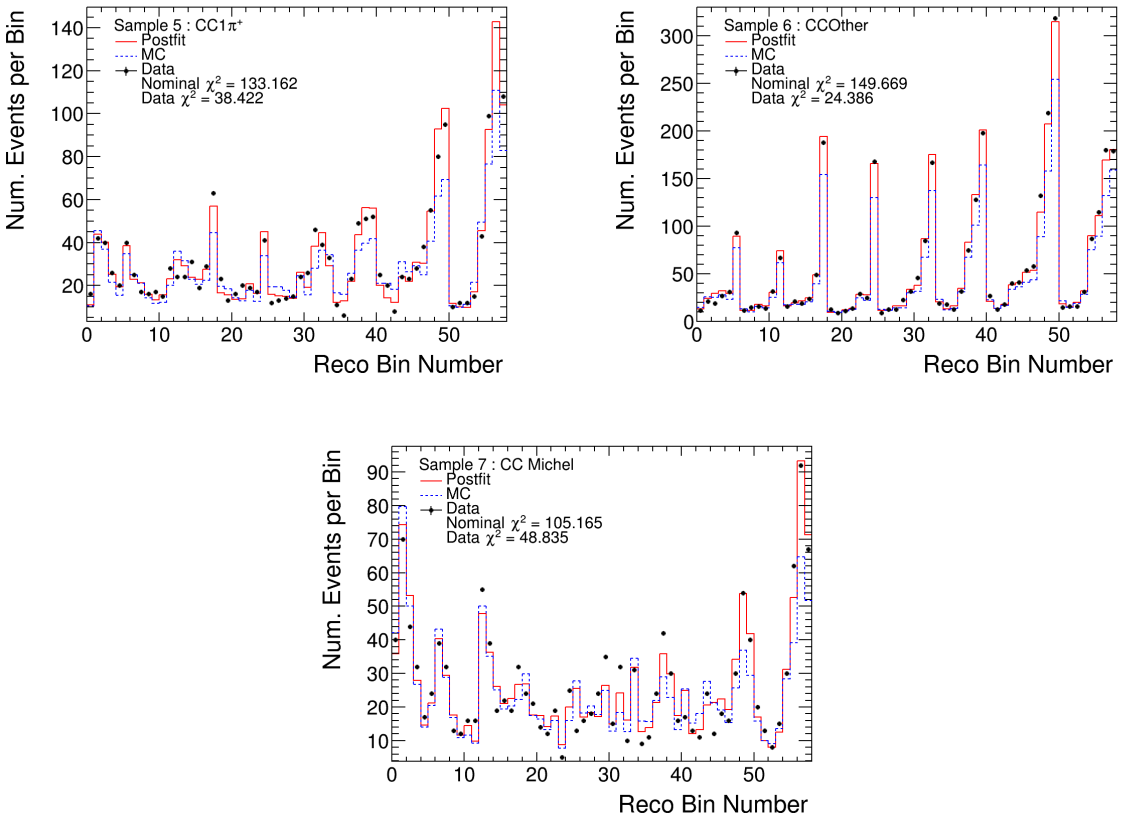

Figure 7.25: Pre/post-fit reconstructed event plots for the fit to systematic parameter variations, ND280 sideband samples only.

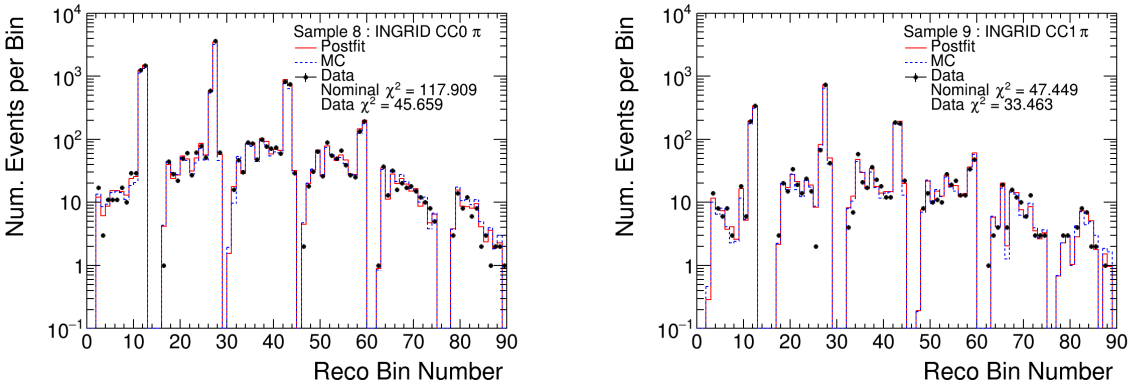

Figure 7.26: Pre/post-fit reconstructed event plots for the fit to systematic parameter variations, INGRID samples only.

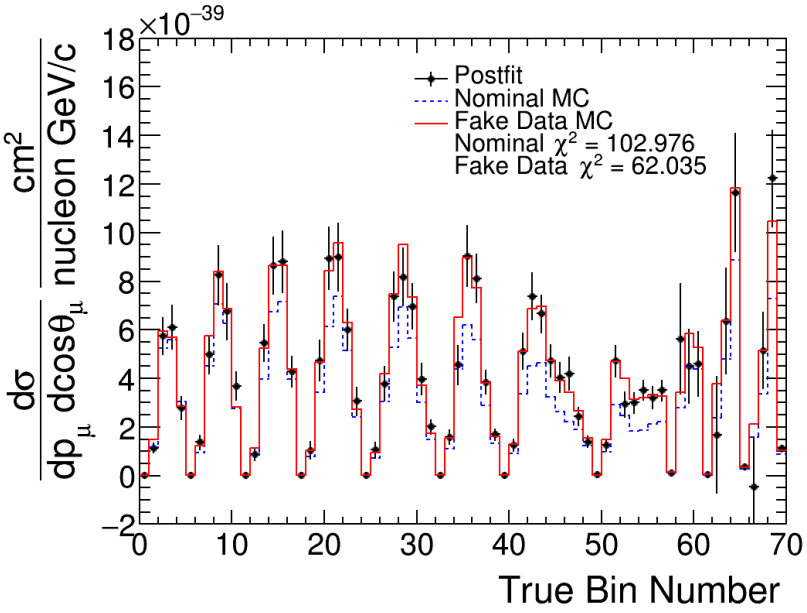

Figure 7.27: Pre/post-fit cross-section plot showing all analysis bins (in true kinematics) for the fit to systematic parameter variations.

7.4 Degrees of freedom

The next step to study the performance of the analysis is to perform several hundred fits to pseudo data and analyze the distribution of results. Several hundred pseudo data sets are produced by statistically and systematically fluctuating the nominal simulation (as in Sec 7.2 and 7.3). The analysis is run using each one of these pseudo data sets and gives a distribution of the expected performance.

The distribution of fit outcomes can be used to estimate the number of degrees of freedom (N) in the analysis. The χ^2 per number of degrees of freedom is an important metric to judge the goodness of fit or agreement for the analysis where $\chi^2/N \simeq 1$ is a reasonable fit given the data is a statistical fluctuation of the parent distribution [104]. To first order the number of degrees of freedom in a statistical fit is the number of data points minus the number of estimated/fitted parameters [93, 104]. This is accurate if the parameters are uncorrelated and the errors are approximately Gaussian. However for correlated parameters and non-Gaussian errors, a more accurate method is to simulate many pseudo experiments and use the resulting χ^2 distribution from the fits to estimate the number of degrees of freedom empirically.

The distribution in Fig. 7.28 was built from 220 pseudo experiments with statistical and systematic fluctuations to the nominal simulation and represents the χ^2 distribution between the extracted cross section and the nominal simulation. Performing a fit to the χ^2 PDF gives an estimate of the degrees of freedom of 66.38 ± 1.21 for the extracted cross section distribution (and is shown as the dotted blue curve).

The box plots in Fig. 7.29 show the distribution of cross section values and their relative errors for each bin. The circle mark is the average value, the dash is the median value, the box contains 25% above and below the median, the whiskers extend to 1.5 times the inner quartile range, and outliers are marked with the x's. For Gaussian distributed data the mean and median will be the same, placed at the center of the box, and the box represents $0.6745 \times \sigma$ where σ is the standard deviation. Most of the cross section bins have a median

and mean that are fairly close together with the largest separation in the low momentum (350 to 500 MeV/c) INGRID bins (bins 58 and 62). The bins with lower statistics show wider distributions of their fitted cross section values which is expected due to the increased statistical error and is very evident in the INGRID bins. This is further reflected in the distributions of relative errors where the low statistic bins have a wide spread of post-fit error.

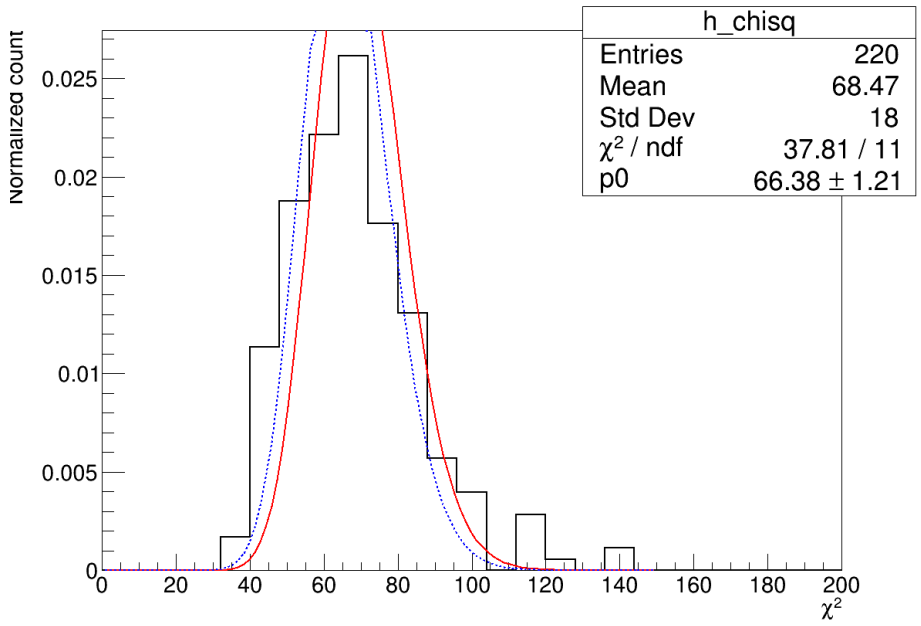

Figure 7.28: Distribution of χ^2 values between the post-fit and the nominal MC cross section for many statistical and systematic fluctuations. The solid red curve corresponds to a theoretical χ^2 distribution with 70 degrees of freedom, and the dashed blue curve corresponds to the fitted χ^2 distribution.

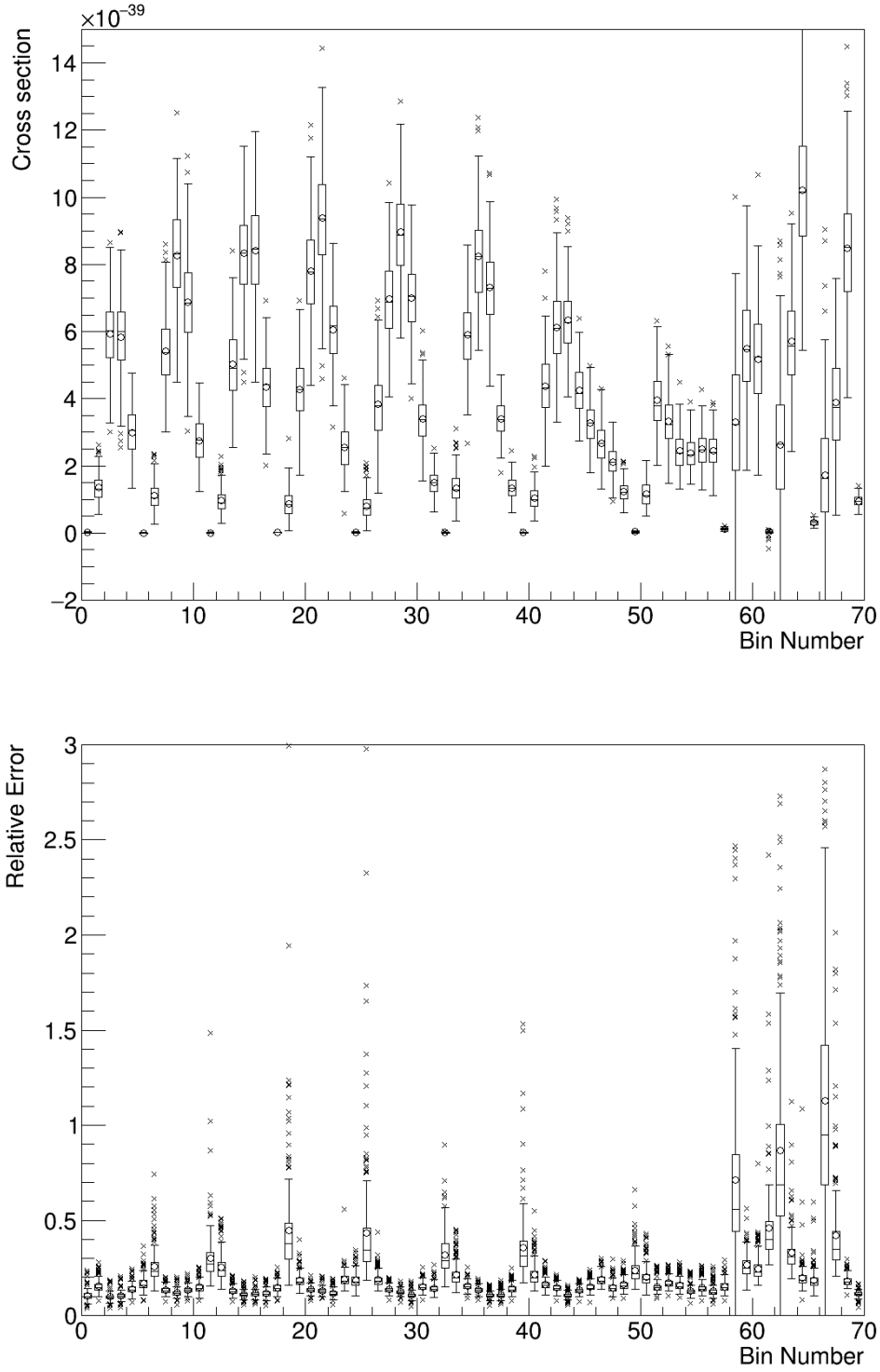

Figure 7.29: Box plots showing the distribution of post-fit cross section values for each bin (top) and the distribution of relative errors for each bin (bottom) for the statistical and systematic fluctuations. The circle mark is the average value, the dash is the median value, the box contains 25% above and below the median, the whiskers extend to 1.5 times the inner quartile range, and outliers are marked with the x's.

7.5 Neutrino energy weights

This study uses pseudo data where the nominal MC simulation was weighted to an arbitrary distribution in true neutrino energy. The pseudo data was built by weighting the nominal MC simulation event-by-event as function of true neutrino energy where the weight is according to the Equation 7.3. The chosen weighting function is not based on any physical process, and is to test how well the fit handles an extreme change compared to the nominal MC. Since the weighting function varies only with true neutrino energy, the expected behavior would be to see the template and flux parameters changing the most, with the flux parameters attempting to follow the shape.

$$w(E_\nu) = \begin{cases} 1 + 0.5/500E_\nu & \text{if } E_\nu < 500 \text{ MeV} \\ 2 - E_\nu/1000 & \text{if } 500 < E_\nu < 1500 \text{ MeV} \\ 0.5E_\nu/500 - 1 & \text{if } 1500 < E_\nu < 2000 \text{ MeV} \\ 1.0 & \text{if } E_\nu > 2000 \text{ MeV} \end{cases} \tag{7.3}$$

The fit result in general shows the expected behavior, with most of the movement in the template and flux parameters, as seen in Fig. 7.30. Both the template and flux parameters show the shape of energy weight function, with events at lower energy (which corresponds to lower momentum) getting a higher weight and correspondingly with higher energy events receiving a lower weight. Most of the cross section parameters show little movement, with the exception of the 2p2h shape dial (index 2) and the low energy pion FSI parameters (index 15, 16, 17). Finally most of the detector parameters show little movement, with a few being pulled relatively far due to a larger prior uncertainty.

The reconstructed event distributions, shown in Figs. 7.31, 7.32, 7.33, give excellent agreement between the post-fit distribution and the input pseudo data points. The final cross section distribution, shown in Fig. 7.34, also gives excellent agreement between the post-fit and pseudo data distribution.

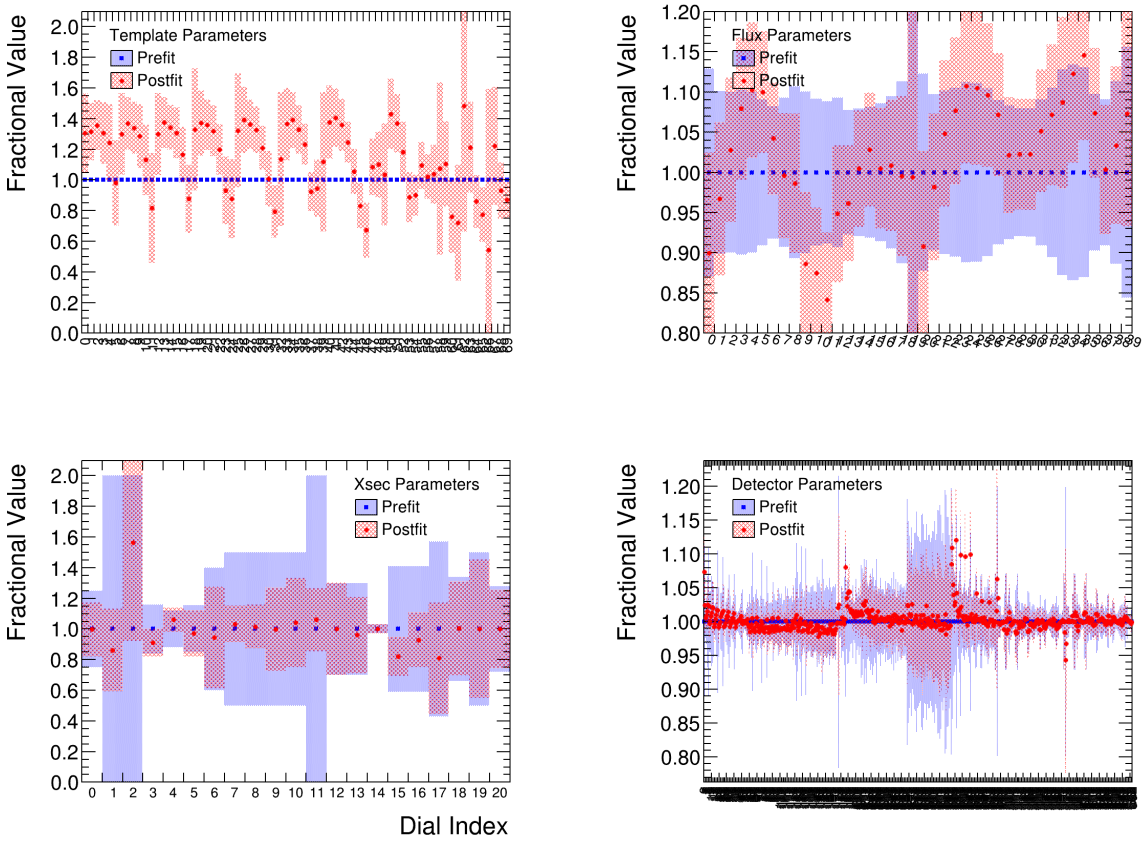

Figure 7.30: Pre/post-fit parameter plots for the fit to neutrino energy variations.

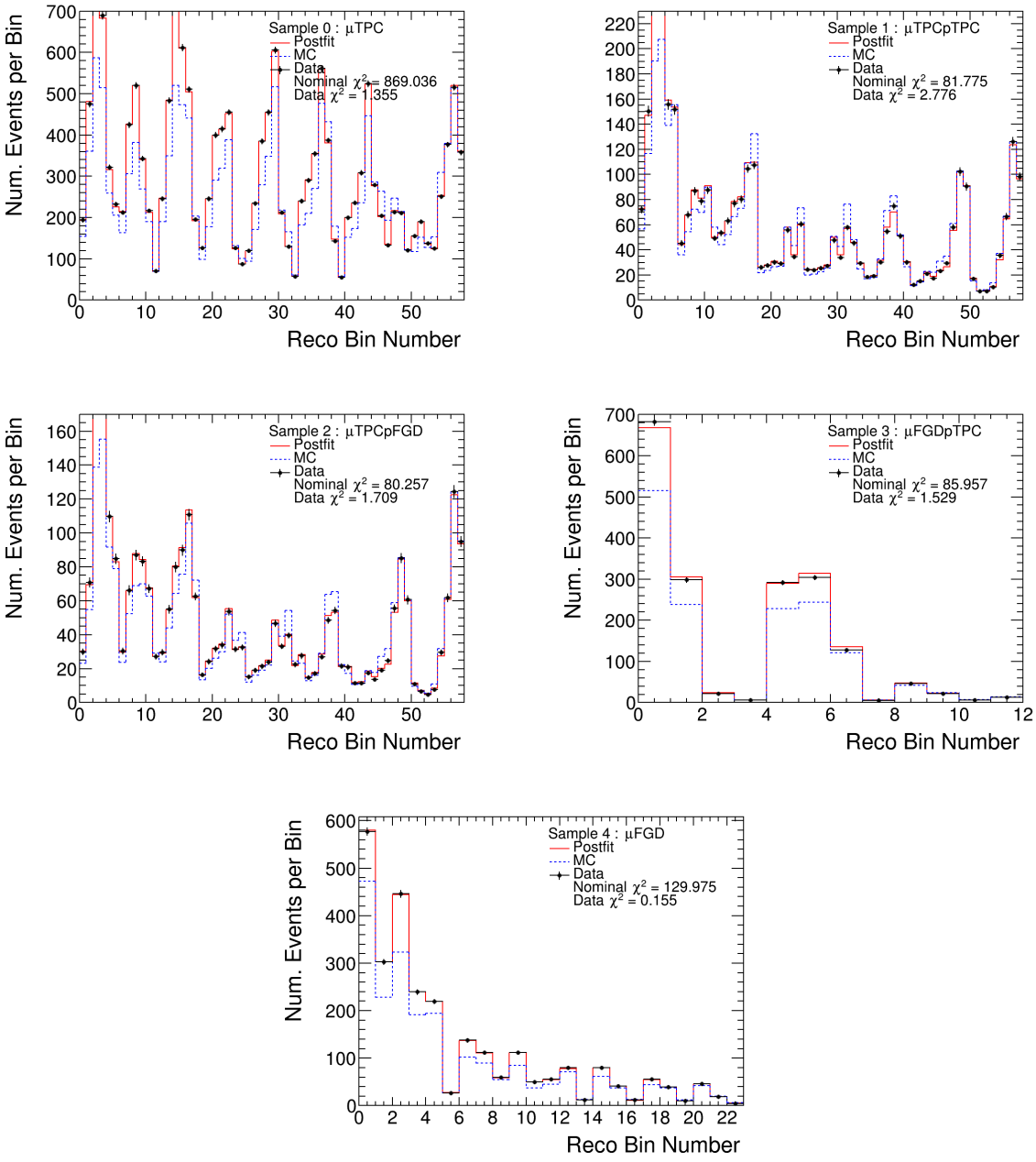

Figure 7.31: Pre/post-fit reconstructed event plots for the fit to neutrino energy variations, ND280 signal samples only.

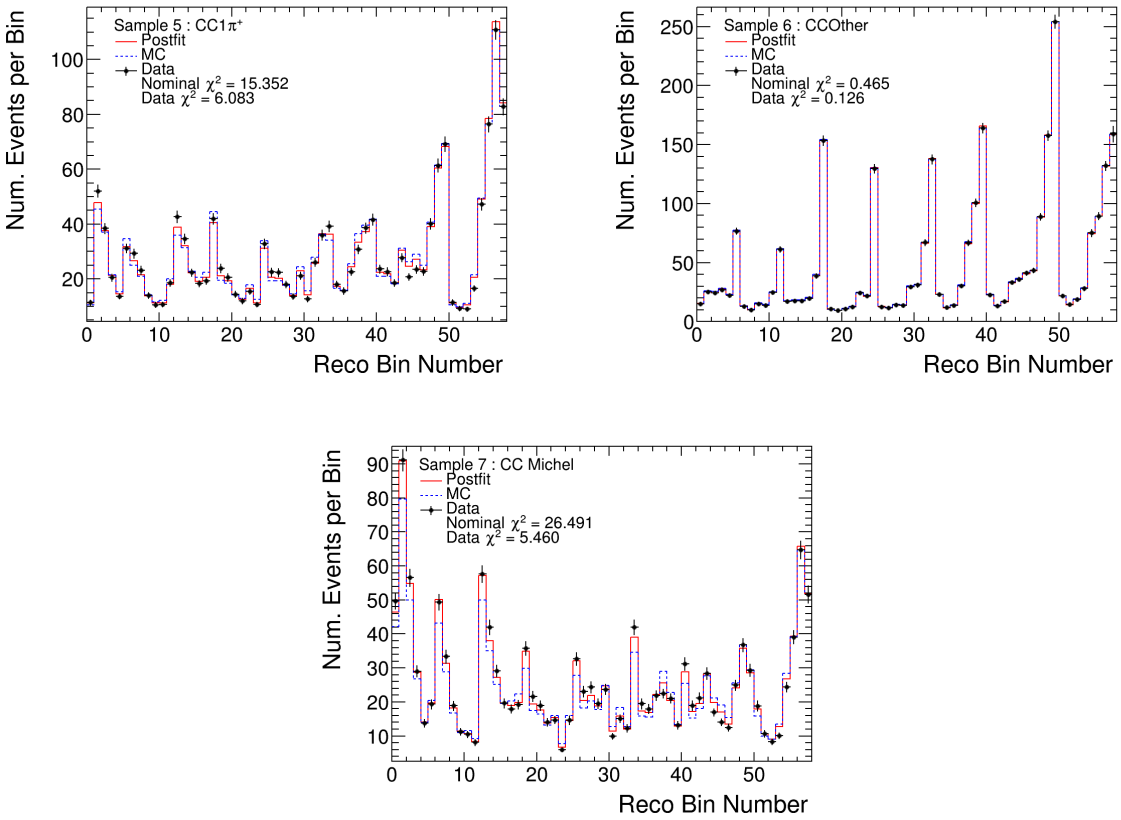

Figure 7.32: Pre/post-fit reconstructed event plots for the fit to neutrino energy variations, ND280 sideband samples only.

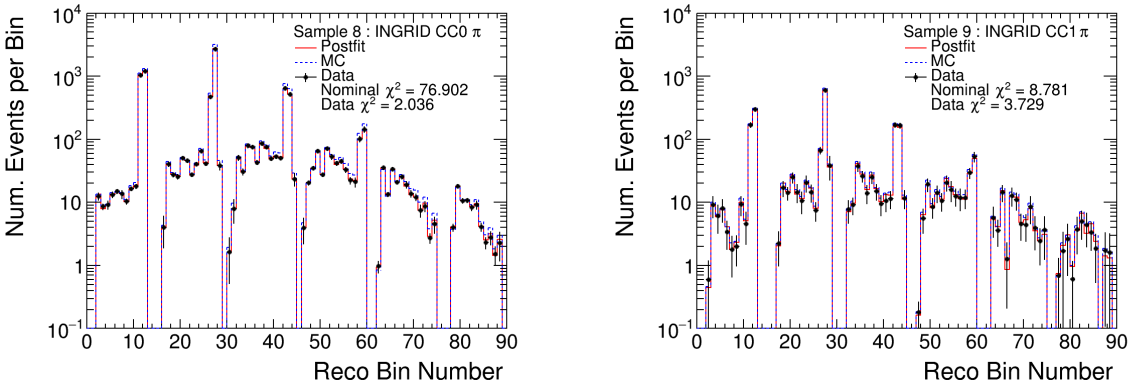

Figure 7.33: Pre/post-fit reconstructed event plots for the fit to neutrino energy variations, INGRID samples only.

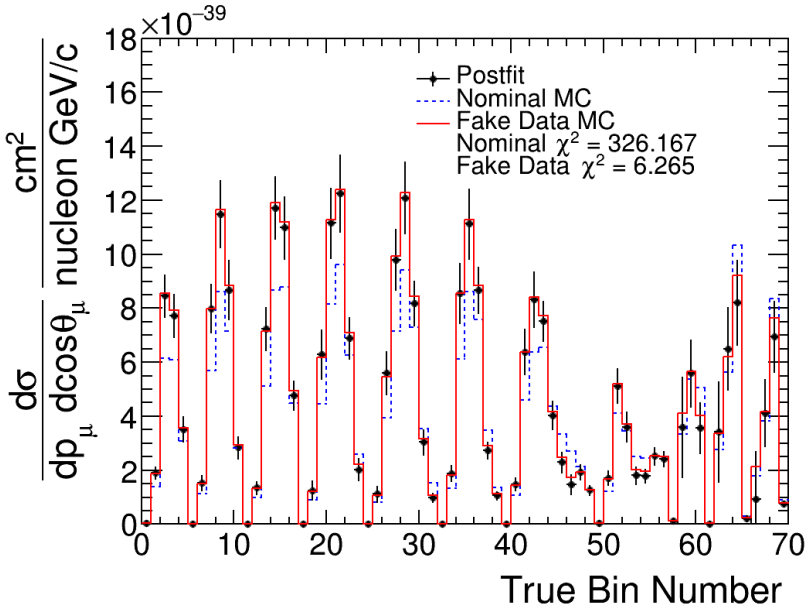

Figure 7.34: Pre/post-fit cross-section plot showing all analysis bins (in true kinematics) for the fit to neutrino energy variations.

7.6 Altered signal weights

This study uses pseudo data where the signal events in the nominal MC simulation were weighted to see if the fit could correctly and exactly recover the change. The pseudo data was built by weighting only the signal events in the nominal MC simulation event-by-event where ND280 events were decreased by 20% and INGRID events were increased by 20%. Since the template parameters have no prior error or penalty for moving, they should be able to exactly recover a simple normalization variation where none of the systematic parameters should move. If the weighting function was something more complicated, for example based on the momentum transfer of the signal events, then slight movement would be expected in the systematic parameters.

The fit results show the expected behavior, with the template parameters moving to the correct values and the systematic parameters essentially not moving from their nominal values. There are a few exceptions, namely the INGRID parameters show slight deviations from the correct value. The low momentum INGRID bins (350 to 500 MeV) show large differences of about 4%, compared to at most 1% for the rest of the template parameters. This is most likely due to the fit stopping early by using too loose of a tolerance, those INGRID bins have issues with low statistics, or it could be related to the slight movement in the 2p2h shape parameter. The rest of the systematic parameters show very little to no movement, however the 2p2h shape parameter (index 2) does end up slightly below its nominal value for about a 2% deviation. Overall the post-fit error is comparable to the results from the Asimov fits.

The reconstructed event distributions show excellent agreement between the post-fit distribution and the pseudo data points, with all the ND280 samples achieving a perfect fit. The INGRID samples have a slight non-zero χ^2, but this is expected given the INGRID template parameters not fitting to the exact correct value. The extracted cross section distribution also shows excellent agreement, with the non-zero χ^2 a result of the inaccuracies in the INGRID parameters as already discussed.

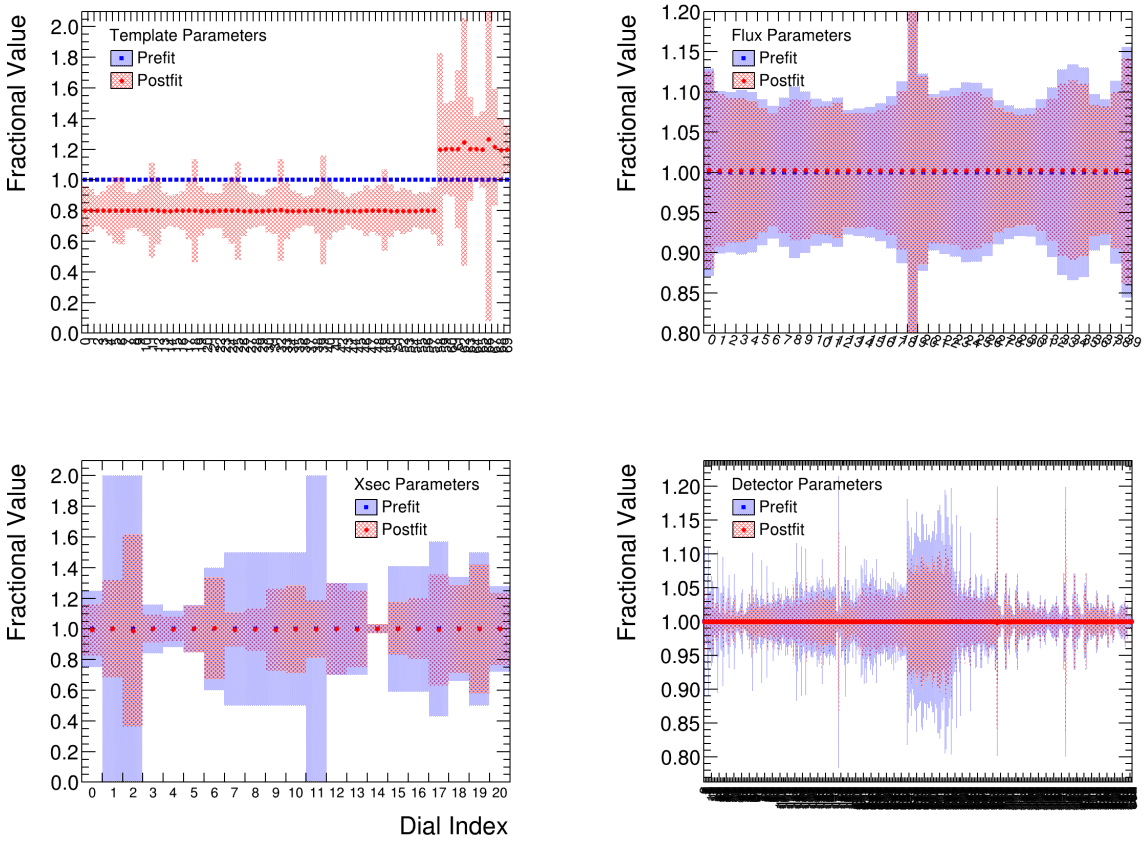

Figure 7.35: Pre/post-fit parameter plots for the fit to signal event variations.

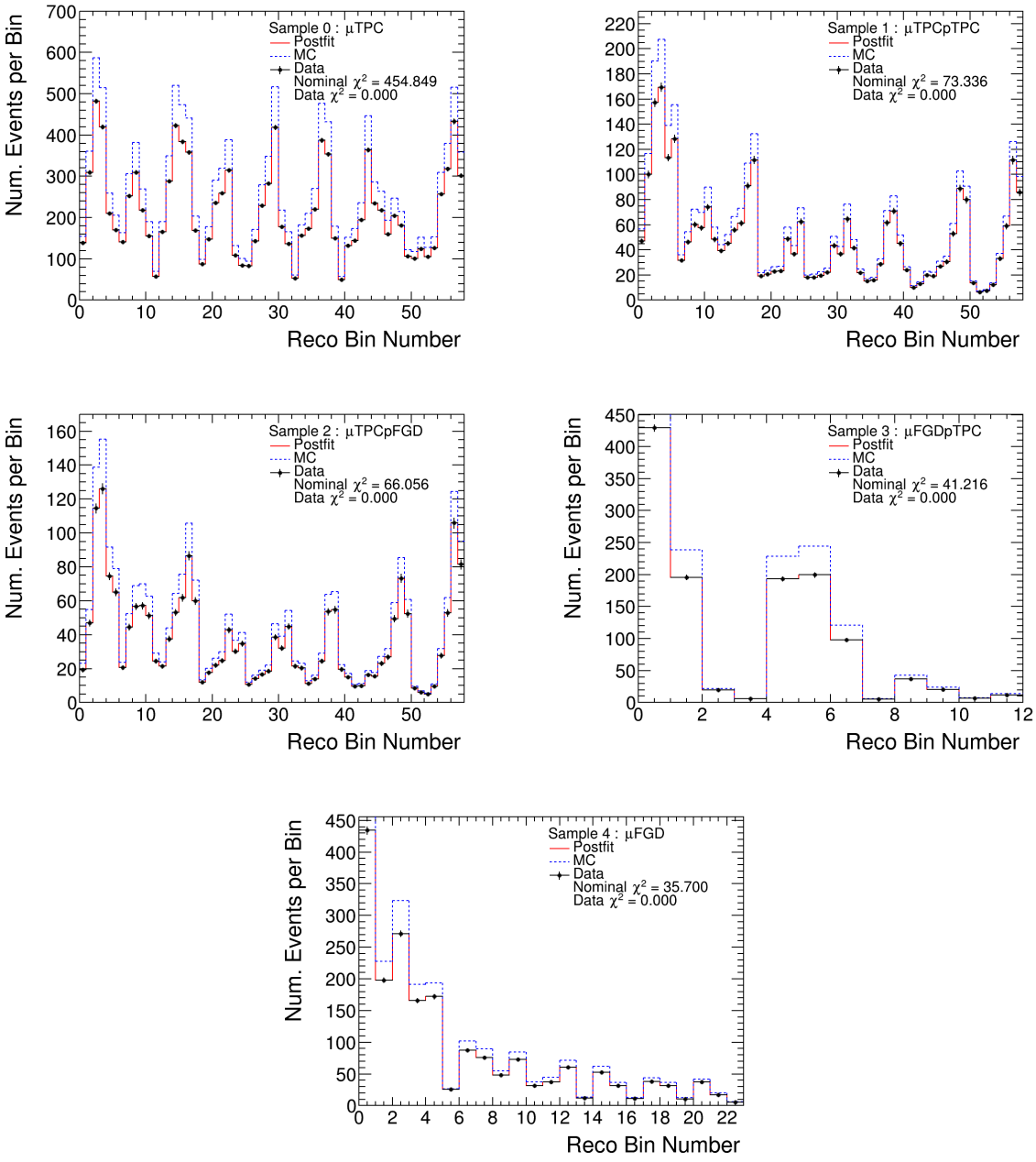

Figure 7.36: Pre/post-fit reconstructed event plots for the fit to signal event variations, ND280 signal samples only.

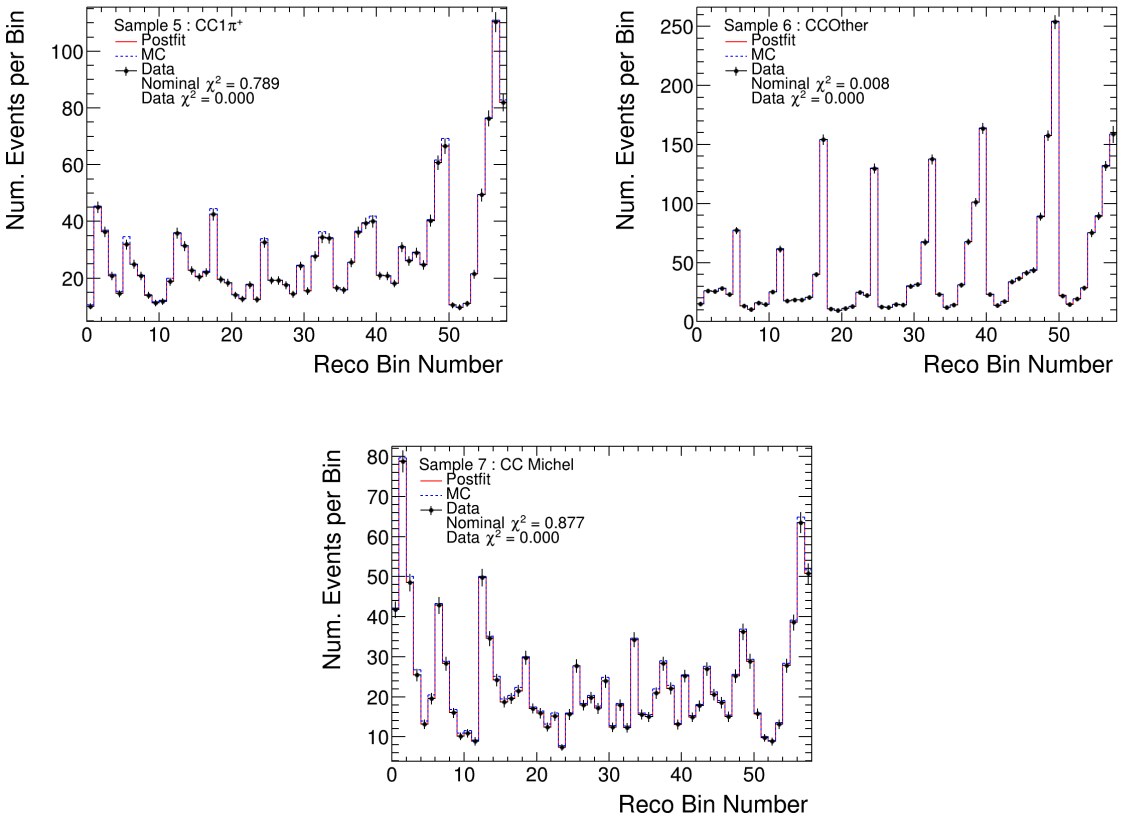

Figure 7.37: Pre/post-fit reconstructed event plots for the fit to signal event variations, ND280 sideband samples only.

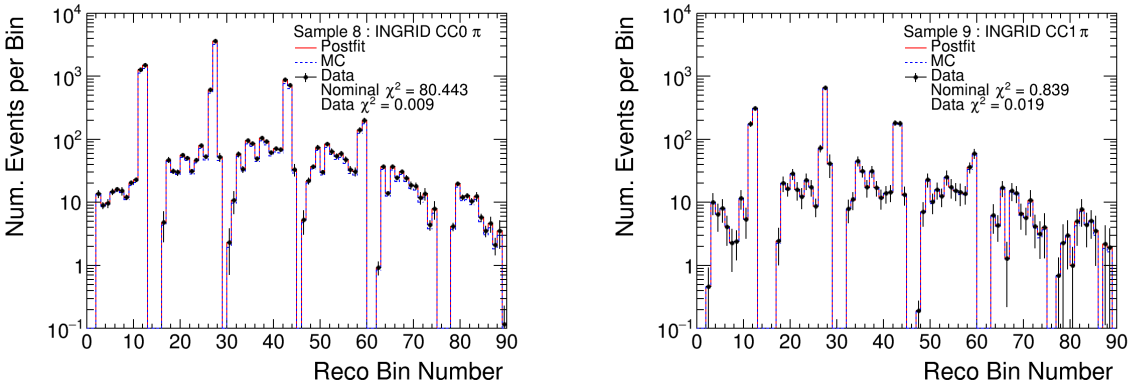

Figure 7.38: Pre/post-fit reconstructed event plots for the fit to signal event variations, INGRID samples only.

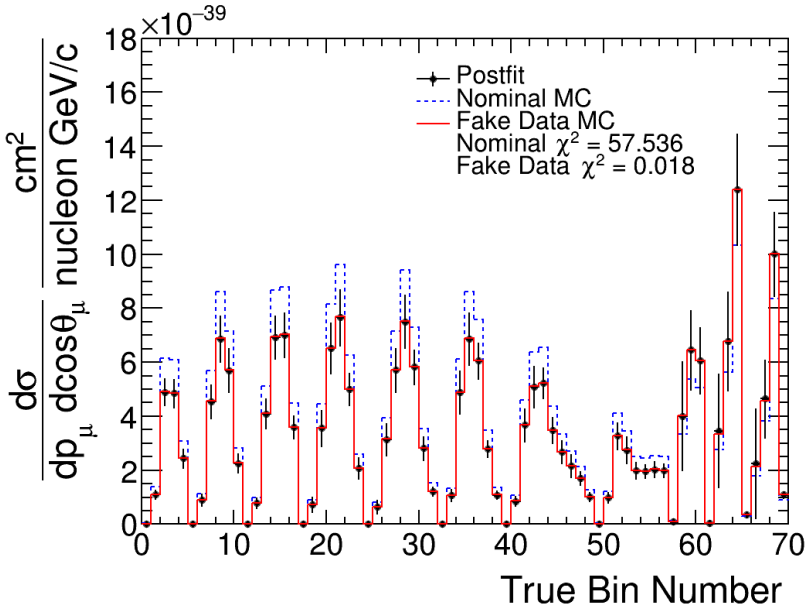

Figure 7.39: Pre/post-fit cross-section plot showing all analysis bins (in true kinematics) for the fit to signal event variations.

7.7 Low Q^2 suppression of resonant events

This study uses pseudo data where true resonant events in the nominal MC simulation were weighted to see how the fit would handle a change in the distribution of resonant pion production events. Resonant pion events most often produce events with a pion in the final state which will contribute to the sideband samples, however the pion can be absorbed or missed and the event can be selected in the signal samples. The expected behavior is then to see fewer CC-1π events mostly in the sideband sample, and see a slight reduction in events in the signal samples. The pseudo data was built by weighting true resonant events in the nominal MC simulation event-by-event as a function of Q^2 according to the following equation:

$$w(Q^2) = \frac{1.01}{1 + \exp(1 - \sqrt{Q^2}/0.156)} \text{ if } Q^2 < 0.7 \text{ GeV}^2 \tag{7.4}$$

The suppression is based on results from MINERvA [105] and MINOS [106] showing a disagreement between their data and MC for low momentum transfer pion production events, with the specific equation for the weights from Ref. [106].

The fit performs as expected, with the largest parameter movement corresponding to the pion production systematic parameters. The suppression of true resonant events will primarily cause a deficit of events in the CC-1π and CC-Michel sidebands, and the fit responds by decreasing the strength of the pion normalization parameters (index 8 and 9) and the coherent pion production normalization (index 11). Additionally the pion FSI parameters corresponding to low energy processes (index 15 and 17) were increased, which also results in decreasing the amount of pion events as pions will escape the nucleus less often. The 2p2h parameters were decreased which is probably due to 2p2h events commonly being misclassified as CC-1π events. In general the fit reduced the most common sources of pion events to achieve the suppression seen in the pseudo data. Most of the template and flux parameters show a slight increase which is largely to balance lowering the pion normalizations.

The reconstructed event distributions show excellent agreement between the post-fit dis-

tribution and the pseudo data points overall. Most of the remaining discrepancy is in the CC-1π and CC-Michel samples, which is largely expected as the Q^2 suppression had the most effect on those samples. The extracted cross section matches quite well with the pseudo data distribution, and shows the expected slightly lower cross section due to the loss of resonant events which end up mis-tagged as CC-0π events.

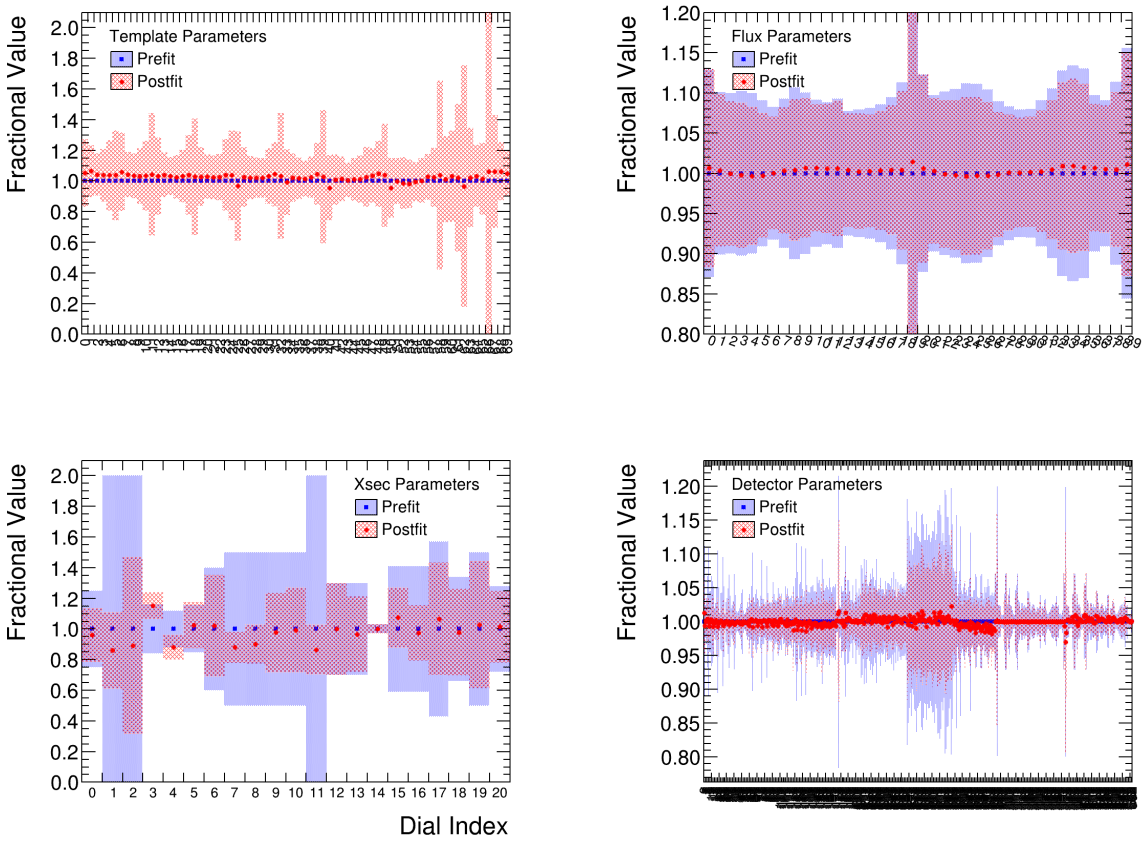

Figure 7.40: Pre/post-fit parameter plots for the fit to low momentum transfer suppressed resonant events.

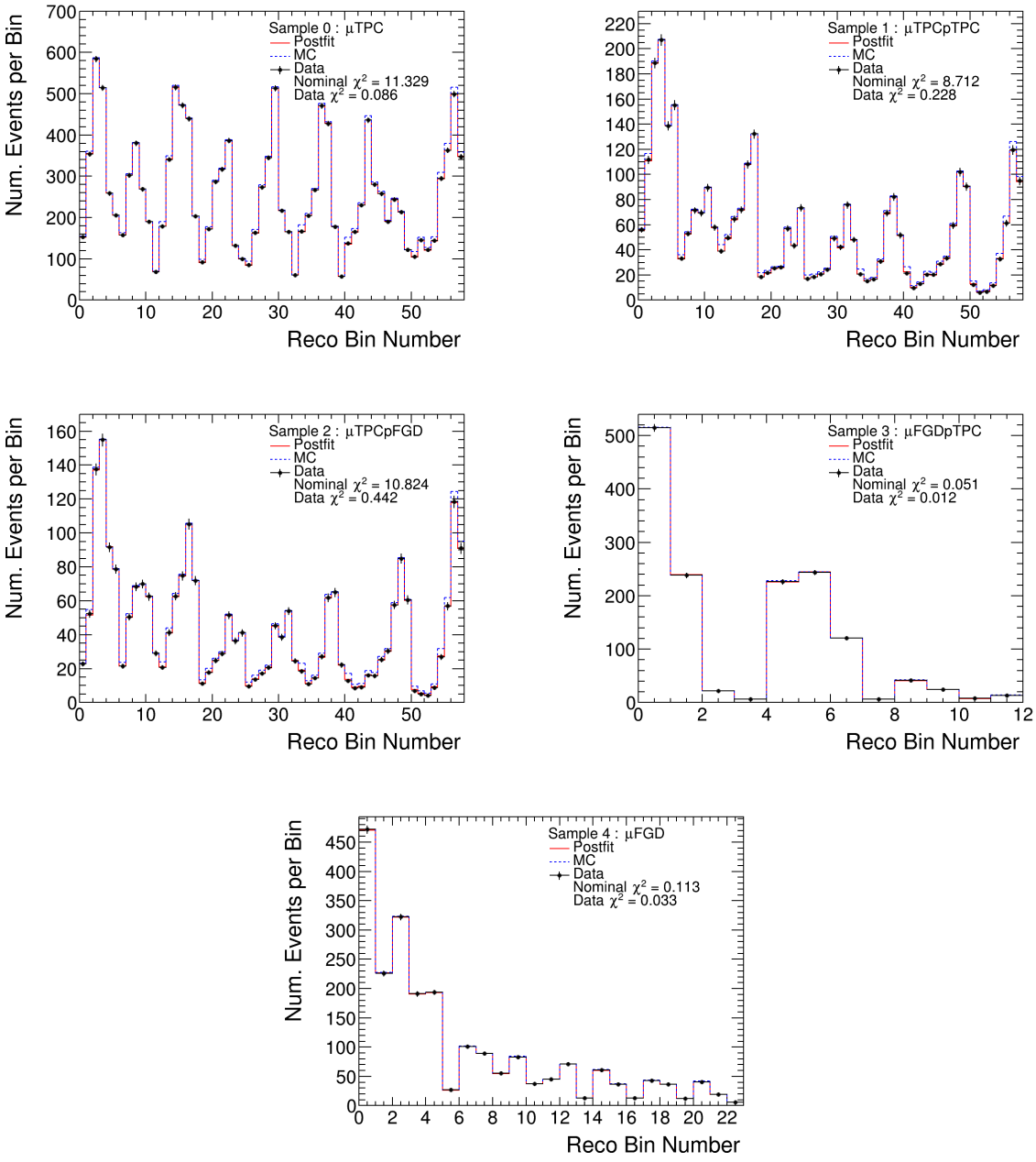

Figure 7.41: Pre/post-fit reconstructed event plots for low momentum transfer suppressed resonant events, ND280 signal samples only.

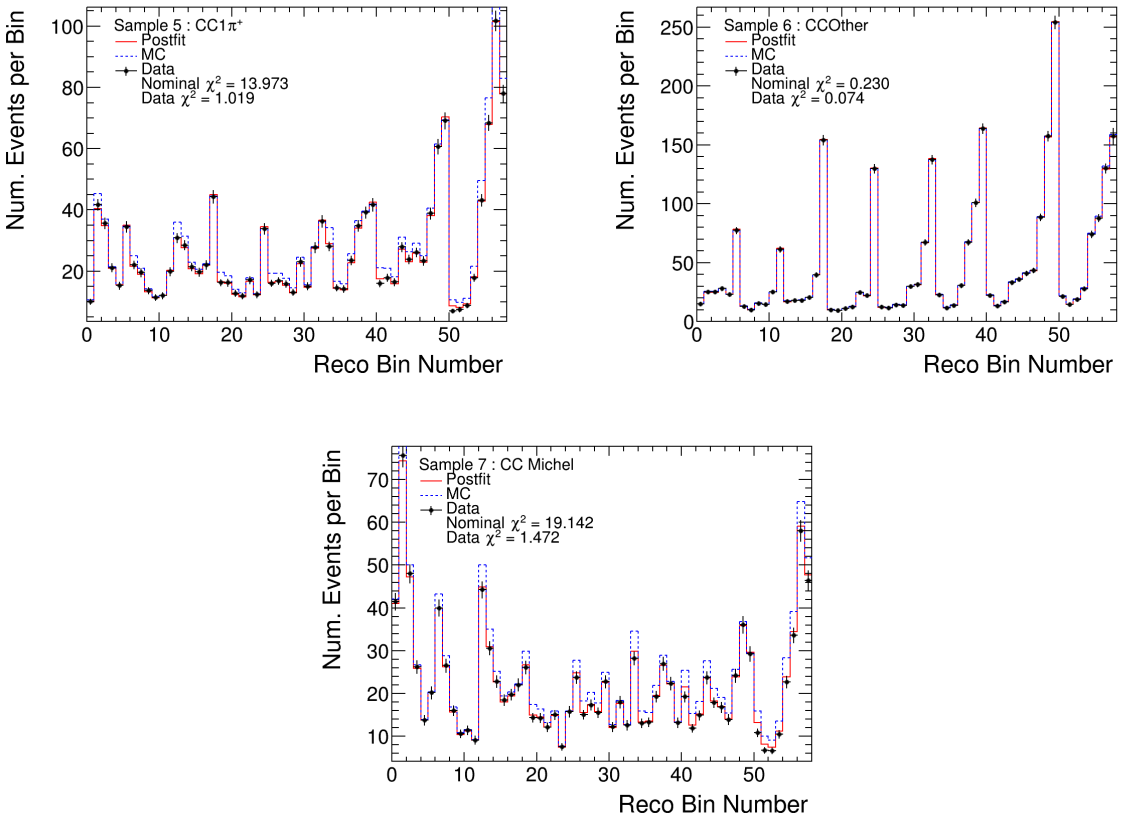

Figure 7.42: Pre/post-fit reconstructed event plots for low momentum transfer suppressed resonant events, ND280 sideband samples only.

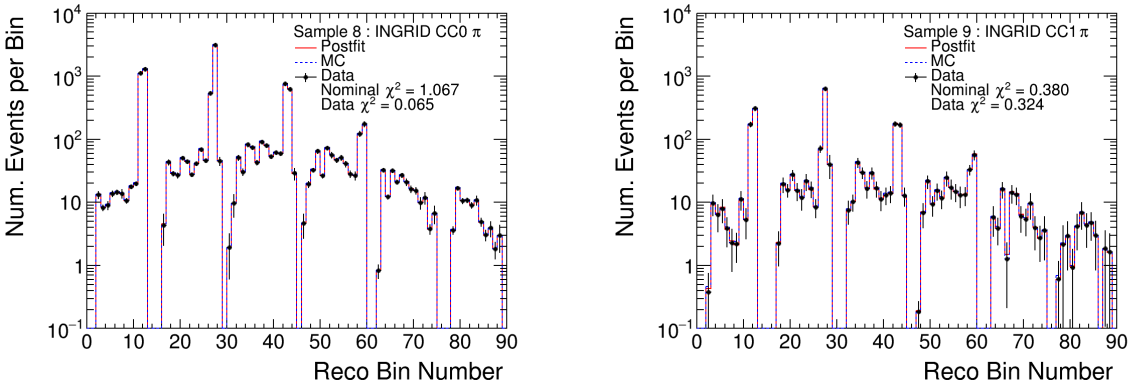

Figure 7.43: Pre/post-fit reconstructed event plots for low momentum transfer suppressed resonant events, INGRID samples only.

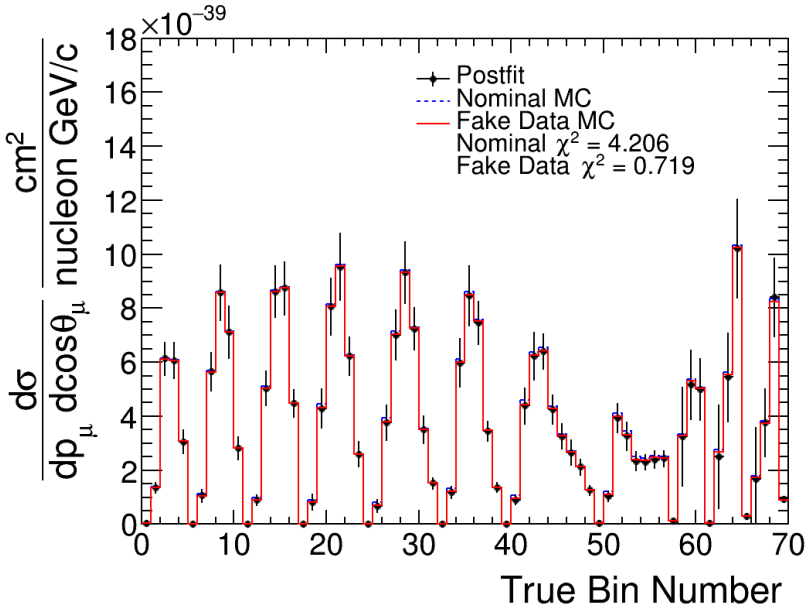

Figure 7.44: Pre/post-fit cross-section plot showing all analysis bins (in true kinematics) for the fit to low momentum transfer suppressed resonant events.

7.8 MINERvA data-driven weights of signal events

This study uses pseudo data where true signal events in the nominal MC simulation were weighted to see how the fit would handle a physically motivated change to the signal distribution. The pseudo data was built by weighting true signal events in the nominal MC simulation event-by-event as a function of Q^2 based on results from MINERvA [107], which showed a disagreement between their data and MC for low momentum transfer.

The fit results are as expected with essentially only the template parameters moving from their nominal value. The alteration is on signal events, the fit will prefer to move the template parameters since they incur zero χ^2 penalty for movement as opposed to the systematic parameters. In general most of the template parameters show a slight increase, which is from the slight enhancement at medium momentum transfer which corresponds to less forward to high angle events. The most forward going events, particularly at low momentum, show a sharp decrease in the template parameters which is expected as low momentum transfer events will primarily be forward going. The rest of the systematic parameters show little to no movement, with the only notable exception being the 2p2h shape parameter, which is common to many of the other fits. The post-fit errors on the parameters are similar to the Asimov fits.

The reconstructed event distributions match well between the post-fit distribution and the pseudo data points. The sideband samples show little difference, which is expected as the variation only affected signal events and the samples are fairly pure. Similar to the template parameters, the signal samples show a slight increase in event rate for less forward to high angle bins, and a noticeable decrease in the most forward going bins. The extracted cross section distribution matches very well with the pseudo data distribution, and again shows the expected enhancement or suppression of bins based on their angle and momentum.

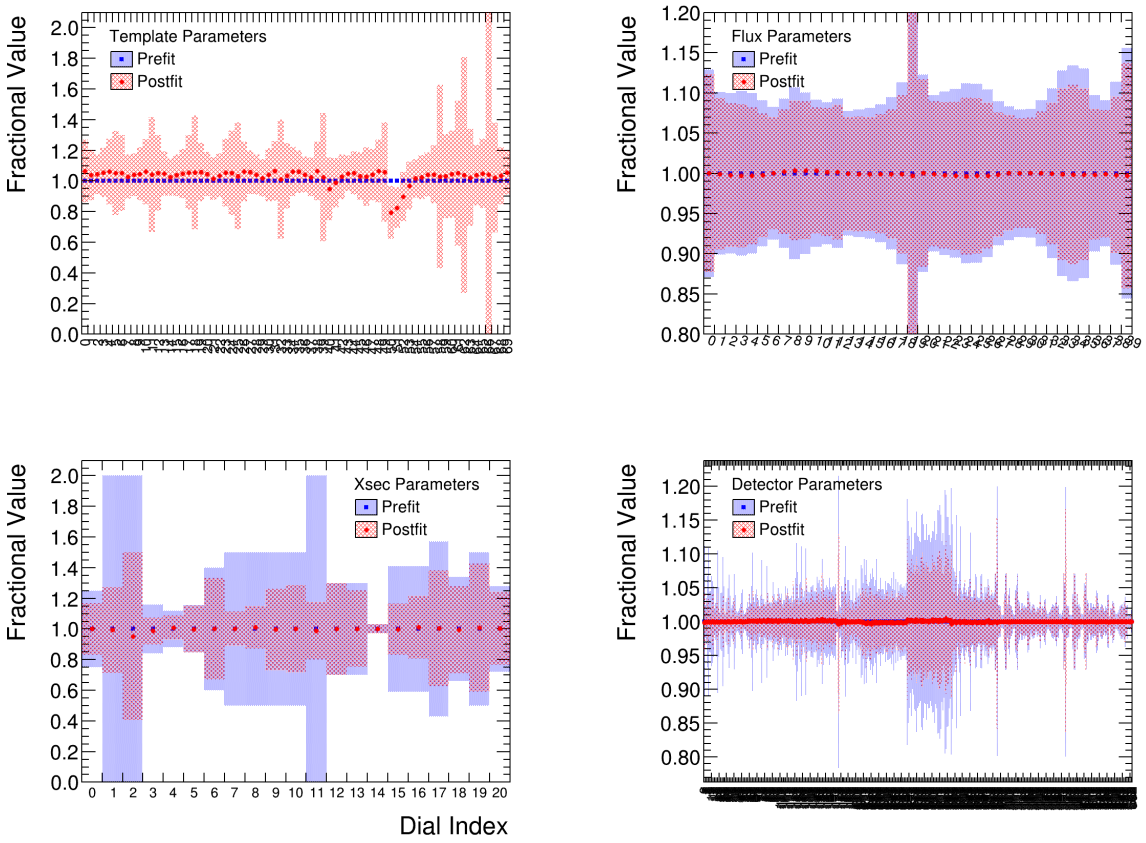

Figure 7.45: Pre/post-fit parameter plots for the fit to low momentum transfer suppressed signal events.

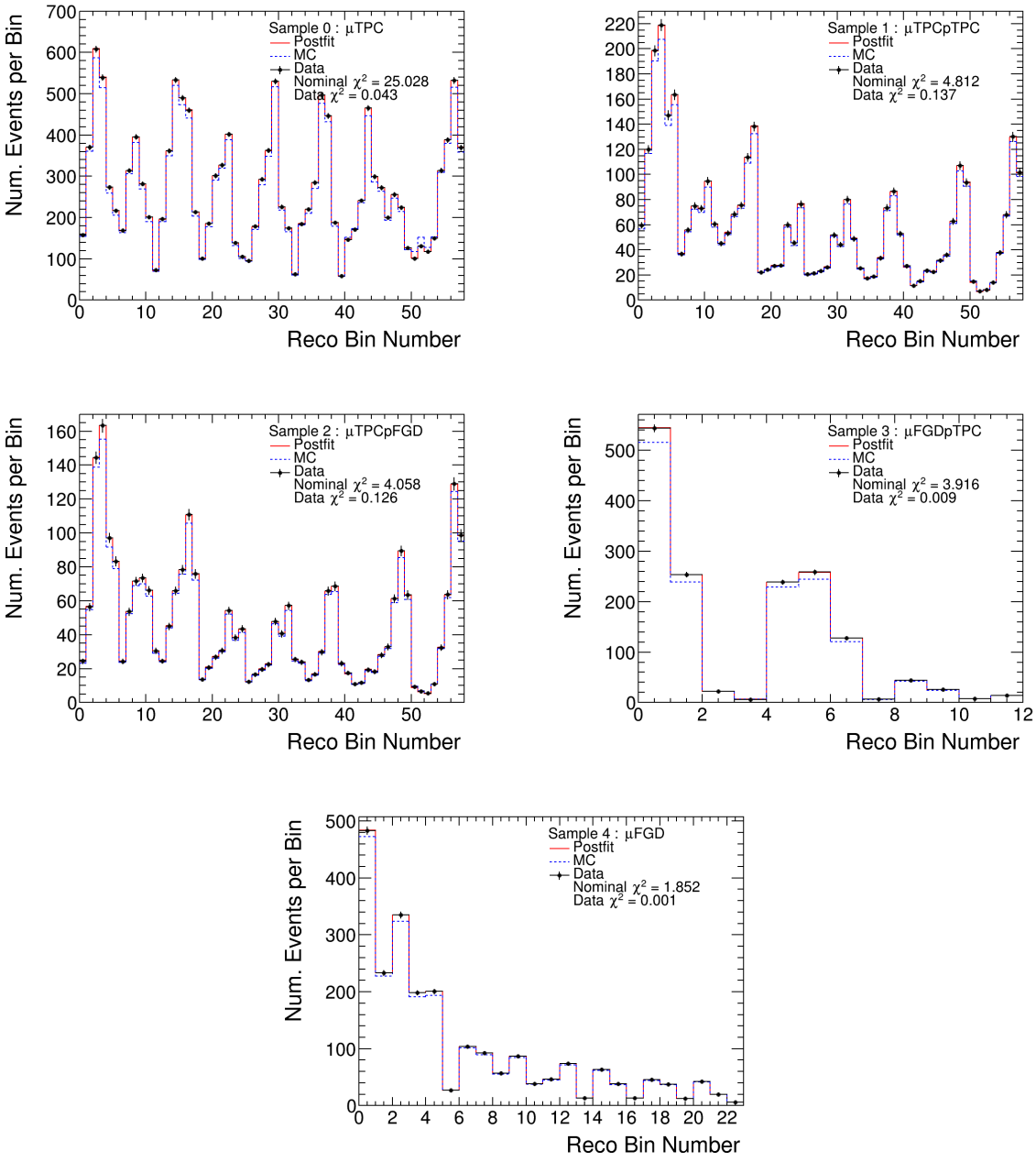

Figure 7.46: Pre/post-fit reconstructed event plots for low momentum transfer suppressed signal events, ND280 signal samples only.

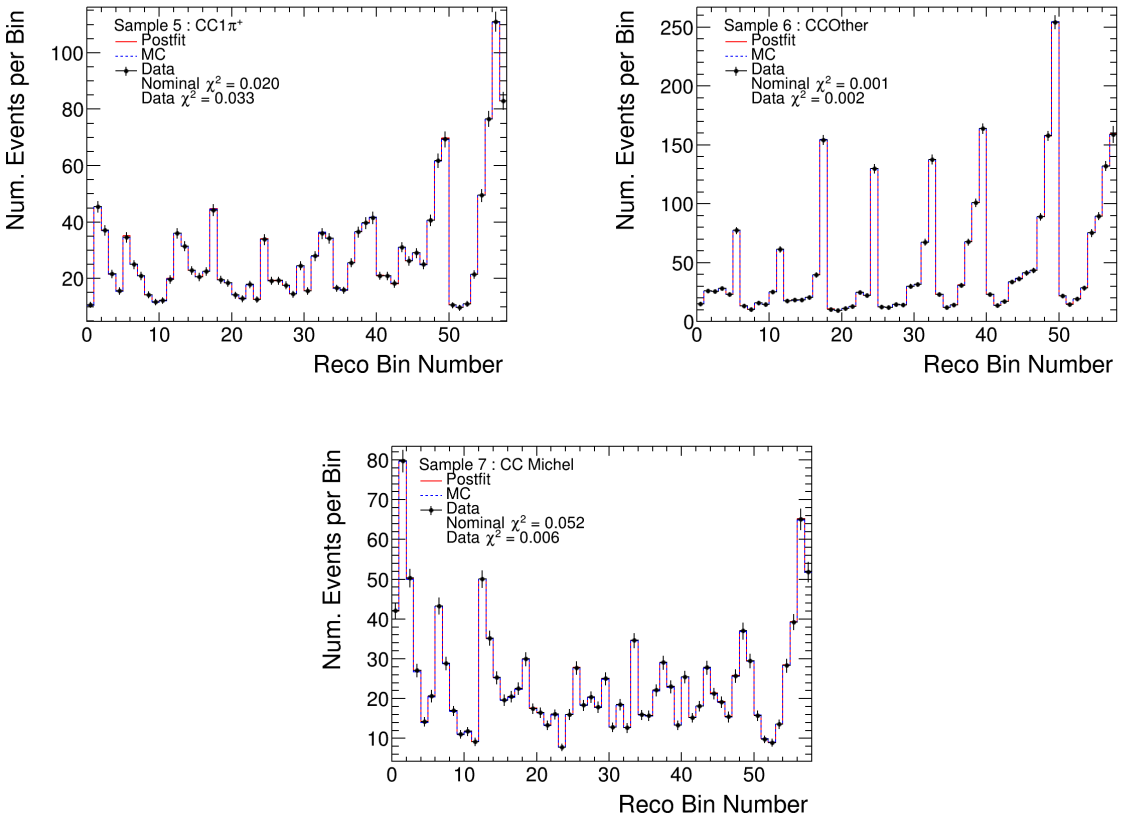

Figure 7.47: Pre/post-fit reconstructed event plots for low momentum transfer suppressed signal events, ND280 sideband samples only.

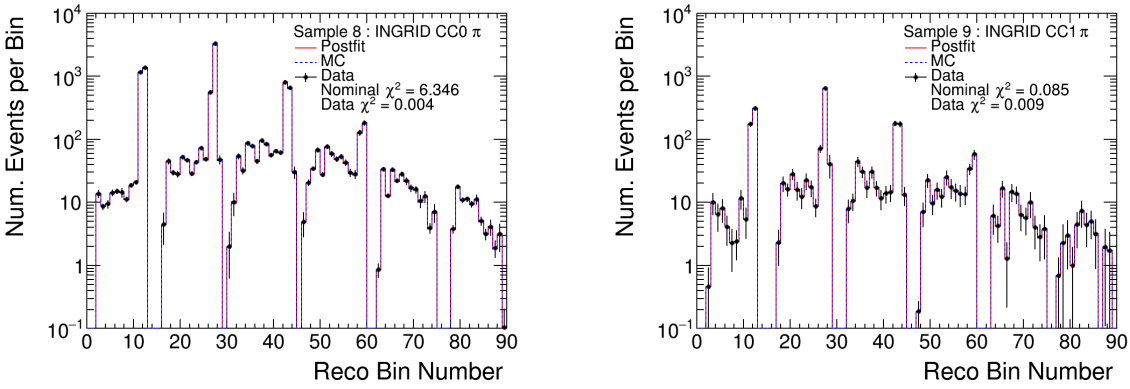

Figure 7.48: Pre/post-fit reconstructed event plots for low momentum transfer suppressed signal events, INGRID samples only.

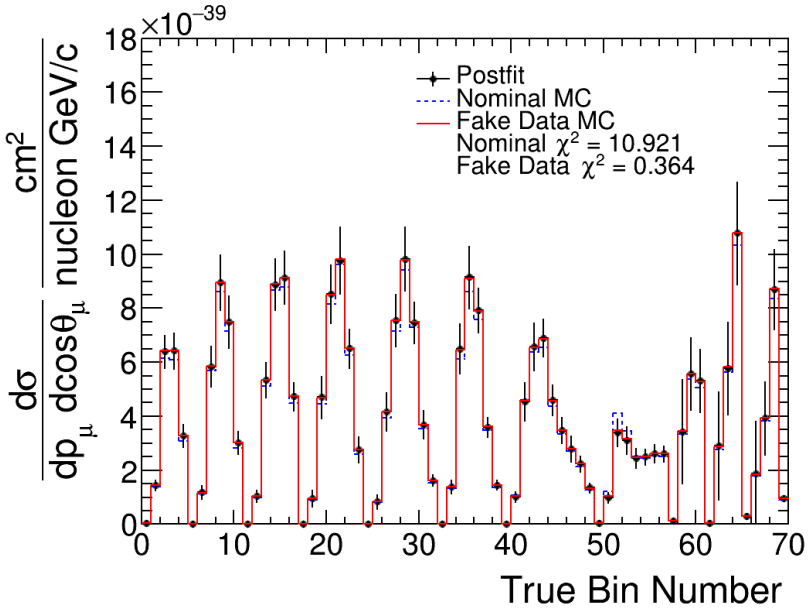

Figure 7.49: Pre/post-fit cross-section plot showing all analysis bins (in true kinematics) for the fit to low momentum transfer suppressed signal events.

7.9 Alternate RPA model

This study uses pseudo data where true CCQE events in the nominal MC simulation were weighted to see how the fit would handle a physically motivated change to the signal distribution. The pseudo data was built by weighting true CCQE events in the nominal MC simulation event-by-event as a function of Q^2 according to the following equation

$$w(Q^2) = \begin{cases} A(1-x')^3 + 3B(1-x')^2x' + 3C(1-x')x'^2 + Dx'^3, & x < U \\ 1 + (D-1)\exp(-E(x-U)), & x > U \end{cases} \tag{7.5}$$

$$C = D + \frac{1}{3}U \times E \times (D-1) \tag{7.6}$$

where $x = Q^2$ and $x' = Q^2/U$. The coefficients and form of the equation were designed to mimic the shape of the Nieves et. al. [13] model RPA correction for CCQE events (shown in Fig. 7.50), and allow for shape variations by changing the values for the coefficients. The values used for A, B, D, E, U are the nominal values used in the T2K oscillation analysis, and are given in Tab. 7.2. The parameterization is denoted as the BeRPA parameterization due to the use of Bernstein polynomials to construct the polynomial form used for $x < U$. The weights were applied to true CCQE events, which are primarily produce signal events but can produce background events through FSI effects. The expected behavior is to see mostly the template parameters move due to the alteration mainly affecting signal events, but it would not be surprising to see slight movement of the nuisance parameters to adjust background events that were true CCQE events.

Overall the fit does well to match the large alteration to the signal model from the application of a different RPA model, however it is not as perfectly matched as the previous tests. The fit parameters show expected movement, with the template parameters experiencing the most movement. Nearly all the template parameters are pulled down to match the suppression from the BeRPA weights as most signal events are at lower momentum transfer. The template parameter values range from a low of about 0.6 to just above 1.0, matching

Parameter	Value
A	0.59
B	1.05
D	1.13
E	0.88
U	1.20

Table 7.2: Parameter values used for the BeRPA weights.

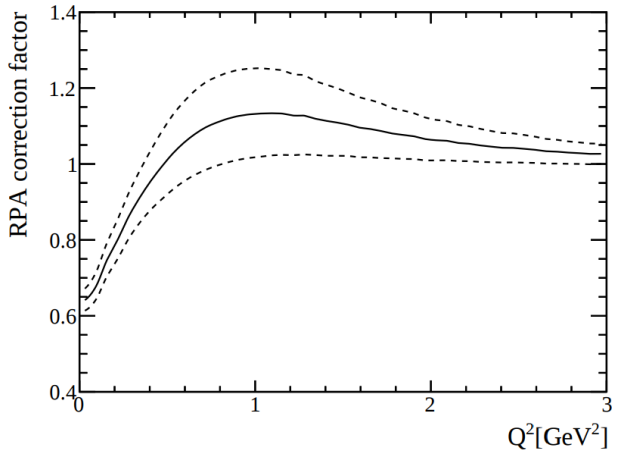

Figure 7.50: The nominal Nieves relativistic RPA correction factor relative to the unmodified CCQE cross section is shown (the solid line) with the $\pm\sigma$ uncertainties (the dotted lines). [2, 13]

the values and shape of the BeRPA function. The flux parameters are also generally pulled down, particularly at neutrino energy below 1 GeV, which corresponds to the region that is being suppressed by the BeRPA weights. The flux parameters are being moved to adjust true CCQE events that produced a background event as the template parameters can only affect true signal events. Most of the cross section parameters show little to no movement, which is expected as the template parameters should primarily be used to adjust the fit. The CC-1π normalization parameters are increased slightly, which is to compensate for the decrease in the flux parameters as the CC-1π and CC-Michel samples were relatively unchanged from the BeRPA weights. The pion absorption FSI parameter shows a large increase, relative to the other parameters, as it is being used to suppress background events (e.g. CC-1π events). The large increase of the 2p2h normalization parameter is probably due to counteract the

decreasing of both the template and flux parameters as the BeRPA weights to not affect true 2p2h events, but the majority of 2p2h events are tagged as signal events.

The reconstructed event distributions in general show excellent agreement between the post-fit distributions and the pseudo data points. The BeRPA weights primarily affected the signal samples, which recover the change quite well. The sideband samples were barely changed from their nominal distributions, and the ND280 CC-1π and CC-Michel samples saw slight improvement between the post-fit distribution and the pseudo data while the ND280 CC-Other and INGRID CC-1π samples actually had sightly worse agreement. This not considered a problem due to how well the samples still agree with the pseudo data, and show similar χ^2 value compared to the rest of the samples. The extracted cross section distribution shows excellent agreement with the pseudo data distribution, however it is not as perfect as the previous Q^2 alterations. The cross section is correctly suppressed in most bins, and the change in the flux parameters is properly handled.

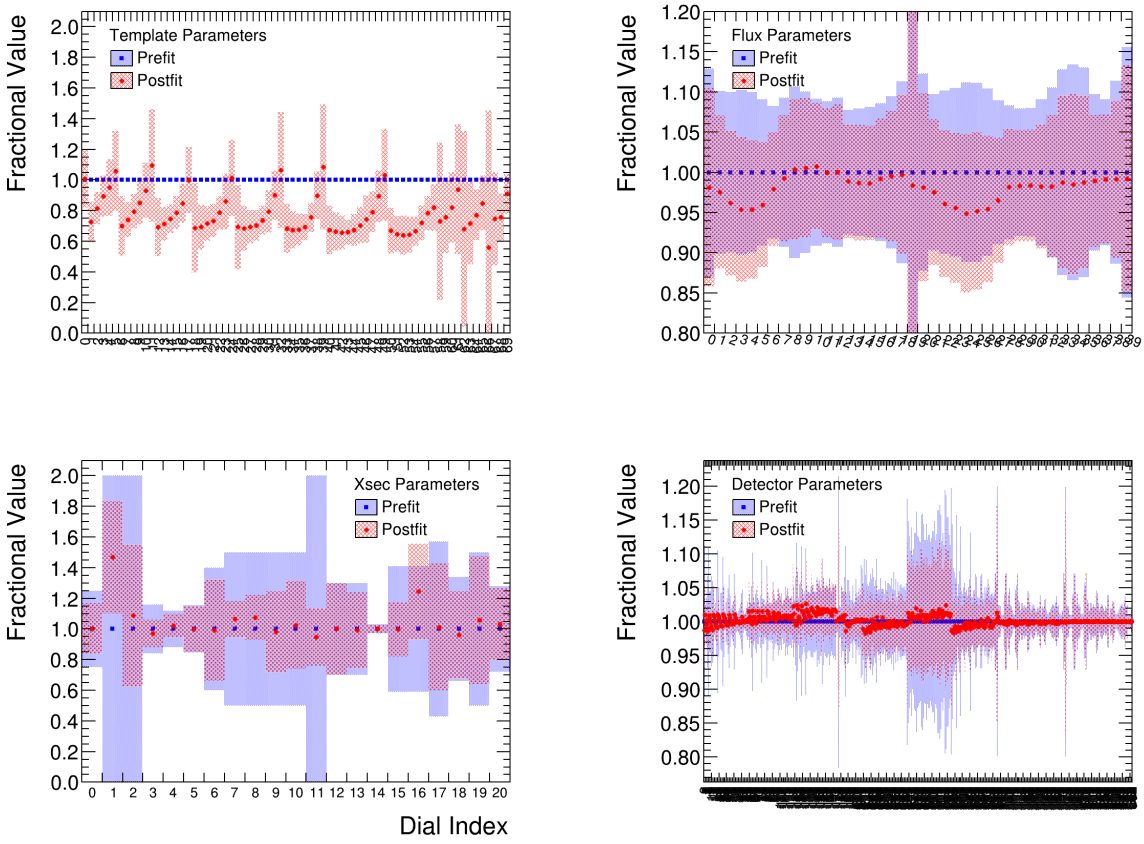

Figure 7.51: Pre/post-fit parameter plots for the fit to an alternate RPA model.

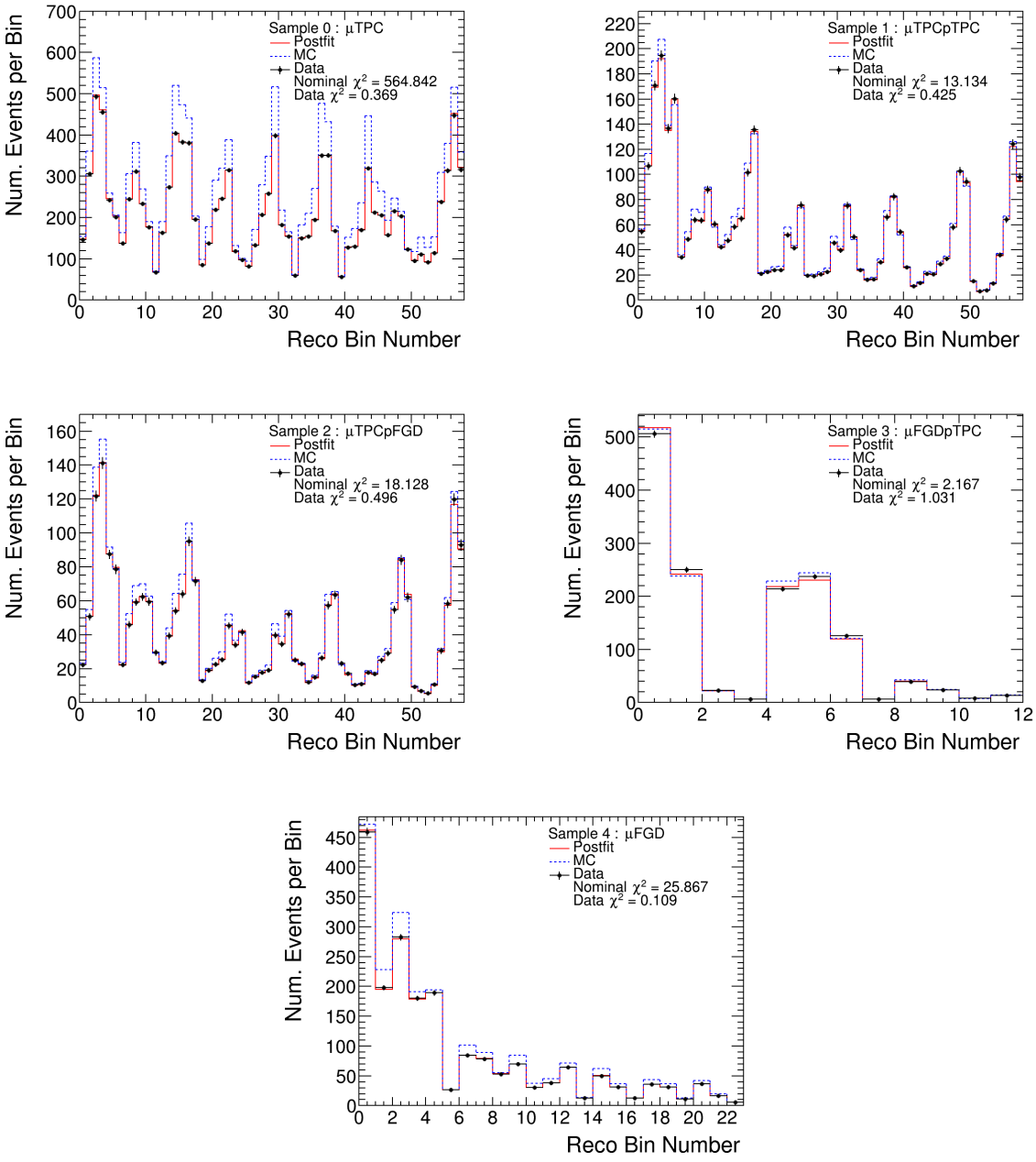

Figure 7.52: Pre/post-fit reconstructed event plots for the fit to an alternate RPA model, ND280 signal samples only.

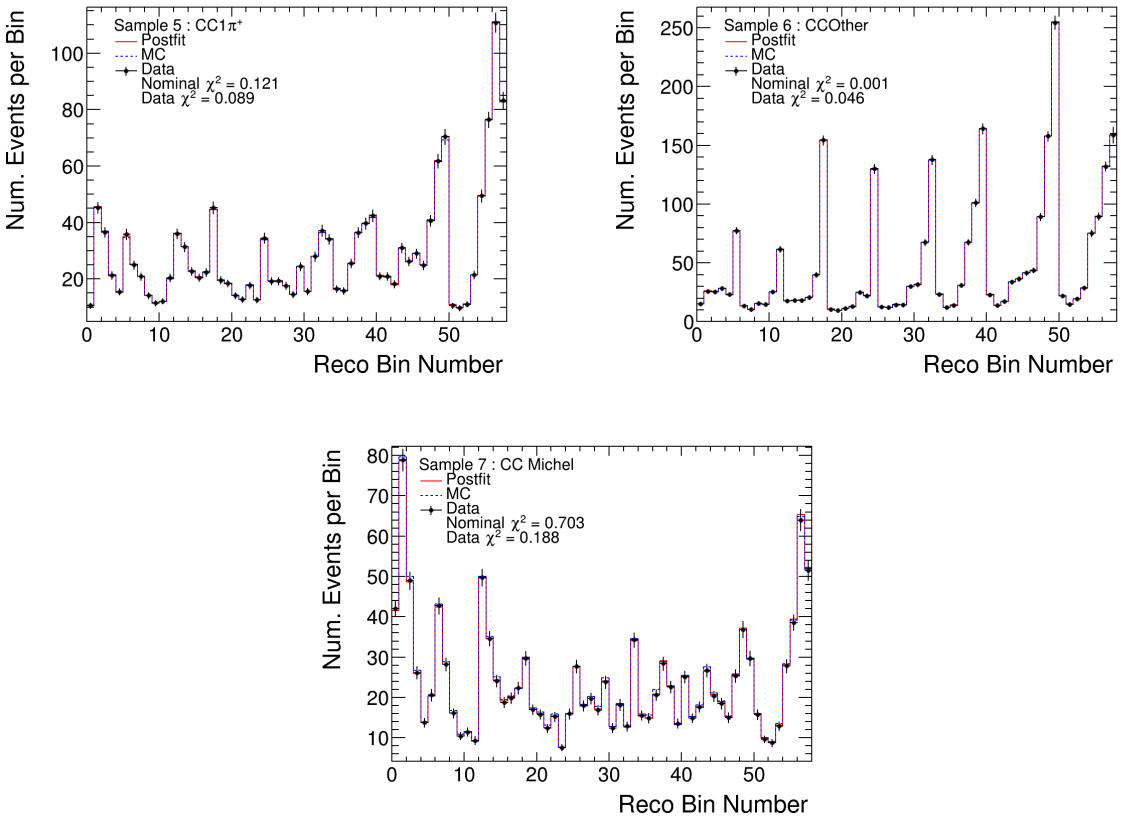

Figure 7.53: Pre/post-fit reconstructed event plots for the fit to an alternate RPA model, ND280 sideband samples only.

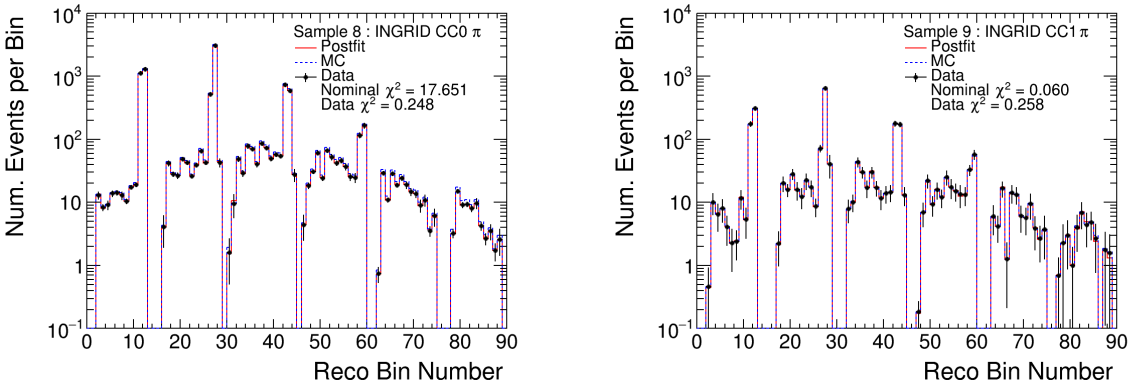

Figure 7.54: Pre/post-fit reconstructed event plots for the fit to an alternate RPA model, INGRID samples only.

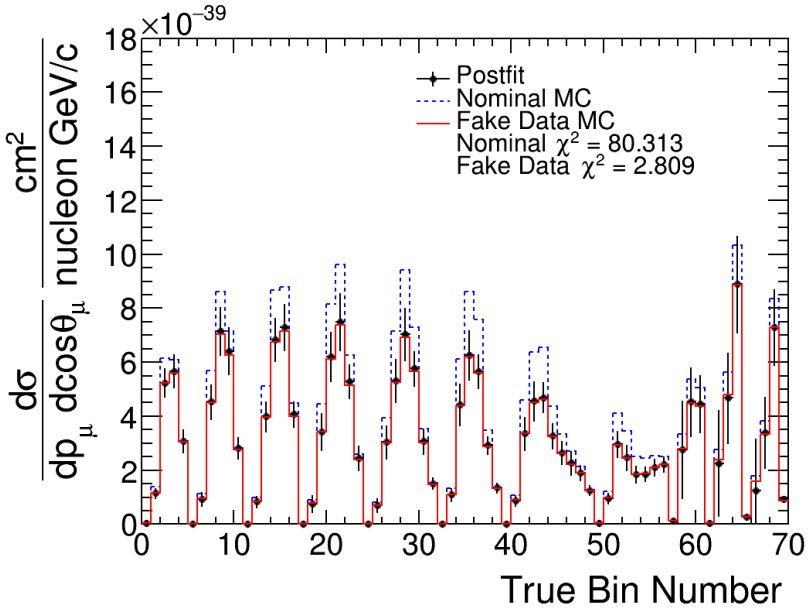

Figure 7.55: Pre/post-fit cross-section plot showing all analysis bins (in true kinematics) for the fit to an alternate RPA model.

7.10 Horn current variation

This study uses pseudo data where the nominal MC simulation was varied by a 3σ increase of the horn current to see how the fit would handle a physically motivated change to the flux. The pseudo data was built by weighting all events in the nominal MC simulation event-by-event as a function of true neutrino energy according to the following histogram in Fig. 7.56, which is the 3σ effect of increasing the horn current according to the flux (using the same binning). Increasing the horn current largely leads to a substantial uniform increase of events, with a few of the ND280 bins seeing a reduction around a few GeV.

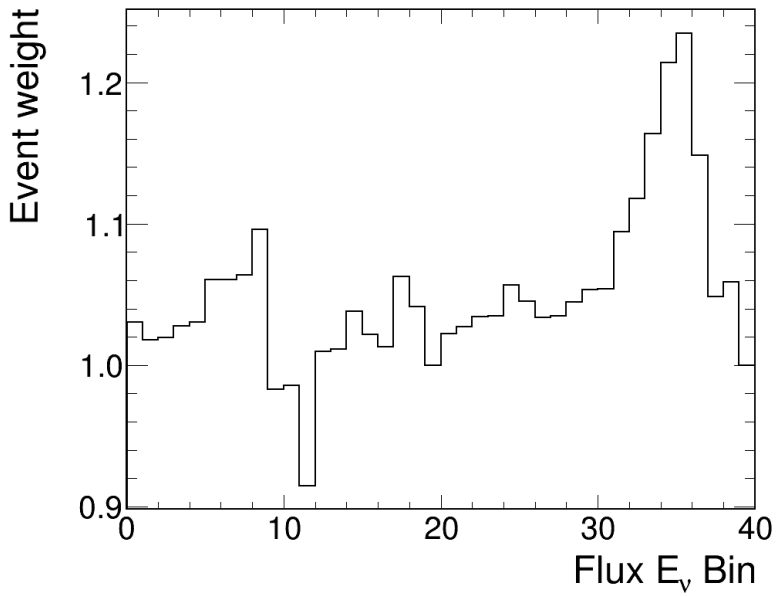

Figure 7.56: Horn current weight histogram, corresponding to a 3σ increase of the nominal horn current. The first 20 bins are ND280, the second 20 are INGRID.

The fit results show the expected behavior with the flux parameters moving toward the shape of the weighting histogram and minimal movement of the rest of parameters. Because the template parameters have no χ^2 penalty, they are used to improve the agreement in addition to the flux parameters. This is reason the flux parameters do not reach the full extent of the weighting histogram as the flux parameters pick up a large χ^2 penalty as they are moved away from nominal, and the fit uses the template parameters to avoid this penalty.

The flux parameters do pick up the shape of the horn current variation quite nicely, including the difference between ND280 and INGRID. The cross section parameters mostly show no movement, remaining at or near their nominal values, with the exception of the 2p2h shape parameter (index 2) and the low energy pion FSI (index 15 and 17), which are all pulled high. This is similar behavior to the other fits where these parameters show larger than expected movement. The post-fit errors are comparable to the Asimov fits.

The reconstructed event distributions show very good agreement between the post-fit distributions and the pseudo data points, with the expected increase of events in the majority of bins. The INGRID samples show a larger increase of events compared to ND280, which is reflected in the weighting histogram. The extracted cross section distribution matches nicely with the cross section using the pseudo data, correctly accounting for the increase the flux integral used to normalize the cross section.

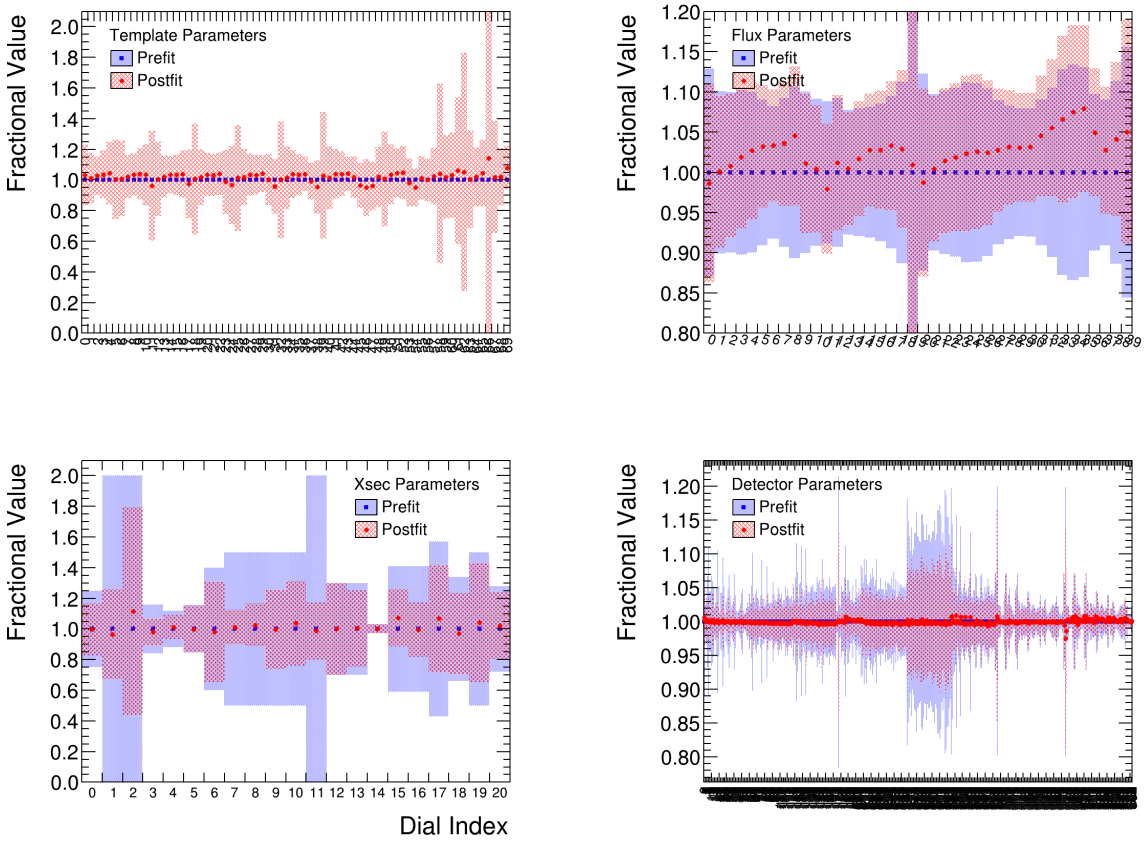

Figure 7.57: Pre/post-fit parameter plots for the fit to increased horn current.

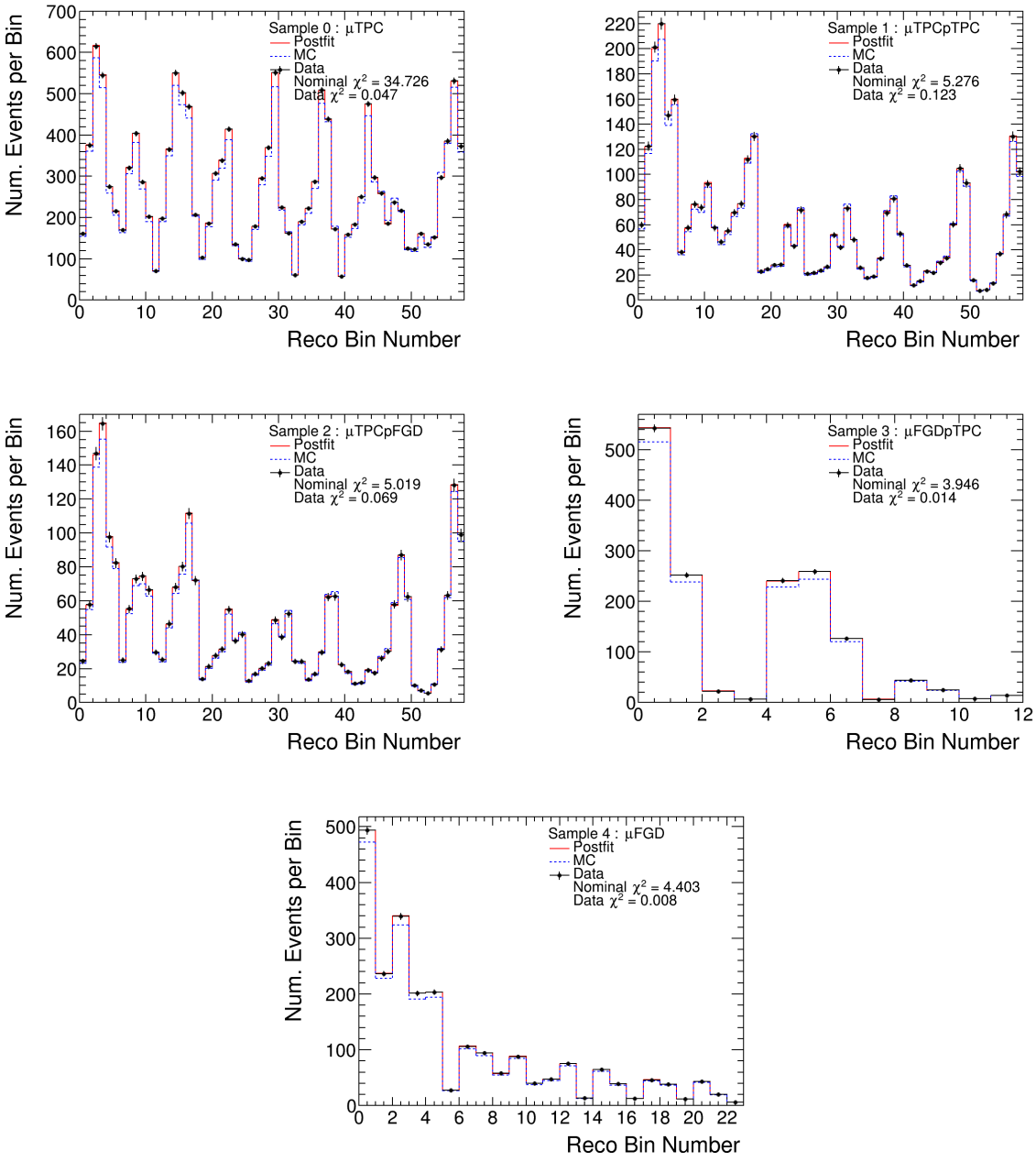

Figure 7.58: Pre/post-fit reconstructed event plots for the fit to increased horn current, ND280 signal samples only.

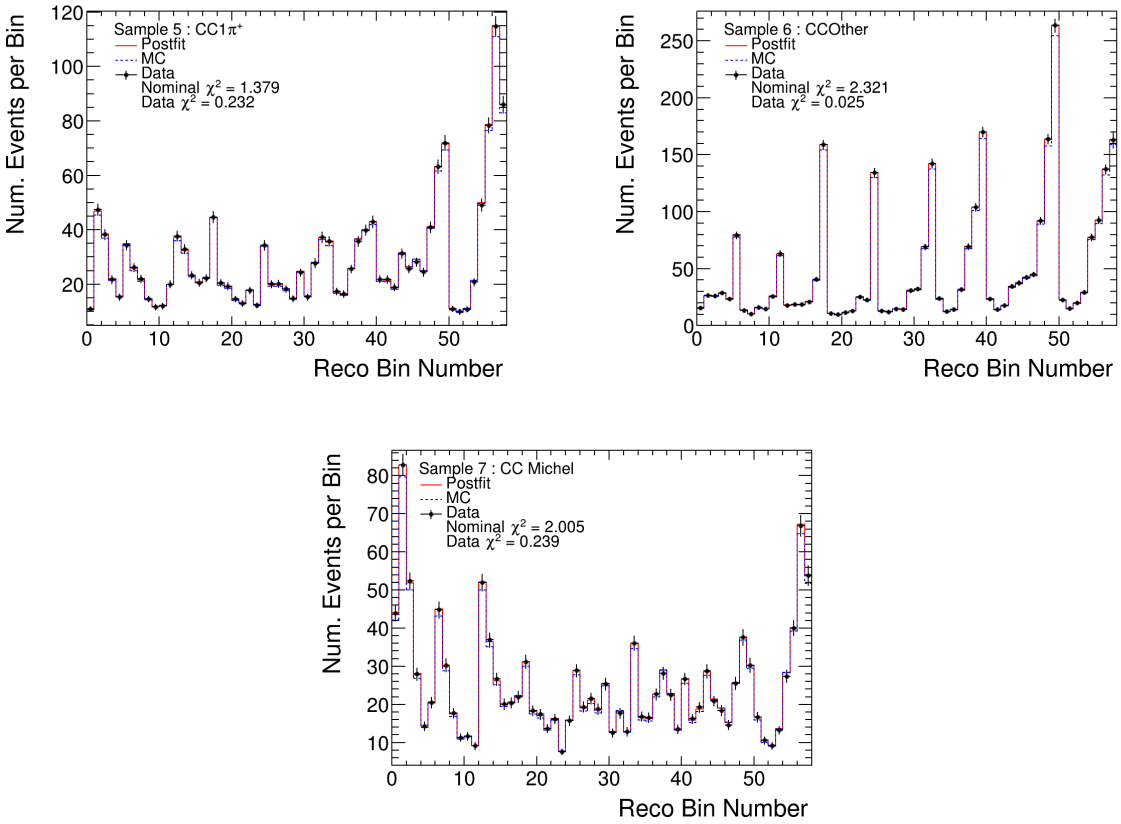

Figure 7.59: Pre/post-fit reconstructed event plots for the fit to increased horn current, ND280 sideband samples only.

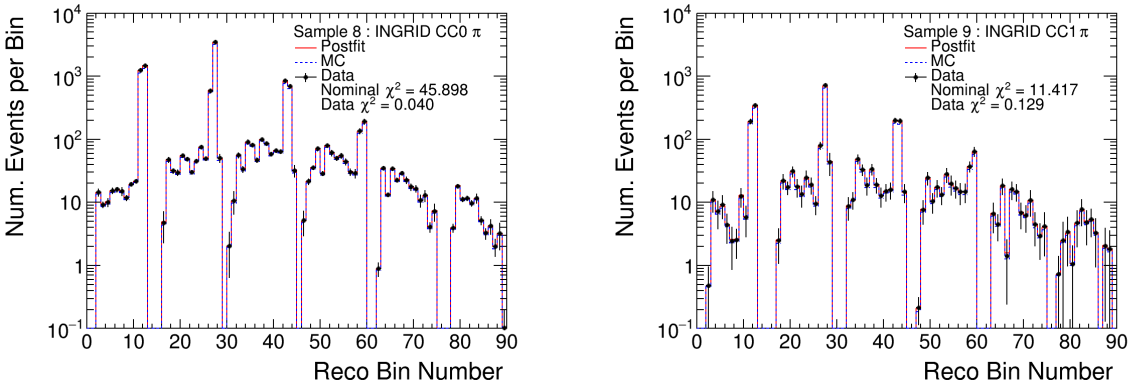

Figure 7.60: Pre/post-fit reconstructed event plots for the fit to increased horn current, INGRID samples only.

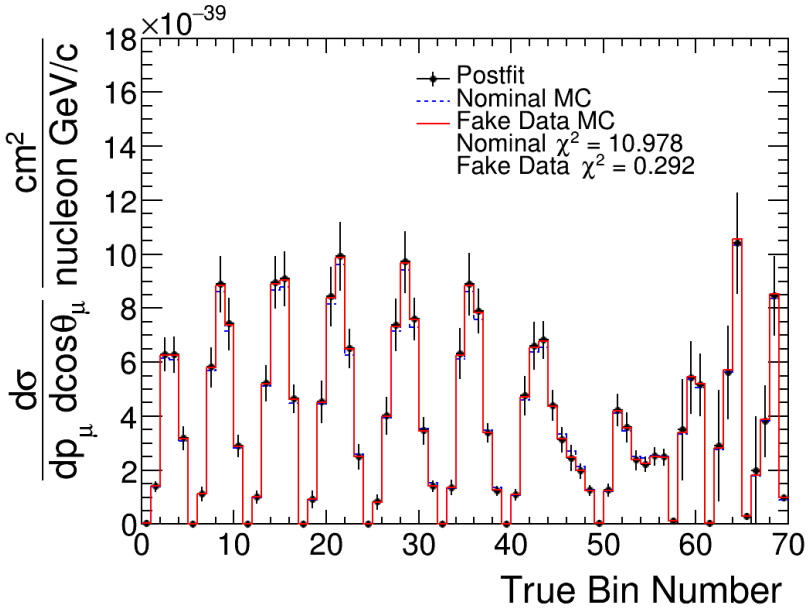

Figure 7.61: Pre/post-fit cross-section plot showing all analysis bins (in true kinematics) for the fit to increased horn current.

7.11 Horn alignment variation

This study uses pseudo data where the nominal MC simulation was varied by a 3σ change of the alignment of horns 2 and 3 to see how the fit would handle a physically motivated change to the flux. The pseudo data was built by weighting all events in the nominal MC simulation event-by-event as a function of true neutrino energy according to the following histogram in Fig. 7.62, which is the 3σ effect of changing the horn 2 and 3 alignment according to the flux simulation.

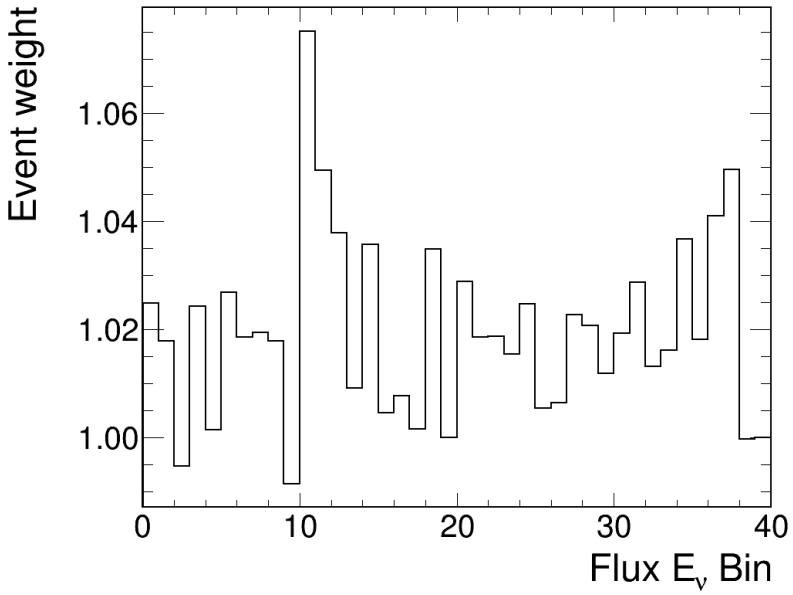

Figure 7.62: Horn alignment weight histogram, corresponding to a 3σ shift of the nominal horn 2 and 3 alignment. The first 20 bins are ND280, the second 20 are INGRID.

The fit results give essentially the same result as varying the horn current, with the fit doing a very good job at fitting the variation. The horn alignment variation is both smaller than the horn current, and more uncorrelated from bin to bin. This is harder for the fit to match as the entire flux systematics are extremely correlated, so the post-fit flux parameters show a fairly smooth change across the energy range. All other parameters show little to no movement, again with the template parameters being used to cover some of the difference in

addition to the flux parameters. The post-fit errors give a similar constraint to the Asimov fits.

The reconstructed event distributions match again quite well between the post-fit distribution and the pseudo data points, with a slight increase of events across all bins as expected from the horn alignment weights. The extracted cross section matches very well with the cross section from the pseudo data, with the horn alignment variation providing little impact on the nominal MC simulation.

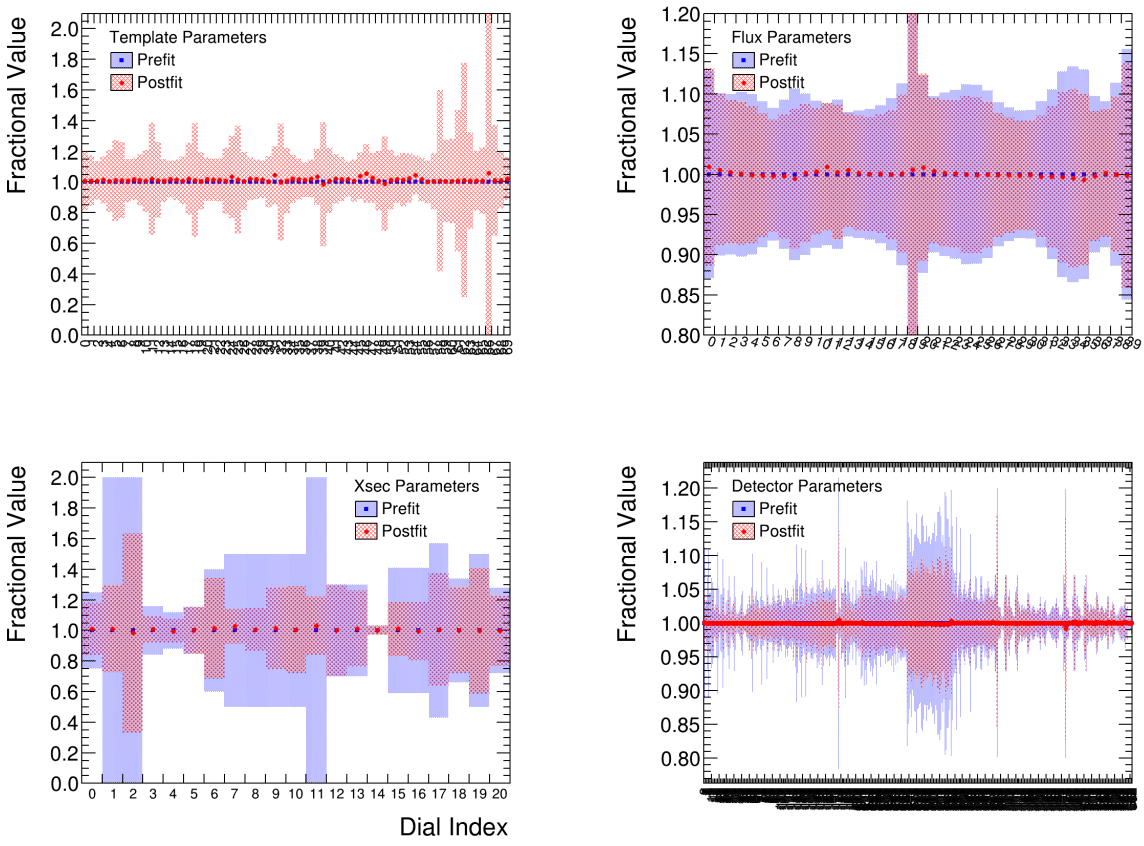

Figure 7.63: Pre/post-fit parameter plots for the fit to varied horn alignment.

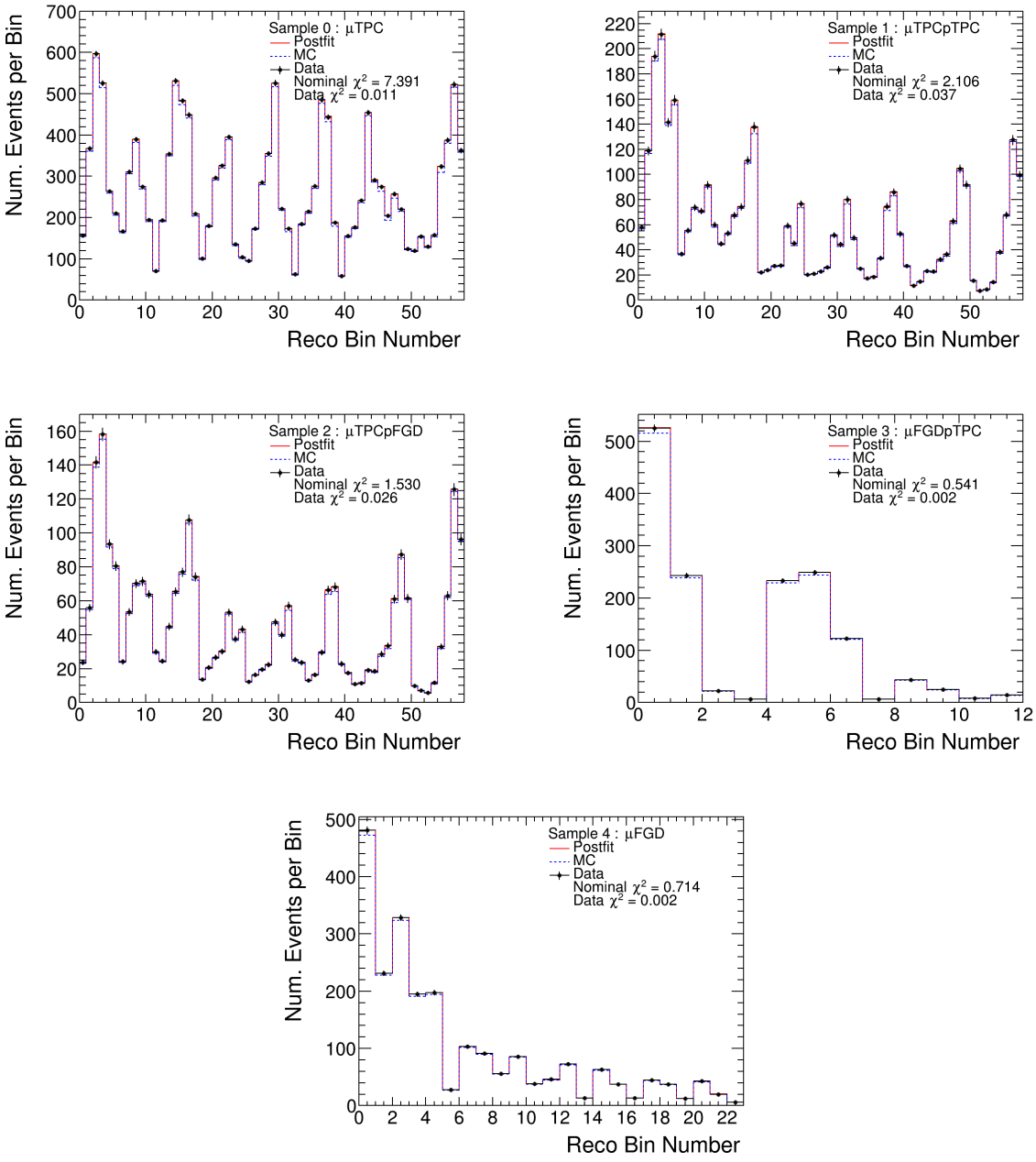

Figure 7.64: Pre/post-fit reconstructed event plots for the fit to varied horn alignment, ND280 signal samples only.

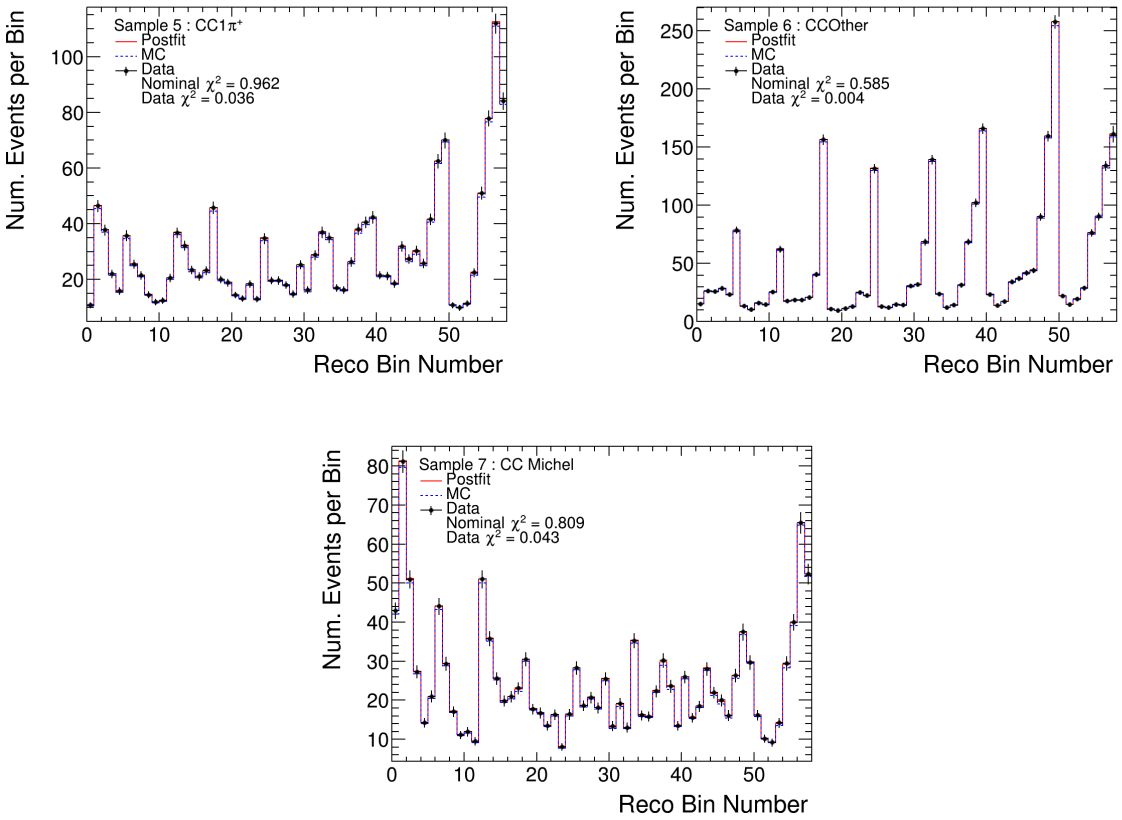

Figure 7.65: Pre/post-fit reconstructed event plots for the fit to varied horn alignment, ND280 sideband samples only.

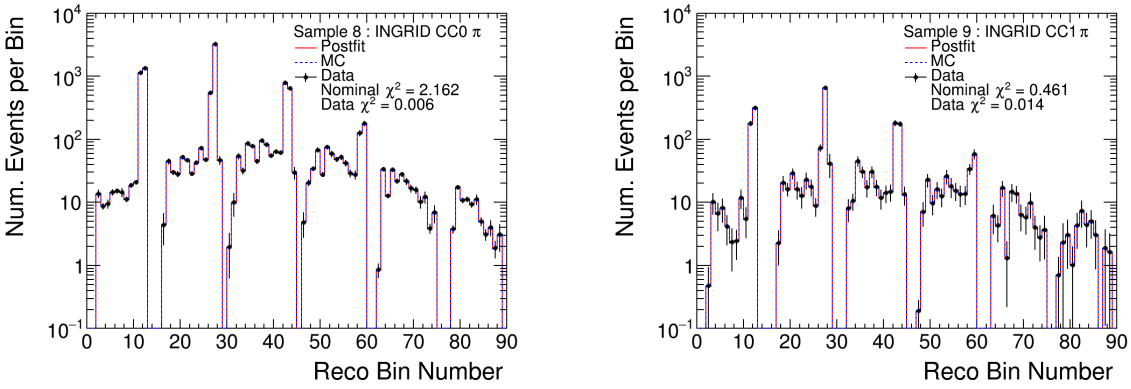

Figure 7.66: Pre/post-fit reconstructed event plots for the fit to varied horn alignment, INGRID samples only.

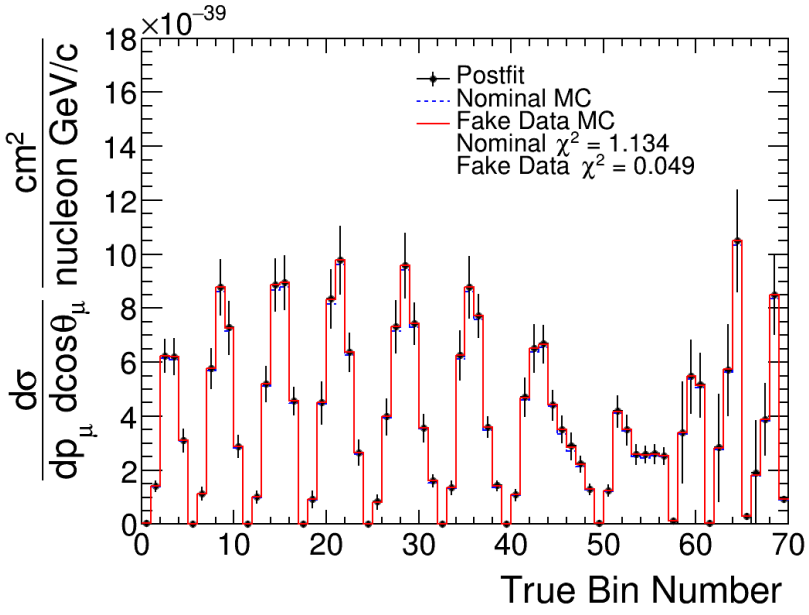

Figure 7.67: Pre/post-fit cross-section plot showing all analysis bins (in true kinematics) for the fit to varied horn alignment.

7.12 Fit failure modes

Through validating and developing the analysis a number of common failure modes and their signs were identified and are described here. These fit failure modes are mostly related to running the minimization routine, and in almost all cases need the fit to be processed again. The most common failure mode is for the Hessian matrix to be forced positive definite after the minimization routine is finished. The Hessian (and the covariance matrix) are required to be positive definite by definition, and is required for the minimization algorithm to work. To that end, if the Hessian is not positive definite after the error estimation, it is forced positive definite by adding a constant to the diagonal of the matrix. Since the Hessian is inverted to give the covariance matrix, adding a constant to the diagonal will reduce the diagonal covariance entries corresponding to artificially reduced errors. This can usually be remedied by adjusting the minimization routine parameters and reprocessing the fit.

The covariance matrix returned by HESSE is calculated using the method of finite differences assuming the likelihood surface is a multivariate Gaussian. If the likelihood surface near the post-fit values is not smooth, it can trick HESSE and give incorrect estimates for the post-fit error. This can be easily diagnosed through unrealistically small error bars on a given parameter or cross section bin, and confirmed by examining the likelihood scan of the parameter in question. An example of a smooth and broken likelihood scan is shown in Fig. 7.68.

7.13 Summary

Overall the fit performed well in every validation test described in this chapter. The fit is very capable at identifying and matching single changes to the system, whether that is a systematic change to the flux model or a physics motivated change of the background model. The post-fit cross section always preferred the pseudo data input (for non-Asimov fits) as indicated through the χ^2 values. These validation tests will be used as the baseline for the fit performance, and to gauge the validity of the real data fit through a detailed unblinding

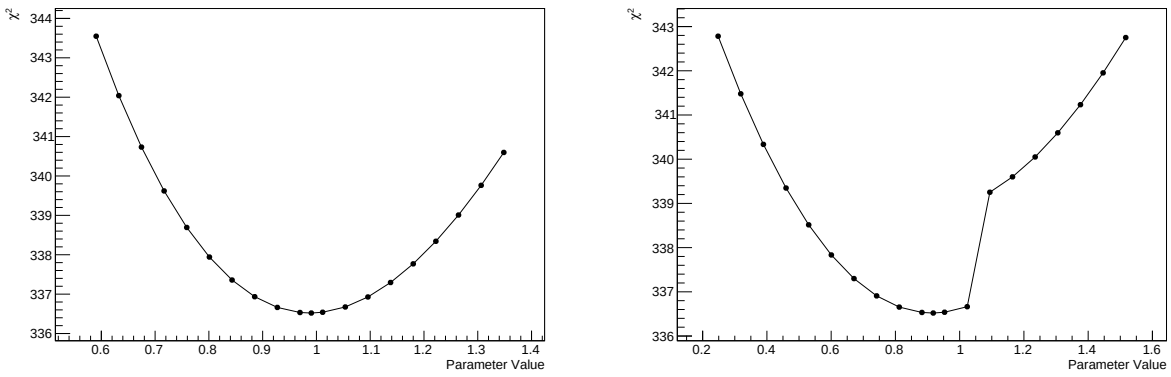

Figure 7.68: Examples of a good likelihood scan (left) and a bad likelihood scan (right) on a single parameter. A good likelihood scan should be approximately Gaussian with no discontinuities.

procedure.

The flux parameters show the expected improved constraint when using samples from both detectors compared to using a single detector, with the ND280 samples providing the better constraint at low energy (less than 1 GeV) and the INGRID samples providing the better constraint at high energy (greater than 1 GeV). The total flux constraint estimated using the Asimov fits gives a reduction in the flux errors for each bin of about one to two percentage points. In general the behavior of the cross section systematic parameters in the fit is driven primarily by the ND280 samples over the INGRID samples which is due to the vastly higher number of events in the ND280 samples compared to the INGRID samples. All the systematic parameters stayed within their prior 1σ uncertainty band, with a few exceptions that were expected given the magnitude of the difference between the nominal MC and the pseudo data (for example the arbitrary neutrino energy variation in Sec. 7.5).

These validation tests illustrate the expected behavior of the fit and will be used to identify possible failure points when running the real data fit. The fit to real data will proceed in two stages, a fit using only the sideband samples, and a fit using all data samples if there are no issues with the sideband only fit. The signs of problems with the fit fall broadly in the following categories: mechanical problems with the minimization routine, issues with the systematic parameters, large differences between post-fit and data in the reconstructed

event distributions, and issues in the error propagation procedure. The mechanical problems have been already discussed in Sec. 7.12 and generally refer to cases where the errors are not calculated correctly. Based on the validation studies and prior guidelines used by T2K, if any of the systematic parameters were pulled outside their prior error band the data and MC distributions should be analyzed for a possible cause of the pull. This is not necessarily a sign of a failed fit as the parameter pull could be explained by a feature in a sideband sample, but would need to be verified.

CHAPTER 8

RESULTS

This chapter presents the results of fits to real data for both ND280 and INGRID single detector configurations and the full joint detector configuration. The results are presented in a similar format to the validation studies in Chapter 7 along with a discussion of the results. The purpose of running single detector configuration fits is to have a reference for how the joint fit compares to fitting each detector by itself. This also allows for more direct comparisons to the results of previous analyses which were used as the foundation for this measurement [3, 5].

8.1 Reconstructed event rate

This section presents the reconstructed data for each sample using the same presentation as Chapter 4. This is the input to the fit and shows the differences between the nominal MC prediction and the measured data before the fit.

8.1.1 ND280 event samples

Overall, the nominal MC prediction for the ND280 samples is generally good with the normalization and shape across all samples, but there are several noticeable features which will influence the performance of the fit. Three of the four the signal samples which tracked the muon using the TPC (shown in Fig. 8.1) show a deficit in forward going muons, while the samples which tracked the muon using the FGD (shown in Fig. 8.2) do not show the same clear deficit at forward angle. The TPC samples each show both an excess and deficit of events compared to the MC prediction around the peak of the momentum distribution, while both of the FGD samples show a fairly large excess of data events at the momentum peak, which may be indicating some detector dependent effects in the MC prediction.

The nominal MC clearly over predicts the number of events in the CC-1π sideband

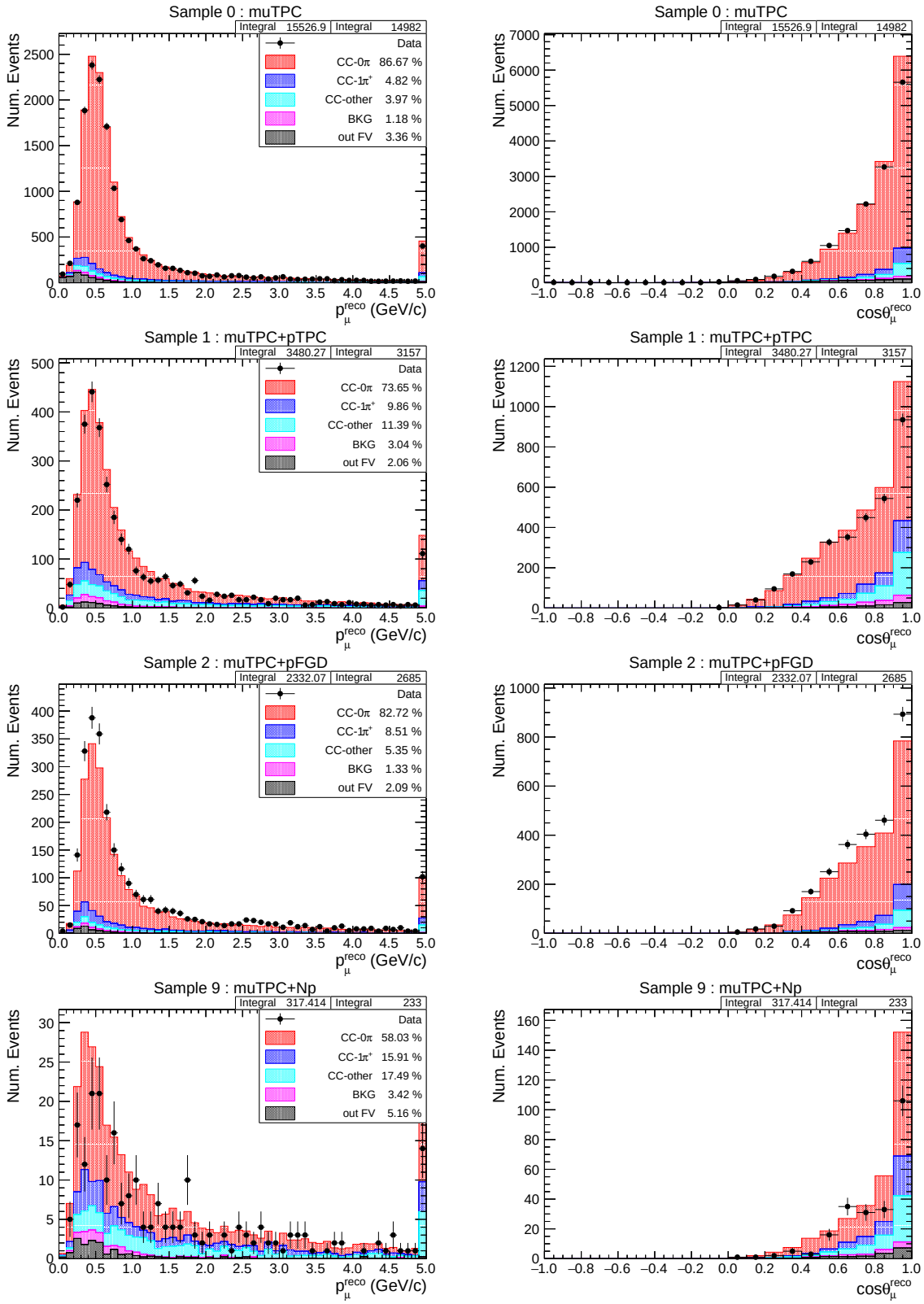

Figure 8.1: Event distribution for measured data and MC prediction in reconstructed muon momentum and angle for the ND280 signal samples with a muon track in the TPC stacked by true topology. The purity of each topology is listed in the legend. The last bin for muon momentum contains all events with momentum greater than 5 GeV/c.

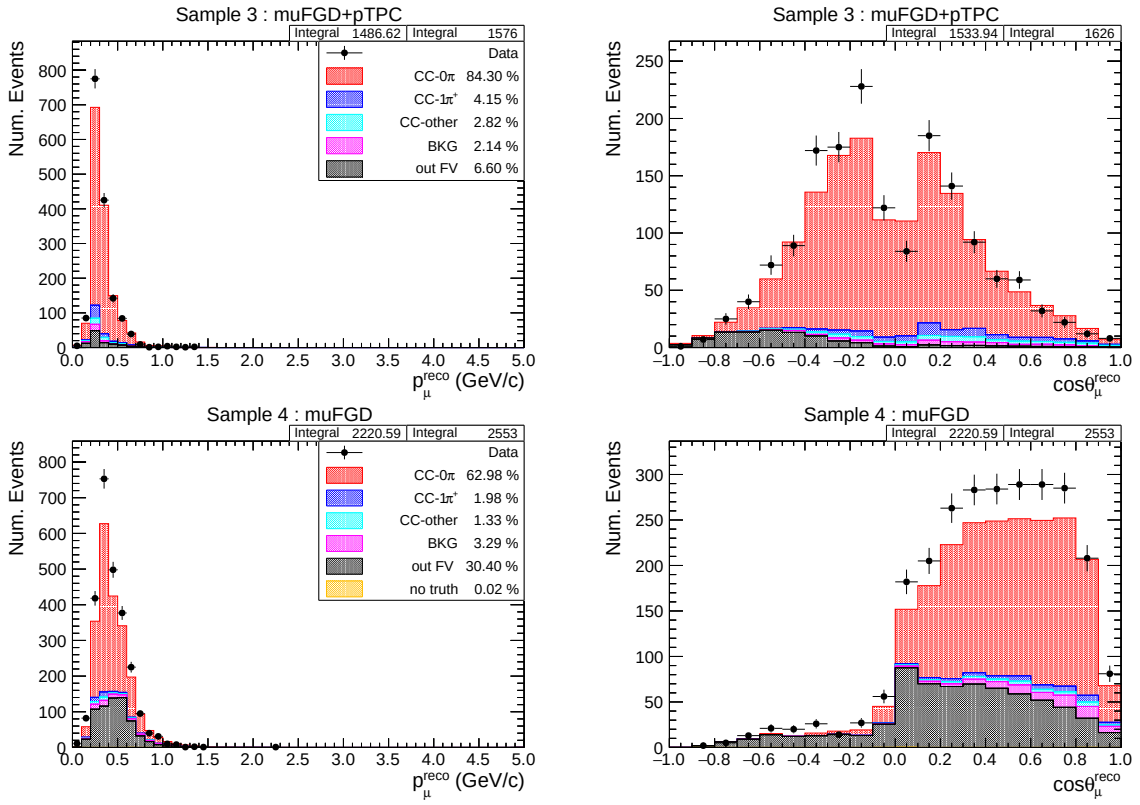

Figure 8.2: Event distribution for measured data and MC prediction in reconstructed muon momentum and angle for the ND280 signal samples with a muon track in the FGD stacked by true topology. The purity of each topology is listed in the legend. The last bin for muon momentum contains all events with momentum greater than 5 GeV/c.

while under predicting the number of events in the CC-Other sideband (both shown in Fig. 8.3), and both effects are more pronounced at the peak of the momentum distribution. Additionally the same over and under prediction is seen at forward going muons for both sideband samples. Finally the CC-Michel sample sees a slight excess at the momentum peak, but the overall normalization is much closer to the nominal prediction.

8.1.2 INGRID event samples

The INGRID signal samples (shown in Fig. 8.4) show a clear excess of signal events in data compared to the nominal MC prediction for both stopping and through-going muons. This excess is concentrated with more forward going events, particularly in the full sample including through going events.

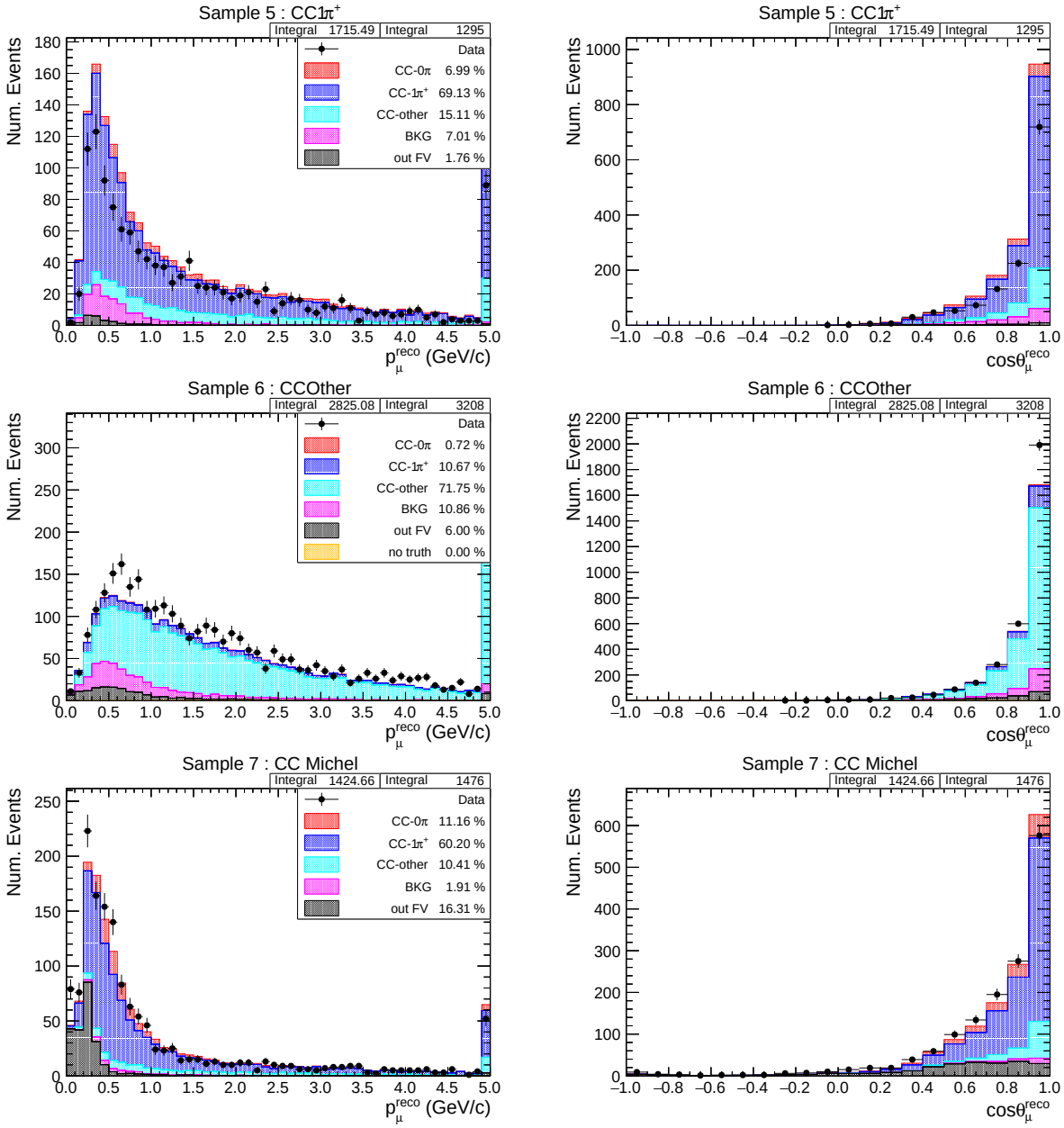

Figure 8.3: Event distribution for measured data and MC prediction in reconstructed muon momentum and angle for the ND280 sideband samples stacked by true topology. The purity of each topology is listed in the legend. The last bin for muon momentum contains all events with momentum greater than 5 GeV/c.

The INGRID sideband samples (shown in Fig. 8.5) show a clear deficit of events across the kinematic phase space, with the exception of the lowest muon momentum/range bin. The drastic difference between data and MC is being investigated and is almost certainly due to a bug in the processing of the MC files.

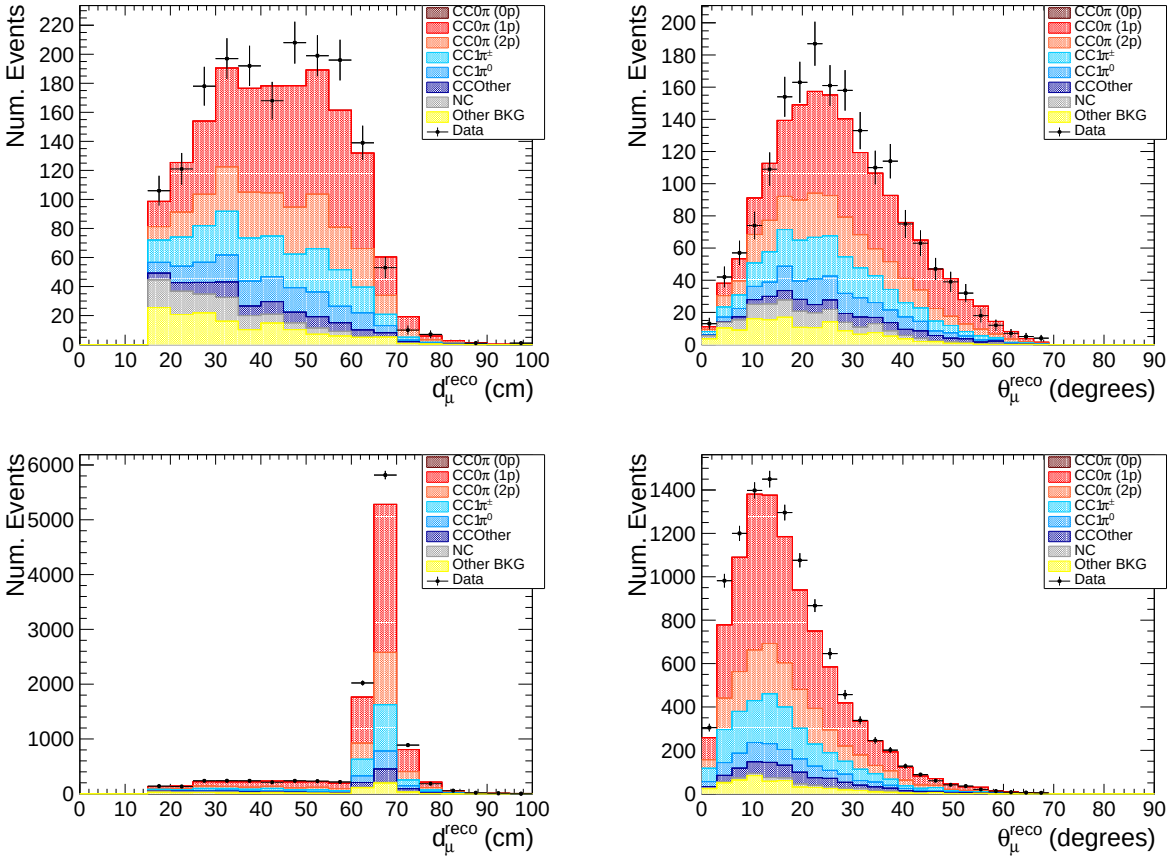

Figure 8.4: Event distribution for measured data and MC prediction in reconstructed muon equivalent distance in iron and angle for the INGRID (early) stopping signal samples (top) and all INGRID signal samples (bottom) stacked by true topology.

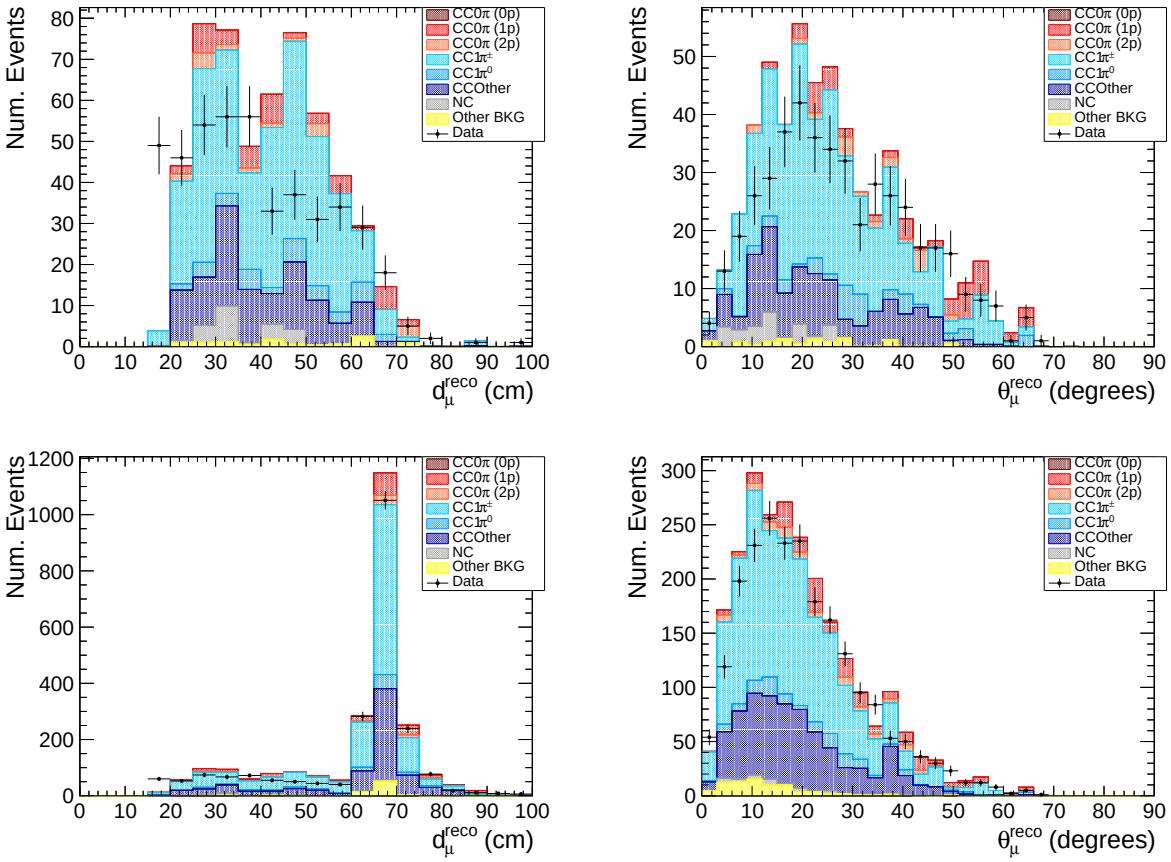

Figure 8.5: Event distribution for measured data and MC prediction in reconstructed muon equivalent distance in iron and angle for the INGRID (early) stopping sideband samples (top) and all INGRID sideband samples (bottom) stacked by true topology.

8.2 ND280 only data fit

The ND280-only data fit converged correctly and the pre- and post-fit results are presented in this section, with the final post-fit reconstructed-level χ^2 listed in Tab. 8.1. Overall the post-fit parameters and the extracted cross section look reasonable with no indications of a mechanical failure (cf. Sec. 7.12). Each reconstructed event sample saw an improvement in the goodness-of-fit metric, with most of the improvement coming in the μTPC sample, as shown in Fig. 8.7 and Fig. 8.8. The samples where the muon was tracked with the TPC all achieved a better fit than the samples where the muon was tracked with the FGD using the χ^2 per degree of freedom metric. This may be an indication of some difference in modeling of the detector performance between the TPC and FGD, or a difference in modeling the high and backward angle muons versus the forward going muons.

The post-fit preferred an overall increase in the flux parameters, resulting in an 8.45% increase in the total flux integral, which corresponds to about a 1σ change according to the total integrated flux error. The energy parameters above 1 GeV had a smaller increase (or even decreased) relative to nominal compared to the parameters below 1 GeV. The parameters around the flux peak (600 MeV) saw the largest increase, about 10% relative to the nominal prediction, and are the majority contributors to the increase in the flux integral. Because of the high correlations among the flux parameters the impact of the parameter pulls is a small contribution to the total χ^2 and is compatible with the nominal flux prediction.

The post-fit neutrino interaction parameters in general stayed within their prior 1σ error bands, with several parameter pulls due to the data in the sideband regions. The CCDIS normalization parameter is pulled high to reflect the excess in data in the CC-Other sideband, and the CC-1π normalization parameters seeing a slight decrease to reflect the deficit in the CC-1π sideband. The large decrease of the CC coherent normalization to nearly zero is expected as the nominal MC used in the analysis is known to over predict the CC coherent cross section (consistent with MINERvA data [108]). Finally, the post-fit preferred to lower the MAQE and 2p2h normalization parameters which will primarily reduce the number of

signal events, and was probably to counteract the higher flux parameters (these parameters are moderately anti-correlated in the post-fit correlation matrix). Similar to the flux parameters, the impact of the parameter pulls for the neutrino interaction parameters is a small contribution to the total χ^2 and is compatible with the nominal model.

The extracted cross section as a function of muon kinematics shown as a 1D function of muon momentum for each muon angle bin is shown in Fig. 8.10 (note the last momentum bin to 30 GeV is not shown, Fig. G.1 and Fig. G.2 in Appendix G contain the last bin). The extracted cross section is slightly lower compared to the nominal MC prediction, particularly at forward going angles (with a cosine greater than 0.90), possibly indicating a suppression of events at low momentum transfer (Q^2). The χ^2 per degrees of freedom for the nominal NEUT model compared to the extracted cross section is 1.992, which indicates not particularly good agreement between the model and data (using the approximation that the number of degrees of freedom is equal to the number of bins).

Source	χ^2	DOF	χ^2/ DOF
μTPC sample	16.101	58	0.278
μTPC+pTPC	47.902	58	0.826
μTPC+pFGD	41.646	58	0.718
μFGD+pTPC	19.354	12	1.613
μFGD	32.108	23	1.396
CC-1π	57.694	58	0.995
CC-Other	62.953	58	1.085
CC-Michel	84.148	58	1.451
Flux parameters	3.200	20	0.160
Detector parameters	19.612	383	0.051
Xsec parameters	13.886	21	0.661
Statistical	361.905	–	–
Systematic	36.699	–	–
Total	398.604	–	–

Table 8.1: Breakdown of the post-fit χ^2 contribution for the ND280 only data fit at the reconstructed event level and for the systematic parameter penalty.

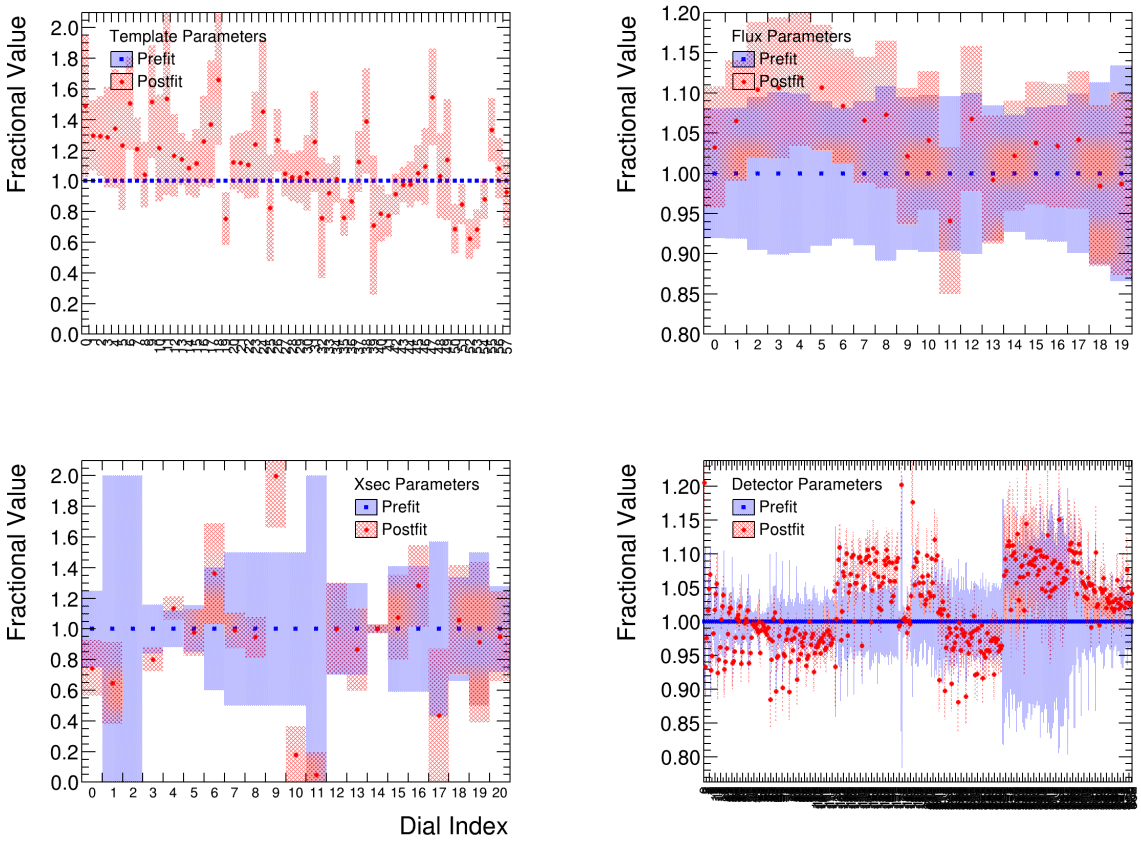

Figure 8.6: Pre/post-fit parameter plots for the ND280 only data fit. Blue is prefit and red is postfit, and the fractional changes and errors are presented.

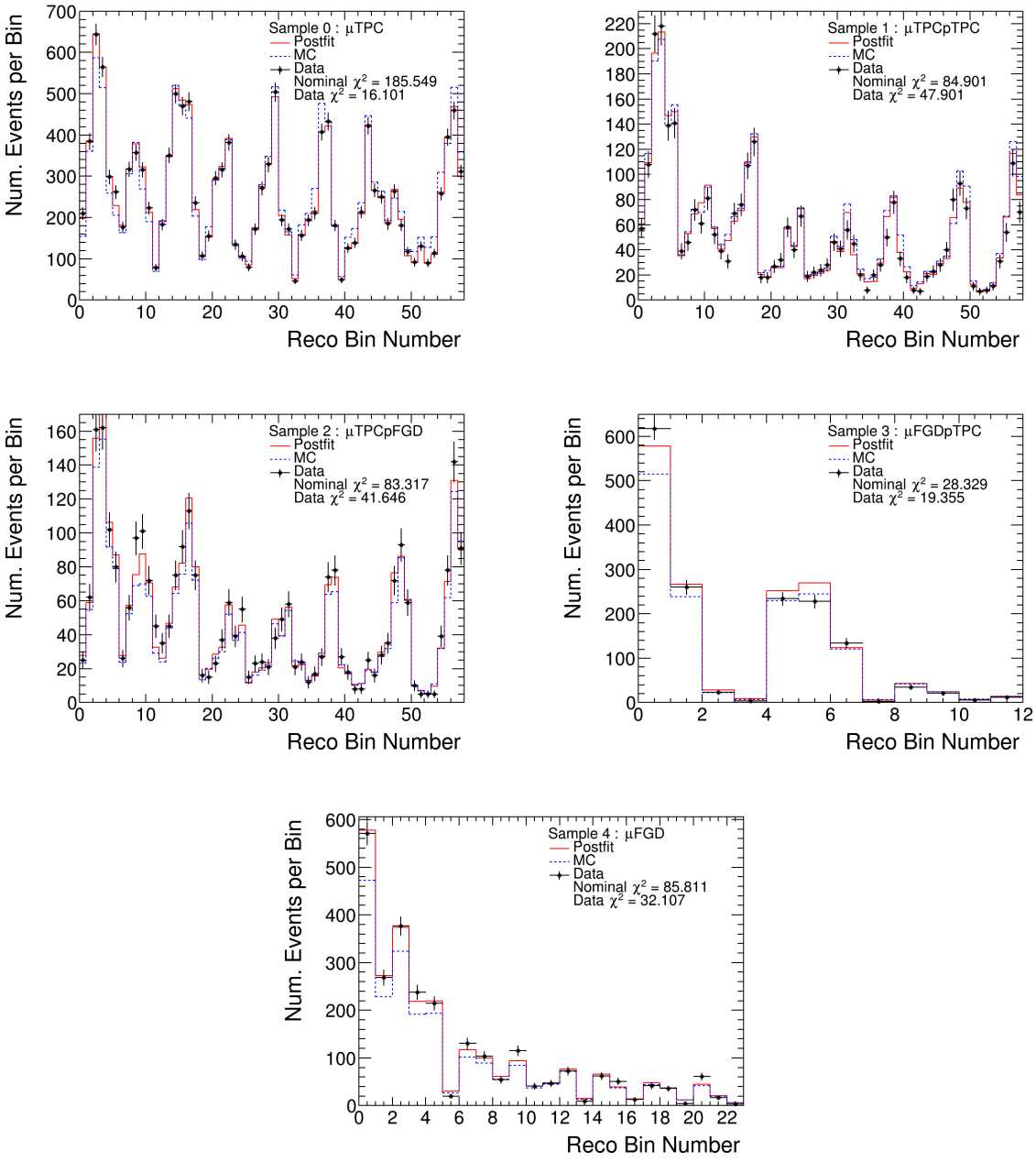

Figure 8.7: Pre/post-fit reconstructed event plots for the ND280 only data fit, signal samples only.

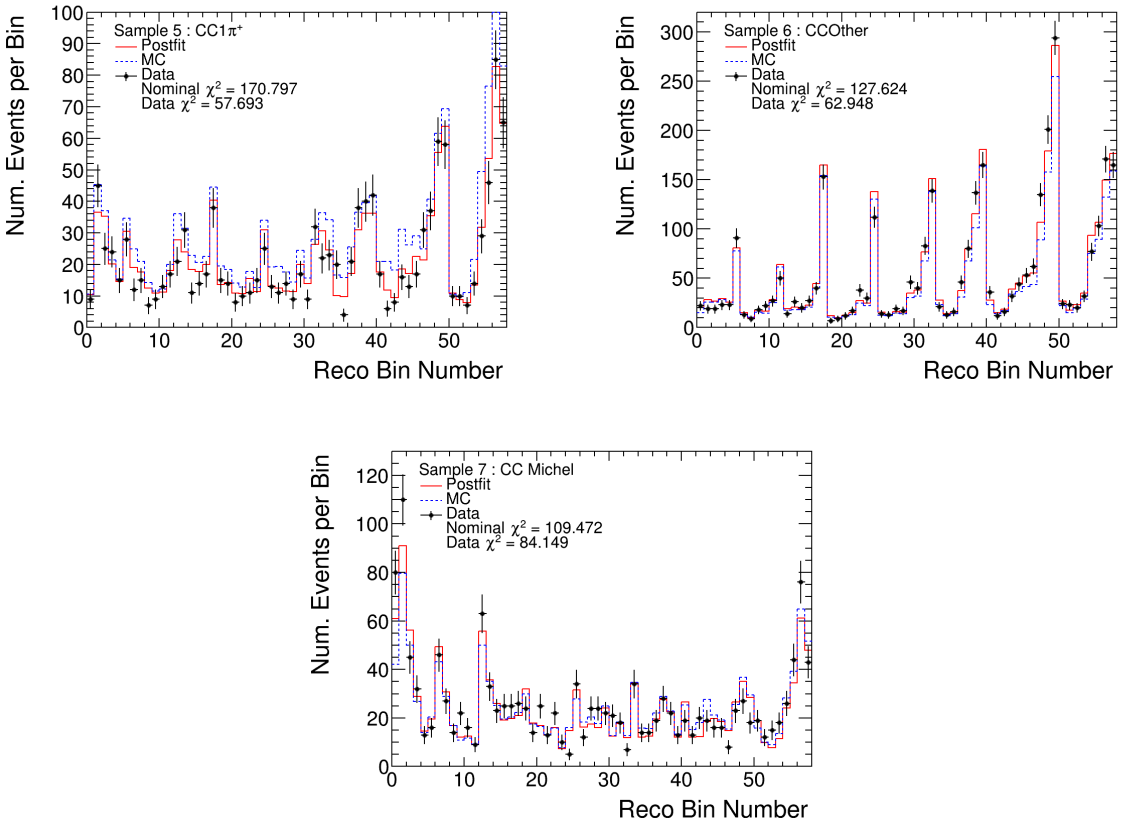

Figure 8.8: Pre/post-fit reconstructed event plots for the ND280 only data fit, sideband samples only.

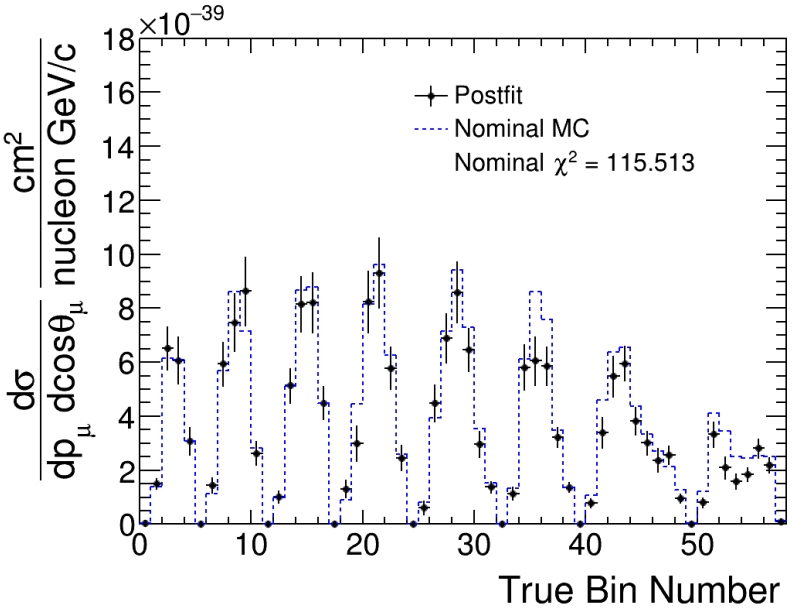

Figure 8.9: Extracted cross-section plot showing all analysis bins (in true kinematics) for the ND280 only data fit. Approximating the number of bins (58) as the degrees of freedom gives 1.992 χ^2/ DOF.

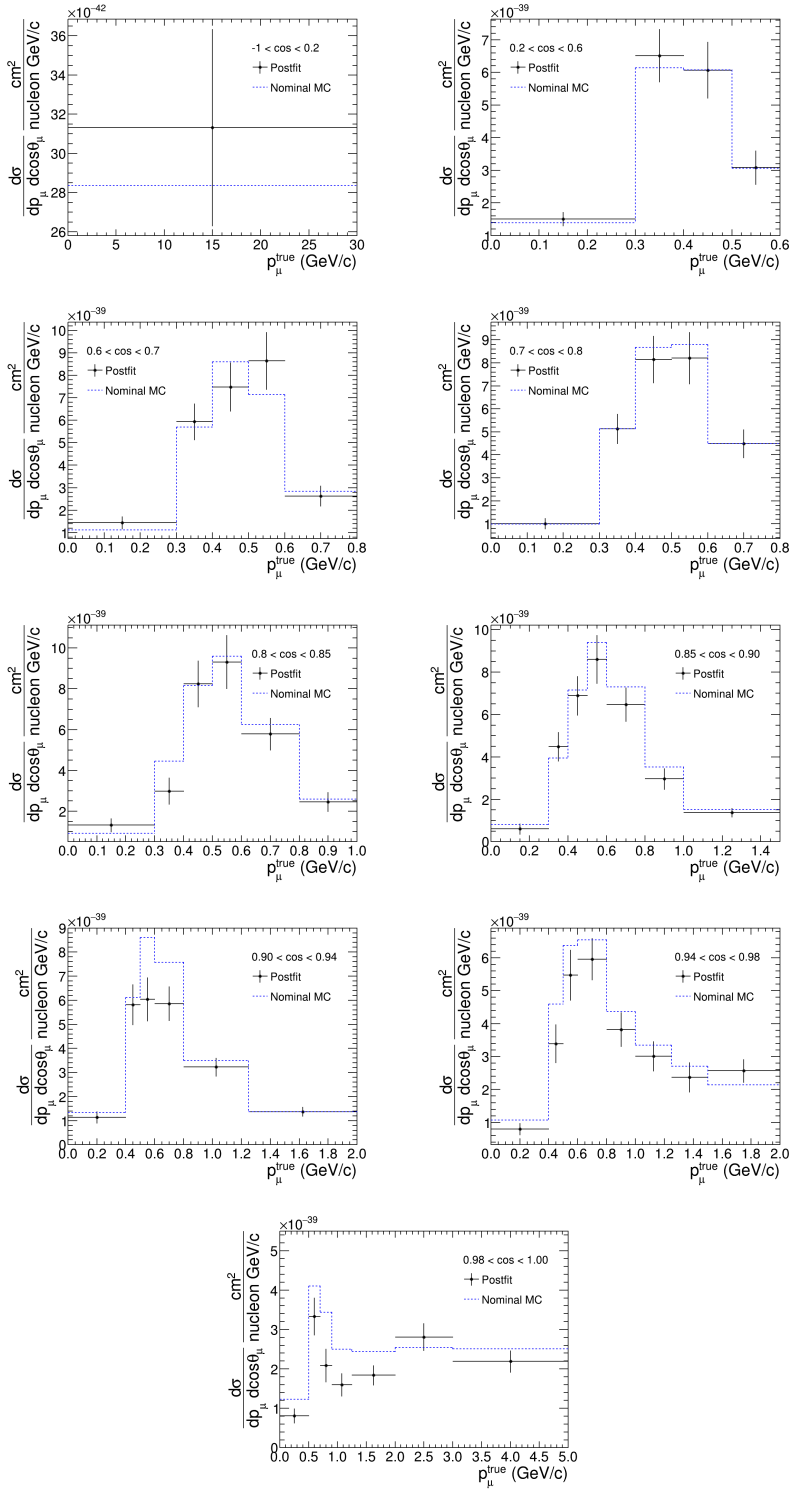

Figure 8.10: Extracted cross section for the ND280 only data fit compared to the nominal MC prediction as a function of muon momentum for slices of muon angle. The last momentum bin to 30 GeV is not shown, and note the y-axis is not the same across all the plots.

8.3 INGRID only data fit

The INGRID-only data fit converged correctly and the pre- and post-fit results are presented in this section, with the final post-fit χ^2 listed in Tab. 8.2. Overall the post-fit parameters and the extracted cross section look reasonable with no indications of a mechanical failure (cf. Sec. 7.12). Both reconstructed event sample saw an improvement in the goodness-of-fit, with the signal sample improving more than the sideband sample as expected, as shown in Fig. 8.12.

The post-fit flux parameters all stayed within 3% of their nominal values, resulting in a 0.8% decrease in the total flux integral, leaving the flux largely unchanged (especially compared to the ND280 only fit). The flux parameters show a slight increase at lower energy around 600 MeV and higher energy around 3 GeV and above, while showing a slight decrease around the INGRID flux peak around 1 GeV. Because of the high correlations among the flux parameters the impact of the parameter pulls is a small contribution to the total χ^2 and is compatible with the nominal flux prediction.

The post-fit neutrino interaction parameters all stayed within their prior 1σ error bands with the exception of the MAQE parameter and are overall not pulled as far as the ND280 only fit. The CC-1π normalization parameters had a large decrease to reflect the deficit of events seen in the sideband region, while the CCDIS normalization parameter stayed very close to its nominal value. The large decrease of the CC coherent normalization to nearly zero is expected as the nominal MC used in the analysis is known to over predict the CC coherent cross section (consistent with MINERvA data [108]) and is consistent behavior with the ND280-only data fit.

The extracted cross section as a function of muon kinematics shown as a 1D function of muon momentum for each muon angle bin is shown in Fig. 8.14 (note the last momentum bin to 30 GeV is not shown, Fig. G.1 and Fig. G.2 in Appendix G contain the last bin). The extracted cross section is compatible with the nominal MC prediction to within 2σ error bars and is hard to discern any trends given the small number of measured kinematic bins.

Source	χ^2	DOF	χ^2/ DOF
CC-0π	67.301	90	0.748
CC-1π	151.331	90	1.681
Flux parameters	0.474	20	0.024
Detector parameters	1.784	180	0.010
Xsec parameters	6.327	21	0.301
Statistical	218.632	–	–
Systematic	8.585	–	–
Total	227.217	–	–

Table 8.2: Breakdown of the post-fit χ^2 contribution for the INGRID only data fit at the reconstructed event level and for the systematic parameter penalty.

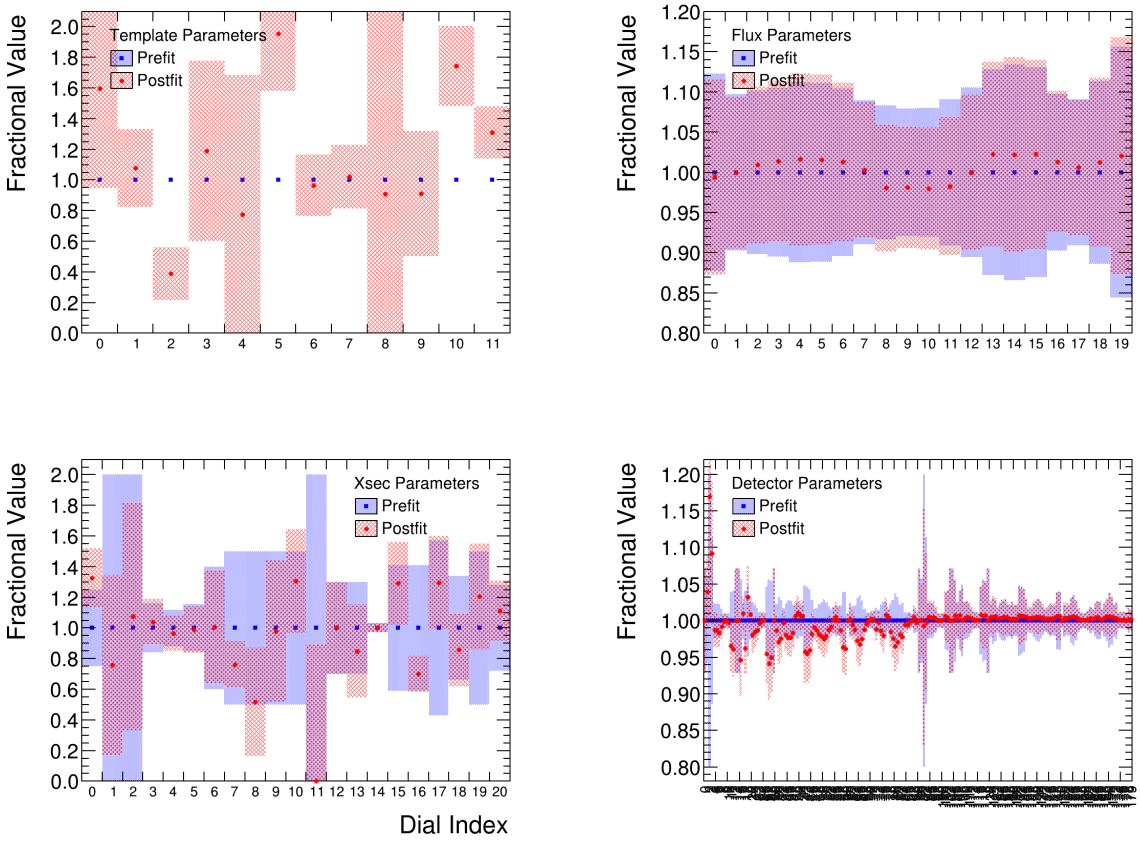

Figure 8.11: Pre/post-fit parameter plots for the INGRID only data fit. Blue is prefit and red is postfit, and the fractional changes and errors are presented.

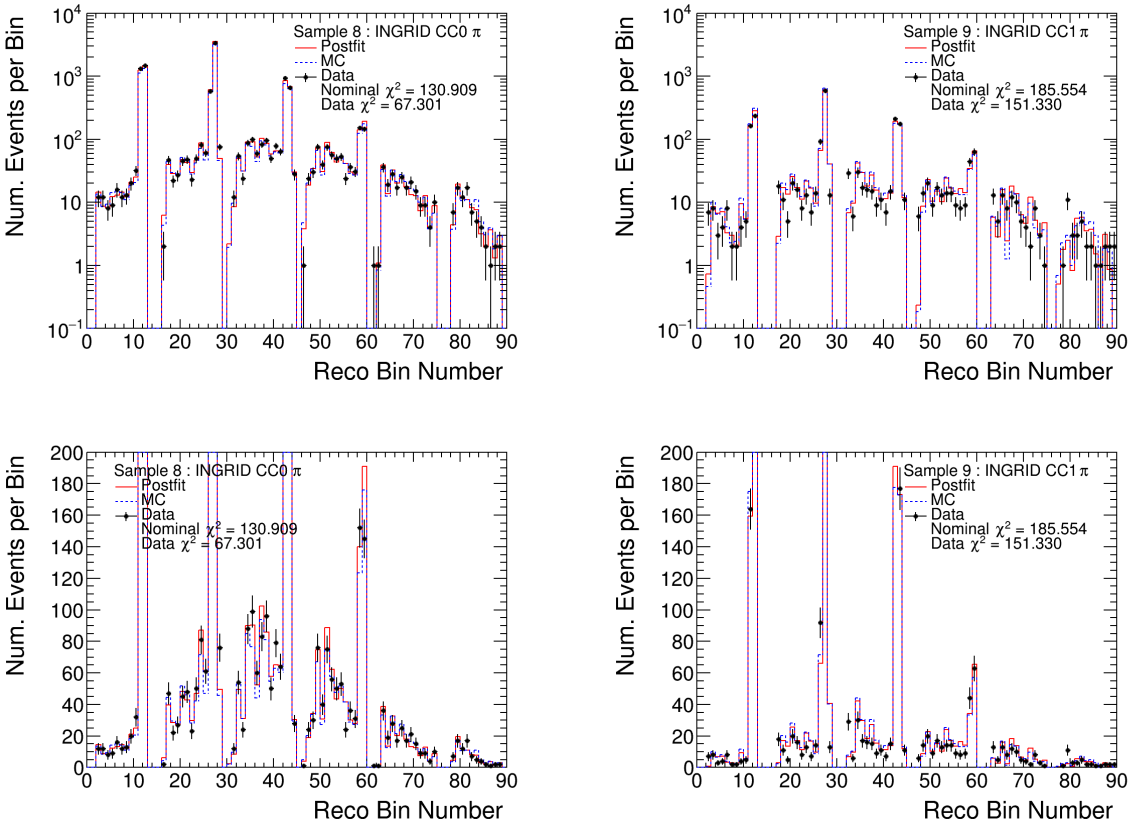

Figure 8.12: Pre/post-fit reconstructed event plots for the INGRID only data fit in both log scale (top) and linear scale (bottom) for the y-axis.

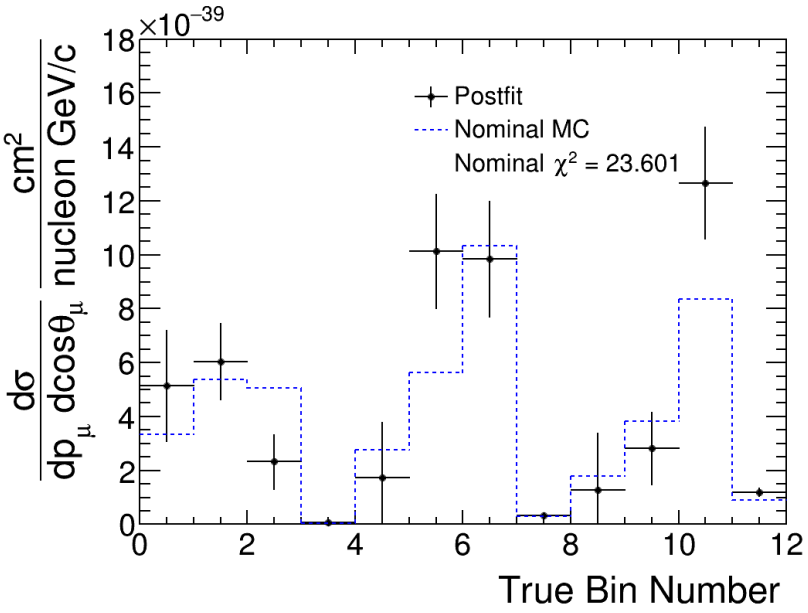

Figure 8.13: Pre/post-fit cross-section plot showing all analysis bins (in true kinematics) for the INGRID only data fit. Approximating the number of bins (12) as the degrees of freedom gives 1.967 χ^2/ DOF.

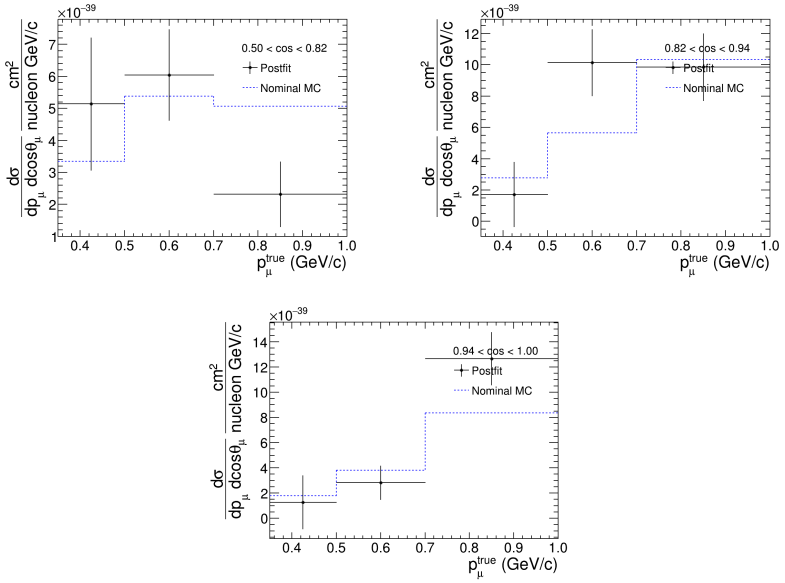

Figure 8.14: Extracted cross section for the INGRID only data fit compared to the nominal MC prediction as a function of muon momentum for slices of muon angle. The last momentum bin to 30 GeV is not shown, and note the y-axis is not the same across all the plots.

8.4 Joint data fit

The joint detector data fit converged correctly and the pre- and post-fit results are presented in this section, with the final post-fit χ^2 listed in Tab. 8.3. Overall the post-fit parameters and the extracted cross section look reasonable with no indications of a mechanical failure (cf. Sec. 7.12). Each reconstructed event sample saw an improvement in the goodness-of-fit, as shown in Fig. 8.16, Fig. 8.17, and Fig. 8.18. Compared to the single detector fits, the post-fit agreement is similar for each sample with most samples having slightly worse agreement. This slightly worse agreement is expected due to the differences in the single detector results as the joint fit had to compromise on the best-fit parameter values where ND280 and INGRID pulled in opposite directions.

The post-fit systematic parameters in general follow similar pulls to the single detector fits, and most parameters stayed within their prior 1σ error bands. The parameter pulls mostly follow the same trend as the ND280 only data fit versus the INGRID only data fit. The flux parameters are slightly closer to the nominal values and are still highly compatible with the nominal model. For the neutrino interaction parameters, the DIS and CC multipi parameters still have large pulls from the nominal values (largely matching the ND280 only fit). Similarly, the CC coherent normalization is pulled close to zero as seen in both single detector fits. Most parameters where pulled to a sort of "weighted average" where the parameter values fell in between the single detector results, with the values usually closer to the ND280 only value. In general, the fit prefers the ND280 values due to ND280 containing the majority of the events and having more samples than INGRID, but INGRID still provides a noticeable influence on the final values.

The extracted cross section as a function of muon kinematics shown as a 1D function of muon momentum for each muon angle bin is shown in Fig. 8.20 and Fig. 8.21 (note the last momentum bin to 30 GeV is not shown, Fig. G.1 and Fig. G.2 in Appendix G contain the last bin). The extracted cross section is compatible with the nominal MC prediction to within 2σ error bars and is similar to the single detector fit results with the INGRID bins

showing a larger impact from the joint fit. The χ^2 per degree of freedom (using 66.4 degrees of freedom from Sec. 7.4) for how well the nominal MC describes the data is slightly worse for the combined fit than either single detector fit at 2.483 (versus ~ 2 for the individual fits), and may indicate some deficiency in the model to predict both distributions taking into account the correlations between the detectors. The difference between the ND280-only single detector fit and the joint fit extracted cross section appears to be a fairly constant normalization change, with the joint fit preferring a larger cross section in nearly every bin.

Source	χ^2	DOF	χ^2/ DOF
μTPC sample	18.525	58	0.319
μTPC+pTPC	49.183	58	0.848
μTPC+pFGD	42.384	58	0.731
μFGD+pTPC	18.264	12	1.522
μFGD	32.976	23	1.434
CC-1π	57.746	58	0.996
CC-Other	67.566	58	1.165
CC-Michel	88.039	58	1.518
INGRID CC-0π	65.620	90	0.726
INGRID CC-1π	175.882	90	1.954
Flux parameters	3.309	40	0.083
Detector parameters	21.537	563	0.38
Xsec parameters	8.909	21	0.424
Statistical	616.185	–	–
Systematic	33.485	–	–
Total	649.670	–	–

Table 8.3: Breakdown of the post-fit χ^2 contribution for the joint data fit at the reconstructed event level and for the systematic parameter penalty.

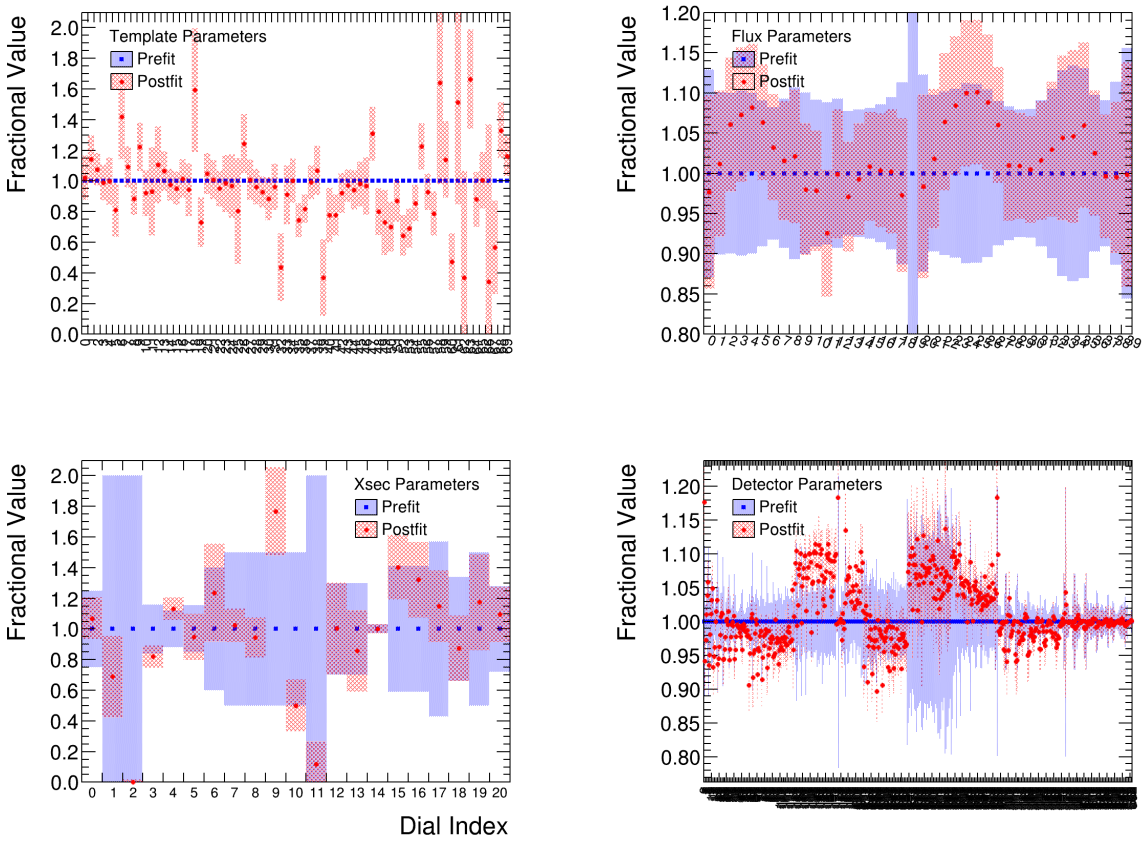

Figure 8.15: Pre/post-fit parameter plots for the joint data fit. Blue is prefit and red is postfit, and the fractional changes and errors are presented.

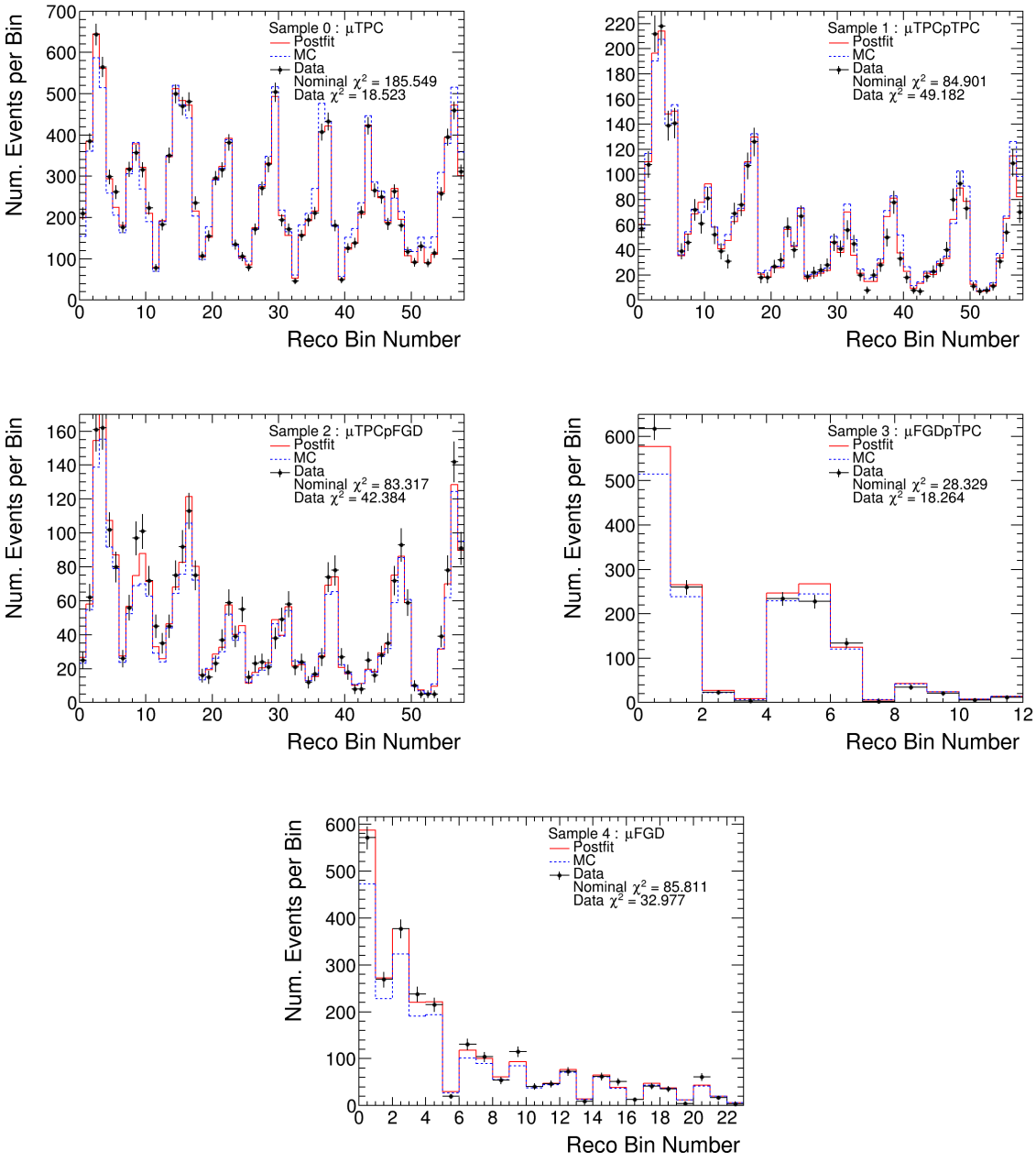

Figure 8.16: Pre/post-fit reconstructed event plots for the joint data fit, ND280 signal samples only.

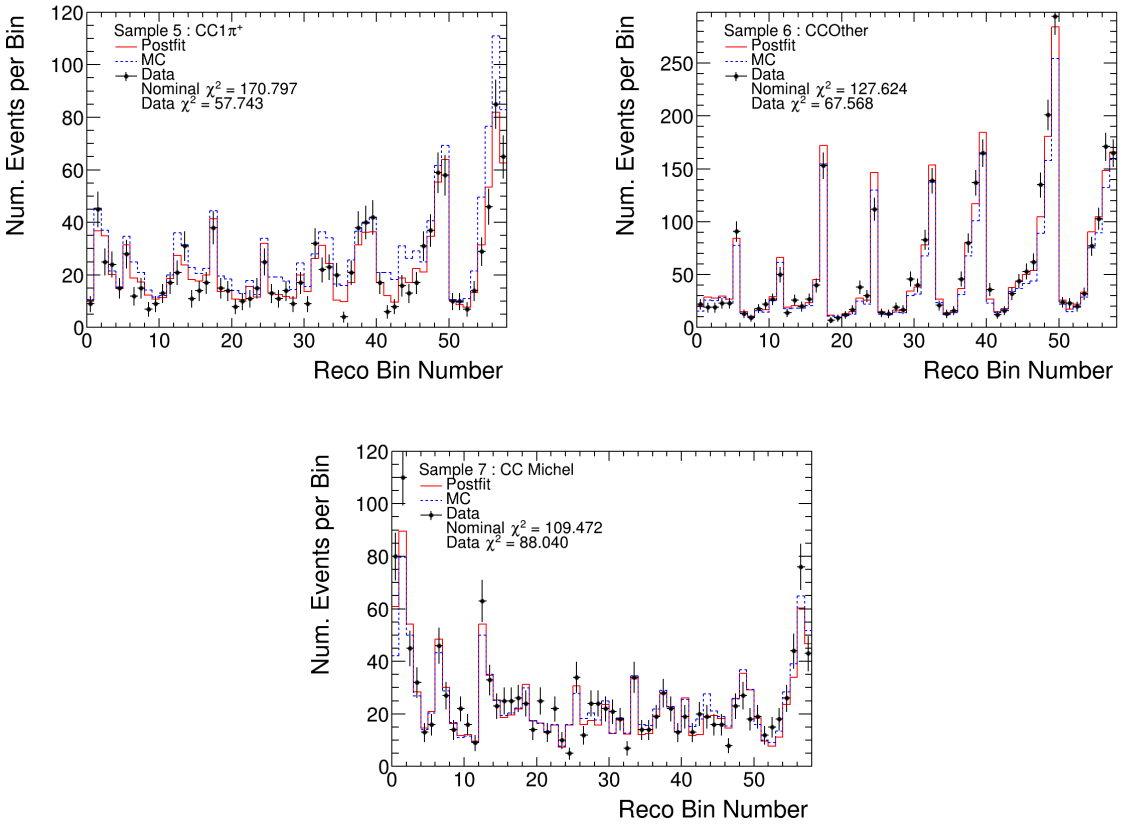

Figure 8.17: Pre/post-fit reconstructed event plots for the joint data fit, ND280 sideband samples only.

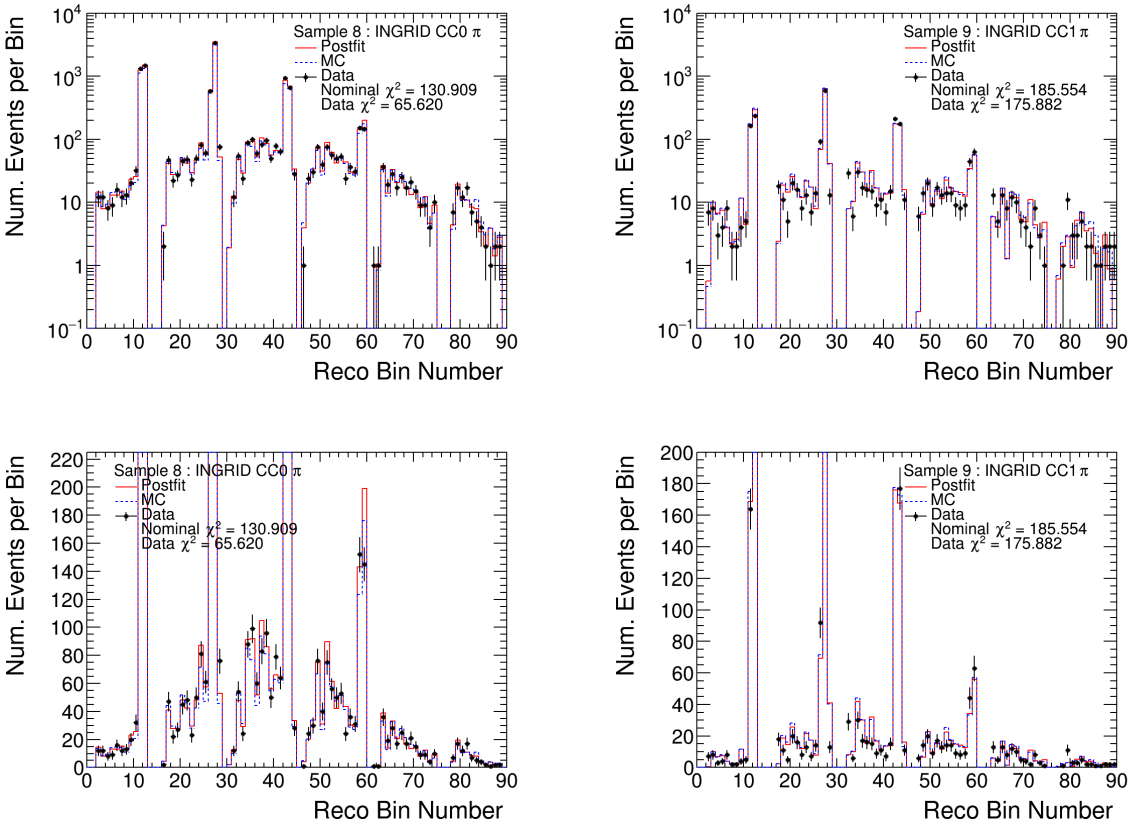

Figure 8.18: Pre/post-fit reconstructed event plots for the joint data fit, INGRID samples only in both log scale (top) and linear scale (bottom) for the y-axis.

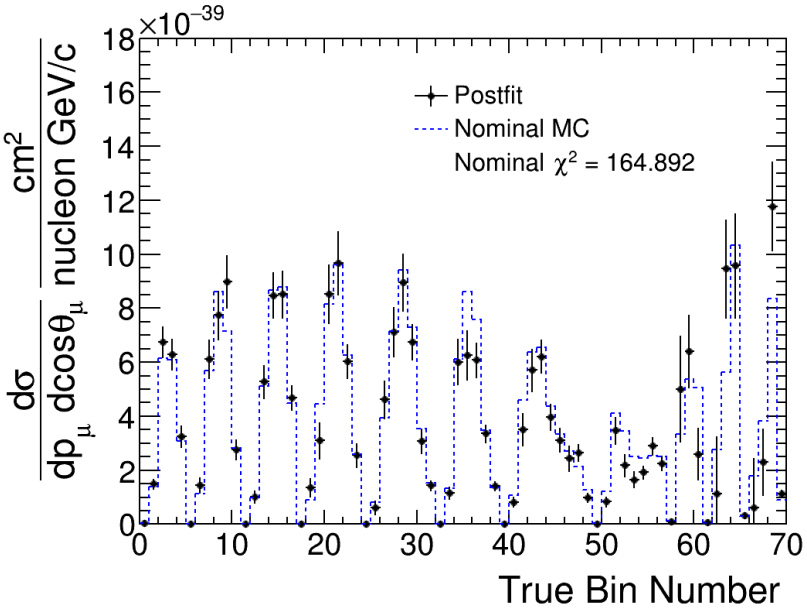

Figure 8.19: Extracted cross-section plot showing all analysis bins (in true kinematics) for the joint data fit where ND280 is the first 58 bins and INGRID are the last 12 bins. The number of degrees of freedom is 66.4 (cf. Sec. 7.4) which gives 2.48 χ^2/ DOF.

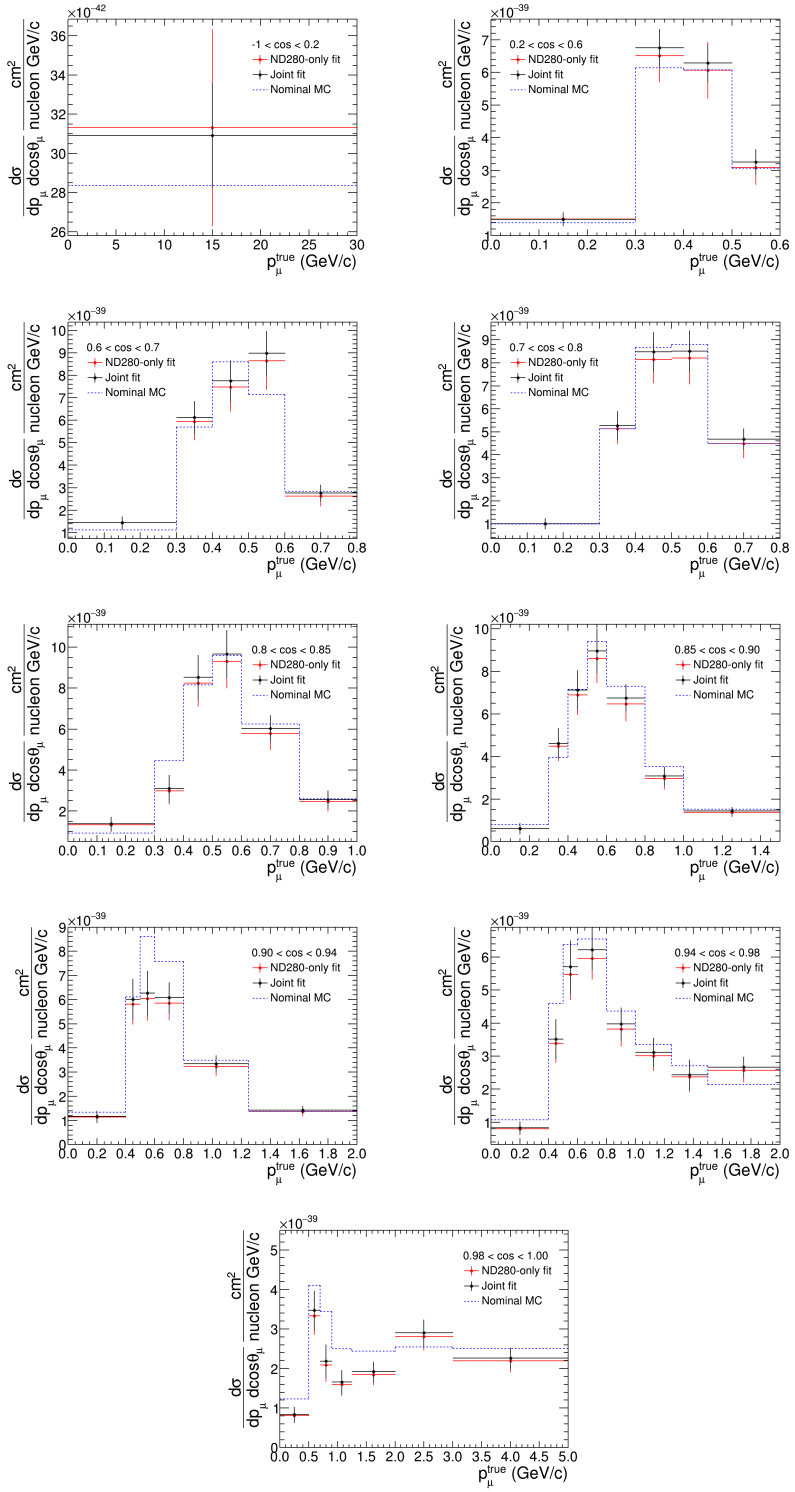

Figure 8.20: ND280 extracted cross section bins for joint data fit compared to the nominal MC prediction as a function of muon momentum for slices of muon angle. The last momentum bin to 30 GeV is not shown, and note the y-axis is not the same across all the plots.

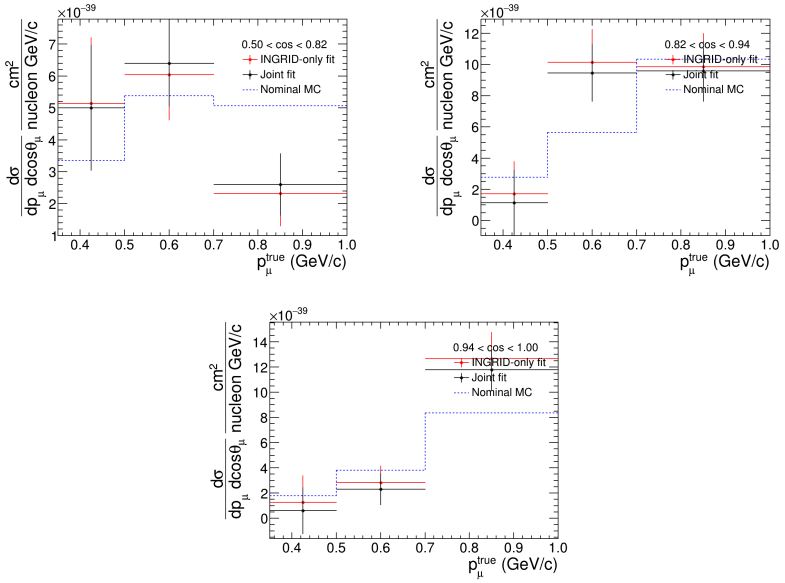

Figure 8.21: INGRID extracted cross section bins for the joint data fit compared to the nominal MC prediction as a function of muon momentum for slices of muon angle. The last momentum bin to 30 GeV is not shown, and note the y-axis is not the same across all the plots.

8.5 Future work

The joint analysis technique is a powerful one for both reducing errors through correlated uncertainties (such as correlations in the flux model) and for extracting more information out of the individual analyses by correlating the result. The joint fit unifies the statistical fit and the treatment of systematic uncertainties of multiple data sets allowing for a consistent interpretation of the results for both detectors. How theoretical models succeed and fail to describe the data at each detector independently and combined is an interesting way to isolate what the model is doing well and is doing poorly, and possibly highlight how the detector may be influencing the result. Going forward new joint analyses can be performed in T2K using on-/off-axis data for water targets or for combinations of neutrino and anti-neutrino data. New detectors at 1.5 degrees off-axis are now taking data using the T2K neutrino beam, and the new data could be used to provide a third off-axis angle for future joint analyses allowing for an even stronger constraint on the flux model.

The result presented in this thesis will be prepared as an official T2K publication and result along with a data release for use by external experiments and theorists. This analysis is currently in T2K internal review undergoing final quality checks, and the results presented in this thesis are preliminary. Internally on T2K, this result will be compared to the model tune used by the oscillation analysis. The comparisons will be particularly interesting since the model tuned used by the oscillation analysis does not include data from INGRID. Additionally, this result will be compared to a wide variety of other Monte Carlo and theoretical predictions (such as NuWro and GENIE) to aid in the neutrino interaction model development for T2K.

8.6 Conclusions

The analysis presented in this thesis has produced a new measurement of the ν_μ CC-0π double differential cross section on plastic scintillator (CH) utilizing numerous updates to the individual ND280 and INGRID analyses, including more ND280 data, and has shown

a successful measurement using the joint fit technique. The disagreement between the extracted cross section and the nominal MC simulation used for neutrino interactions on T2K indicates some deficiency or a missing piece in the theoretical models used to predict the cross section. The differences between the individual and joint fits also point to additional difficulty for the interaction model to simultaneously describe the data from both detectors.

Performing joint measurements between detectors and interaction channels is the future for the T2K cross section program. This analysis is the first joint on-/off-axis measurement on T2K showcasing the performance of the joint analysis technique and provides a framework to examine how including information from all the near detectors could impact the T2K oscillation analysis. The result will be used to test the validity of the interaction models relevant for the oscillation analysis, such as the quasi-elastic, multinucleon, and resonant pion production models. Quasi-elastic and multinucleon events are responsible for most of the signal events at the T2K flux peak energy (600 MeV), and improvements are needed for multinucleon modeling and outgoing lepton–hadron correlations. The joint fit result can be used to probe the parameterization of the flux model and where it is possibly deficient. The flux uncertainty is a large systematic uncertainty contribution for neutrino cross section measurements and is still an important contribution to the oscillation analysis. Improved knowledge of neutrino interactions and the flux model is critical for current and future measurements of neutrino oscillation parameters which are gained through new measurements such as the one presented in this thesis.

APPENDICES

APPENDIX A

FIT SOFTWARE

This analysis uses the Super-xslllh fitting framework to perform the multi-dimensional likelihood fit. This is an updated/upgraded version over the original cross-section likelihood fitter used in TN-214, TN-287, TN-337, and TN-338 [3, 75, 109, 110]. The development of the code is done in a Git repository which is publicly hosted on GitLab at https://gitlab.com/cuddandr/xsLLhFitter. Documentation for the fit can be found in the repository in the docs directory or online at https://cuddandr.gitlab.io/xsLLhFitter/.

APPENDIX B

BARLOW-BEESTON

This analysis uses the Barlow-Beeston method [94, 111] to include the statistical uncertainty of finite generated Monte Carlo (MC) statistics. The Barlow-Beeston method assumes there exists some true MC value or distribution from which the generated MC sample is drawn from, and that the true value and generated value are related by a simple scaling parameter. For the case of a binned likelihood fit, assuming each bin follows an independent Gaussian distribution, there is one scaling parameter β_j for each bin j such that

$$N_j^{\text{true}} = \beta_j N_j^{\text{gen}} \tag{B.1}$$

If the scaling parameters can be determined, then the true MC value can be used in place of the generated value in the likelihood function. These scaling parameters are treated as nuisance parameters in the likelihood, adding a Gaussian penalty term to the likelihood like so

$$-2\ln\mathcal{L}_{stat} = \chi^2_{\text{stat}} = \sum_j^{\text{bins}} 2\left(\beta_j\mu_j - k_j + k_j\ln\frac{k_j}{\beta_j\mu_j} + \frac{(\beta_j-1)^2}{2\sigma_j^2}\right) \tag{B.2}$$

where β is the scaling parameter, μ is the generated MC value, σ^2 is the relative variance of the MC value[1], and k is the data for each bin j. The nominal value for each scaling parameter is defined to be one. Nominally this procedure adds extra fit parameters equal to the number of data bins, however with the assumption that each bin follows an independent Gaussian distribution, the scaling parameters can be solved for analytically by maximizing the likelihood with respect to β. Taking the partial derivative with respect to β_j and setting

[1]For weighted MC events, $\sigma^2 = \sum w_i^2 / \left(\sum w_i\right)^2$ where w_i is the weight for event i.

it to zero gives

$$\frac{\partial \ln \mathcal{L}}{\partial \beta_j} = \frac{k_j}{\beta_j} - \mu_j - \frac{(\beta_j - 1)}{\sigma_j^2} = 0 \tag{B.3}$$

which results in the following quadratic equation for β_j for each bin j

$$\beta^2 + (\mu\sigma^2 - 1)\beta - k\sigma^2 = 0 \tag{B.4}$$

where β is the scaling parameter, μ is the generated MC value, σ^2 is the relative variance of the MC value, and k is the data for each bin j. Solving the quadratic gives the following equation for β

$$\beta = \frac{1}{2}\left(-(\mu\sigma^2 - 1) + \sqrt{(\mu\sigma^2 - 1)^2 + 4k\sigma^2}\right) \tag{B.5}$$

where the negative root is non-physical. By solving for each β_j analytically, no new parameters need to be added to the fit, as β_j is calculated for each fit iteration using the equation above. This will increase the time it takes to perform each iteration of the fit, but in general this is a small impact compared to adding new parameters (additionally the calculation of β_j can be vectorized since they are independent).

APPENDIX C

REGULARIZATION

The template likelihood fit/unfolding is an example of an inverse problem, where finding the best fit parameters is an "ill-posed problem". An "ill-posed problem" is commonly defined by a problem where there are multiple/many solutions (i.e. the solution is not unique) or the solution is unstable [112]. This can arise from fit parameters with similar effects on the event distribution and from the smearing between true bins to reconstructed bins. Because events in one true bin can map to multiple different reconstructed bins, the fit can often freely raise the number of events in one true bin as long as it reduces the number of events in the adjacent true bins while still having nearly the same reconstructed distribution. This gives multiple solutions which give nearly the same χ^2 and introduces strong anti-correlations and high variance between the fit parameters.

These issues can be (partially) alleviated by increasing the number of reconstructed bins or decreasing the number of true bins, or by reducing the overlap of true bins by limiting the phase space of the selected events. This however reduces the cross section resolution or the statistical power of the measurement. One alternative method is to use regularization to impose an additional constraint on the fit motivated by the assumption that, between thin bins, cross sections (or event rates) should be relatively smooth. This is included in the fit as an additional penalty term in the χ^2 as follows:

$$-2\ln\mathcal{L}_{reg} = \chi^2_{\text{reg}} = \lambda \sum_{i}^{N-1} (c_i - c_{i+1})^2 \tag{C.1}$$

where c_i are the template weights for the i^{th} and the $i^{th}+1$ true bins and λ is the regularization strength. The regularization strength is a tunable parameter, and as $\lambda \to 0$ the fit approaches the unregularized case. This adds a penalty for having large differences in the number of events between adjacent bins relative to the input MC, or in other words it biases the result towards the shape of the input MC (but not necessarily the normalization of the

input MC).

This method or choice of regularization is known as Tikhonov regularization (L_2 regularization) or ridge regression, and aims to reduce the variance of the solution at the cost of increased bias [93, 96, 97, 102]. Other forms of regularization are possible, such as LASSO regularization and Maximum Entropy regularization which use different functional forms [93, 96], but Tikhonov regularization was chosen for this analysis for its simplicity and as a suggestion from previous T2K analyses [65]. The regularization can alternatively be implemented as a pseudo-covariance matrix penalty term as done in T2K-TN-287 [110] (and shown in Ref. [97]) which gives identical results to the implementation presented here.

The difficulty in implementing regularization in the fit is choosing the strength of the regularization, λ. If the strength is too small, then the regularization will not help separate between different solutions, but if the strength is too large then the fit will be biased heavily toward the shape of the input MC. A simple method for choosing λ is the 'L-curve' technique presented in [97, 113] where a compromise is found between the impact from the regularization (defined by the normalized regularization penalty $\chi^2_{\text{reg}}/\lambda$) and the bias added to the fit (overall χ^2 value). The ideal strength λ is the value which maximizes the curvature of the resulting L-shaped curve. An example L-curve plot is shown in Fig. C.1, where the maximum curvature occurs at $\lambda \sim 1$. In addition the regularization strength is varied around the point of maximum curvature to verify the robustness of the fit; small changes to the regularization strength should have little to no change on the result of the fit. The final value of the regularization strength will depend on the fit to data as the L-curve will change as the fit results change.

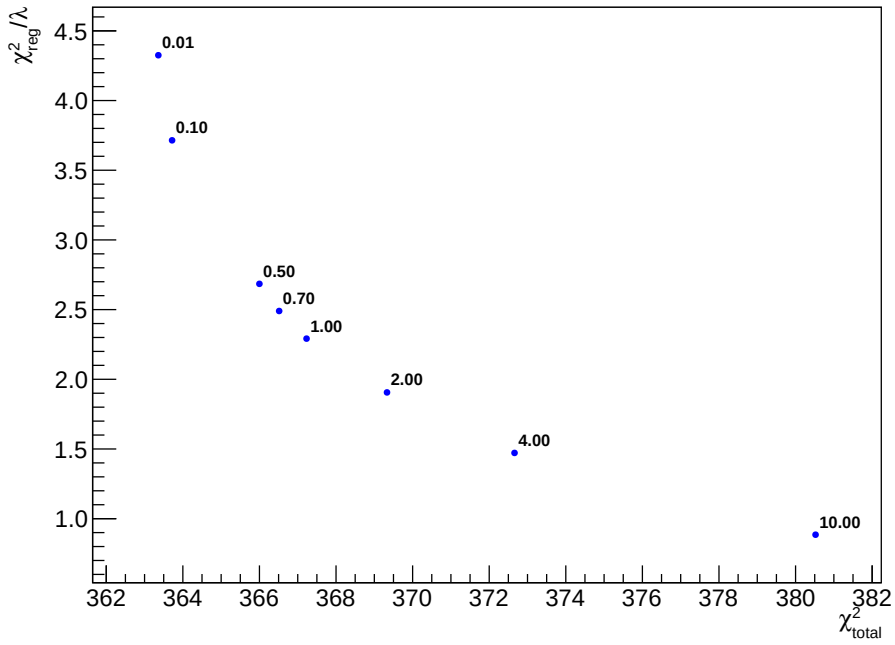

Figure C.1: Example L-curve plot. Each point is labeled with the regularization strength λ, and the point of maximum curvature for this plot occurs at $\lambda \sim 1.0$.

APPENDIX D

PRINCIPAL COMPONENT ANALYSIS

The number of fit parameters for each T2K cross section analysis continues to increase as more data, detectors, targets, and neutrino flavors are added to perform various combined measurements. As the number of fit parameters increases, the fit takes longer to process and can become unstable (no longer converging). This is undesirable for both accuracy/correctness and slows down development and testing of the fit. This section describes two methods used to improve stability of the fit and reduce the time to converge by eigen-decomposing the covariance matrix and performing principle component analysis (PCA) to reduce the dimensionality of the fit. These methods are optional for any given analysis and can be used only during development or as part of the final fit to data, and have been developed to be general tools for T2K cross section analyses.

D.1 Eigen-decomposition

One method to improve stability of the fit is to reduce the number of highly correlated fit parameters, and transform the covariance matrix to an orthogonal matrix. This can be achieved by eigen-decomposing the covariance matrix and using the resulting eigenvalues as the fit parameters, as the eigen-decomposed space is uncorrelated (or orthogonal) [103]. An intrinsic property of the covariance matrix is that it is positive semi-definite and symmetric. For every real symmetric matrix, the eigenvalues are real and the eigenvectors can be chosen such that they are orthogonal [114, 115], thus the covariance matrix can be decomposed as:

$$\Sigma = Q\Lambda Q^{-1} \tag{D.1}$$

where Σ is the covariance matrix, Q is an orthogonal matrix whose columns are the eigenvectors of the covariance matrix, and Λ is a diagonal matrix whose entries are the eigenvalues of the covariance matrix. This can be achieved by standard eigen-decomposition routines or

by performing singular value decomposition on the covariance matrix [102, 103].

When providing the nominal values of the fit parameters to Minuit2, the eigenvalues of the covariance matrix are used corresponding to each fit parameter. The fit then proceeds using the eigen-decomposed values to perform the minimization. However due to the data and MC not being transformed to the eigen-decomposed space, the fit parameters need to be undecomposed when applying the new parameters to the MC each iteration of the fit. To transform the fit parameters to and from the eigen-decomposed space, the matrix of eigenvectors is used. Given a vector of fit parameters, they can be transformed to the decomposed space by multiplying by Q^{-1} and then transformed back by multiplying by Q.

Tests of the fit show that using the eigen-decomposed space gives the same best fit values and improves the performance of the fit, specifically doing a better job exploring the parameters space resulting in correlations which better match expectations. Ideally, the data and the MC would also be transformed to the decomposed space rather than just the fit parameters, but this is currently not possible due to how the separate covariance matrices are calculated and used.

D.2 Dimensionality reduction

The time taken to minimize a multi-dimensional problem has superlinear scaling with respect to the number of function parameters. At small numbers of parameters this is acceptable, however as the number of parameters gets larger the minimization will take far too much time to allow for efficient development of the analysis, and may even exceed the available computing resources. The simple solution is to remove parameters from the fit, however this can cause the fit to give different results and introduce bias, so it must be performed carefully if used. This analysis uses the information contained in the eigenvalues of the covariance matrix to perform principal component analysis (PCA) and identify which parameters to remove. The relative magnitudes of the eigenvalues corresponding to each parameter is a measure of how much variance (or information) in the system that parameter

represents. Parameters with large eigenvalues compared to others contribute more variance than others, while parameters with small eigenvalues contribute little variance when describing the system. Parameters with small eigenvalues representing a small variance have a small impact on the fit and can potentially be neglected without much loss in accuracy [115, 116].

There are multiple methods for choosing which parameters to keep (or neglect), and the method this analysis uses is based on the cumulative percentage of the total variation [116]. Parameters are kept starting with the largest eigenvalue until the cumulative percentage of the total variance meets or exceeds a specified threshold (with the eigenvalues ordered largest to smallest).

$$V(p) = \frac{\sum_{m=0}^{p} \lambda_m}{\sum_{m=0}^{M} \lambda_m} \tag{D.2}$$

$$V(p) \geq V^* \tag{D.3}$$

where $V(p)$ is the cumulative variance fraction of the largest p eigenvalues, λ_m is the m^{th} eigenvalue of M total eigenvalues (ordered largest to smallest), and V^* is the variance threshold. It can be shown that for a covariance matrix the variance of a given eigenvector is equal to its eigenvalue [116].

For a given variance threshold, the parameters corresponding to the first p eigenvalues are kept in the fit while parameters corresponding to the remaining eigenvalues are fixed in the fit. Fixing parameters in the fit reduces the total number of fitted parameters, reducing the run time of the fit and increasing rate of convergence. The choice of how much variance to retain is analysis dependent and can depend on one or more factors such as total number of fit parameters, loss of accuracy, etc. and the variance threshold can be further refined by cross-validation techniques [116].

APPENDIX E

ND280 SAMPLE RECONSTRUCTED BINNING

Most ND280 samples use the reconstructed binning shown in Section 4.5. However to prevent empty bins in the detector covariance (and when running the fit) the μFGD and μFGD+pTPC samples have a different binning. These samples require a muon to be detected as an FGD track which causes the muon kinematic distribution to have lower momentum and higher angle muons (as seen in Fig 4.5). These two samples use the following binning shown in Tab. E.1, while all other ND280 samples use the same binning as the analysis binning shown in Tab. E.2.

Bin index	$\cos\theta_\mu$	p_μ [GeV/c]
0	-1, 0.0	0.0, 0.3
1	-1, 0.0	0.3, 0.45
2	-1, 0.0	0.45, 0.6
3	-1, 0.0	0.6, 30
4	0.0, 0.6	0.0, 0.3
5	0.0, 0.6	0.3, 0.45
6	0.0, 0.6	0.45, 0.7
7	0.0, 0.6	0.7, 30
8	0.6, 0.85	0.0, 0.6
9	0.6, 0.85	0.6, 0.9
10	0.6, 0.85	0.9, 30
11	0.85, 1.0	0.0, 30

Bin index	$\cos\theta_\mu$	p_μ [GeV/c]
0	-1, 0.2	0.0, 30
1	0.2, 0.6	0.0, 0.3
2	0.2, 0.6	0.3, 0.4
3	0.2, 0.6	0.4, 0.5
4	0.2, 0.6	0.5, 0.7
5	0.2, 0.6	0.7, 30
6	0.6, 0.7	0.0, 0.4
7	0.6, 0.7	0.4, 0.6
8	0.6, 0.7	0.6, 30
9	0.7, 0.8	0.0, 0.4
10	0.7, 0.8	0.4, 0.5
11	0.7, 0.8	0.5, 0.6
12	0.7, 0.8	0.6, 0.9
13	0.7, 0.8	0.9, 30
14	0.8, 0.85	0.0, 0.6
15	0.8, 0.85	0.6, 0.9
16	0.8, 0.85	0.9, 30
17	0.85, 0.9	0.0, 0.6
18	0.85, 0.9	0.6, 1.0
19	0.85, 0.9	1.0, 30
20	0.9, 1.0	0, 0.7
21	0.9, 1.0	0.7, 1.2
22	0.9, 1.0	1.2, 30

Table E.1: ND280 reconstructed binning used for the μFGD sample (left) and μFGD+pTPC sample (right).

Bin index	$\cos\theta_\mu$	p_μ [GeV/c]
0	-1, 0.2	0, 30
1	0.2, 0.6	0, 0.3
2	0.2, 0.6	0.3, 0.4
3	0.2, 0.6	0.4, 0.5
4	0.2, 0.6	0.5, 0.6
5	0.2, 0.6	0.6, 30
6	0.6, 0.7	0, 0.3
7	0.6, 0.7	0.3, 0.4
8	0.6, 0.7	0.4, 0.5
9	0.6, 0.7	0.5, 0.6
10	0.6, 0.7	0.6, 0.8
11	0.6, 0.7	0.8, 30
12	0.7, 0.8	0, 0.3
13	0.7, 0.8	0.3, 0.4
14	0.7, 0.8	0.4, 0.5
15	0.7, 0.8	0.5, 0.6
16	0.7, 0.8	0.6, 0.8
17	0.7, 0.8	0.8, 30
18	0.8, 0.85	0, 0.3
19	0.8, 0.85	0.3, 0.4
20	0.8, 0.85	0.4, 0.5
21	0.8, 0.85	0.5, 0.6
22	0.8, 0.85	0.6, 0.8
23	0.8, 0.85	0.8, 1.0
24	0.8, 0.85	1.0, 30
25	0.85, 0.9	0, 0.3
26	0.85, 0.9	0.3, 0.4
27	0.85, 0.9	0.4, 0.5
28	0.85, 0.9	0.5, 0.6
29	0.85, 0.9	0.6, 0.8
30	0.85, 0.9	0.8, 1.0
31	0.85, 0.9	1.0, 1.5
32	0.85, 0.9	1.5, 30
33	0.9, 0.94	0, 0.4
34	0.9, 0.94	0.4, 0.5
35	0.9, 0.94	0.5, 0.6
36	0.9, 0.94	0.6, 0.8
37	0.9, 0.94	0.8, 1.25
38	0.9, 0.94	1.25, 2.0
39	0.9, 0.94	2.0, 30
40	0.94, 0.98	0, 0.4
41	0.94, 0.98	0.4, 0.5
42	0.94, 0.98	0.5, 0.6
43	0.94, 0.98	0.6, 0.8
44	0.94, 0.98	0.8, 1.0
45	0.94, 0.98	1.0, 1.25
46	0.94, 0.98	1.25, 1.5
47	0.94, 0.98	1.5, 2.0
48	0.94, 0.98	2.0, 3.0
49	0.94, 0.98	3.0, 30
50	0.98, 1.0	0, 0.5
51	0.98, 1.0	0.5, 0.7
52	0.98, 1.0	0.7, 0.9
53	0.98, 1.0	0.9, 1.25
54	0.98, 1.0	1.25, 2.0
55	0.98, 1.0	2.0, 3.0
56	0.98, 1.0	3.0, 5.0
57	0.98, 1.0	5.0, 30

Table E.2: ND280 reconstructed binning for all non μFGD samples.

APPENDIX F

EVENT DISTRIBUTIONS IN Q^2

The signal and background event distributions as described in Chapter 4 as a function of true momentum transfer (Q^2).

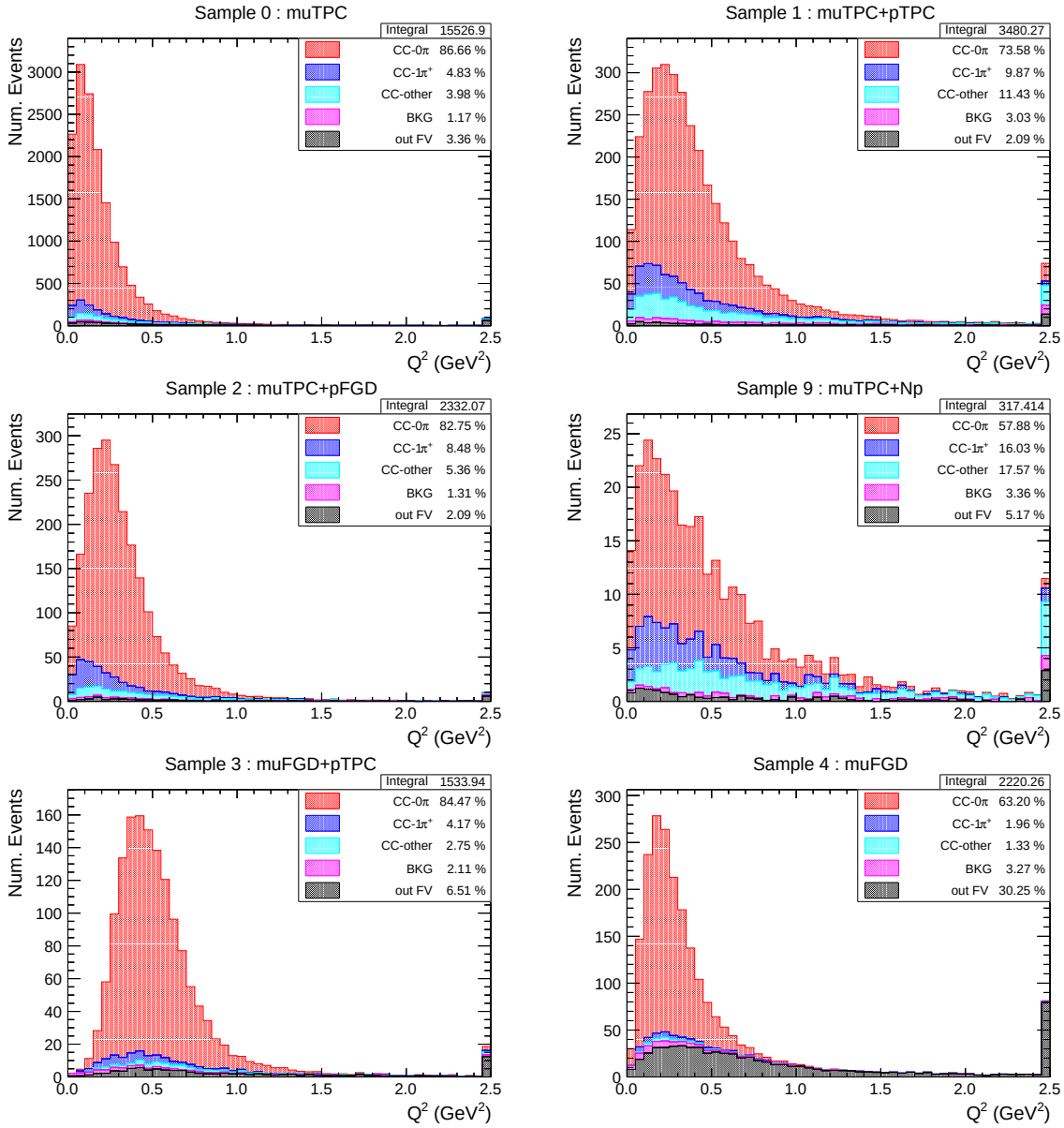

Figure F.1: Event distribution for true momentum transfer (Q^2) for the ND280 signal samples stacked by true topology. The purity of each topology is listed in the legend. The last bin contains all events with $Q^2 > 2.5$ GeV^2.

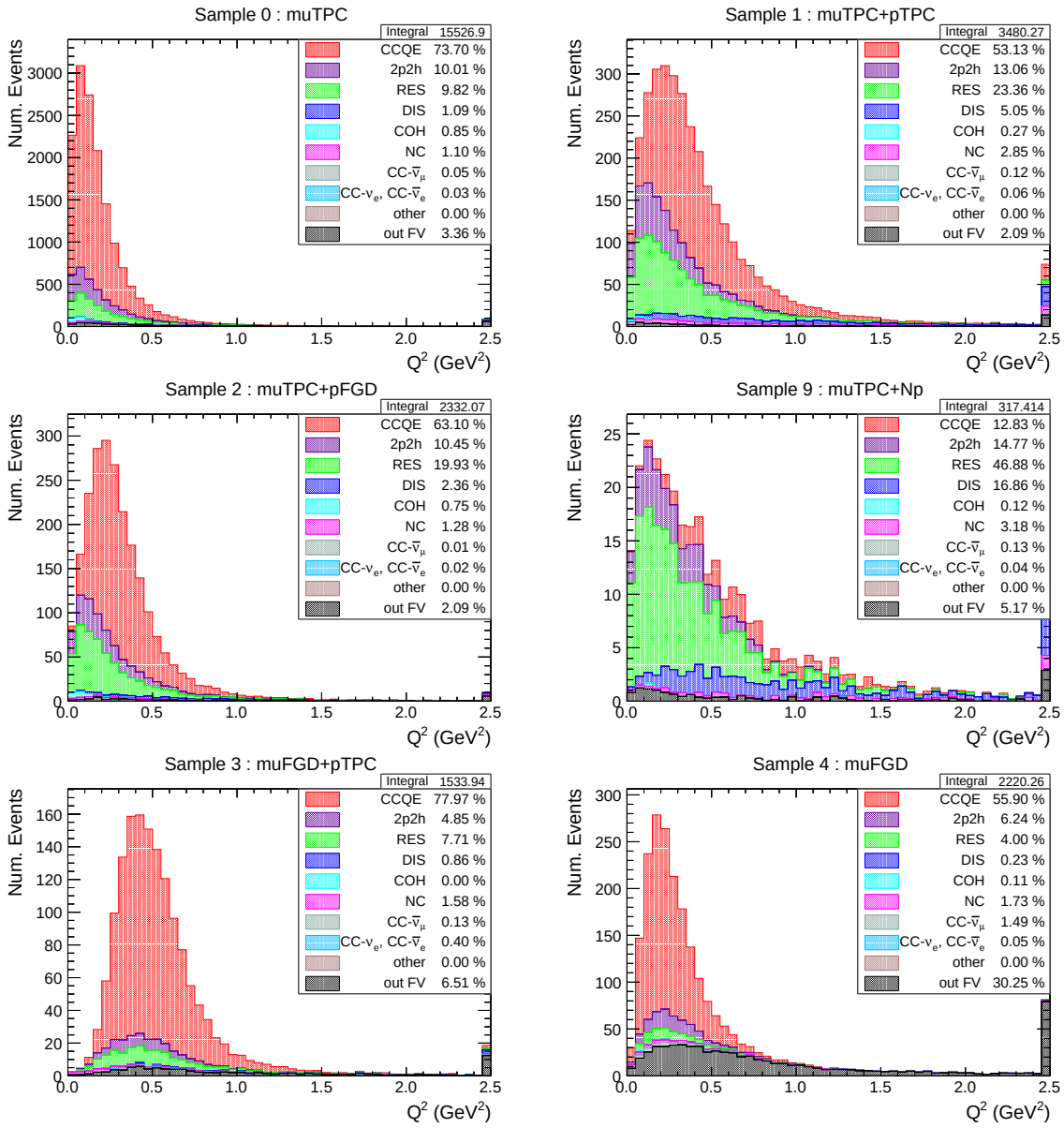

Figure F.2: Event distribution for true momentum transfer (Q^2) for the ND280 signal samples stacked by true reaction. The purity of each reaction is listed in the legend. The last bin contains all events with $Q^2 > 2.5$ GeV^2.

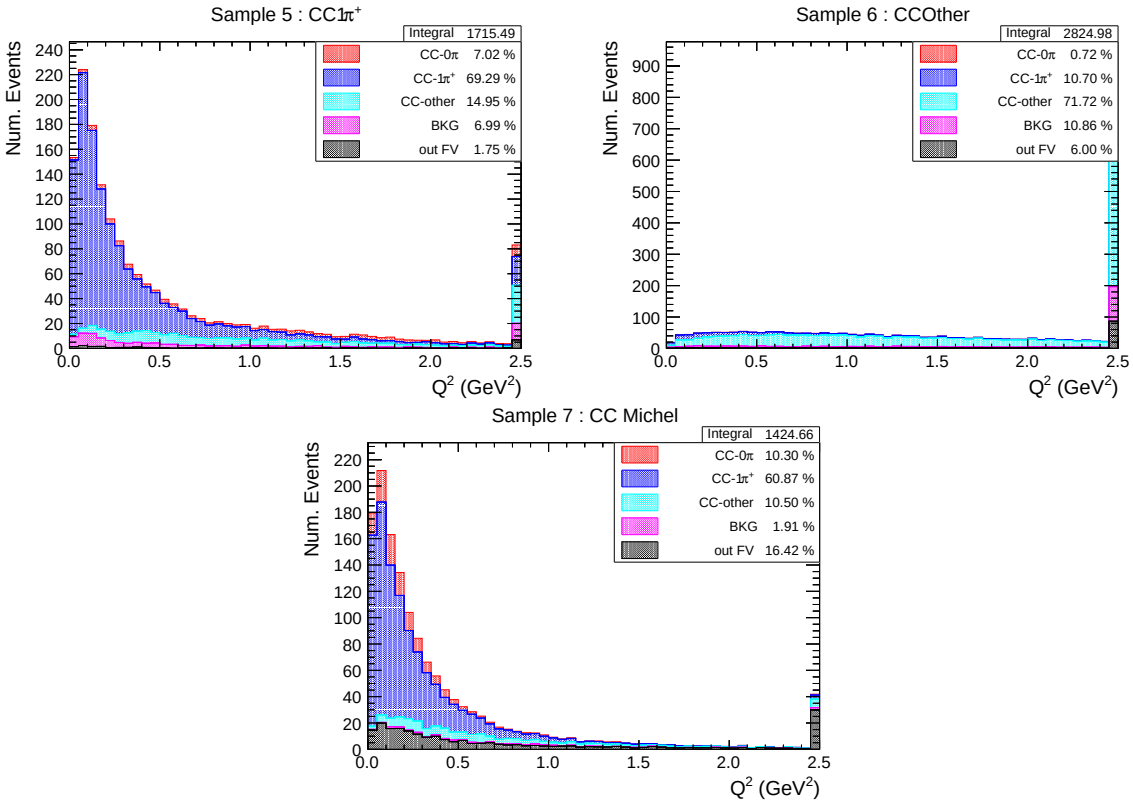

Figure F.3: Event distribution for true momentum transfer (Q^2) for the ND280 sideband samples stacked by true topology. The purity of each topology is listed in the legend. The last bin contains all events with $Q^2 > 2.5$ GeV^2.

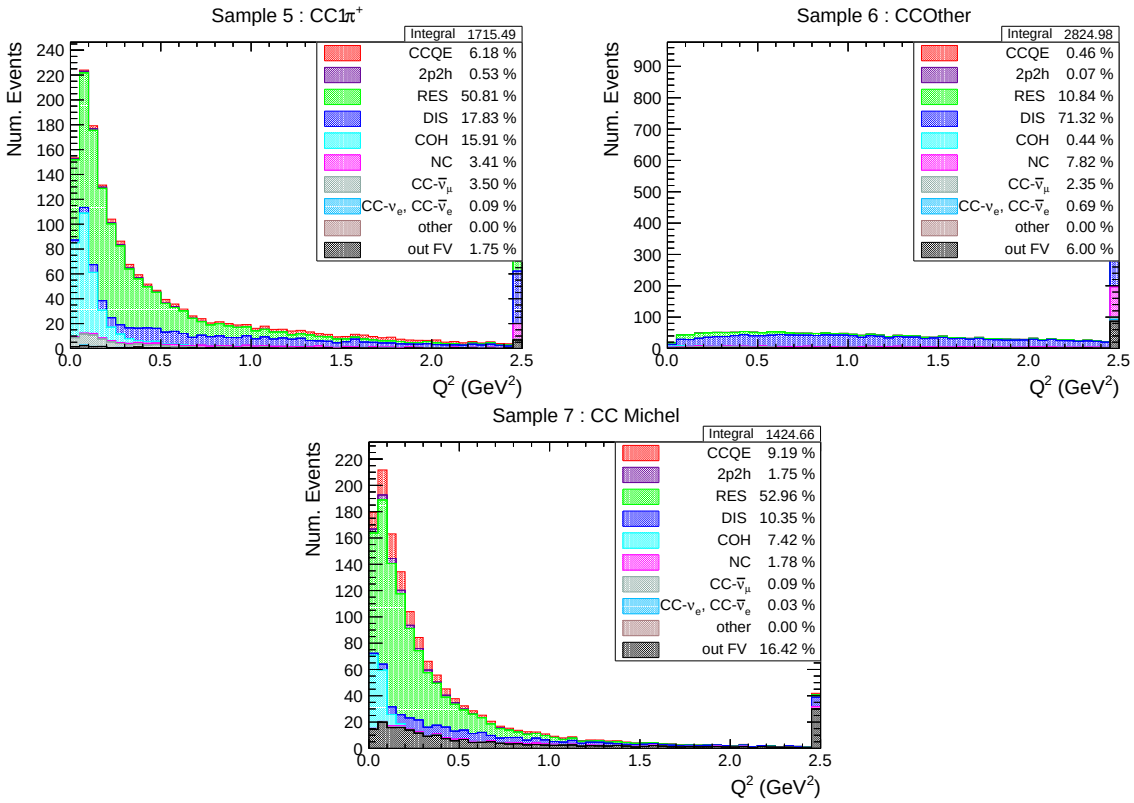

Figure F.4: Event distribution for true momentum transfer (Q^2) for the ND280 sideband samples stacked by true reaction. The purity of each reaction is listed in the legend. The last bin contains all events with $Q^2 > 2.5$ GeV^2.

APPENDIX G

EXTRACTED CROSS SECTION ADDITIONAL PLOTS

This appendix contains additional plots to show the extracted cross section.

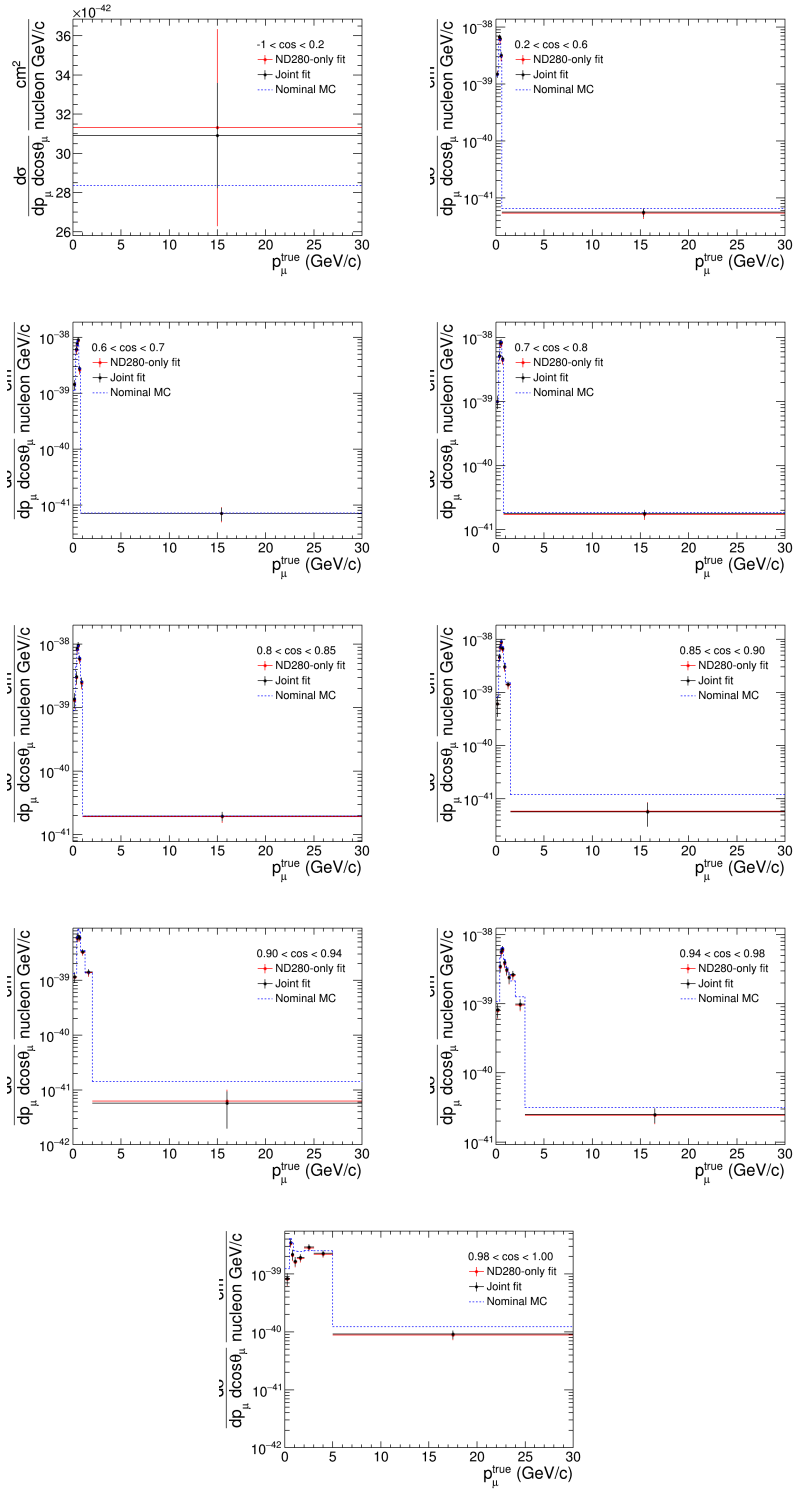

Figure G.1: ND280 extracted cross section bins for joint data fit compared to the nominal MC prediction as a function of muon momentum for slices of muon angle. Note the y-axis is not the same across all the plots.

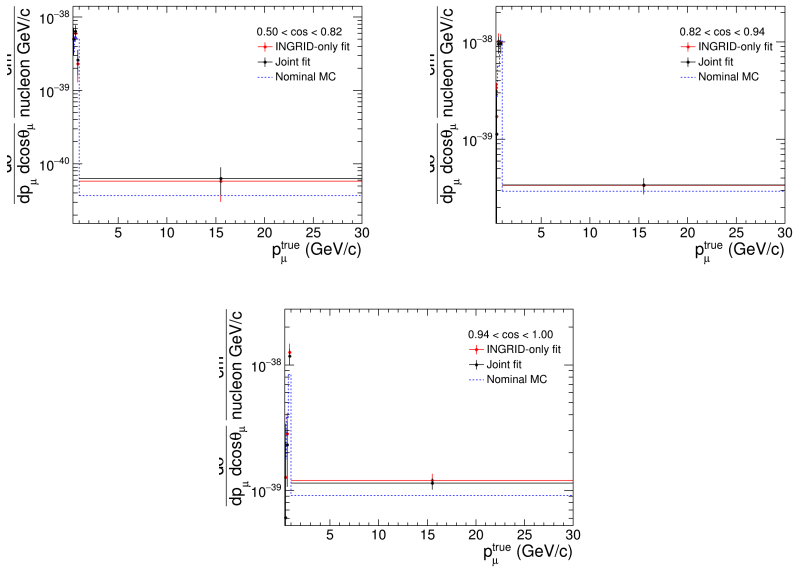

Figure G.2: INGRID extracted cross section bins for the joint data fit compared to the nominal MC prediction as a function of muon momentum for slices of muon angle. Note the y-axis is not the same across all the plots.

BIBLIOGRAPHY

BIBLIOGRAPHY

[1] M. Tanabashi et al. (Particle Data Group), "Review of Particle Physics", Phys. Rev. D vol. 98 p. 030001 (2018), doi:10.1103/PhysRevD.98.030001, URL https://link.aps.org/doi/10.1103/PhysRevD.98.030001

[2] Sara Bolognesi et al., "NIWG model and uncertainties for 2017 oscillation analysis", Tech. Rep. TN-315, T2K (2017), URL https://t2k.org/docs/technotes/315/TN_NIWG_2017_v5

[3] Ciro Riccio et al., "Measurement of ν_μ and $\bar{\nu}_\mu$ CC-0π cross-section on carbon", Tech. Rep. TN-337, T2K (2018), https://t2k.org/docs/technotes/337/t2k-tn-337-v7

[4] Scott Oser, "Elemental Composition of the FGD XY Modules", Tech. Rep. TN-091, T2K (2010), https://t2k.org/docs/technotes/091/xy-chemcomp-v1.2.pdf

[5] Benjamin Quilain et al., "Measurement of the ν_μ cross-section on hydrocarbon and water through the CC-0π channel using the on-axis detectors", Tech. Rep. TN-204, T2K (2018), https://t2k.org/docs/technotes/204/PMWMCC0piv1.3

[6] Fred Reines and Clyde Cowan Jr., "The Reines-Cowan Experiments: Detecting the Poltergeist", Los Alamos Science vol. 25 (1997), URL https://permalink.lanl.gov/object/tr?what=info:lanl-repo/lareport/LA-UR-97-2534-02

[7] K. Abe et al. (The T2K Collaboration), "Measurement of neutrino and antineutrino oscillations by the T2K experiment including a new additional sample of ν_e interactions at the far detector", Phys. Rev. D vol. 96 p. 092006 (2017), doi:10.1103/PhysRevD.96.092006, URL https://link.aps.org/doi/10.1103/PhysRevD.96.092006

[8] K. Abe et al. (Super-Kamiokande Collaboration), "Atmospheric neutrino oscillation analysis with external constraints in Super-Kamiokande I-IV", Phys. Rev. D vol. 97 p. 072001 (2018), doi:10.1103/PhysRevD.97.072001, URL https://link.aps.org/doi/10.1103/PhysRevD.97.072001

[9] M. G. Aartsen et al. (IceCube Collaboration), "Measurement of Atmospheric Neutrino Oscillations at 6–56 GeV with IceCube DeepCore", Phys. Rev. Lett. vol. 120 p. 071801 (2018), doi:10.1103/PhysRevLett.120.071801, URL https://link.aps.org/doi/10.1103/PhysRevLett.120.071801

[10] P. Adamson et al., "Combined Analysis of ν_μ Disappearance and $\nu_\mu \to \nu_e$ Appearance in MINOS Using Accelerator and Atmospheric Neutrinos", Phys. Rev. Lett. vol. 112 p. 191801 (2014), doi:10.1103/PhysRevLett.112.191801, URL https://link.aps.org/doi/10.1103/PhysRevLett.112.191801

[11] M. A. Acero et al. (NOvA Collaboration), "New constraints on oscillation parameters from ν_e appearance and ν_μ disappearance in the NOvA experiment", Phys. Rev. D

vol. 98 p. 032012 (2018), doi:10.1103/PhysRevD.98.032012, URL https://link.aps.org/doi/10.1103/PhysRevD.98.032012

[12] K. Abe et al. (T2K Collaboration), "Search for CP Violation in Neutrino and Antineutrino Oscillations by the T2K Experiment with 2.2×10^{21} Protons on Target", Phys. Rev. Lett. vol. 121 p. 171802 (2018), doi:10.1103/PhysRevLett.121.171802, URL https://link.aps.org/doi/10.1103/PhysRevLett.121.171802

[13] Juan Nieves et al., "Inclusive charged-current neutrino-nucleus reactions", Phys. Rev. C vol. 83 p. 045501 (2011), doi:10.1103/PhysRevC.83.045501, URL https://link.aps.org/doi/10.1103/PhysRevC.83.045501

[14] K. Abe et al. (T2K Collaboration), "T2K neutrino flux prediction", Phys. Rev. D vol. 87 p. 012001 (2013), doi:10.1103/PhysRevD.87.012001, URL https://link.aps.org/doi/10.1103/PhysRevD.87.012001

[15] Arturo Fiorentini et al., "Flux Prediction and Uncertainty Updates with NA61 2009 Thin Target Data and Negative Focussing Mode Predictions", Tech. Rep. TN-217, T2K (2018), https://www.t2k.org/docs/technotes/217/update-for-the-full-run-1-9-flux-after-pub-board-review-comments

[16] K. Abe et al., "The T2K experiment", Nuclear Instruments and Methods in Physics Research Section A: Accelerators, Spectrometers, Detectors and Associated Equipment vol. 659 (1) pp. 106 – 135 (2011), doi:https://doi.org/10.1016/j.nima.2011.06.067, URL http://www.sciencedirect.com/science/article/pii/S0168900211011910

[17] N. Abgrall et al., "Time projection chambers for the T2K near detectors", Nuclear Instruments and Methods in Physics Research Section A: Accelerators, Spectrometers, Detectors and Associated Equipment vol. 637 (1) pp. 25 – 46 (2011), doi:https://doi.org/10.1016/j.nima.2011.02.036, URL http://www.sciencedirect.com/science/article/pii/S0168900211003421

[18] C. L. Cowan et al., "Detection of the Free Neutrino: a Confirmation", Science vol. 124 (3212) pp. 103–104 (1956), doi:10.1126/science.124.3212.103, https://science.sciencemag.org/content/124/3212/103.full.pdf, URL https://science.sciencemag.org/content/124/3212/103

[19] G. Danby et al., "Observation of High-Energy Neutrino Reactions and the Existence of Two Kinds of Neutrinos", Phys. Rev. Lett. vol. 9 pp. 36–44 (1962), doi:10.1103/PhysRevLett.9.36, URL https://link.aps.org/doi/10.1103/PhysRevLett.9.36

[20] K. Kodama et al., "Observation of tau neutrino interactions", Physics Letters B vol. 504 (3) pp. 218 – 224 (2001), doi:https://doi.org/10.1016/S0370-2693(01)00307-0, URL http://www.sciencedirect.com/science/article/pii/S0370269301003070

[21] ALEPH et al., "Precision electroweak measurements on the Z resonance", Physics Reports vol. 427 (5) pp. 257 – 454 (2006), doi:https://doi.org/10.1016/j.physrep.2005.12.006, URL http://www.sciencedirect.com/science/article/pii/S0370157305005119

[22] J. N. Abdurashitov et al., "Solar neutrino flux measurements by the Soviet-American gallium experiment (SAGE) for half the 22-year solar cycle", Journal of Experimental and Theoretical Physics vol. 95 (2) pp. 181–193 (2002), doi:10.1134/1.1506424, URL https://doi.org/10.1134/1.1506424

[23] M. Cribier et al., "Results of the whole GALLEX experiment", Nuclear Physics B - Proceedings Supplements vol. 70 (1) pp. 284 – 291 (1999), doi:https://doi.org/10.1016/S0920-5632(98)00438-1, proceedings of the Fifth International Workshop on topics in Astroparticle and Underground Physics, URL http://www.sciencedirect.com/science/article/pii/S0920563298004381

[24] V. Gribov and B. Pontecorvo, "Neutrino astronomy and lepton charge", Physics Letters B vol. 28 (7) pp. 493 – 496 (1969), doi:https://doi.org/10.1016/0370-2693(69)90525-5, URL http://www.sciencedirect.com/science/article/pii/0370269369905255

[25] B. Pontecorvo, "Mesonium and anti-mesonium", Sov. Phys. JETP vol. 6 p. 429 (1957), [Zh. Eksp. Teor. Fiz.33,549(1957)]

[26] Ziro Maki, Masami Nakagawa, and Shoichi Sakata, "Remarks on the Unified Model of Elementary Particles", Progress of Theoretical Physics vol. 28 (5) pp. 870–880 (1962), doi:10.1143/PTP.28.870, URL https://doi.org/10.1143/PTP.28.870

[27] Q. R. Ahmad et al. (SNO Collaboration), "Direct Evidence for Neutrino Flavor Transformation from Neutral-Current Interactions in the Sudbury Neutrino Observatory", Phys. Rev. Lett. vol. 89 p. 011301 (2002), doi:10.1103/PhysRevLett.89.011301, URL https://link.aps.org/doi/10.1103/PhysRevLett.89.011301

[28] Y. Fukuda et al. (Super-Kamiokande Collaboration), "Evidence for Oscillation of Atmospheric Neutrinos", Phys. Rev. Lett. vol. 81 pp. 1562–1567 (1998), doi:10.1103/PhysRevLett.81.1562, URL https://link.aps.org/doi/10.1103/PhysRevLett.81.1562

[29] Carlo Giunti and Chung W. Kim, Fundamentals of Neutrino Physics and Astrophysics, Oxford University Press (2007)

[30] Francis Halzen and Alan D. Martin, Quarks and Leptons: An introductory course in modern particle physics, Wiley (1984)

[31] C.H. Llewellyn Smith, "Neutrino reactions at accelerator energies", Physics Reports vol. 3 (5) pp. 261 – 379 (1972), doi:https://doi.org/10.1016/0370-1573(72)90010-5, URL http://www.sciencedirect.com/science/article/pii/0370157372900105

[32] R. Bradford, A. Bodek, H. Budd, and J. Arrington, "A New Parameterization of the Nucleon Elastic Form Factors", Nuclear Physics B - Proceedings Supplements vol. 159 pp. 127 – 132 (2006), doi:https://doi.org/10.1016/j.nuclphysbps.2006.08.028, proceedings of the 4th International Workshop on Neutrino-Nucleus Interactions in the Few-GeV Region, URL http://www.sciencedirect.com/science/article/pii/S0920563206005184

[33] Bhubanjyoti Bhattacharya, Richard J. Hill, and Gil Paz, "Model-independent determination of the axial mass parameter in quasielastic neutrino-nucleon scattering", Phys. Rev. D vol. 84 p. 073006 (2011), doi:10.1103/PhysRevD.84.073006, URL https://link.aps.org/doi/10.1103/PhysRevD.84.073006

[34] Stephen Dolan, Probing Nuclear Effects in Neutrino-Nucleus Scattering at the T2K Off-Axis Near Detector Using Transverse Kinematic Imbalances, Ph.D. thesis, University of Oxford (2017), URL https://ora.ox.ac.uk/objects/uuid:16cef4e8-b52b-48c4-a954-81fba0b7536b

[35] J. W. Van Orden and T. W. Donnelly, "Nuclear theory and event generators for charge-changing neutrino reactions", Phys. Rev. C vol. 100 p. 044620 (2019), doi:10.1103/PhysRevC.100.044620, URL https://link.aps.org/doi/10.1103/PhysRevC.100.044620

[36] R.A. Smith and E.J. Moniz, "Neutrino reactions on nuclear targets", Nuclear Physics B vol. 43 pp. 605 – 622 (1972), doi:https://doi.org/10.1016/0550-3213(72)90040-5, URL http://www.sciencedirect.com/science/article/pii/0550321372900405

[37] Joanna E. Sobczyk, "Intercomparison of lepton-nucleus scattering models in the quasielastic region", Phys. Rev. C vol. 96 p. 045501 (2017), doi:10.1103/PhysRevC.96.045501, URL https://link.aps.org/doi/10.1103/PhysRevC.96.045501

[38] Omar Benhar and Adelchi Fabrocini, "Two-nucleon spectral function in infinite nuclear matter", Phys. Rev. C vol. 62 p. 034304 (2000), doi:10.1103/PhysRevC.62.034304, URL https://link.aps.org/doi/10.1103/PhysRevC.62.034304

[39] R. González-Jiménez et al., "Extensions of superscaling from relativistic mean field theory: The SuSAv2 model", Phys. Rev. C vol. 90 p. 035501 (2014), doi:10.1103/PhysRevC.90.035501, URL https://link.aps.org/doi/10.1103/PhysRevC.90.035501

[40] G. D. Megias et al., "Meson-exchange currents and quasielastic predictions for charged-current neutrino-^{12}C scattering in the superscaling approach", Phys. Rev. D vol. 91 p. 073004 (2015), doi:10.1103/PhysRevD.91.073004, URL https://link.aps.org/doi/10.1103/PhysRevD.91.073004

[41] Stephen Dolan, Guillermo Megias, and Sara Bolognesi, "Implementation of the SuSAv2-MEC 1p1h and 2p2h models in GENIE and analysis of nuclear effects in T2K measurements", (2019), 1905.08556

[42] Arie Bodek and Tejin Cai, "Removal energies and final state interaction in lepton nucleus scattering", The European Physical Journal C vol. 79 (4) p. 293 (2019), doi:10.1140/epjc/s10052-019-6750-3, URL https://doi.org/10.1140/epjc/s10052-019-6750-3

[43] Alexander Fetter and John Walecka, Quantum theory of many-particle systems, McGraw-Hill (1971)

[44] Dieter Rein and Lalit M. Sehgal, "Coherent π^0 production in neutrino reactions", Nuclear Physics B vol. 223 (1) pp. 29 – 44 (1983), doi:https://doi.org/10.

1016/0550-3213(83)90090-1, URL http://www.sciencedirect.com/science/article/pii/0550321383900901

[45] Ch. Berger and L. M. Sehgal, "Partially conserved axial vector current and coherent pion production by low energy neutrinos", Phys. Rev. D vol. 79 p. 053003 (2009), doi:10.1103/PhysRevD.79.053003, URL https://link.aps.org/doi/10.1103/PhysRevD.79.053003

[46] Xilin Zhang and Brian D. Serot, "Coherent neutrinoproduction of photons and pions in a chiral effective field theory for nuclei", Phys. Rev. C vol. 86 p. 035504 (2012), doi:10.1103/PhysRevC.86.035504, URL https://link.aps.org/doi/10.1103/PhysRevC.86.035504

[47] L. Alvarez-Ruso et al., "NuSTEC White Paper: Status and challenges of neutrino-nucleus scattering", Progress in Particle and Nuclear Physics vol. 100 pp. 1 – 68 (2018), doi:https://doi.org/10.1016/j.ppnp.2018.01.006, URL http://www.sciencedirect.com/science/article/pii/S0146641018300061

[48] Yoshinari Hayato, "A neutrino interaction simulation program library NEUT", Acta Phys. Polon. vol. B40 pp. 2477–2489 (2009)

[49] C. Andreopoulos et al., "The GENIE neutrino Monte Carlo generator", Nuclear Instruments and Methods in Physics Research Section A: Accelerators, Spectrometers, Detectors and Associated Equipment vol. 614 (1) pp. 87 – 104 (2010), doi:https://doi.org/10.1016/j.nima.2009.12.009, URL http://www.sciencedirect.com/science/article/pii/S0168900209023043

[50] Tomasz Golan, Cezary Juszczak, and Jan T. Sobczyk, "Effects of final-state interactions in neutrino-nucleus interactions", Phys. Rev. C vol. 86 p. 015505 (2012), doi:10.1103/PhysRevC.86.015505, URL https://link.aps.org/doi/10.1103/PhysRevC.86.015505

[51] T. Leitner, O. Buss, L. Alvarez-Ruso, and U. Mosel, "Electron- and neutrino-nucleus scattering from the quasielastic to the resonance region", Phys. Rev. C vol. 79 p. 034601 (2009), doi:10.1103/PhysRevC.79.034601, URL https://link.aps.org/doi/10.1103/PhysRevC.79.034601

[52] M. Betancourt et al., "Comparisons and challenges of modern neutrino scattering experiments (TENSIONS2016 report)", Physics Reports vol. 773-774 pp. 1 – 28 (2018), doi:https://doi.org/10.1016/j.physrep.2018.08.003, comparisons and challenges of modern neutrino scattering experiments (TENSIONS2016 report), URL http://www.sciencedirect.com/science/article/pii/S0370157318302175

[53] Véronique Bernard, Latifa Elouadrhiri, and Ulf-G Meißner, "Axial structure of the nucleon", Journal of Physics G: Nuclear and Particle Physics vol. 28 (1) pp. R1–R35 (2001), doi:10.1088/0954-3899/28/1/201, URL https://doi.org/10.1088%2F0954-3899%2F28%2F1%2F201

[54] R. Gran et al. (K2K Collaboration), "Measurement of the quasielastic axial vector mass in neutrino interactions on oxygen", Phys. Rev. D vol. 74 p. 052002 (2006), doi:10.1103/PhysRevD.74.052002, URL https://link.aps.org/doi/10.1103/PhysRevD.74.052002

[55] A. A. Aguilar-Arevalo et al. (MiniBooNE), "First Measurement of the Muon Neutrino Charged Current Quasielastic Double Differential Cross Section", Phys. Rev. vol. D81 p. 092005 (2010), doi:10.1103/PhysRevD.81.092005, 1002.2680

[56] V Lyubushkin et al. (NOMAD), "A Study of quasi-elastic muon neutrino and antineutrino scattering in the NOMAD experiment", Eur. Phys. J. vol. C63 pp. 355–381 (2009), doi:10.1140/epjc/s10052-009-1113-0, 0812.4543

[57] M. Martini, M. Ericson, G. Chanfray, and J. Marteau, "Neutrino and antineutrino quasielastic interactions with nuclei", Phys. Rev. C vol. 81 p. 045502 (2010), doi:10.1103/PhysRevC.81.045502, URL https://link.aps.org/doi/10.1103/PhysRevC.81.045502

[58] K. Abe et al., "Proposal for an Extended Run of T2K to 20×10^{21} POT", (2016), 1609.04111

[59] Hyper-Kamiokande Proto-Collaboration, K. Abe et al., "Physics potential of a long-baseline neutrino oscillation experiment using a J-PARC neutrino beam and Hyper-Kamiokande", Progress of Theoretical and Experimental Physics vol. 2015 (5) (2015), doi:10.1093/ptep/ptv061, 053C02, https://academic.oup.com/ptep/article-pdf/2015/5/053C02/7697513/ptv061.pdf, URL https://doi.org/10.1093/ptep/ptv061

[60] K. Abe et al. (T2K Collaboration), "Indication of Electron Neutrino Appearance from an Accelerator-Produced Off-Axis Muon Neutrino Beam", Phys. Rev. Lett. vol. 107 p. 041801 (2011), doi:10.1103/PhysRevLett.107.041801, URL https://link.aps.org/doi/10.1103/PhysRevLett.107.041801

[61] K. Abe et al. (T2K Collaboration), "Observation of Electron Neutrino Appearance in a Muon Neutrino Beam", Phys. Rev. Lett. vol. 112 p. 061802 (2014), doi:10.1103/PhysRevLett.112.061802, URL https://link.aps.org/doi/10.1103/PhysRevLett.112.061802

[62] K. Abe et al. (T2K Collaboration), "First measurement of the ν_μ charged-current cross section on a water target without pions in the final state", Phys. Rev. D vol. 97 p. 012001 (2018), doi:10.1103/PhysRevD.97.012001, URL https://link.aps.org/doi/10.1103/PhysRevD.97.012001

[63] K. Abe et al. (T2K Collaboration), "Measurement of inclusive double-differential ν_μ charged-current cross section with improved acceptance in the T2K off-axis near detector", Phys. Rev. D vol. 98 p. 012004 (2018), doi:10.1103/PhysRevD.98.012004, URL https://link.aps.org/doi/10.1103/PhysRevD.98.012004

[64] K. Abe et al. (The T2K Collaboration), "Measurement of $\overline{\nu}_\mu$ and ν_μ charged current inclusive cross sections and their ratio with the T2K off-axis near detector", Phys. Rev.

D vol. 96 p. 052001 (2017), doi:10.1103/PhysRevD.96.052001, URL https://link.aps.org/doi/10.1103/PhysRevD.96.052001

[65] K. Abe et al. (The T2K Collaboration), "Characterization of nuclear effects in muon-neutrino scattering on hydrocarbon with a measurement of final-state kinematics and correlations in charged-current pionless interactions at T2K", Phys. Rev. D vol. 98 p. 032003 (2018), doi:10.1103/PhysRevD.98.032003, URL https://link.aps.org/doi/10.1103/PhysRevD.98.032003

[66] K. Abe et al. (The T2K Collaboration), "Measurement of the ν_μ charged current quasielastic cross section on carbon with the T2K on-axis neutrino beam", Phys. Rev. D vol. 91 p. 112002 (2015), doi:10.1103/PhysRevD.91.112002, URL https://link.aps.org/doi/10.1103/PhysRevD.91.112002

[67] T.T. Böhlen et al., "The FLUKA Code: Developments and Challenges for High Energy and Medical Applications", Nuclear Data Sheets vol. 120 pp. 211 – 214 (2014), doi:https://doi.org/10.1016/j.nds.2014.07.049, URL http://www.sciencedirect.com/science/article/pii/S0090375214005018

[68] A. Ferrari, P.R. Sala, A. Fasso, and J. Ranft, "FLUKA: a multi-particle transport code", Tech. Rep. CERN-2005-10, INFN/TC_05/11, SLAC-R-773 (2005)

[69] M. Apollonio et al. (HARP Collaboration), "Forward production of charged pions with incident protons on nuclear targets at the CERN Proton Synchrotron", Phys. Rev. C vol. 80 p. 035208 (2009), doi:10.1103/PhysRevC.80.035208, URL https://link.aps.org/doi/10.1103/PhysRevC.80.035208

[70] N. Abgrall et al. (NA61/SHINE Collaboration), "Measurements of cross sections and charged pion spectra in proton-carbon interactions at 31 GeV/c", Phys. Rev. C vol. 84 p. 034604 (2011), doi:10.1103/PhysRevC.84.034604, URL https://link.aps.org/doi/10.1103/PhysRevC.84.034604

[71] N. Abgrall et al. (NA61/SHINE Collaboration), "Measurement of production properties of positively charged kaons in proton-carbon interactions at 31 GeV/c", Phys. Rev. C vol. 85 p. 035210 (2012), doi:10.1103/PhysRevC.85.035210, URL https://link.aps.org/doi/10.1103/PhysRevC.85.035210

[72] N. Abgrall et al. (NA61/SHINE Collaboration), "Measurements of production properties of K^0_S mesons and Λ hyperons in proton-carbon interactions at 31 GeV/c", Phys. Rev. C vol. 89 p. 025205 (2014), doi:10.1103/PhysRevC.89.025205, URL https://link.aps.org/doi/10.1103/PhysRevC.89.025205

[73] S. Assylbekov et al., "The T2K ND280 off-axis pi–zero detector", Nuclear Instruments and Methods in Physics Research Section A: Accelerators, Spectrometers, Detectors and Associated Equipment vol. 686 pp. 48 – 63 (2012), doi:https://doi.org/10.1016/j.nima.2012.05.028, URL http://www.sciencedirect.com/science/article/pii/S0168900212005153

[74] S. Agostinelli et al., "Geant4—a simulation toolkit", Nuclear Instruments and Methods in Physics Research Section A: Accelerators, Spectrometers, Detectors and Associated Equipment vol. 506 (3) pp. 250 – 303 (2003), doi:https://doi.org/10.1016/S0168-9002(03)01368-8, URL http://www.sciencedirect.com/science/article/pii/S0168900203013688

[75] Margherita Buizza Avanzini et al., "Measurement of flux-integrated cross-section on oxygen and oxygen/carbon ratio of CC-0π events in the FGD1 and FGD2", Tech. Rep. TN-338, T2K (2018), https://t2k.org/docs/technotes/338/TN338v41

[76] Anselmo Cervera et al., "CC-0πMulti-Topology selection and systematics in FGD1", Tech. Rep. TN-216, T2K (2015), https://t2k.org/docs/technotes/216/fgd1numuccqeselsysv0

[77] Laura Monfregola, Muon neutrino charged current quai-elastic interactions in the T2K off-axis near detector, Ph.D. thesis, Universtitat de Valencia (2015), URL http://www.t2k.org/docs/thesis/063/LauraMonfregolaThesis

[78] Claudio Giganti and Marco Zito, "Particle Identification with the T2K TPC", Tech. Rep. TN-001, T2K (2009), https://t2k.org/docs/technotes/001/dEdxnote_v2

[79] Clarence Wret, Minimising systematic uncertainties in the T2K Experiment using near-detector and external data, Ph.D. thesis, Imperial College London (2018), URL https://t2k.org/docs/thesis/097/clarencewretthesis

[80] Caio Liccardi and Mauricio Barbi, "Particle identification with the Fine Grained Detectors", Tech. Rep. TN-103, T2K (2010), https://t2k.org/docs/technotes/103/FGDPIDNote_caio_v1.pdf

[81] Yoav Freund and Robert E Schapire, "A Decision-Theoretic Generalization of On-Line Learning and an Application to Boosting", Journal of Computer and System Sciences vol. 55 (1) pp. 119 – 139 (1997), doi:https://doi.org/10.1006/jcss.1997.1504, URL http://www.sciencedirect.com/science/article/pii/S002200009791504X

[82] P Speckmayer, A Höcker, J Stelzer, and H Voss, "The toolkit for multivariate data analysis, TMVA 4", Journal of Physics: Conference Series vol. 219 (3) p. 032057 (2010), doi:10.1088/1742-6596/219/3/032057, URL https://doi.org/10.1088%2F1742-6596%2F219%2F3%2F032057

[83] Lucie Maret et al., "Improved measurement of the flux-integrated ν_μ CC-0π cross section on carbon and water with the FGD1 and FGD2 detectors", Tech. Rep. TN-380, T2K (2019), https://t2k.org/docs/technotes/380/tn380_v0r1

[84] K. Abe et al. (T2K Collaboration), "Measurements of neutrino oscillation in appearance and disappearance channels by the T2K experiment with 6.6×10^{20} protons on target", Phys. Rev. D vol. 91 p. 072010 (2015), doi:10.1103/PhysRevD.91.072010, URL https://link.aps.org/doi/10.1103/PhysRevD.91.072010

[85] P. Bartet et al., "ν_μCC event selections in the ND280 tracker using Run 2+3+4 data", Tech. Rep. TN-212, T2K (2015), https://t2k.org/docs/technotes/212/tn-212-v-2-1.1

[86] Matthieu et al., "Differential measurement of the ν_μ CC-1π cross section on H_2O and CH and of the H_2O/CH cross section ratio using the on-axis detectors", Tech. Rep. TN-352, T2K (2018), https://t2k.org/docs/technotes/352/TN352v3.0

[87] D. Rein, "Angular distribution in neutrino-induced single pion production processes", Zeitschrift für Physik C Particles and Fields vol. 35 (1) pp. 43–64 (1987), doi:10.1007/BF01561054, URL https://doi.org/10.1007/BF01561054

[88] Dieter Rein and Lalit M Sehgal, "Neutrino-excitation of baryon resonances and single pion production", Annals of Physics vol. 133 (1) pp. 79 – 153 (1981), doi:https://doi.org/10.1016/0003-4916(81)90242-6, URL http://www.sciencedirect.com/science/article/pii/0003491681902426

[89] Torbjörn Sjöstrand, "High-energy-physics event generation with PYTHIA 5.7 and JETSET 7.4", Computer Physics Communications vol. 82 (1) pp. 74 – 89 (1994), doi:https://doi.org/10.1016/0010-4655(94)90132-5, URL http://www.sciencedirect.com/science/article/pii/0010465594901325

[90] M. Glück, E. Reya, and A. Vogt, "Dynamical parton distributions revisited", The European Physical Journal C - Particles and Fields vol. 5 (3) pp. 461–470 (1998), doi:10.1007/s100529800978, URL https://doi.org/10.1007/s100529800978

[91] A. Bodek and U. K. Yang, "Modeling Neutrino and Electron Scattering Cross Sections in the Few GeV Region with Effective LO PDFs", AIP Conference Proceedings vol. 670 (1) pp. 110–117 (2003), doi:10.1063/1.1594324, URL https://aip.scitation.org/doi/abs/10.1063/1.1594324

[92] L.L. Salcedo, E. Oset, M.J. Vicente-Vacas, and C. Garcia-Recio, "Computer simulation of inclusive pion nuclear reactions", Nuclear Physics A vol. 484 (3) pp. 557 – 592 (1988), doi:https://doi.org/10.1016/0375-9474(88)90310-7, URL http://www.sciencedirect.com/science/article/pii/0375947488903107

[93] Glen Cowan, Statistical Data Analysis, Oxford University Press (1998)

[94] Roger Barlow and Christine Beeston, "Fitting using finite Monte Carlo samples", Computer Physics Communications vol. 77 (2) pp. 219 – 228 (1993), doi:https://doi.org/10.1016/0010-4655(93)90005-W, URL http://www.sciencedirect.com/science/article/pii/001046559390005W

[95] G. D'Agostini, "A multidimensional unfolding method based on Bayes' theorem", Nuclear Instruments and Methods in Physics Research Section A: Accelerators, Spectrometers, Detectors and Associated Equipment vol. 362 (2) pp. 487 – 498 (1995), doi:https://doi.org/10.1016/0168-9002(95)00274-X, URL http://www.sciencedirect.com/science/article/pii/016890029500274X

[96] Frank Porter and Ilya Narsky, Statistical Analysis Techniques in Particle Physics, Wiley-VCH (2014)

[97] Luca Lista, Statistical Methods for Data Analysis in Particle Physics, Springer, second edn. (2017)

[98] Stefan Schmitt, "Data Unfolding Methods in High Energy Physics", EPJ Web Conf. vol. 137 p. 11008 (2017), doi:10.1051/epjconf/201713711008, URL https://doi.org/10.1051/epjconf/201713711008

[99] Francesco Spanò, "Unfolding in particle physics: a window on solving inverse problems", EPJ Web of Conferences vol. 55 p. 03002 (2013), doi:10.1051/epjconf/20135503002, URL https://doi.org/10.1051/epjconf/20135503002

[100] Fred James and Matthias Winkler, Minuit 2, CERN (2018), https://root.cern.ch/guides/minuit2-manual

[101] W. Davidon, "Variable Metric Method for Minimization", SIAM Journal on Optimization vol. 1 (1) pp. 1–17 (1991), doi:10.1137/0801001, URL https://doi.org/10.1137/0801001

[102] William H. Press, Saul A. Teukolsky, William T. Vetterling, and Brian P. Flannery, Numerical Recipes in C, Cambridge University Press, second edn. (1992)

[103] James E. Gentle, Matrix Algebra, Springer, second edn. (2017)

[104] Philip R. Bevington and D. Keith Robinson, Data Reduction and Error Analysis for the Physical Sciences, McGraw-Hill, third edn. (2003)

[105] C. L. McGivern et al. (MINERvA Collaboration), "Cross sections for ν_μ and $\overline{\nu}_\mu$ induced pion production on hydrocarbon in the few-GeV region using MINERvA", Phys. Rev. D vol. 94 p. 052005 (2016), doi:10.1103/PhysRevD.94.052005, URL https://link.aps.org/doi/10.1103/PhysRevD.94.052005

[106] P. Adamson et al. (MINOS Collaboration), "Study of quasielastic scattering using charged-current ν_μ-iron interactions in the MINOS near detector", Phys. Rev. D vol. 91 p. 012005 (2015), doi:10.1103/PhysRevD.91.012005, URL https://link.aps.org/doi/10.1103/PhysRevD.91.012005

[107] D. Ruterbories et al. (MINERνA Collaboration), "Measurement of quasielastic-like neutrino scattering at $\langle E_\nu \rangle \sim 3.5$ GeV on a hydrocarbon target", Phys. Rev. D vol. 99 p. 012004 (2019), doi:10.1103/PhysRevD.99.012004, URL https://link.aps.org/doi/10.1103/PhysRevD.99.012004

[108] A. Higuera et al. (MINERvA Collaboration), "Measurement of Coherent Production of $\pi^\pm$ in Neutrino and Antineutrino Beams on Carbon from E_ν of 1.5 to 20 GeV", Phys. Rev. Lett. vol. 113 p. 261802 (2014), doi:10.1103/PhysRevLett.113.261802, URL https://link.aps.org/doi/10.1103/PhysRevLett.113.261802

[109] Sara Bolognesi et al., "Model independent ν_μ CC-0π cross-section in ND280", Tech. Rep. TN-214, T2K (2014), http://www.t2k.org/docs/technotes/214/cc0piFitterV1.5

[110] David Coplowe et al., "Probing nuclear effects with a CC-0π +Np differential cross-section measurement", Tech. Rep. TN-287, T2K (2016), URL https://t2k.org/docs/technotes/287/probing-nuclear-effects-with-a-cc0pi-np-differential-cross-section-measurement-tn287v11

[111] Harrison B. Prosper and Louis Lyons (Eds.), Proceedings, PHYSTAT 2011 Workshop on Statistical Issues Related to Discovery Claims in Search Experiments and Unfolding, CERN,Geneva, Switzerland 17-20 January 2011, CERN, CERN, Geneva (2011), doi:10.5170/CERN-2011-006

[112] Sergey Kabanikhin, "Definitions and Examples of Inverse and Ill-Posed Problems", Journal of Inverse and Ill-Posed Problems vol. 16 pp. 317–357 (2008), doi:10.1515/JIIP.2008.019

[113] Per Christian Hansen, "Analysis of Discrete Ill-Posed Problems by Means of the L-Curve", SIAM Review vol. 34 (4) pp. 561–580 (1992), doi:10.1137/1034115

[114] James R. Schott, Matrix Analysis for Statistics, Wiley, third edn. (2016)

[115] Rene Vidal, Yi Ma, and S. Shankar Sastry, Generalized Principal Component Analysis, Springer, first edn. (2016)

[116] I. T. Jolliffe, Principal Component Analysis, Springer, second edn. (2002)